Quantifying Electromigration Processes in

Sn-0.7Cu Solder with

Lab-Scale X-Ray Computed Micro-Tomography

by

James Charles Edwin Mertens

A Dissertation Presented in Partial Fulfillment
of the Requirements for the Degree
Doctor of Philosophy

Approved April 2015 by the
Graduate Supervisory Committee:

Nikhilesh Chawla, Chair
Yang Jiao
Narayanan Neithalath
Terry Alford

ARIZONA STATE UNIVERSITY

May 2015

ABSTRACT

For decades, microelectronics manufacturing has been concerned with failures related to electromigration phenomena in conductors experiencing high current densities. The influence of interconnect microstructure on device failures related to electromigration in BGA and flip chip solder interconnects has become a significant interest with reduced individual solder interconnect volumes. A survey indicates that x-ray computed micro-tomography (μXCT) is an emerging, novel means for characterizing the microstructures' role in governing electromigration failures. This work details the design and construction of a lab-scale μXCT system to characterize electromigration in the Sn-0.7Cu lead-free solder system by leveraging *in situ* imaging.

In order to enhance the attenuation contrast observed in multi-phase material systems, a modeling approach has been developed to predict settings for the controllable imaging parameters which yield relatively high detection rates over the range of x-ray energies for which maximum attenuation contrast is expected in the polychromatic x-ray imaging system. In order to develop this predictive tool, a model has been constructed for the Bremsstrahlung spectrum of an x-ray tube, and calculations for the detector's efficiency over the relevant range of x-ray energies have been made, and the product of emitted and detected spectra has been used to calculate the effective x-ray imaging spectrum. An approach has also been established for filtering 'zinger' noise in x-ray radiographs, which has proven problematic at high x-ray energies used for solder imaging. The performance of this filter has been compared with a known existing method and the results indicate a significant increase in the accuracy of zinger filtered radiographs.

The obtained results indicate the conception of a powerful means for the study of failure causing processes in solder systems used as interconnects in microelectronic packaging devices. These results include the volumetric quantification of parameters which are indicative of both electromigration tolerance of solders and the dominant mechanisms for atomic migration in response to current stressing. This work is aimed to further the community's understanding of failure-causing electromigration processes in industrially relevant material systems for microelectronic interconnect applications and to advance the capability of available characterization techniques for their interrogation.

ACKNOWLEDGMENTS

I would like to acknowledge the guidance and support of my Advisor, Professor Nikhilesh Chawla, without whom, my research would not be possible. I would like to acknowledge the expert advice, support, and contributions of Arizona State University Research Scientist, Dr. Jason Williams, in completing this dissertation. Dr. Jason Williams was instrumental in overcoming the technical challenges in the design of the CT system here described, assisting with the scan program routine implementation in LabVIEW, helping establish data processing code and philosophy, and had independently implemented both the cone-beam reconstruction algorithm as well as the beam hardening cupping artifact correction which are both used throughout this work. I would also like express my gratitude toward my committee members, Professor Terry Alford, Professor Yang Jiao, and Professor Narayanan Neithalath for their time and interest in the evaluation of my doctoral research and my academic progress. I would like to acknowledge the financial support of the Semiconductor Research Corporation (SRC) through task #1292.086/.087, research direction from the SRC review panel, and technical guidance from the Task's industrial liaison's, Minhua Lu (IBM), Mario Pacheco (Intel), and Brett Wilkerson (Freescale Semiconductor). I would like to acknowledge my predecessors for their pioneering accomplishments related to this research, including but not limited to Eric Padilla and Dr. Huxiao Xie. I would also like to also acknowledge all of my colleagues in Professor Chawla's Research Group for their help and collaboration.

I want to thank my parents, David and Melissa, for passing on to me their passion for learning and for all of their support along the way. I thank my father for providing me with an affinity toward careful and logical thought, and for instilling in me a curiosity in the mysterious physical world in which we live. I thank my mother for teaching me to seek the perspective of others and for passing forth her organized and methodical nature. I would like to also acknowledge the unrelenting support of my fiancé, Amy Elizabeth Saaty, for always encouraging my aspirations, and supporting the countless long days and late nights that I have invested in this work. Finally, I would like to thank all of my family for their love and support and for always believing in me. Thank you!

TABLE OF CONTENTS

Page

LIST OF TABLES ix

LIST OF FIGURES xii

CHAPTER

1 INTRODUCTION 1

2 A REVIEW OF RELEVANT LITERATURE: INTERCONNECT ARCHITECTURES AND MATERIALS, ELECTROMIGRATION PHENOMENA, ELECTROMIGRATION TESTING, AND MICROSTRUCTURAL CHARACTERIZATION 8

Solder Alloys and Microstructures Relevant to Microelectronics Packaging 9

Failure Modes and Testing of Microelectronic Solder Interconnects 12

Electromigration Principles 15

Electromigration Testing of Lead-Free Solder Interconnects 22

X-Ray Computed Tomography of Solders 29

Objective for In Situ Lab-Scale µXCT Characterization of Electromigration Damage Processes 33

3 THE DEVELOPMENT OF A LAB-SCALE X-RAY COMPUTED TOMOGRAPHY SYSTEM FOR THREE-DIMENSIONAL MATERIALS CHARACTERIZATION 34

Introduction 34

System Performance Goals 37

Design Methodology 39

CHAPTER Page

X-Ray Source Selection 42

X-Ray Detector Design and Component Selection 48

Rotation Stage Selection 59

Tomography Computing and Methodology 59

Auxiliary Component Selection and Integration 61

Summary... 63

4 MODELING AND CHARACTERIZATION OF X-RAY YIELD IN A POLYCHROMATIC, LAB-SCALE, X-RAY COMPUTED TOMOGRAPHY SYSTEM 65

Introduction 65

X-Ray Detector Design and Modeling of Detection Yield in a Lens-Coupled Scintillator-CCD-Camera Tandem 66

Modeling a Polychromatic X-Ray Output Using a Bremsstrahlung Approximation 76

Measured Performance for Model Analysis 85

Summary... 93

5 A METHOD FOR ZINGER ARTIFACT REDUCTION IN HIGH-ENERGY X-RAY COMPUTED TOMOGRAPHY 96

Introduction 96

Reduction of Zinger Noise 100

Zinger Reduction Through Physical Detector Design 100

The Effect of X-Ray Imaging Parameters on Zinger Prevalence 103

CHAPTER Page

Data Acquisition and Processing 108

Results and Analysis 116

Summary... 137

6 A VOLUMETRIC MICROSTRUCTURE ANALYSIS OF A NEAR-EUTECTIC 63SN-37PB SOLDER 139

Introduction 139

Materials and Methods 144

Results and Discussion 154

Beam Hardening Artifact Reduction 160

3D Quantification of Lead-Free Dendrite Structures 168

Acquisition of 4D 63Sn-37Pb Response to Tensile Stress 188

Summary... 191

7 ELECTROMIGRATION DAMAGE IN A FREE-SURFACE SN-0.7CU SOLDER 193

Introduction 193

Materials and Methods 194

Results....... 233

Analysis and Discussion 253

Summary... 264

8 ELECTROMIGRATION DAMAGE IN SURFACE ENCAPSULATED SN-0.7CU SOLDERS 265

Introduction 265

CHAPTER Page

Materials and Methods..267

Results....... 285

Analysis and Discussion 290

Summary... 301

9 CONCLUSION 302

REFERENCES 307

LIST OF TABLES

Table Page

1. Select Thermal and Mechanical Properties for Eutectic Sn-X Solders 13

2. Parameters that Determine the Critical Product of Current Density and Conductor Length in the Design of Components for Electromigration Resistance 19

3. Spatial Resolution Achievable at 50% Contrast Based on a Lens Used in the Microtomography System (NA=0.1758) Using YAG:Ce of Varying Thickness Based on Equation 18 51

4. The Effective X-Ray to Optical Light Conversion Efficiency Calculated for Various Scintillator Materials..71

5. Physical Properties for Various Scintillator Materials...73

6. Tabulated Performance Data for the Standard Algorithm (Algorithm 1) with a 3x3 Window Operating on the Simulated Projection Stack at 10% Zinger Density 128

7. Tabulated Performance Data for the Temporal Selective Frame Averaging Filter (Algorithm 2) Operating on the Simulated Projection Stack at 10% Zinger Density 129

8. Global Phase Analysis from the 3D Segmentation of Interfacial Pores and Lead Dendrites Formed as a Result of the Solder Reflow Process 176

9. Individual Particle Analysis from the 3D Segmentation of Interfacial Pores and Lead Dendrites Formed as a Result of the Solder Reflow Process 177

10. Calculated Current Density through an Ideal 250μm Diameter Solder Joint (Shown in *Figure 50*) From Various Applied Current Magnitudes Achievable with the Employed Power Supply (Agilent E3633A) 210

Table Page

11. Measured Conductor Cross Section, Targeted Current density, and Calculated Current for Accelerated Electromigration Testing Using Tomography Data for the Pre-Electromigration Sn-0.7Cu Joint,'Sample 03202014JointD' 231

12. Measured Tin-Rich and Copper-Tin Intermetallic Volume Prior to and After Failure by 220 Hours of $1x10^4 A/cm^2$ at 100°C in 'Sample 03202014JointD' 248

13. Measured Phase Volume Change by 220 Hours of Electromigration in 'Sample 03202014JointD' at $1x10^4 A/cm^2$ and 100°C 249

14. Physical Properties of Copper, Tin, and Cu_6Sn_5 at STP 250

15. Calculated Expected Cu6Sn5 Reaction Product Volume Based on Measured Changes in Tin-Rich Volume and Copper Volume Loss and the Deviation from the Measured Value of Intermetallic Volume by Assuming Complete Reaction and Complete Resolution of the Intermetallic 252

16. Summary of Atomic Flux Analysis of Tin and Copper Due to Electromigration, and the Resulting Calculations of the Product of Effective Diffusivity and Effective Charge and a Comparison of the Values Between Tin and Copper 263

17. Test Sample Identification Codes and Accelerated Electromigration Testing Conditions and Observed Response for Surface Encapsulated Sn-0.7Cu Solder Butt-Joints on <250μm Diameter Copper Wire Substrates 272

18. Testing Conditions, Expected Copper Saturation Limit in Tin, X, and The Expected Diffusivity Value, D, Along the a-axis of Tin for Copper and Tin for the Samples Tested in Accelerated Electromigration 291

Table Page

19. Measured Values from Electromigration Tests via Segmented X-Ray Tomography Data 292

20. Effective Charge Values for Copper and Tin Inferred from Literature Values for a-axis Diffusivity Along the a-axis of Tin, the Effective Charge Ratios of Copper to Tin, and the Effective Diffusivity of Tin as Inferred from Literature Reported Values for the Effective Charge of Tin in Electromigration, as Measured Through the Observed Phases 295

LIST OF FIGURES

Figure Page

1. The Minimum System Resolution Limited by Different Focal Spot Sizes and the Detector Pixel Size as a Function of System Magnification 44

2. CAD Model Showing the System Configuration with both X-Ray Target Heads Being Implemented 47

3. Detector Assembly in CAD Model 57

4. Scintillator Tube Housing Assembly in CAD Model..58

5. Interior View of the Constructed X-Ray MicroCT Scanner 64

6. The Relative Emission Spectra of Three Scintillation Materials of Relatively Good Fit with the Detector's Efficiency for the CCD/Optical System at Various Light Wavelengths 69

7. The Results of the *DQE* Model for the X-Ray Detector as a Function of X-Ray Energy using *Equation 25* Assuming Scintillator Emission Solely at the Wavelength of Maximum Intensity 75

8. Diagram of the Model Used to Portray X-Ray Number-Energy Dependence on Accelerating Voltage and Target Power 78

9. Modeled X-Ray Beam Spectra Transmitted Through the X-Ray Window and a Steel Filter as a Function of X-Ray Energy Using *Equation 32* 81

10. The Modeled Detected Signal Rate with a 250μm Thick LuAG:Ce Scintillator with 380μm Steel X-Ray Beam Filtering Based on *Equation 25* and *Equation 32* 83

Figure Page

11. Modeled X-Ray System Count Rate Dependency on Scintillator Composition and Thickness as a Function of Accelerating Voltage Using *Equation 35* for 870μm Beryllium Window Filtering and 380μm Steel Filtering........................86

12. The Measured Effect of Accelerating Voltage and Scintillating Crystal Choice on the Normalized Signal Yield with No X-Ray Beam Filtering 89

13. The Measured Effect of Steel Filtering on the Normalized Detection Count Rate for Varying Steel Filter Thickness and for Varying Accelerating Voltage as Measured with the 50μm LuAG:Ce Scintillator..90

14. The Modeled and Measured Count Rates Independent of Target Current and Detector Geometry for the Steel Filtered and Unfiltered (Intrinsic Beryllium X-Ray Window Filtered) X-Ray Beam as a function of X-Ray Voltage.................92

15. The Effect of Design Revisions on Zinger Noise from a 28 Second Dark Frame Exposure Image (Camera Shutter Closed)..102

16. Area Fraction of the CCD Chip which is Corrupted by Zinger Noise at Different Exposures, with the X-Ray Source Unfiltered and Operating at 150kV and 150μA Target Current..105

17. Area Fraction of the CCD Chip which is Corrupted by Zinger Noise at Different X-Ray Target Currents, with the X-Ray Source Unfiltered and Operating at 150kV with the Area Fraction Normalized by Exposure Time 106

Figure Page

18. Area Fraction of the CCD Chip which is Corrupted by Zinger Noise at Different X-Ray Tube Accelerating Voltages, with the X-Ray Source Unfiltered and Operating at 150μA Target Current with the Area Fraction Normalized by Exposure Time 107

19. A Sub-Region of an Experimentally Acquired Flat and Dark Field Corrected Radiograph 115

20. Simulated Forward Projections of the Shepp-Logan Phantom at 0°..................117

21. Histogram of Artificially Added and Randomly Positioned Zinger Pixels by Intensity Value in the Highest Zinger Density Implemented on the Simulated Shepp-Logan Phantom Forward Projection Stack where More Low than High Intensity Zingers are Used to Match Experimental Observation, Modeled here with a Normal Distribution..121

22. Comparison of Zinger Identification between the Standard Method of Varying Window Size as a Function of Tolerance Factor...122

23. Comparison of Zinger Identification between the Standard Method with the Optimal Window Size and the Newly Constructed Selective Temporal Frame Averaging Approach as a Function of Tolerance Factor..................................123

24. Comparison of Zinger Identification Between the Optimized (Tolerance Factor = 0.01) Standard and Selective Frame Averaging Methods for Zinger Removal 125

Figure Page

25. The Relative Difference Images Between the Ground Truth and the Zinger Filtered Images by Both the Optimized (Tolerance Factor = 0.01) Standard and Selective Frame Averaging Methods for the 0° Projection 130

26. Comparison of Zinger Filtering Method as a Function of Tolerance Factor by Analyzing All Filtered Projections' Sum of Square Differences for All Projections and the Ground Truth Data for All Pixels 132

27. Histogram of Zinger Affected Pixel Intensity *above* the Ground Truth Intensity after Filtering the 10% Zinger Density Projection Stack Using the Standard Zinger Removal Method (*Algorithm 1*) 133

28. Histogram of Zinger Affected Pixel Intensity *Above* the Ground Truth Intensity after Filtering the 10% Zinger Density Projection Stack Using the Newly Implemented SFA Method (*Algorithm 2*)..134

29. Difference Image of the Shepp-Logan-Filtered Back Projection Reconstructions of the Central (51 of 100) Reconstruction Plane 136

30. Processing Flow-Chart for the Preparation of Copper Wire 'Substrates' for Butt-Joint Fabrication 145

31. Schematic of Reflow Assembly Used for Sub-Millimeter Butt-Joint Fabrication 147

32. Reflow Profile for the 410µm Eutectic Pb-Sn Joint Used for XCT Imaging and Surface Microscopy 148

Figure Page

33. Optical Bright Field Micrograph of a Near-Eutectic Pb-Sn Butt-Joint Reflowed onto a Roughly 410µm Diameter Copper Wire with a Cooling Rate of Approximately 1°C/s 150

34. The [100] Pole Figure for Cubic Crystals and a Graphical Representation of Dendrite Growth Along the [100] Directions for Cubic Crystals 152

35. A Sample Cross Section (Reconstruction Plane Prior to Segmentation) of the Eutectic Pb-Sn Solder Joint Reconstruction Acquired via µXCT 156

36. A Sample Cross Section of the Eutectic Pb-Sn Solder Joint Reconstruction Acquired via µXCT where the Vertical Direction is Parallel to the Rotation Axis, and Various Visible Phases are Labeled and the Volume Histogram..........157

37. Comparison of Pb-Sn Microstructural Features Resolved in X-Ray CT and Optical Microscopy 158

38. Beam-Hardening Cupping Reduction in a µXCT Reconstruction Plane..........166

39. A Line Profile Across the Same µXCT Reconstruction Plane in *Figure 35* 167

40. Demonstration of the 3D Region Growth Segmentation of a Single Lead-Rich Dendrite from the µXCT Dataset..........170

41. Segmented Microstructure of the Eutectic Pb-Sn Solder Joint Imaged Using µXCT 172

42. Segmented Microstructure of the Eutectic Pb-Sn Solder Joint Using µXCT with Only Dendrite Features Shown 173

43. Voids Formed as a Result of the Flux Reactive Process During Solder Reflow 175

Figure Page

44. Selected Neighboring Dendrites from the Segmented Population Rendered in Separate Colors for Distinction 179

45. Measurement of Secondary Dendrite Arms Spacing from Grayscale Data 182

46. Segmented Renderings from Lab-Scale μXCT Showing Three of the Lead Dendrites which had Distinct Nodules from the Base of the Secondary Arms Enabling Secondary Arm Spacing Measurement 183

47. Abnormally Structured Segmented Dendrites 185

48. Segmented Dendrites which have Formed at the Copper Substrate Interface and Possessing at Most Three Primary Arms 187

49. Qualitative Strain Response of a 63Sn-37Pb Solder Joint in a Tomography Section through the Grayscale CT Volume 190

50. The Reflow Profile Applied to All Sn-0.7Cu Solder Joints for Fabrication in this Study 197

51. A Bright Field OM Micrograph of a Polished Sn-0.7Cu Butt-Joint Fabricated by Reflow onto <500μm Diameter Copper Wires and Aged 24 Hours at 190°C after Reflow 198

52. Modeling X-Ray Mass Attenuation Contrast between Pure Sn and Cu_6Sn_5 of Unit Thickness as a Function of X-Ray Energy and Modeling the Relative Detected X-Ray Energy Spectrum 201

53. One Projection of the 741 Projection Stack that Results from Data Processing after XCT Data Acquisition..205

Figure Page

54. Cross Sections Parallel to the Rotation Axis of an XCT Reconstruction Volume for a Sn-0.7Cu Solder Bonded to ~230µm Copper Wires Under Different Intensity Scaling to Accentuate the Contrast between Different Sets of Phases 207

55. Cross Sections of a XCT reconstruction Volume of a Sn-0.7Cu Solder Bonded to ~230µm Copper Wires Showing the Degree of Solder Coverage on the Contact..235

56. CAD Model Representation of the EM Fixture Designed for *in situ* µXCT Imaging..240

57. A CAD Rendering of the Electromigration Fixture for *in situ* µXCT Shown with a Ceramic Resistive Heater 241

58. A CAD Rendering of the Electromigration Fixture Configured for *in situ* µXCT Experimentation 243

59. Mounting of a Sn-0.7Cu Butt-Joint 'Sample 03202014JointD' in the EM Test Fixture after Polishing to a Depth of approximately ½ of the Joint's Diameter..245

60. Bright-Field Optical Micrograph with a Side View of 'Sample 03202014JointD' Mounted within the EM Fixture before Testing 246

61. 2D Orthogonal Views of the 3D Reconstruction Volume of the Sn-0.7Cu solder 'Sample 03202014JointD' Prior to Accelerated EM Testing 254

Figure Page

62. Segmentation Visualization of the Sn-0.7Cu Solder Joint 'Sample 03202014JointD' Tomography Volume Prior to Accelerated Electromigration Testing 259

63. Bright Field Optical Micrographs of Sample '03202014JointD' after 100 Hours of Electromigration at 10^4A/cm² and 100°C, Still Contained within the Electromigration Fixture 235

64. Surface Images of Failed Sn-0.7Cu 'Sample 03202014JointD' after 220 Hours of Electromigration at 10^4A/cm² and 100°C, Still Contained within the Electromigration Fixture 240

65. Three 2D Orthogonal Views of the 3D Reconstruction Volume of the Sn-0.7Cu solder 'Sample 03202014JointD' After Accelerated EM Testing 241

66. Visualization of CT Volume Phase Segmentation for EM Failed 'Sample 03202014JointD' through Three Identically Positioned Slices 243

67. Volume Rendering of the Post-EM Segmentation for 'Sample 03202014JointD' 245

68. Comparison of the Post-EM Volume Segmentation with Destructive Surface Imaging Observations 246

69. The Diffusion of Copper and Tin Along the A-Axis of Tetragonal Tin as a Function of Temperature 254

70. Segmented Rendering Overlay of the Post-EM Solder Volume with that of the As-Processed Solder Volume Highlighting the Mass Transport of the Tin-Rich Solder Phase 259

Figure | Page

71. A Sn-0.7Cu Solder on <250μm Copper Wire Butt-Joint Test Specimen Used for Accelerated Electromigration Testing 268

72. Experimental Setup for Electromigration Testing Including a Testing Fixture, Convection Furnace, Electrical Power Supply, Thermocouple, and Control Station 271

73. Recorded Electrical Current Applied Versus Recorded Time in Electromigration Testing of Sample 092414 273

74. Recorded Test Resistance and Temperature Versus Recorded Time in Electromigration Testing of Sample 092414 274

75. Recorded Electrical Current Applied Versus Recorded Time in Electromigration Testing of Sample 101014 275

76. Recorded Test Resistance and Temperature Versus Recorded Time in Electromigration Testing of Sample 101014 276

77. Recorded Electrical Current Applied Versus Recorded Time in Electromigration Testing of Sample 120214 277

78. Recorded Test Resistance and Temperature Versus Recorded Time in Electromigration Testing of Sample 120214 278

79. Data Processing Flowchart for Analysis of Four-Dimensional Imaging Data Containing Electromigration Induced Structural Evolution 280

80. Data Processing Flowchart for Analysis of Four-Dimensional Imaging Data Containing Electromigration Induced Structural Evolution 283

Figure Page

81. A Single and Identical Tomography Slice of the 101014 Sample Volume Imaged After Current Stressing Compared Between the Filtered State for Copper/Solder Segmentation, the Filtered State for IMC Segmentation, and the Full Segmentation 284

82. Segmented X-Ray Computed Tomography Representations of Electromigration Induced Microstructural Evolution in Sample 092414 287

83. Segmented X-Ray Computed Tomography Representations of Electromigration Induced Microstructural Evolution in Sample 101014 288

84. Segmented X-Ray Computed Tomography Representations of Electromigration Induced Microstructural Evolution in Sample 120214 289

85. The Measured Product of the Effective Diffusivity and Effective Charge for Copper at 150°C as a Function of Current Density Applied 298

86. The Measured Product of the Effective Diffusivity and Effective Charge for Tin at 150°C as a Function of Current Density Applied 299

87. The Inferred Effective Charge of Tin and Copper at 150°C as a Function of Current Density Applied if Diffusion is Predominantly Along the a-axis in Tin, Based on Calculated Values for Diffusivity in Tin Along the a-axis....................300

CHAPTER 1

INTRODUCTION

Solders, a term used for low-melting-temperature metals and alloys, have long been used in a wide variety of applications due to their associated ease of processing (Hobart, 1906). In microelectronic packaging, solder materials are one of the preferred interconnect choices due to their success in achieving a high density of electrical and mechanical connections between microchip components (Abtew and Selvaduray, 2000). Tin-based solders are ubiquitous and essentially unrivaled in microelectronic packaging due to their relatively low cost, low processing temperatures, superior wetting characteristics which yield high surface coverage, and the formation of metallizations with common conductors (including copper and nickel) yielding a quality bond (Wood and Nimmo, 1994). Typically, a high density of solder interconnects are used within the chip's package to mount a silicon die to a substrate, and a lower density of connections are used to mount the package to the printed circuit board (PCB) (Tu and Zeng, 2001). The solder connection between the die and the package substrate is made with the controlled-collapse-chip-connection, called the C4 joint (Gilleo, 2004). The larger solder interconnects, between the package and the PCB, is simply called a ball grid array (BGA) (Gilleo, 2004).

Several factors have caused increased attention from the microelectronic packaging community on the design of solder interconnects and their role in component failure. One ongoing trend in microchip manufacturing is embodied by Moore's Law (Moore *et al.*, 1965), which roughly predicts the transistor density in microprocessors to double every

two years, similarly requiring the processor package to possess a high density of interconnections (Datta *et al.*, 2004). As the density of the solder interconnect increases, the size of each interconnect must similarly decrease. As the size of each interconnect decreases, the role of the solder microstructure and solder-bond interface plays an increased role in the electrical and mechanical properties of the solder, and the role of the microstructure in the performance of the package is enhanced. Simultaneously, lead as a solder alloying constituent has recently been all but completely eliminated from consumer electronics due to increased concerns over lead toxicity, particularly in regards to electronic wastes and their accumulation sites (Ogunseitan, 2007). The ramifications of the elimination of lead from soldering alloys are realized through degradation in several solder properties, including increased processing temperatures and decreased ductility (Kang and Sarkhel, 1994). Together, these trends have enhanced the focus of the microelectronics community on the design and processing of solder interconnects in high density packaging applications (Abtew and Selvaduray, 2000).

One mode through which solder interconnects may fail is through electromigration (EM) (Liu *et al.*, 2000). Electromigration of metals experiencing high current densities has been studied for over fifty years (Huntington and Grone, 1961). The interest in electromigration studies boomed in the late sixties in regard to migration of conducting aluminum (Black, 1969, Blech and Meieran, 1969, Ghate, 1967, Howard and Ross, 1967), gold (Huntington and Grone, 1961, Hartman and Blair, 1969), and silver (Ho and Huntington, 1966) traces experiencing very high current densities . During this time, experimental methods for measuring atomic flux in EM were established and

mechanisms for electromigration were proposed (Huntington and Grone, 1961), and Black's model was proposed for conductor lifetimes as a function of testing parameters (Black, 1969), enhancing general understanding of electromigration phenomena in solid conductors. More recently, electromigration has been studied in solder relevant to microelectronic packaging, which typically operate at a much higher homologous melting temperature than aluminum conductors (Mizuishi, 1984, Huntington and Hu, 1984, Hu and Huntington, 1982, Hu and Huntington, 1985). These studies have looked both at the migration of conducting contact species into the solder system (Hu and Huntington, 1982, Hu and Huntington, 1985) and at the migration of the solder species themselves (Mizuishi, 1984, Huntington and Hu, 1984). Black's model for electromigration life in aluminum traces has been applied to solder microbump failure even more recently (Ding, 2007, Basaran *et al.*, 2009, Ramanathan *et al.*, 2007, Zhang *et al.*, 2013) and other methods have been established for measuring the EM resistance of solder alloys (Huynh *et al.*, 2001, Tu, 2003, Gan *et al.*, 2002). The microstructure of solder bumps resulting from EM failure has been studied in great detail (Yeh *et al.*, 2002, Ke *et al.*, 2011). The effect of the contact under-bump metallization (UBM) (Lee *et al.*, 2001, Shao *et al.*, 2004, Lin *et al.*, 2009b, Lin *et al.*, 2009a, Hsiao *et al.*, 2009, Wu *et al.*, 2012) and the solder-contact interfacial metallization layers (Liang *et al.*, 2010) have been characterized. Studies have been performed focusing on the effect of electromigration on the formation and evolution of intermetallic phases at the anode and the cathode (Alam *et al.*, 2006, Chen and Chen, 2001). Studies have been performed analyzing the temperature dependence on the dominant EM failure mode (Ke *et al.*, 2011), whether metallization consumption or void formation. The effect of the tin grain orientation in tin-rich solder

electromigration has also been investigated (Wu *et al.*, 2004, Lu *et al.*, 2008, Lu *et al.*, 2009, Lara, 2013). The formation of stress gradients within the solder joints due migration has been measured (Ma *et al.*, 2012b), and the role of the stress gradient on EM dynamics has been analyzed. EM induced void formation dynamics have been measured using interrupted μXCT, providing a 4D understanding of damage evolution in a particular sample (Tian *et al.*, 2011, Xie *et al.*, 2014). Studies have been performed comparing the EM performance of lead-containing solder alloys with their lead-free successors (Lee *et al.*, 2001), and comparing various front-runner Pb-free alloys (Lin *et al.*, 2009a, Chen and Chen, 2001, Lu *et al.*, 2008, Lu *et al.*, 2009, Xie *et al.*, 2014). Current crowding effects on the mechanisms of void formation resulting from flip-chip and BGA circuit geometry have been reported (Yeh *et al.*, 2002). The Joule heating induced temperature distribution inside solder interconnects has been simulated (Basaran *et al.*, 2009, Ramanathan *et al.*, 2007, Yang *et al.*, 2007, Liu *et al.*, 2008, Yamanaka *et al.*, 2010) and measured experimentally (Chiu *et al.*, 2006, Hsiao *et al.*, 2008). Current crowding and joule heating produce temperature gradients in the solder, another driving force for the migration of atoms, called thermomigration (Yang *et al.*, 2008b, Yang *et al.*, 2008a). The importance of this effect on the actual migration processes has been emphasized, and is typically coupled with electromigration should temperature gradients become sufficiently high (Yang *et al.*, 2008b, Yang *et al.*, 2008a). The effect of electromigration on the mechanical properties of solder alloys has also been studied (Ren *et al.*, 2006). These reports have provided essential insight to EM processes in modern microelectronic solder interconnects and design solutions for minimizing EM failure in these components.

Microstructural characterization and failure analysis of the solder interconnects have been performed through a variety of techniques. Surface microscopy, including optical microscopy (OM) and scanning electron microscopy (SEM), is prevalent and informative technique for the analysis of solder microstructures. SEM in particular can provide relatively high resolution and can be coupled with (EDS) or (WDS) to determine chemical information (Yang *et al.*, 2007, Xia *et al.*, 2006, Bertheau *et al.*, 2014b) and with electron back scattered diffraction (EBSD) to obtain crystallographic information on a surface (Lu *et al.*, 2008, Lu *et al.*, 2009, Lara, 2013). The drawbacks of surface characterization include the generally required polishing steps which are of a destructive nature. Although a destructive technique, serial sectioning can be performed using either conventional polishing coupled with SEM or OM imaging (Dudek and Chawla, 2008), or focused-ion-beam (FIB) sectioning coupled with SEM imaging (Yazzie *et al.*, 2012a, Maleki *et al.*, 2014) to obtain high resolution, three dimensional microstructural data. Recently, synchrotron x-ray microtomography (μXCT) beamlines have been used to characterize the three dimensional microstructure of solder alloys (Bertheau *et al.*, 2014b, Yazzie *et al.*, 2012a, Maleki *et al.*, 2014, Tsuritani *et al.*, 2007, Tsuritani *et al.*, 2011). This technique has been applied to small volumes obtained manually (Xie *et al.*, 2014, Maleki *et al.*, 2014, Tsuritani *et al.*, 2007), through focused ion beam milling (Yazzie *et al.*, 2012a, Maleki *et al.*, 2014), and to full bumps in flip chip packages (Tian *et al.*, 2011, Tsuritani *et al.*, 2011). Lab-scale μXCT, employing microfocus x-ray tube sources, has recently been used to study full microscale solder joint volumes (Xie *et al.*, 2014, Dudek *et al.*, 2010, Jiang *et al.*, 2011, Padilla *et al.*, 2012). The strength of the μXCT technique is realized through its relatively non-destructive nature, where by applying μXCT with

interrupted or *in situ* stimulus, four dimensional datasets have be obtained representing the evolution of solder microstructure in response to thermal stimulus (Tsuritani *et al.*, 2007, Tsuritani *et al.*, 2011), mechanical stimulus (Padilla *et al.*, 2012), and accelerated EM (Xie *et al.*, 2014). Lab-scale x-ray computed microtomography (µXCT) has thus demonstrated a capability to quantify microstructure features and damage evolution three-dimensionally in small-scale solder joints.

Although 3D imaging of solder alloys wherein (at least) two distinct solid phases are resolved has been demonstrated using µXCT beamlines at synchrotron tomography beamlines (Tian *et al.*, 2011, Bertheau *et al.*, 2014b, Yazzie *et al.*, 2012a, Maleki *et al.*, 2014, Tsuritani *et al.*, 2007, Tsuritani *et al.*, 2011), a literature survey indicates that this has not been accomplished using lab-scale µXCT systems. The lab-scale studies which have been identified have resolved only cracks and pores from the solder itself (Xie *et al.*, 2014, Jiang *et al.*, 2011, Padilla *et al.*, 2012). One reason that synchrotron µXCT studies in interconnects have not been performed may be the required duration of EM testing, up to over 1000 hours (Ke *et al.*, 2011). Thus, lab-scale µXCT systems pose an attractive means for performing long term experimentation. The previously described studies using lab-scale µXCT for solder imaging have employed commercially available systems, and have not demonstrated the capability to resolve second phases in the microstructure which have relatively small differences in x-ray attenuation (Xie *et al.*, 2014, Jiang *et al.*, 2011, Padilla *et al.*, 2012). Compared to the synchrotron studies performed at relatively low energy on samples less than 100µm in thickness, the lab-scale µXCT studies have

employed relatively higher x-ray energies and have studied samples over 500µm in thickness.

This dissertation primarily regards the quantification of migrating species in micro-scale lead-free solder joints by using time-dependent volumetric datasets with a resolved second phase acquired with a modular, high-resolution lab-scale µXCT tool of a custom construction built for this purpose. The three dimensional datasets were expected to provide unique opportunities to study tin-rich solder migration, metallization consumption, intermetallic formation, and void formation. The quantification of the evolution of these phases was expected to provide a novel means for estimation of atomic flux under electrically assisted atomic migration, and the technique was expected to provide a new understanding of the evolution of the solder microstructure in three-dimensions. For this work a custom lab-scale x-ray computed tomography system and *in situ* multi-modal sample testing fixture were designed. The design of a custom lab-scale µXCT system for achieving high spatial resolution and sufficient contrast of solder microstructures, a review of the design principles which were applied, the characterization of the system's imaging performance, and the design of a custom testing fixture are presently described.

CHAPTER 2

A REVIEW OF RELEVANT LITERATURE

2.1 INTRODUCTION

Microelectronic packaging covers a wide field of processing techniques required for mounting a silicon die within a usable and robust package. One critical aspect of microelectronic packaging involves the electrical and mechanical connection between the die and its substrate, where solder ball arrays can be used. It has been shown that a device may fail at the solder interconnect level through a variety of mechanisms. Previous work has shown that one primary phenomenon responsible for failure of the solder interconnect is caused by electromigration of atoms in response to an electrical current. Mechanistic models for the electromigration process have been presented by previous researchers and have prevailed in the community. Many researchers have investigated the lifetime and the microstructure evolution of solder micro-volumes under accelerated electromigration testing. X-ray computed micro-tomography has demonstrated a capability to resolve three-dimensional microstructural features in micro-scale solder joints, and in some instances, the evolution of 3D features in response to stimuli. Design principles and plans for lab-scale μXCT systems have been detailed by previous researchers, and models which govern their design and performance have been proposed. Techniques for data processing and tomographic reconstruction are an ongoing research area across many disciplines, and many techniques for performing tomographic scanning and reconstruction have been published in the open literature.

2.2 SOLDER ALLOYS AND MICROSTRUCTURES RELEVANT TO MICROELECTRONICS PACKAGING

In microelectronic packaging, solder is commonly used for mounting various levels of components to one another, particularly the silicon die, the package substrate, and the printed circuit board (PCB). The role of solder in electronic packaging takes place at mostly two distinct levels in the device. A high density of solder interconnects may be used within the chip's package to mount a silicon die to a substrate, and a lower density of connections are used to mount the package to the printed circuit board (PCB) (Tu and Zeng, 2001). The solder connection between the die and the package substrate is made with the controlled-collapse-chip-connection process (C4) joint (Gilleo, 2004). Alternatively, a wirebond, typically copper, may be used to attach the die to the substrate, but the C4 process has become more prevalent due to a higher interconnect density (Abtew and Selvaduray, 2000). The C4 solder bump is roughly 100μm in diameter (Gilleo, 2004). These are both referred to as Level 1 connections. For mounting the package onto the PCB, Level 2 connections are used. Level 2 connections can either be pin-through-hole (PTH) or surface mount technology (SMT). SMT approaches include both the use of leads and the use of solder ball arrays. In SMT Level 2 packaging, the solder array between the package and the PCB is called a ball grid array (BGA) (Gilleo, 2004). The BGA is around 760μm in diameter (Gilleo, 2004). In 2011, it was reported that three-dimensional integrated circuit architecture was under development where through silicon via (TSV) connections are made with solder bumps ~20μm in diameter at the back end of the die itself (Gilleo, 2004). In 2014, interest in the development of a next

generation of even higher density solder interconnect continues to grow (Bertheau *et al.*, 2014b, Bertheau *et al.*, 2014a).

Although lead (Pb) offers low processing temperatures, enhanced ductility, reduction of tin pesting, and reduced surface tension in tin (Sn) based solders, it has been phased out of consumer electronics due to legal, environmental, and technological concerns (Abtew and Selvaduray, 2000). Some of the various properties highlighting the superiority of eutectic tin-lead over eutectic tin-X components are provided in *Table 1*.

The equilibrium lead-tin eutectic microstructure can be characterized by a lead-rich and a tin-rich phase (Tu and Zeng, 2001). Under non-equilibrium cooling, lead-dendrites may form throughout the solder (Mertens *et al.*, 2014b). Upon soldering with copper or nickel, an interfacial intermetallic layer is formed between the solder and the substrate metal, where tin is the reactive species for metallization formation (Lee *et al.*, 2001). Thus there is concern for excessive metallization consumption with Sn-rich alloys (Lee *et al.*, 2001).

In the Sn-3.5Ag eutectic system, the equilibrium microstructure is a Sn-rich phase with Ag_3Sn needles dispersed (Sidhu and Chawla, 2004, Sidhu and Chawla, 2006). The microstructure can also display tin rich dendrites after solidification depending on the thermal processing (Deng *et al.*, 2003). The intermetallic formed on the solder side of the metal interface for the case of copper is Cu_6Sn_5. On the copper side of the tin-rich solder couple, a copper rich Cu_3Sn intermetallic layer may form (Deng *et al.*, 2004). In the Sn-0.7Cu eutectic composition, the equilibrium microstructure consists of Cu_6Sn_5 particles

dispersed in a Sn-rich phase. When soldered to copper, a Cu_6Sn_5 intermetallic is present on the solder interface and a Cu_3Sn layer may form after aging (Tu and Zeng, 2001, Deng *et al.*, 2003). For Sn-0.7Cu solder on a nickel substrate, a Ni_3Sn_4 reaction layer is observed (Chen and Chen, 2001).

The formation of intermetallics at the metal-solder interface is complicated by the addition of ternary elements to the solder system and by the deposition of UBM barrier layers such as nickel and phosphorous. For a Sn-0.4Cu solder joint, a multitude of intermetallic layers may form, including $(Cu,Ni)_3Sn_4$, Ni_3P, and NiP, and NiSnP with the implementation of an electroless nickel immersion gold (ENIG) UBM layer (Yoon and Jung, 2005). Without copper in the mix initially, for the case of Sn-3.5Ag on a Ni-P layer, a Ni_3Sn_4 intermetallic layer and a P-rich layer are observed (Kumar *et al.*, 2005). After aging extensively, the copper beneath the Ni-P layer had mixed into the interface, resulting in a $(Cu_x,Ni_{1-x})_6Sn_5$ layer (Kumar *et al.*, 2005). For the case of a Sn-3.8Ag-0.7Cu solder on a NiP layer, a $(Cu_x,Ni_{1-x})_6Sn_5$ intermetallic layer is reported (Li *et al.*, 2005). For the case of Sn-07.Cu solder on a NiP layer, a $(Cu,Ni)_3Sn_4$ layer is observed (Jang *et al.*, 2000). Depending on the exact solder composition, UBM layers, and heat treatment implemented, a variety of different interface morphologies and solder microstructures are seen (Dudek and Chawla, 2008, Ma *et al.*, 2003, Ma *et al.*, 2006, Sun *et al.*, 2006, Zeng *et al.*, 2010, Marques *et al.*, 2014).

2.3 FAILURE MODES AND TESTING OF MICROELECTRONIC SOLDER INTERCONNECTS

Microelectronic packages may fail at the solder interconnect through a multitude of mechanisms, and often through a combination of many. During processing, poor wetting characteristics of the solder or insufficient dwell times may result in an open circuit rendering the device inoperable (Abtew and Selvaduray, 2000) (Rizvia *et al.*, 2006). After solder solidification, bumps may be in a state of shear stress due to thermal mismatch between the components being soldered leading to premature failure (Tu and Zeng, 2001). When the device is in use, interconnects may experience thermal mechanical cycling caused by temperature gradients or thermal-expansion mismatch (Abtew and Selvaduray, 2000, Kariya *et al.*, 2004).

Table 1

*Select Thermal and Mechanical Properties for Eutectic Sn-X Solders (Abtew and Selvaduray, 2000) * Eutectic Temperature **Wetting Time on a Copper Substrate with Aqueous Clean Flux and at 62°C Above T_e*

Alloy	T_e* (°C)	Surface Tension in Air (mN/m)	Surface Tension in N_2 (mN/m)	t_w ** (s)	E (GPa)	UTS (MPa) [20°C/100°C]	Elong. (%) [25°C]	Shear Strength (MPa) [20°C/100°C]	CTE (10E-6/K)
63Sn-37Pb	183	417	464	0.385	39	19/4	40	34/21	21
Sn-0.7Cu	227	491	461	0.400	-	-	-	-	-
Sn-3.5Ag	227	431	493	-	50	37/-	42.5	38/23	22

Aging and reflow effects on the microstructural evolution in lead free solder joints have been investigated (Deng *et al.*, 2003, Li *et al.*, 2005, Liu *et al.*, 2009, Prabhu *et al.*, 2011), and the influence of reflow and thermal aging on the mechanical performance has been studied (Ma *et al.*, 2006, Deng *et al.*, 2005). Fracture or cracking in solder joints has been reported to occur in both ductile and brittle fashion depending on the microstructure, composition, and environment (Sundelin *et al.*, 2006, Xie *et al.*, 2011, Yazzie *et al.*, 2012b). A fracture may occur through the bulk of the solder in a ductile fashion although has also been observed to traverse through a brittle intermetallic interfacial layer, or along the interface itself (Sundelin *et al.*, 2006, Xie *et al.*, 2011, Yazzie *et al.*, 2012b). Whether in distribution or in use, a device may experience a mechanical shock or vibrations, causing high strain rates. Yazzie *et al.* (Yazzie *et al.*, 2012b) have looked at the strain rate dependence of the type of fracture and its location within the microstructure of the joint, where a brittle fracture becomes dominate at high strain rates.

For the Sn-3.5Ag system, brittle fracture along the interfacial intermetallic was reported on the ENIG metallization, but not on electrolytic Ni/Au or on Cu (Koo and Jung, 2005). It's been reported that increasing silver content in the Sn-Ag-Cu (SAC) alloy system gives rise to an increase in strength (Kariya *et al.*, 2004). Similarly, it's been reported that high silver SAC alloys above 3 at. % exhibit mixed ductile and brittle fracture where as the low silver alloys exhibit ductile fracture (Kim *et al.*, 2003). As the interconnect ages, the thickness of the intermetallic layer is known to increase (Xia *et al.*, 2006, Deng *et al.*, 2003) and may render the solder volume brittle. It's been reported that cracks in SAC solder joints have formed by initiation in intermetallic particles and triple junctions and

linked up to cause intergranular failures, and that the addition of lead to the system greatly improved the solder joint reliability (Zbrzezny *et al.*, 2007).

Solder joints are known to achieve high homologous temperatures in use, and therefore creep and other thermally activated failure mechanisms become a concern (An *et al.*, 2011). The electrical interconnects may experience a high current density at high homologous melting temperatures, leading to electrically and thermally assisted migration of atoms, or electromigration (EM), which may cause voiding at an interconnect interface (Mizuishi, 1984). A primary effort of the microelectronic packaging community working with solder interconnects involves mitigating the prevalence of the aforementioned failure modes through careful design of the package and through material design of the interconnect microstructure and contact interface (Tu, 2011).

2.4 ELECTROMIGRATION PRINCIPLES

In a metal conductor exposed to a static electrostatic field, the motion of atoms is theorized to depend on two primary driving forces: the electrostatic force of the electric field on metal ions and the wind force created by the interaction of conducting electron or holes with the metal atoms themselves (Ho and Huntington, 1966). The total resulting force on an ion in an electric field, F_t, is then expressed as:

$$F_t = eEZ^* = eE\left(Z - Z'\right), \tag{1}$$

where e is the charge of the conducting species, E is the applied electric field, eZ^* is the effective valence charge, Z is the valence of the metal, and eEZ' is the electron drag, or wind, force (Ho and Huntington, 1966). Determining the value of Z' is a central challenge of theoretical analysis of EM phenomena (Ho and Huntington, 1966). The value of Z' can, however, been determined experimentally (Gan *et al.*, 2002, Lee *et al.*, 2001, Chen and Chen, 2001). Using the Nernst-Einstein equation, the drift velocity, v_d, can be expressed as the mobility of the ions, μ, into the effective force on the ion, F_t, or:

$$v_d = \mu F_t = \frac{D}{kT} F_t, \quad (2)$$

where D is the diffusivity, k is Boltzmann's constant, and T is the absolute temperature (Ho and Huntington, 1966). Rewriting *Equation 2* yields:

$$v_d = \frac{D}{kT} eEZ^* . \quad (3)$$

Using Ohm's law, one can rewrite the drift velocity in terms of the applied current density, j, and the resistivity, ρ, of the material (Lee *et al.*, 2001):

$$v_d = \frac{D}{kT} eZ^* \rho j. \quad (4)$$

Taking the atomic flux in the conductor due to electromigration as, J_{EM}, equal to the product of the average electromigration drift velocity, v_d, and the atomic density, C, the atomic flux is:

$$J_{EM} = C\frac{D}{kT}eZ^{*}\rho j. \tag{5}$$

This theoretical treatment predicts electromigration is proportional to current density, j, atom motion is toward the anode if the wind force dominates and vice-versa, in hole conducts atom migration is always toward the cathode, and temperature dependence of electromigration is governed by D/T (Ho and Huntington, 1966). It should also be noted that Z^* is a slight function of temperature as well, through the resistance variation with temperature in the conductor.

Further, it has been shown that during electromigration where electron wind force dominates, a stress builds up on the anode side of the conductor, and a stress gradient, $\Delta\sigma/\Delta x$, is produced (Blech and Tai, 1977). This gradient results in a flux of atoms from high compressive stress to low compressive stress which opposes the electromigration flux, known as the 'Blech-effect', and can be expressed as:

$$J_{\sigma} = Cv_b = C\mu\Omega\frac{\Delta\sigma}{\Delta x} = C\frac{D}{kT}\Omega\frac{\Delta\sigma}{\Delta x}, \tag{6}$$

Where v_b is the average drift velocity of ion due to the presence of a compressive stress gradient, and Ω is the atomic volume of the ions. The effective atomic flux due to electromigration considering the Blech-effect, J_{Eff}, can then be expressed as:

$$J_{Eff} = J_{EM} + J_{\sigma} = C\frac{D}{kT}eZ^{*}\rho j + C\frac{D}{kT}\Omega\frac{\Delta\sigma}{\Delta x} \quad . \tag{7}$$

Practical application of the above formula can be realized by the design goal of having a net flux of zero across the conductor, or $J_{Eff}=0$. For a interconnect line or bump of length, $l \approx \Delta x$, with a concentration of a migrating species of C, the critical current-density-length-product $(jl)_c$, below which net migration of atoms is null is:

$$(jl)_c = \frac{\Omega\Delta\sigma}{eZ^{*}\rho} \quad . \tag{8}$$

The $(jl)_c$ value for copper and aluminum is roughly 1000 A/cm, and approximately two orders of magnitude smaller for tin, which is why electromigration can occur in solder bumps at two orders of magnitude lower current density than for Cu or Al interconnects (Tu, 2011), as shown in *Table 2*.

Table 2

Parameters that Determine the Critical Product of Current Density and Conductor Length, $(jl)_c$, in the Design of Components for Electromigration Resistance (Ding, 2007, Chen et al., 2010)

	Ω (cm^3)	ρ (10^{-6} Ωcm)	Z*	j (A/cm^2)
Solder	~3x10-23	10~20	-33 ~-39	10^3-10^4
Al or Cu	~2x10-23	2~3	-6.4~-4.8	10^6

Often with conductors which are observed to relieve stress through growths or bulges at free surfaces, the back stress component is assumed to be equal to zero (Lee *et al.*, 2001, Xie *et al.*, 2014). What is can typically be measured during electromigration experiments with solder microbumps is the cross sectional area of the conductor, A, the volume of void formation, V_{EM}, and the length of time under which electromigration has taken place, t. Thus, one has:

$$J_{Eff} \approx J_{EM} \approx C\frac{D}{kT}eZ^{*}\rho j \approx \frac{V_{EM}}{\Omega\,(A\cdot t)} \tag{9}$$

The electromigration resistance of a solder system is typically expressed as the product of the diffusivity due to thermally controlled migration mechanisms and the effective charge due to the interaction of the metal ions with the conducting species as well as the electrostatic force on the ions, as DZ^* (Gan *et al.*, 2002, Lee *et al.*, 2001, Chen and Chen, 2001, Xie *et al.*, 2014).

This parameter, DZ^*, can be expressed simplistically in terms of the measureable parameters as:

$$DZ^{*} \approx \frac{k\,T\,V_{EM}}{C\,\rho\,j\,e\,\Omega\,(A\cdot t)}. \tag{10}$$

It has also been demonstrated that the overall atomic flux depends on the flux of atoms due to chemical potential in non-equilibrium structures, J_{chem}, particularly important tin-

rich solder on copper-based substrates (Gan and Tu, 2002) where a concentration gradient, $\Delta C/\Delta x$, exists. This is expressed as:

$$J_{chem} = D\frac{\Delta C}{\Delta x} \quad . \tag{11}$$

Furthermore, the atomic migration has been shown to also be controlled by a phenomena known as thermomigration, wherein temperature gradient, $-\Delta T/\Delta x$, drives atomic migration where a transport heat Q^* exists which is the difference between the heat carried by a moving atom and the initial state (Huntington and Grone, 1961, Yang *et al.*, 2007, Yang *et al.*, 2008b, Yang *et al.*, 2008a, Chen *et al.*, 2010, Campbell and Huntington, 1969). The flux due to thermomigration driving force is notated as J_{TM}.

$$J_{TM} = C\frac{D}{kT}\frac{Q^*}{T}\left(\frac{-\Delta T}{\Delta x}\right) \quad . \tag{12}$$

In the full treatment, the total atomic flux is a product of these factors, and can be expressed as:

$$J_{Eff} = J_{chem} + J_{EM} + J_{TM} + J_{\sigma} \quad . \tag{13}$$

2.5 ELECTROMIGRATION TESTING OF LEAD-FREE SOLDER INTERCONNECTS

Although the initial work in electromigration in metals used as thin film conductors for microelectronics such as aluminum (Black, 1969), silver (Ho and Huntington, 1966), and gold (Hartman and Blair, 1969), the focus has more recently been applied also to solder alloys used as microelectronic interconnects (Mizuishi, 1984, Huntington and Hu, 1984). A common means for performing electromigration in the early studies involved monitoring surface marker motion, temperature, or failure modes in small specimens electrically clamped with stress free, cooled fixtures (Huntington and Grone, 1961, Ho and Huntington, 1966, Campbell and Huntington, 1969, Routbort, 1968), films deposited on silicon without active cooling (Black, 1969, Howard and Ross, 1967, Hartman and Blair, 1969, Blech and Tai, 1977), and on films deposited on silicon without cooling and made for *in situ* TEM observation (Blech and Meieran, 1969). Early studies performed on migration in solder system included using radioisotope trace elements in metallization like copper (Hu *et al.*, 1983), silver and nickel (Hu and Huntington, 1982), and gold (Hu and Huntington, 1985) in lead-rich lead-tin alloys to measure impurity diffusion due to thermally driven diffusion in soldered rods (Hu and Huntington, 1985). All of these metals form interstitial defects with lead and tin and thus have considerable diffusion rates even at room temperature. Early studies of solder migration also focused on the migration of the solder itself, and the resulting compressive stresses which are observed to cause undesirable growths including whiskering (Mizuishi, 1984). Increasing tin content in the lead-rich solders was shown to increase the diffusivity of silver in the

solder (Hu and Huntington, 1982), but to decrease the diffusivity of copper and gold (Hu and Huntington, 1982, Hu and Huntington, 1985).

Reports in the literature on the electromigration of solder had apparently reduced for some time. Even with lead-containing solder alloys, electromigration became an increased concern around 2001 as solder interconnects approached the 50µm scale (Liu *et al.*, 2000, Huynh *et al.*, 2001). With the trend for lead-free solders at this scale, even more interest was lent to this topic, both comparing leaded with unleaded solder alloys (Lee *et al.*, 2001) and comparing two lead-free eutectic alloys performance (Chen and Chen, 2001). On the study of <100µm solder interconnect between copper traces, Huynh *et al.* (Huynh *et al.*, 2001) found that lead was the dominant diffusing species and that lattice was the dominant diffusing mechanism in eutectic alloy at ~ $0.93T_m$, and report a Z^* value of 33. Lee *et al.* (Lee *et al.*, 2001) studied electromigration at 120°C in eutectic Pb-Sn and Sn-3.8Ag-0.7Cu alloys using the flip-chip package structure with copper contacts and an electroless nickel UMB at the cathode and report a DZ^* value of ~1.85E-10 atoms/cm²/s. They found that the effective charge number in eutectic Pb-Sn was 30-100 atoms/cm²/s, but were not able to approximate the effective charge for the SAC alloy. They also noted dissolution of the nickel UBM and the formation of Ni-Cu-Sn compounds in the interior. Chen *et al.* (Chen and Chen, 2001) reported the effect of electromigration on the interface between the binary eutectic Sn-Cu and Sn-Ag alloys on nickel substrates. They have reported measured values for the diffusivity and effective charge number of tin in the tin-silver eutectic as well as in nickel for several temperatures.

The study of electromigration in lead-free solder alloys has shown a significant effect of electric fields on the formation or dissolution of copper interfaces (Gan and Tu, 2002). Hu *et al.* (Hu *et al.*, 1983) have shown that due to the fast interstitial diffusion rate of copper into the solder joint, that UBM dissolution can be a reliability concern. In 2003, Hu *et al.* (Hu *et al.*, 2003) demonstrated the need for barrier layers and reduced current crowding to avoid failure by rapid dissolution of copper into solder bumps at high current density and temperature.

In the work of Liang *et al.* (Liang *et al.*, 2010) studying the electromigration behavior of Sn-0.7Cu, it was found that growth structures at the anode were suppressed when large amounts of intermetallic were within the solder joint. In the same work, they also report large volumes of copper dissolution under 1.3E4 A/cm^2 and 100°C. They had speculated that the reduction in hillock and whisker growth was due to intermetallic structures acting as a barrier to the tin diffusion. Similar EM strengthening effects through intermetallic compound (IMC) formation were reported in SAC by the addition of nickel, further enhancing the tendency of copper to form IMC in the bulk (Ma *et al.*, 2011). In 2008, Xu *et al.* (Xu *et al.*, 2008) showed that copper pillar structures have superior electromigration resistance due to reduced current crowding effects. Although, they also observe a high amount of copper pillar dissolution into the joint at 1.6E4 A/cm^2 and 135°C, leading to an almost completely intermetallic interconnect with brittle mechanical properties. The work of Ke *et al.* (Ke *et al.*, 2011) is another example of electromigration studies where a large amount of copper is migrated from the cathode into the bulk of the solder, observed to form extensive amounts of copper-tin intermetallic compound. Their work concluded that

at moderately low temperatures, the interstitial diffusion of copper dominates (giving rise to what Lu *et al.* (Lu *et al.*, 2009) describe as Type II failure) and that at high temperatures the self diffusion of tin becomes competitive with interstitial diffusion (favoring Type II failure described by Lu *et al.*(Lu *et al.*, 2009)).

With the observation of rapid copper dissolution in Sn-rich solders, much research has recently focused on the efficacy of UBM barrier layers toward copper and other conductors used in packaging (Wu *et al.*, 2012). Lin *et al.* (Lin *et al.*, 2005) have studies the flip chip structure with eutectic Pb-Sn alloy, and reported a long incubation period followed by a rapid void propagation after initiation. In their work, they observe total melting upon interconnect failure, and subsequent sectioning had revealed large amounts of copper UBM dissolution and the formation of Cu_6Sn_5 intermetallic at the anode interface. A primary conclusion of their study was that simulating the incubation time for void formation is a more sensible way of approaching lifetime predictions for solder interconnects.

Yeh *et al.* (Yeh *et al.*, 2002) showed the mechanism of void formation in the flip chip architecture, and the formation of pancake voids at the cathode interface due to the effect of current crowding. Shao *et al.* (Shao *et al.*, 2004) have reported on electromigration in the Sn-3.5Ag system in the flip chip geometry. They note that at 150°C and 1E4A/cm^2 applied, Joule heating became a serious concern, measuring a 53°C temperature increase. At a 150°C and 5E3 A/cm^2 applied, Joule heating was much less serious, measuring only a 9.1°C temperature increase. They also emphasize the effect of current crowding. Xu and coworkers (Xu and Pang, 2006) measured the effect of current density on the Joule heating derived temperature increase in the flip chip bump structure. They note a 100°C increase in temperature can be reached at 3E4A/cm^2. They also have reported on the effect of EM on the IMC in the Ni/SAC/Cu and Cu/SAC/Cu systems, and note that intermetallic formation was faster on the anode side in either system, and was more prevalent than in isothermal aging. They have also applied digital image correlation to joints experiencing current and thermal stressing, and remark that the strain was the highest in the corner of the bump where current crowding had occurred. Coupled with emerging studies on current crowding phenomena and joule heating, reports surfaced on the effect of current crowding and the thermal properties of the package giving rise to large temperature gradients in solder interconnects which make reliability a concern from the point of view of thermomigration (Chiu *et al.*, 2006, Xu and Pang, 2006). Infrared microscopy has been used to measure thermal gradients as a function of applied current density, and gradients of up to 600°C/cm are simulated at 0.59A in ~100µm bumps.

Ren *et al.* (Ren *et al.*, 2006) have studied the mechanical performance of SAC solder joints subjected to different current densities and for different times. They report a decrease in both strength and ductility after the initial period of electromigration. As EM damage progressed, a further decrease in strength was observed. Their work shows that after electromigration damage ensues, rupture always occurs at the cathode interface. As electromigration damage becomes more extensive, a transition from fracture through the solder and solder-IMC interface transitions to brittle fracture solely along the solder-IMC. They note that combinations of alarming low current densities and stresses can cause failure in relatively short time frames.

The effect of tin grain orientation has also been studied, due to a known drastic anisotropy for diffusion along the c-axis orientation of tin's body centered tetragon structure (Lu *et al.*, 2008, Lu *et al.*, 2009). Using EBSD to compare EM behavior in eutectic Sn-Cu with eutectic Sn-Ag solders, in was found that the microstructural differences were responsible for varying EM mechanisms (Lu *et al.*, 2008). It was observed that in Sn-0.7Cu that many grains exist, and that as EM takes place a reorientation of grains with the c-axis perpendicular to the electrode interface, leading to what is described as Type II failure, implying dissolution of the cathode UBM. It was observed that Sn-3.5Ag joints had fewer grains, one or several, which were more stable under accelerated EM testing, minimizing propensity for Type II failure and resulting in superior EM resistance. It was also showed that the Sn-3.5Ag system was dominated by Type I failure, implying solder void formation as the dominant failure causing mechanism (Lu *et al.*, 2009). At relatively low temperatures (80°C), grain refinement

through microalloying was found to reduce the electromigration performance while increasing mechanical performance (Lin *et al.*, 2009a). The reduction in EM performance is conceivably due to high atomic mobility along the grain boundaries than the bulk. Chiu *et al.* report that supersaturation of constituents can occur within the Sn-rich phases upon application of high electric fields, which can give rise to recrystallization after the electric field is terminated (Chiu *et al.*, 2011). This has obvious repercussions on the electromigration resistance of alloys experiencing this effect.

A key challenge in EM testing of solder joints is feedback of parameters being measured into environmental effects which affect the parameters being measured, where a prime example is Joule heating experienced in the solder. Measuring the temperature of a microscale solder bump is a challenge on its own, and the existence of temperature gradients in the bumps under current stressing has already been established. One method put forth by Yang *et al.* in 2008 (Yang *et al.*, 2008b) involves using the temperature-coefficient-of-resistance method to measure the temperature at the joint accurately. This method characterizes the resistance increase with temperature and the resistance increase with current to use the measured resistance at varying current as a means to indirectly monitor the temperature in the joint. Others have used this method for temperature measurement during EM testing to predict solder lifetimes with varying temperature and current density, and have shown that surface measurements can be inaccurately low (Ramanathan *et al.*, 2007). In 2009, Basaran *et al.* reported on the EM lifetimes of SAC solder in BGA test structures (Basaran *et al.*, 2009). For this study, Black's equation was used to model the mean time to failure as a function of temperature for the test structure

studied. This study again emphasized the joint's resistance not only varied with temperature, but with current density as well. A formula is provided for correlating the current density and resistance to the temperature, as an indirect means to remove joule heating induced resistance changes from the overall resistance change during EM testing, to deal with the complication of resistance being both temperature and current density dependent. The TCR method was shown by Yamanaka *et al.* (Yamanaka *et al.*, 2010) to be accurate within 2°C up to a 100% resistance change in the joint due to electromigration voiding.

2.6 X-RAY COMPUTED TOMOGRAPHY OF SOLDERS

From a microelectronic manufacturing point of view, x-ray imaging and x-ray tomography has been applied to automated quality inspection of solder array structures (Teramoto *et al.*, 2007, Li *et al.*, 2014). X-ray tube imaging techniques have thus long been used for solder inspection, including analysis of bump geometry, voids, and poor wetting. X-ray tube based imaging however, has essentially been limited to these features of the solder microstructure, that is, it is challenging to resolve the individual solid phases of the microstructure including two-phase systems, intermetallics, and dendrites.

Synchrotron x-ray imaging, however, has demonstrated the capability to resolve the individual phases of solder microstructures. In synchrotron x-ray imaging, a much higher intensity, lower energy, monochromatic and parallel x-ray source is utilized, which can provide much higher reconstructed image resolution, better feature contrast, and less image noise (Stock, 2009). In 2007, Tsuritani *et al.* (Tsuritani *et al.*, 2007) utilized an

imaging beamline at the SPring-8 synchrotron in Japan to image the coarsening of the eutectic Pb-Sn microstructure with thermal aging, giving rise a four-dimensional understanding of microstructural evolution . In this study, a single bump was reflowed onto the tip of a steel needle for imaging.

The use of synchrotron imaging to study the thermal evolution in solder interconnects was extended by Tsuritani *et al.* (Tsuritani *et al.*, 2011) to study the effect of thermal cycling on microstructural evolution and crack formation in flip chip eutectic Pb-Sn interconnects subjected to thermal cycling induced fatigue cracking. The ability to resolve microstructural phase evolution *in situ* without the effect of the free surface was unprecedented. In addition to the four-dimensional interplay of crack formation with microstructural imaging, their studies showed that µXCT was a powerful tool to monitor interconnects' response in 3D to a multitude of environmental conditions.

The lead-tin system is an attractive material system for microstructural phase resolution, due to a high x-ray attenuation contrast between the Pb-rich and Sn-rich phases (Yazzie *et al.*, 2012a). The capability of synchrotron x-ray imaging to resolve individual phases within the lead-free microstructure has been recently been demonstrated by Yazzie *et al.* using micropillar volumes made from FIB lathing. (Yazzie *et al.*, 2012a). Within the Sn-3.8Ag-0.7Cu system, the 3D segmentation of tin dendrites, Ag_3Sn precipitates, and Cu_6Sn_5 particles was performed.

Even more recently, this technique has been demonstrated on larger samples of SAC405, and the evolution of the intermetallic particle volume with aging on copper at 150°C was measured (Maleki *et al.*, 2014). X-ray tomography has also recently been applied to studying microstructures and interfaces in 25µm solder bumps on copper pillars (Bertheau *et al.*, 2014b) and the image their solidification during reflow (Bertheau *et al.*, 2014a, Ma *et al.*, 2012a, Qu *et al.*, 2014) .

Obtaining access to synchrotron beam lines for frequent or long term experimentation can be a challenge. Lab-scale x-ray tomography systems for high resolution imaging implementing microfocus x-ray sources offer a promising alternative (Schena *et al.*, 2005). The capability of lab-scale x-ray imaging systems utilizing high-resolution microfocus x-ray sources has recently demonstrated a capability to resolve microscale defects within solder joints through the resolution of preexisting void content due to solder reflow processing (Dudek *et al.*, 2010, Jiang *et al.*, 2011, Padilla *et al.*, 2012, Li *et al.*, 2014, Li *et al.*, 2012) and in electromigration void formation (Xie *et al.*, 2014). Of these initial studies using lab-scale sources to study interfacial porosity resulting from flux outgasing on reflow, modeling approaches are used to emphasize the consequences of stress concentration resulting in strain localizations which can cause premature failures (Dudek *et al.*, 2010, Jiang *et al.*, 2011). More recently, four-dimension *in situ* studies have been implemented to compare modeling predictions of solder joint failure with those observed experimentally and show good agreement (Padilla *et al.*, 2012). Still, the capability of lab-scale µXCT systems to resolve a second solid phase within solder microstructures has yet to be demonstrated. These studies have demonstrated the

emerging capabilities to resolve defect evolution in 3D solder joint microstructures, something which is also demanded for the characterization of electromigration processes.

A critical challenge in quantifying atomic migration in solder interconnects due to electromigration is the challenge accurately measuring void formation and growth. This challenge can be met by applying non-destructive 3D imaging of solder joints experiencing current stressing, such as x-ray computed microtomography (μXCT) (Tian *et al.*, 2011). Synchrotron μXCT was used in 2011 by Tian *et al.* (Tian *et al.*, 2011) to quantify void volume evolution with progressing electromigration damage states, demonstrating the capability of μXCT imaging to accurately measure atomic migration phenomena in solder interconnect volumes. In 2014, Xie *et al.* (Xie *et al.*, 2014) demonstrated the capability of lab-scale x-ray CT systems to resolve the existence and growth of voids in microscale solder joints during electromigration. This work showed the capability of lab-scale μXCT monitor void formation in absence of current crowding, and to quantify the migration of the solder alloy. Using the tomography data, the effective charge for the Sn-3.9Ag-0.7Cu alloy was accurately measured. This work also involved the potential performance improvement offered through microalloying with cerium.

2.7 OBJECTIVE FOR *IN SITU* LAB-SCALE µXCT CHARACTERIZATION OF ELECTROMIGRATION DAMAGE PROCESSES

The novel capabilities of high-resolution XCT have been demonstrated. An increased concern from the microelectronic packaging community over electromigration related failures has been established. The primary motivation for implementing XCT lied in the non-destructive and volumetric nature of the technique, enabling the *in situ* 3D characterization of electromigration processes solder interconnects. The issues associated with obtaining a microstructural understanding of electromigration processes have also been detailed.

The objective of the current work is to further the understanding of EM processes and mechanisms which limit reliability in solder interconnects used in microelectronic packaging. In order to study EM processes volumetrically and non-destructively over long periods of time, a custom lab-scale XCT system was sought. The primary objectives of the application of lab-scale high-resolution XCT toward EM studies included:

- 4D quantification of metallization consumption
- 4D quantification of void formation
- 4D quantification of solder migration, growths, and volume compression
- 4D quantification of void formation and growth
- Accurate measurement of effective charge for electromigration
- Understanding of compositional and microstructure effect
- Understanding of environmental effects of failure mode
- Insight into dominate migration mechanisms

CHAPTER 3

THE DEVELOPMENT OF A LAB-SCALE X-RAY COMPUTED TOMOGRAPHY SYSTEM FOR THREE-DIMENSIONAL MATERIALS CHARACTERIZATION

3.1 INTRODUCTION

3D imaging of material microstructures has typically been limited to destructive techniques such as serial-sectioning[1]; in more recent times, the nondestructive approach of x-ray micro-computed tomography (XCT) has demonstrated unique 3D imaging capabilities in the study of microstructures and material behavior phenomena (Padilla *et al.*, 2012, Williams *et al.*, 2010). X-ray-tomography techniques have long been used in the medical field, but have become increasingly applicable to materials science research as the imaging resolution has approached a scale which is suitable to study material microstructures (Stock, 2009). Advanced facilities which employ synchrotron light sources in XCT experiments (ex. Beamline 2BM, Advanced Photon Source, Argonne National Laboratories) are high in demand due to a limited number of facilities resulting from their high cost, requiring users to run experiments over short time frames and at low frequencies. Accordingly, lab-scale devices (Xradia, Inc.- CA, USA, Bruker Corporation - WI, USA) have been commercially developed for high resolution XCT studies without synchrotron light.

Bench-top systems have fallen short of synchrotron facilities primarily due to the nature of the x-ray source (Flynn *et al.*, 1994). In-house XCT systems utilize braking-radiation

derived x-rays, rather than synchrotron derived x-ray beams, leading to a less brilliant, polychromatic cone-beam rather than a highly brilliant, monochromatic parallel beam. The brilliance affects the necessary scan time, whereas the conic polychromatic beam leads to image artifacts that must be corrected (Feldkamp *et al.*, 1984). The resolution of these in-house systems has been limited by, among other issues, the x-ray source and detector limitations (Schena *et al.*, 2005). It is understood that advances in components for x-ray generation and imaging are continually advancing in performance, further bridging the gap between synchrotron imaging. However, these are slow to arrive in commercial systems, which are also extremely expensive. Furthermore, systems are sought which have a higher degree of modularity for experimental versatility and *in situ* capability.

The goal is to design and construct a custom system by incorporating state-of-the-art components for high-resolution 3D imaging of solder electromigration processes. Previous researchers (Schena *et al.*, 2005, Flynn *et al.*, 1994, Schena *et al.*, 2007, Uesugi *et al.*, 2011, Uhlmann *et al.*, 2008, Dierick *et al.*, 2008) have shown the potential and efficacy of custom built detectors as well as (almost) full lab-scale CT instruments, and have provided valuable insight to many crucial aspects of the design process. Of which studies, for those that have focused on custom detector design theory, the approach has either been focused on application to synchrotron beamline imaging (Koch *et al.*, 1998, Uesugi *et al.*, 2011), or have focused on concepts for the fiber-optic scintillator-lens coupling design (Schena *et al.*, 2005). Of those studies that have been focused on detector optimization for lab-scale system application, a mere survey of commercially available

detectors has been performed (Uhlmann *et al.*, 2008, Dierick *et al.*, 2008). Although Flynn *et al.* (Flynn *et al.*, 1994) have detailed the importance of maximizing x-ray flux through the sample in lab-scale systems for optimizing signal, a design approach for optimizing detection efficiency from the detector parameters has not been provided. This system and the following description of the instrument's design provide a consolidation of these design principles to yield a new, truly optimized lab-scale x-ray microtomography system.

This system, and the following description of the instrument's design, provides a consolidation of these design principles to yield a, optimized lab-scale system in terms of imaging resolution, the brightness of the x-ray source, and the detection efficiency. Specifically, detector design considerations for improvement in regards to efficiency and resolution are offered by considering a lens-coupled design, where the characteristics of the optically phosphorescent (scintillating) medium, optical lens itself, and digital sensor are employed, in conjunction with the intensity and resolution limits of a dual-target x-ray tube and the scintillating medium's response to the *polychromatic* x-ray beam. Additionally, the design and component selection for more accurate alignment of the x-ray source, detector and rotation axis is offered for accurate reconstruction and increased capacity for sample and experiment adaptability.

The design and construction of a unique, lab-scale system for *in situ*, high-resolution and multi-scale, material studies is detailed. The novelty of this design approach lies in the modularity, allowing for control in the balance between spatial resolution and detection

efficiency. The instrument possesses capability to be tailored for experimental and imaging goals at hand, where system characteristics are adjusted all the way from the x-ray source generation mechanism energy and power, the scintillator composition and thickness, the optical coupling lens' magnification, resolution, numeric aperture and field of view (FOV), the x-ray flux through the sample, the x-ray magnification, control over data acquisition via a custom programmed interface, and in the future, the painless incorporation of new exotic equipment which has yet to be realized. Other lab-scale systems, whether commercial or research derived, do not realize this magnitude of controllability and experimental versatility, and have not fully optimized the performance characteristics of the deployed equipment with respect to one another.

3.2 SYSTEM PERFORMANCE GOALS

To justify the design and construction of the CT system used in this work, the performance goals established for the characterization tool will be outlined prior to a discussion of the approach implemented to achieve them. The most fundamental components for lab-scale XCT system are the x-ray source, sample rotation stage, detection system, and computing systems. Many options for each existed commercially, and all affect the performance of the system.

The design of this system is motivated by a need to study materials wherein many features of interests are even smaller than one micrometer, coupled with the need to perform high resolution non-destructive 3D experimentation in absence of synchrotron imaging beamlines. In cone-beam radiography, the spatial resolution can be limited by

blurring from the x-ray source, the resolution in the scintillating medium, the physical size of the detector elements, and the resolution limits of any optics. In tomography, the resolution of the 3D reconstruction may commonly be limited by imperfections in object rotation, the number of projections acquired with unique orientation, algorithmic accuracy, and artifact presence. This tool's design to minimize these limitations is discussed.

Another goal of this work is accommodating the range of sample sizes which may be of interest. This system's design targets imaging samples of tens of microns to several centimeters in diameter: An example of each may be an industry-scale solder-bump or a 1mm dog-bone tensile specimen contained within an *in situ* mechanical loading jig 5cm in diameter. The design approach for achieving this is discussed.

The design also targeted a flexibility to adapt the system to a wide gamut of experimental chambers and new equipment: A prime example is mechanical, thermal, or environmental chambers which may be sample dependent and unique. This concern coupled with maintenance and component upgradability concerns corroborated the logicality of implementing a modular design, wherein commercially available components are integrated with custom components to yield a fully functional instrument.

After an investigation into the limitations of lab-scale XCT, the performance targets of the XCT system were realistically refined. The following performance goals were established:

- Spatial resolution of less than 1μm
- Imaging of specimens of up to 10mm in diameter
- Imaging of high atomic number sample compositions
- Capacity for *in situ* chamber up to 5kg and 10cm dia.
- Programmable and modular for incorporation of nearly any component for future advancements, replacements, and extended lifetime

3.3 DESIGN METHODOLOGY

In any digital imaging system, there is a trade-off between the FOV and the feature resolution in any given single frame, where the compromise is made by optimizing the magnification (Paciornik and de Pinho Mauricio, 2004). This is due to limitations on the digital detection system's chip pixel count and spatial sampling frequency. The ability to resolve features is also affected by the contrast in the image between the feature of interest and the surroundings as well as the feature spacing, commonly shown using the point-spread function, line-spread function, edge-spread function, modulation-transfer function, contrast-transfer function, or the optical-transfer function, and usually with the full-width at one-half the peak's maximum signal criterion for resolution (Stock, 2009) (Schena *et al.*, 2007). In radiography, the contrast between features is largely controlled by the difference in the average linear x-ray attenuation coefficient of the feature of interest and that of the surrounding at the energy of the incident x-rays, and the exposure time. The difference in detected intensity, I, between a pixel sampling a feature and that of a pixel sampling the surrounding area determines the contrast of that feature. Thus, higher counts in longer exposures can yield better contrast for features in thicker/denser

samples or for features with a low difference in x-ray attenuation compared to that of the surrounding medium. The transmission, I/I_0 , where I_0 is the transmitted intensity, of monochromatic x-ray through the sample, decays exponentially through the thickness, x, and is a function of the average density, ρ, and mass attenuation coefficient, (μ/ρ), related through the Beer-Lambert law as:

$$I/I_0 = exp\left(-(\mu/\rho)\rho x\right). \quad (14)$$

A detected intensity, I, is determined for every detector element over many known orientations of the sample. The usefulness of longer exposures is limited by thermal, electronic, or electromagnetic noise at the digital detector as well as bit-depth of the detector, beam stability, and throughput necessity. Thicker samples, with a larger x, require larger values of I_0, or longer exposures for the same detected intensity. Therefore, in addition to requiring a larger FOV and thus experiencing a lower spatial sampling frequency, the resolution possible to obtain in large samples is further challenged. To detect a given number of counts through larger samples, higher x-ray energies/intensities are required, degrading the resolution by penumbral blurring as described by Chaney *et al.* (Chaney and Hendee, 1974) and G. Schena *et al.* (Schena *et al.*, 2007). Imaging resolution is highly dependent on the contrast of the imaged feature, as discussed by S. Paciornik *et al.* (Paciornik and de Pinho Mauricio, 2004), which in the case of x-ray imaging is dictated by dissimilarity in the feature's and surroundings' effective x-ray attenuation coefficient. This difference in attenuation is typically measured using fluorescing mediums which emit optical light with intensity proportional to the incident

x-ray intensity: Therefore, the spatial resolution of a system relying on phosphorescence can be limited by the spatial sensitivity of the phosphor. In the case of lens-coupled single-crystal-scintillator x-ray detection systems, the imaging resolution is also limited by the optical characteristics of the light conversion medium and numeric aperture of the optical relay components, due to refraction in the scintillator, the optical depth-of-field, and classical diffraction-limited lens resolution as described by A. Koch *et al.* (Koch *et al.*, 1998).

The ideal x-ray source for accurate CT is one which emits parallel, monochromatic x-rays such as at synchrotron beam-lines. The use of monochromatic x-rays allows for determination of the actual linear x-ray attenuation coefficient in a voxel, whereas with an untreated x-ray tube such accuracy is precluded by a polychromatic nature. X-ray tubes, used in bench-top systems, produce *Bremsstrahlung* radiation in a cone of emission. To reconstruct the 3D attenuation structure of a sample from projections acquired with cone-beam x-rays, reconstruction algorithms such as the Fourier-transform-based Feldkamp-Davis-Kress (FDK) (Feldkamp *et al.*, 1984) or iterative Algebraic-Reconstruction-Techniques (ART) (Mueller *et al.*, 1999) are implemented, which approximate the attenuation coefficient at each voxel by accounting for the variation in the angle of the beam path from pixel to pixel and back projecting into the sample space using known scan geometries. These algorithms commonly use weighting functions, such as the Shepp-Logan or Ram-Lak filter function, to improve signal-to-noise and sharpen edges in a reconstructed sample plane image, as discussed by T. Taylor *et al.* (Taylor and Lupton, 1986). The accuracy of these algorithms depends very strongly on physical

parameters such as component perpendicularity, axis alignment, beam-to-central-axis angle at the extremities of the rotating sample, and the amount of orientation information obtained. Accurate reconstructions are more challenging should aspects of the sample move out of the detector's FOV during rotation, discussed by R.M. Lewitt *et al.* (Lewitt and Bates, 1978). Hence, it must be ensured that samples intended for imaging can be rotated as perfectly as possible, and positioned very accurately over a full rotation while residing within the FOV of the detector.

3.4 X-RAY SOURCE SELECTION

In the selection of an x-ray source for high resolution imaging, the selection is limited to a microfocus x-ray source. That is, the x-rays are emitted from a micrometer-sized (typically one to several micrometers) area in the target. In the evaluation of microfocus x-ray sources, all parameters were considered, including power range, voltage range, focal spot size as a function of power, the minimum focus-to-object distance (FOD) which can limit x-ray flux through the sample, the type of the target, the target composition, whether the target is cooled, rotated or interchangeable, the lifetime of the tube in the case of a vacuum sealed source, or the lifetime of the filament in the case of a vacuum-pumped source, the maneuverability and compatibility with the system design.

The resolution limit of the system based on the x-ray focal spot size conditions and the pixel size of the selected imaging chip (15μm) is shown in *Figure 1.* This concept is critical for determining the optimal system magnifications for a given combination of x-ray source/generating conditions and digital imaging chip deployed into a system. This

magnification, M, can be determined for a given focal spot size, F, and pixel size, P by the succinctly summarized equation shown by G. Schena *et al.* (Schena *et al.*, 2005):

$$M = (2P / F) + 1 \qquad (15)$$

The total system magnification can be determined for a given x-ray focal spot size and imaging sensor's physical pixel size at which neither parameter is limiting the resolution of the system. The total system magnification is a function of x-ray geometric magnification and optical magnification:

$$M_{System} = M_{Optical}\, M_{X\text{-}ray} \ . \qquad (16)$$

One application of *Figure 1* and *Equation 16* is the determination of system magnification, x-ray generating target configuration (transmission vs. reflection), the x-ray tube accelerating voltage and x-ray target current to achieve a particular targeted spatial resolution: The system magnification required to reach a certain resolution can be determined from the sensor pixel size (see G. Schena *et al.* (Schena *et al.*, 2005).), the focal spot size can be then be determined which does not limit resolution, and the x-ray accelerating voltage, target current, and target type can be adjusted to achieve a focal spot of this size (see Chaney and Hendee (Chaney and Hendee, 1974)). A direct application of this relation is considering the focal spot size of any candidate x-ray source as a function of target power or x-ray intensity in conjunction with the imaging goals at hand, and designing the detector to achieve the necessary magnification.

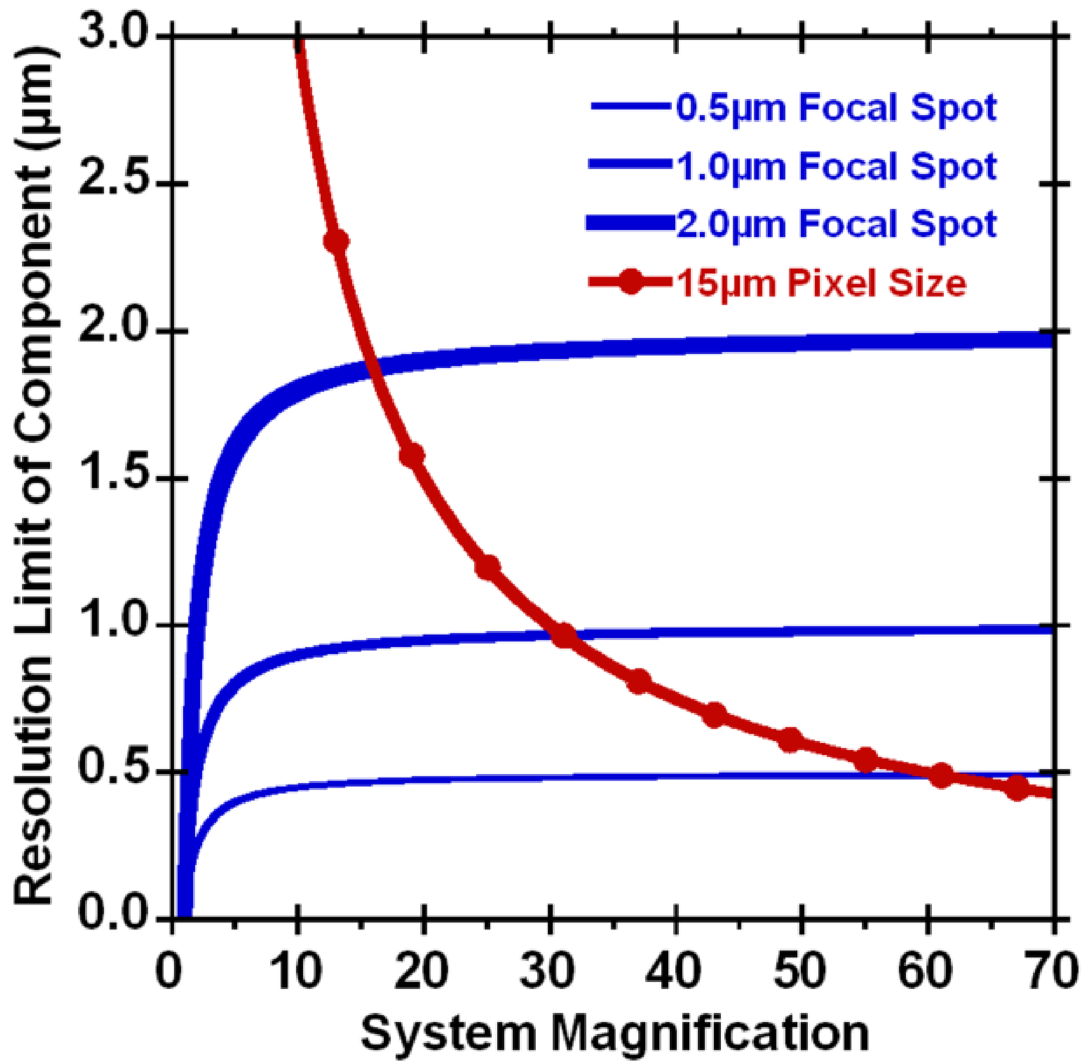

Figure 1. The Minimum System Resolution Limited by Different Focal Spot Sizes and the Detector Pixel Size as a Function of System Magnification (Mertens *et al.*, 2014c)

The achievable x-ray magnification can be limited by the component separation distances necessary, the size of the x-ray detecting screen and the camera's FOV. The relevant component separation distances are the Source-to-Detector-Distance (*SDD*) and Source-to-rotation-Axis Distance (*SAD*), and are related to the x-ray magnification by

$$M_{X\text{-}ray} = SDD\ /SAD\ . \tag{17}$$

The emission area of a source's x-ray producing target, i.e. the focal spot, limits the resolution of the system at large magnifications. Transmission targets limit lateral spreading of the electron beam within the target by being thinner than the normal x-ray producing interaction depth in a bulk material, effectively yielding the smallest focal-spot for the highest resolution imaging. Conversely the reflection-type target configuration can be loaded at much higher power densities yielding a more energetic or brighter beam for denser samples, as discussed by B.C. Masschaele *et al.*(Masschaele *et al.*, 2007). Ultimately, this amounts to detail detectabilities of hundreds of nanometers via a transmission target configuration, and in the range of 1µm with the reflection target configuration for thicker/denser samples.

The x-ray source implemented in this system (X-RAY WorX GmbH XWT-160-SE/TC - Garbsen, Germany) was selected based on an optimization with respect to system performance goals: This source is capable of 160kV of accelerating potential yielding high energy x-rays to maximize transmission through large samples, is capable of a very small focal spot size for high resolution imaging, and has dual-target

(transmission/reflection) interchangeability to perform multi-scale imaging. The manufacturer of this source specifies a minimum detail detectability of <0.3 micrometers and a maximum power of 3W with the high resolution transmission target and a minimum detail detectability of <2.0 micrometers and a maximum power of 280W with the reflection target.

Using computer aided design (CAD) software tools, a dual-target x-ray cradle was designed to maintain beam position and emission axis when switching between x-ray source target heads, critical for multi-scale 3D imaging (*Figure 2*). This was accomplished using tight tolerance machining of precision ground aluminum plate and steel rod to construct the cradle, wherein mounting positions were determined via x-ray target position per computer model within the x-ray heads respectively. Other implementations of CAD design included positioning and alignment trials of all the components considered for selection, and the design of component-to-component adapter plates in both the sample and the detector component ‘stack’.

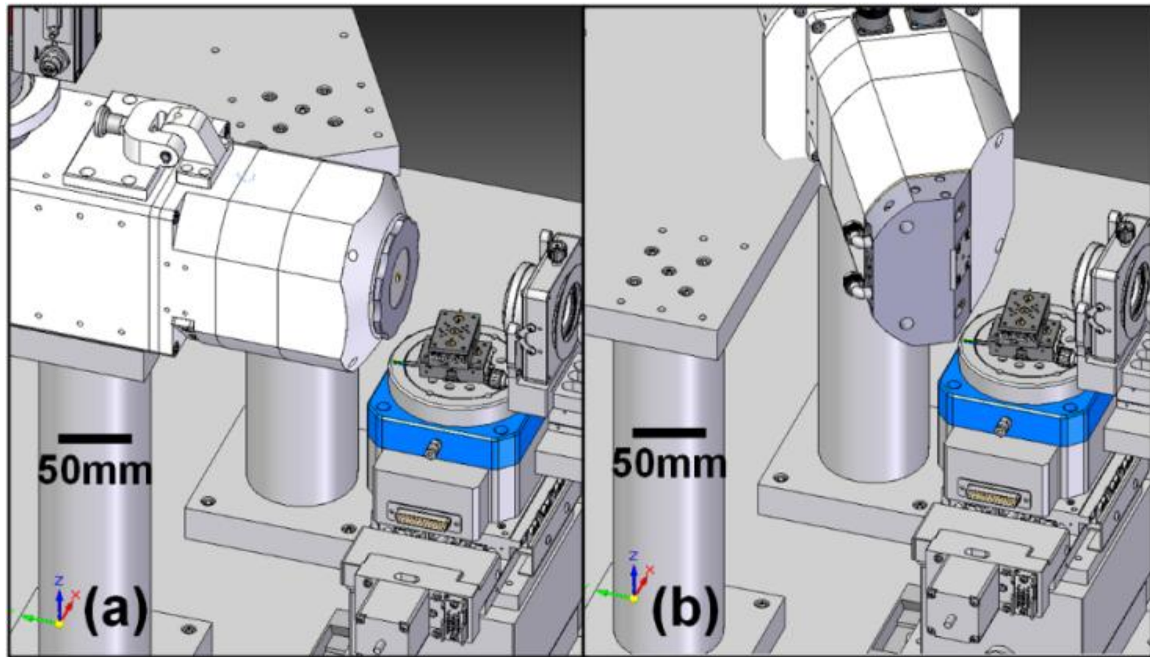

Figure 2. CAD Model Showing the System Configuration with both X-Ray Target Heads Being Implemented *a*) Transmission Target, and *b*) Reflection Target

3.5 X-RAY DETECTOR DESIGN AND COMPONENT SELECTION

There exist a wide variety of configurations for digitizing sampled x-ray intensities, most relying on scintillating materials to convert x-rays of a given intensity to a proportional amount of optical light, coupled to a light sensitive imaging chip. Phosphors can vary in microstructure from single crystal to columnar-grained to powder-compacted (Stock, 2009, Packham, 2010, Martin and Koch, 2006, Sato *et al.*, 2000, Tous *et al.*, 2007), imaging chips namely include complimentary metal-oxide semiconductor (CMOS) and charge-coupled devices (CCD) types (Graafsma and Martin, 2008), and the mode of transferring the scintillated light to the light-sensitive detector elements can vary from lens to fiber-optic to direct contact of the phosphor and chip (Aslund *et al.*, 2010, Uesugi *et al.*, 2011).

The imaging system designed adopted the lens-coupled configuration, providing what was determined to be the highest resolution, light transfer efficiency, and versatility. Specific to the decision of a fiber optic versus lens coupled sensor/phosphor design, three factors were most influential: The ease with which the scintillating medium can be interchanged in the lens-coupled design, the ability to construct the lens-coupling in-house, and the added magnification variability of the lens-coupled configuration. Another function of the sensor-phosphor coupling is the capability to remove the light sensor out of the x-ray path, which can give rise 'zingers' in x-ray images caused by non-signal x-ray interaction with the sensor itself (Hardy *et al.*, 1999). With fiber coupled configurations, the fiber-bundle length should allow for camera removal from the beam path. In the case of lens-coupled configuration, the use of mirrors has been used for

optical signal diversion from the x-ray path to the sensor. Two obvious solutions exist in placing a right-angle mirror in front of the camera lens (Stampanoni *et al.*, 2002) or behind the camera lens (Uesugi *et al.*, 2011), where the prior has the added advantage of also removing the lens from the beam path potentially preventing burnishing (a darkening or browning of the optical glass (Koch *et al.*, 1998) which leads to a loss in optical transmission). For the first solution, a longer working distance lens is required, and for the second a longer optical path behind the lens is required. The longer optical path behind the lens, although easily accomplished with infinity corrected objective lens, may affect the range of magnification possible with finite-focus lens.

Selecting the optimum scintillator requires careful consideration of many parameters including composition, thickness, emission spectra, density and light yield for maximizing detection efficiency over a range of x-ray energy balanced against factors such as the thickness, index of refraction and numeric aperture of the lens system (if applicable) for high resolution imaging capability (Packham, 2010, Tous *et al.*, 2007, Valais *et al.*, 2009). Particularly, the thickness of the selected scintillator must be carefully optimized in the trade-off between x-ray conversion efficiency and the resolution limit of the system based on the spatial sampling frequency of the camera system and the resolution of the x-ray source. Due to that fact that scintillator thickness can limit the resolution, but also determines the amount of signal achievable in a given time frame of data acquisition, extreme care must be taken to optimize the thickness of the scintillator with the performance goals in mind.

Many studies provide insight into the resolution achievable using lens-coupled single crystal scintillators, demonstrating that thin scintillator screens are necessary for achieving high imaging resolution (Koch *et al.*, 1998, Martin and Koch, 2006). These studies also demonstrate that image resolution in low numeric-aperture lenses is diffraction limited, with only a small dependence on scintillator thickness. Similarly, with high *NA* lenses, higher resolution is possible than with low NA lenses, but requires thinner scintillators. Numerical simulations for imaging with a YAG:Ce scintillator, where refractive index n = 1.95, emission wavelength λ = 550nm, and assuming a lens of some NA is focused on the scintillator, show that a suitable model for calculating the spatial resolution in terms of the full width at 50% of the integrated line-spread-function (LSF) is

$$R=\sqrt{(p/NA)^2+(qtNA)^2} \quad , \tag{18}$$

where the constants p = 0.18µm and q = 0.075, t is the thickness is micrometers, and *NA* is the numeric aperture of the lens system used (Koch *et al.*, 1998). Taking *NA*= 0.1758, numerical approximations of achievable resolution using YAG:Ce of varying thickness can be demonstrated, as shown in *Table 3*. This should be considered for all candidate scintillating materials using the appropriate values for modeling.

Table 3

Spatial Resolution Achievable at 50% Contrast Based on a Lens Used in the Microtomography System (NA=0.1758) Using YAG:Ce of Varying Thickness Based on Equation 18

YAG:Ce Thickness, t (µm)	5	25	50	100	250	500
Resolution, R (µm)	1.03	1.08	1.22	1.67	3.45	6.67

A competing factor for determining the optimum thickness of a scintillator implemented for a given task is the fraction of absorbed x-rays within the scintillator itself, which are able to participate in photoelectric absorption and ultimately the scintillation of optical light (Koch *et al.*, 1998). The ultimate consequence of this compromise is degraded detector quantum efficiency (*DQE*) in detectors capable of high-resolution. This trade-off forces the instrument designer to determine what spatial resolution is desired, and whether the resulting *DQE* with a scintillator of an appropriate thickness to achieve that resolution provides a reasonable required exposure time per projection considering the flux of the x-ray source used (which is limited by the target resolution in the case of vacuum-tube x-ray sources).

The goal of this design was to achieve one micrometer imaging resolution capability, while simultaneously optimizing the detector's *DQE* for high energy x-ray scanning conditions. Using the approach of Koch *et al.* (Koch *et al.*, 1998) the *DQE* of this system was analyzed as a function of energy under different hypothetical scintillator compositions of varying thickness in conjunction with the candidate image sensors and lens coupling options using *Equation 19*,

$$DQE = \frac{SNR_{OUT}^2}{SNR_{IN}^2} = \eta_{abs}(E^x) \cdot \left(1 + \frac{1 + 1/\eta_{\lambda/e}}{\eta_{coll} \cdot (E^x/E^\lambda)\eta_{x/\lambda}}\right)^{-1}. \tag{19}$$

Here, *DQE* is the detection efficiency, $\eta_{abs}(E^x)$ is the absorption efficiency at x-ray energy, E^x, $\eta_{\lambda/e}$ is the light to electron conversion efficiency of the detector, η_{coll} is the

light collection efficiency of the lens based on the numeric aperture and the scintillator index of refraction, $\eta_{x/\lambda}$ is the effective x-ray to optical light conversion efficiency, and E^{λ} is the energy of the optical light being detected by the CCD. The density (6.73 g/c.c. for LuAG:Ce and 4.55 g/c.c. for YAG:Ce), the light yield of the scintillating material per keV of deposited energy (20 photons/keV for LuAG:Ce, 45 photons/keV for YAG:Ce), the refractive index (1.82 for LuAG:Ce, 1.85 for YAG), the relative emission spectra available from product vendors, and the photoelectric mass attenuation coefficient as a function of energy (calculated from NIST's X-COM x-ray absorption calculator (NIST, 2014)) were polled and used to calculate the *DQE* of the detector being designed in order to aid in the selection of an optimal scintillator. While many scintillator compositions and thicknesses were considered, ultimately, the selection analysis was limited to compositions and dimensions which were commercially available. Another realistic restriction is the size of imaging area of a certain scintillator of a certain thickness.

Given the multi-scale yet high resolution goals of this instrument, the approach of interchangeable scintillators of different composition and thickness was adopted, which is a practical necessity for systems to be used for samples of different size/composition under different target resolutions. Nonetheless, a scintillator composition and thickness was identified with respect to the optical lens' highest numeric aperture setting and optimal magnification factor (3.5x), aided by calculations of the resulting *DQE* when integrated with the selected CCD chip and lens system. The higher attenuation of LuAG:Ce at high x-ray energy for a given thickness is preferred for high energy radiography. Note that this is not the case for systems, such as synchrotron facilities,

which use low energy x-rays near 20-30kV. The thickness was selected to maximize the theoretically achievable *DQE* while maintaining the resolution of the optical system. The scintillator selected for the detector in this configuration was a single crystal LuAG:Ce circular disk, selected based on achievable resolution, the resulting *DQE* with the camera and lens, and commercial availability in a wide range of thicknesses. The material was selected over YAG:Ce based on the resulting calculated *DQE* of the detector at high energy (discussed further in the next section). The scintillator currently in use is a 250 micrometer thick LuAG:Ce crystal mounted in an Aluminum ring (Crytur, spol.s r. o., Turnov, Czech Republic), chosen as the best single optimized thickness for our initial performance goals, as the resolution was determined to safely coincide with the nominal effective pixel size of the CCD/lens combination (4.29µm) adopted using the aforementioned modeling approach. A thinner scintillator can be used where a higher resolution is needed at the scintillating medium, and conversely a thicker scintillator can be used where detection efficiency is more of a concern than spatial resolution or if lower optical magnification is desirable.

The selected camera (Alta U230, Apogee Imaging Systems, Inc. - CA, USA) in this system contains a high cosmetic-grade large format 2048x2048 back-illuminated CCD array (CCD230-42, e2v technologies inc., UK) composed of 15µm square pixels, 16-bit dynamic range, and a peak quantum efficiency of about 95% at 550nm corresponding to the peak emission spectra of LuAG:Ce (cerium-doped lutetium aluminum garnet), YAG:Ce (cerium-doped yttrium aluminum garnet), and CsI:Tl (thallium doped cesium iodide). Selecting a scintillator with a peak emission wavelength near that of the

candidate imaging chip's peak quantum efficiency (*QE*) helps to maximize count rates and minimize scan time for a given projection of a given sample. High *QE* is achieved by the back-lit architecture, a green-sensitive 'mid-band' coating to the CCD chip, and thermoelectric cooling to -30°C. A large dynamic range sensor is important for x-ray detectors in order to maximize the number of counts possible before pixel saturation. This is critical when attempting to achieve contrast between phases with similar x-ray attenuation coefficients at the x-ray energy used for imaging. The camera's large-format CCD chip did come with the challenge of identifying a suitable lens for high-resolution imaging which was also able to utilize the entire area of such a large chip. The lens selected for this purpose (Micro-Symmar 2.8/50mm, Schneider Optics, Inc. - NY, USA) is a finite-focus macro-lens selected on imaging resolution, a relatively large numeric aperture, low image distortion, and magnification variability. As a finite-focus lens, the magnification of the lens system can be tailored by altering the length of the optical track length to the chip, which also changes to working distance of the lens. This lens' image quality is optimized for a magnification factor of 3.5x, although a magnification range of 2x to 5x is practically achievable. The optical track length can be changed using the adjustable length optical tube, or by adding and removing optical extension tubes, both of which are visible behind the lens in *Figure 3*.

The camera and scintillator-housing design and their physical linkage were facilitated by CAD tools (*Figure 3*). A camera support bracket was designed to mount onto a larger plate, which also supports the scintillator. The scintillator housing is required to provide a stable support for the scintillator, and provide alignment capability for rotation and pitch

in order to realize a scintillator which is perpendicular to both the x-ray source cone axis and the camera/lens assembly. Another requirement is the ability to adjust the spacing between the scintillator and the camera lens, i.e., the working distance. For this mode of control, it is desirable to have highly linear motion in order to maintain a flat, focused image field on the scintillator. Another important consideration is keeping dust from settling on the scintillator surface, which results in dead-zones in the detection system. This nuisance can be alleviated by proper scintillator containment in the housing design, the approach here being to contain the scintillator within a sealed optical tube.

The scintillator and its supporting substrate were mounted within an optical tube (SM1L10, Thorlabs Inc., NJ, USA) between two low stress retaining rings (SM1LTRR. Thorlabs Inc., NJ, USA) as shown in *Figure 4*. The 'front' of the scintillator assembly was sealed off by a 0.001" thick layer of Kapton film, pinned to the front of the tube with a third retaining ring. The assembly was necessarily performed in a clean room environment. The back of the scintillator tube was sealed by a 6mm leaded glass window: Any dust settled on this surface is well out of focus, 2mm away from the scintillator. Additionally, the leaded glass offers minor shielding of the lens from x-rays, but transmitting scintillating light. The tube was optically sealed at the front by a graphite spray and in the back by a bellows linking the tube to the lens. The material at the front of the tube attenuates x-rays to some extent, and must be minimized. This was accomplished by using very thin, low attenuating film.

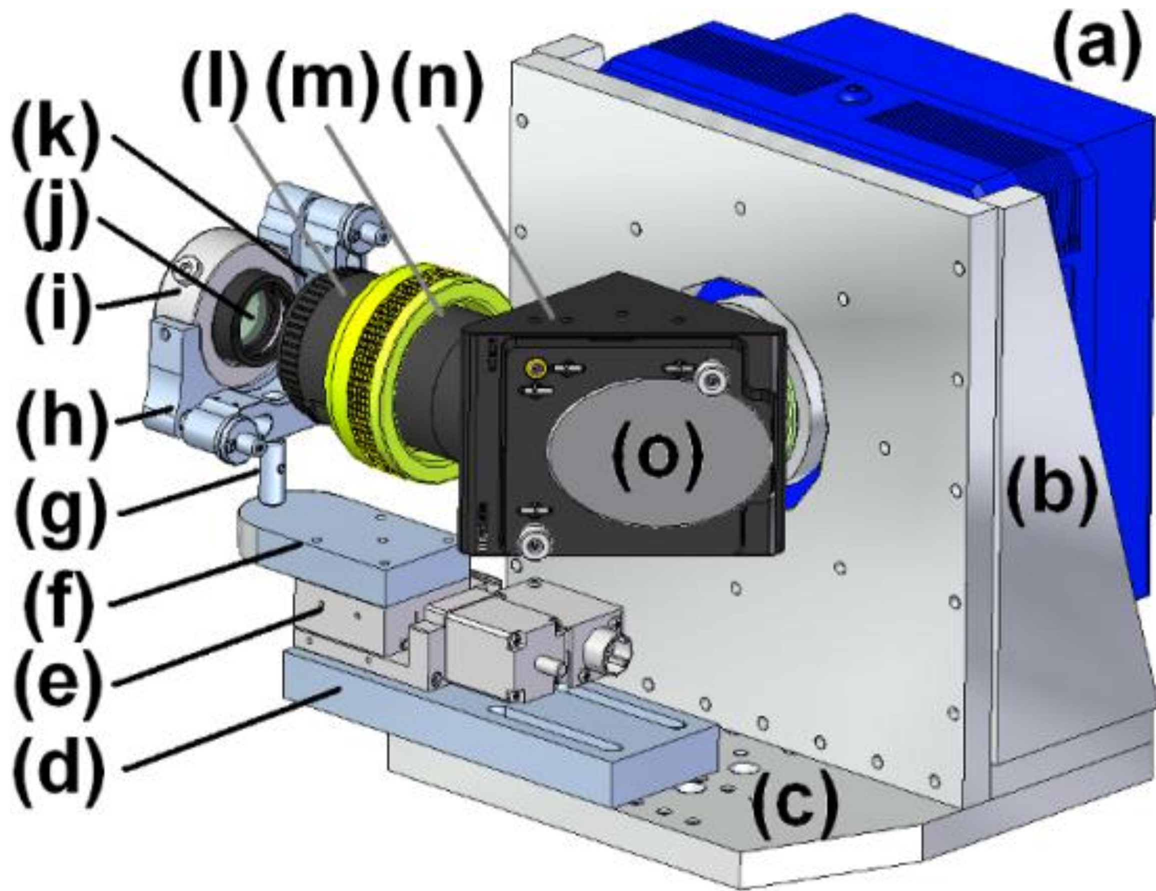

Figure 3. Detector Assembly in CAD Model: *a*) Camera *b*) Camera Support and Shield *c*) Base Plate d) Long-Range Extension Plate, for Varying Extension Tubes *e*) Focusing Stage *f*) Mirror-Mount-to-Focusing-Stage Adapter *g*) Mirror-Mount Post *h*) Mirror Mount *i*) Shaft Collar Support *j*) Optical Tube Assembly *k*) Bellows (not shown) *l*) Lens *m*) Extension Tubes *n*) Right-Angle Mirror Housing *o*) Right-Angle Mirror

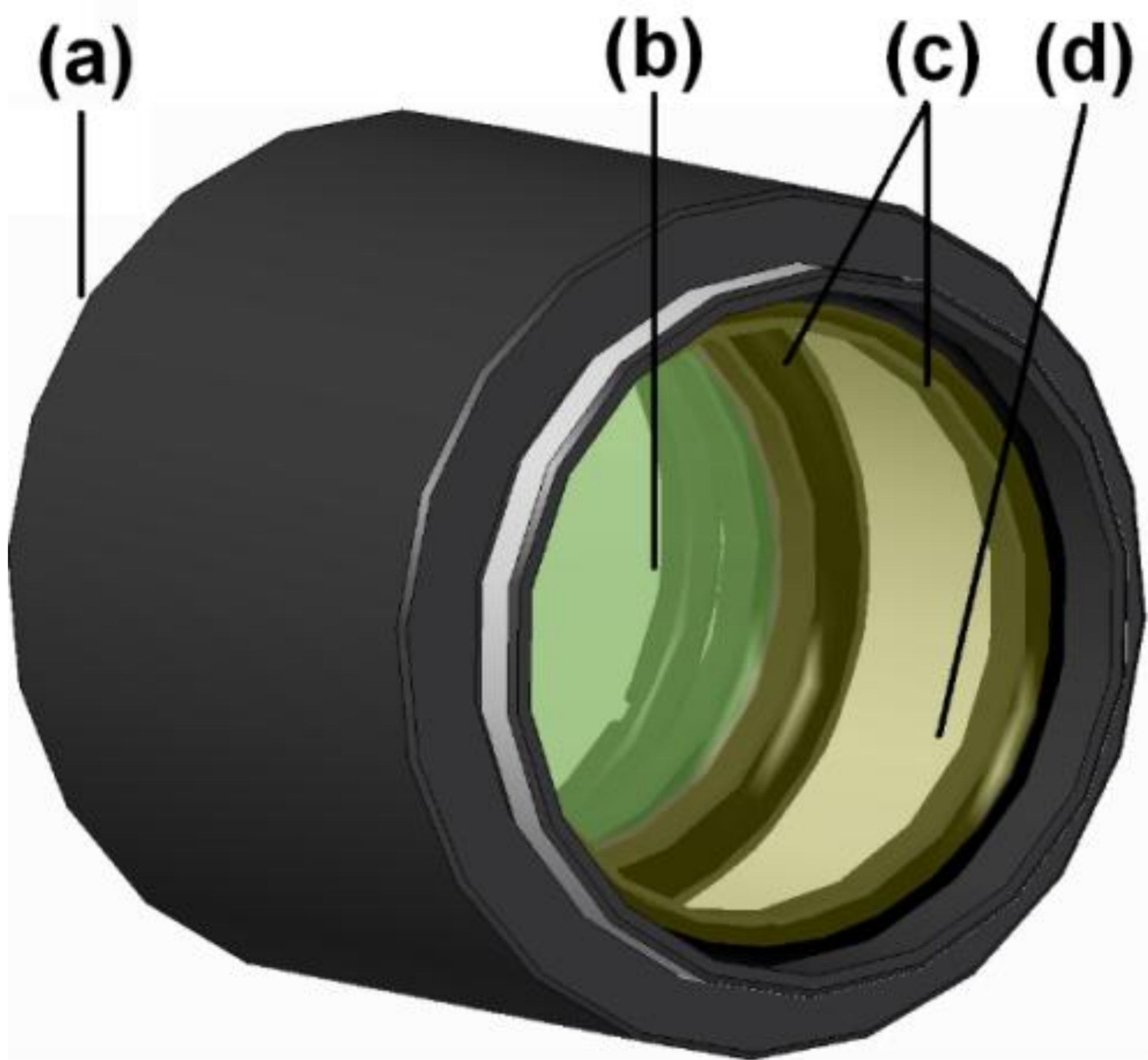

Figure 4. Scintillator Tube Housing Assembly in CAD Model, *a*) Optical Tube *b*) Scintillator *c*) Retaining Rings *d*) Kapton Film

3.6 ROTATION STAGE SELECTION

XCT reconstructions rely on acquiring projections at many sample orientations. A stage which provides perfect rotation without any physical distortion and which provides precise and accurate positioning is desired. It is also ideal that the sample rotation stage have a small footprint and a high load capacity. In actual rotation stages, some undesirable procession, tilt, wobble or run-out may occur during rotation, and the precision of positioning is finite. The rotation stage in this system (ORT-101-L Air Rotary Air Bearing with a Delta Tau MAC-MC-1A-SD Controller, Nelson Air Corp. - NH, USA) was selected to maintain the system's imaging resolution, providing 27kg load capacity, high positioning precision within 0.00001 degree, and low distortions of less than +/-.025µm at 11rpm 6" from the spindle face.

3.7 TOMOGRAPHY COMPUTING AND METHODOLOGY

Two workstations have been implemented in this system in order to increase the flow of data: One for the control of the data acquisition software and equipment, and a second for projectuion processing, tomography reconstruction, and post-reconstruction image processing. Although reconstruction is computationally intensive, post reconstruction can also be very computationally demanding, including volume segmentation, visualization, and quantification. The performance specifications of the reconstruction computer are of most significance: The CPU on this workstation utilized an Intel Core i5-2500 3.3GHz quad-core processor (Intel Corporation, CA, USA). More importantly, the system employs a 448 core 6GB CUDA enabled GPU (Tesla c2075, NVIDIA Corporation, CA, USA for graphic hardware accelerated reconstruction. Of critical importance for

performing reconstruction on large datasets without the use of a computer cluster is the size of the RAM on the system. Reconstruction was performed using MATLAB (MathWorks). The reconstruction algorithm implemented was a modified version of open-source implementations of the FDK (Feldkamp *et al.*, 1984) fast-fourier transform back-projection method made available by Rezvani *et al.* (Rezvani *et al.*, 2007) and K. Kim (Kim, 2014). The code was modified by Arizona State University research scientist, Dr. Jason Williams, for more efficient use of built-in MATLAB functions, code acceleration on graphics hardware, and added minor functionality. Roughly twice the projection data set, in single precision, plus 5-10GB is required to run cone-beam reconstructions, that is, without breaking the data up into smaller subsets. This system has 32GB of RAM. To give perspective, a 1441 image dataset (i.e., 1/8° steps over 180°) acquired using 2048 x 2048 elements per frame is roughly 22.5GB, making it necessary to reconstruct such a large dataset in subsets.

The workstation used for data acquisition primarily acted as a scan control station. The x-ray tomography scan routine was written in LabVIEW (National Instruments). The scan program enabled control of the exposure time, CCD binning, scan rotation start angle, scan rotation end angle, scan rotation increment, the number of frames acquired for each orientation for frame averaging, the frequency of reference and dark field imaging for calibration, the position of the reference stage for reference imaging, the position of the reference stage for sample imaging, the x-ray source accelerating voltage, the x-ray source target current, and the x-ray source electron beam centering interval. Without

considering *in situ* equipment, this system consumed three USB ports, one Ethernet port, and one 9-pin RS232 serial port on the workstation.

3.8 AUXILIARY COMPONENT SELECTION AND INTEGRATION

In additional to the aforementioned critical components of the XCT system, several other components are essential to make XCT scanning practical. Sufficiently thick x-ray shielding is required, depending on the x-ray source, and the design of the chamber can be a challenge. Equipment layout, chamber ventilation, temperature stability, operator access, and the assembly site must be considered. Another necessity is the ability to shield the sensitive components of the XCT system from environmental vibrations. A vibration-damping breadboard table top and air-floating vibration isolator support columns (RS2000-36-8 & S-2000A-428, Newport Corporation - CA, USA) were selected as the foundation for the system components, based on an ability to minimize any vibrations and facilitate component mounting/assembly. The top also allows for very large x-ray magnifications due to its 6 ft. (~2m) length.

Centering the specimen to be imaged on the center of the rotation stage is a practical necessity in order to maximize the FOV. Two linear-axis piezo centering stages of 5kg load capacity and 2nm resolution (PPS-28, Micos USA LLC - CA, USA) were implemented for this purpose. The high load capacity enables large *in situ* experimentation chambers and the step resolution enables precise positioning of the sample.

Obtaining reference images is another practical necessity, wherein the beam is engaged under the same conditions for imaging but with no sample in place in order to calibrate the data for any defects in the optical system and variability in the CCD elements' sensitivity. This is accomplished in this system by utilizing a high-load, long-range motorized linear stage with high repeatability (XA10A-R2, Kohzu Precision, Alio Industries - CO, USA) established orthogonal to the central axis of the x-ray beam. This is critical in order to remove the sample from the beam path at predefined increments, acquire a 'reference frame', and return the sample accurately to its original position for scanning. This stage has a 20kg load capacity and ±0.2μm repeatability for this purpose.

In addition to these components, long-range linear stages (Unislide A6012, Velmex, Inc. - NY, USA) were implemented in order to align and position the sample and detector with each other and with the central axis of the x-ray cone. Thus, the long range linear manipulators acting parallel to the central axis of the cone-beam emission were selected based on the range of magnifications desired and the necessary load capacity to support the components assembled upon each.

The selection and verification of component compatibility, and integration into the system design, was made possible by use of CAD and simulation, by incorporating part models made available from equipment manufacturers. With these tools, it was possible to design the dual-target x-ray cradle in this system to maintain beam position and emission axis when switching between x-ray source target heads, critical for multi-scale 3D imaging (*Figure 2*). Even more challenges tackled with CAD included positioning

and alignment trials of all the components considered for selection, and the design of component-to-component adapter plates in both the sample and the detector component 'stack'. A photograph of the system operating with the directional style x-ray target can be seen in *Figure 5*.

3.9 SUMMARY

The motivation for designing and constructing a modular x-ray computed tomography system has been established. By understanding the limitations and trade-offs for micro-XCT, and implementing a modular design approach, realistic performance goals were outlined for the system: The approach for meeting these goals has been highlighted. The process for component selection and the design of the system based on the selected components has been detailed. The selected components themselves have been discussed, as well as the approach for integrating both critical and auxiliary components into a fully functional microCT system.

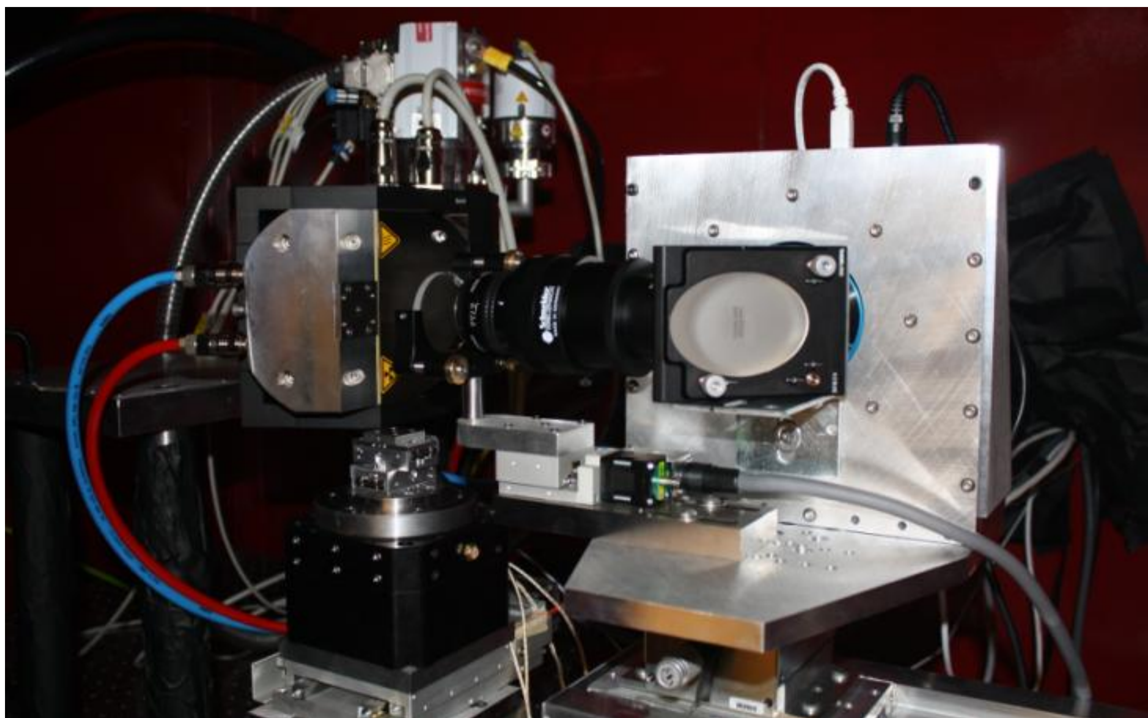

Figure 5. Interior View of the Constructed X-Ray MicroCT Scanner Shown with the X-Ray Source Mounted on a Custom Cradle (Upper Left), the Sample Rotation Stage on the x-y-z Translating Motion Stack (Lower Left), and the Detector Assembly Including the CCD Camera and Scintillator Assembly Mounted on a x-y-z Translating Motion Stack (Right) (For Scale, the Light Shaded Oval Mirror in the Detector Assembly is 2 in. Tall)

CHAPTER 4

MODELING AND CHARACTERIZATION OF X-RAY YIELD IN A POLYCHROMATIC, LAB-SCALE, X-RAY COMPUTED TOMOGRAPHY SYSTEM

4.1 INTRODUCTION

In x-ray imaging, it is desirable to have both a high signal rate and high imaging resolution. In the low x-ray flux environment of cone-beam, lab-scale imaging, the importance of x-ray detection efficiency is particularly important (Flynn *et al.*, 1994). In microfocus x-ray tubes, the x-ray power is inversely proportional to the spatial resolution (in lp/mm), that is, the spatial resolution typically decreases (gets worse) with increasing x-ray signal (Chaney and Hendee, 1974, Schena *et al.*, 2005). On the x-ray detector side, a similar situation is realized, particularly for the case of a thin scintillator screen lens-coupled to a digital (CCD) detector configuration (Koch *et al.*, 1998), as employed in the μXCT system used in the current study (Mertens *et al.*, 2014c, Mertens *et al.*, 2014a). Simply put, thicker scintillator screens have higher absorption efficiency and thus give a higher ultimate detected signal. However, the increased thickness also decreases the detector's spatial resolution.

Previous researchers have shown the utility of custom built detectors as well as complete lab-scale CT instruments and have provided insight to many modeling approaches in the design process (Schena *et al.*, 2005, Koch *et al.*, 1998, Mertens *et al.*, 2014c, Mertens *et al.*, 2014a, Uhlmann *et al.*, 2008, Uesugi *et al.*, 2011, Dierick *et al.*, 2008). A fully

customized lab-scale x-ray computed micro-tomography (μXCT) instrument implementing a commercially available microfocus x-ray source and a lens-coupled CCD-to-scintillator x-ray detector for performing micrometer-scale imaging of material systems was recently constructed (Mertens *et al.*, 2014a, Mertens *et al.*, 2014b). A compromise is needed between the detected signal rate and the spatial resolution from control over both the x-ray generation mechanisms (accelerating voltage and target current/power) and the x-ray detection mechanisms (scintillator composition and thickness). Here a new approach is provided for modeling the energy-sensitive detector's interaction with the polychromatic x-ray source. The modeling methods are detailed and the modeling predictions are compared with measured values for a specific system. The characterization of the imaging parameters' effect on spatial resolution is beyond the scope of the present work, although it is required for a full understanding of the competition between spatial resolution and x-ray yield. This study aims to elucidate and quantify the imaging system's detection yield as a function of various controllable parameters for the x-ray computed tomography system with the understanding that the spatial resolution is typically inversely affected.

4.2. X-RAY DETECTOR DESIGN AND MODELING OF DETECTION YIELD IN A LENS-COUPLED SCINTILLATOR-CCD-CAMERA TANDEM

The imaging system in this design is that of lens-coupled configuration, providing what was determined to be the highest resolution, light transfer efficiency, and versatility. Specific to the decision of a fiber optic versus lens coupled sensor/phosphor design, three factors were most influential: The ease with which the scintillating medium can be

interchanged in the lens-coupled design, the ability to construct the lens-coupling in-house, and the added magnification variability of the lens-coupled configuration. Another function of the sensor-phosphor coupling is the capability to remove the light sensor out of the x-ray path, which can give rise 'zingers' in x-ray images caused by non-signal x-ray interaction with the sensor itself (Hardy *et al.*, 1999). With fiber coupled configurations, the fiber-bundle length should allow for camera removal from the beam path. In the case of lens-coupled configuration, the use of mirrors has been used for optical signal diversion from the x-ray path to the sensor. At least two solutions exist in placing a right-angle mirror in front of the camera lens (Stampanoni *et al.*, 2002) or behind the camera lens (Uesugi *et al.*, 2011), where the prior has the added advantage of also removing the lens from the beam path potentially preventing burnishing (a darkening or browning of the optical glass (Koch *et al.*, 1998) which leads to a loss in optical transmission). For the first solution, a longer working distance lens is required, and for the second a longer optical path behind the lens is required. The longer optical path behind the lens, although easily accomplished with infinity corrected objective lens, may affect the range of magnification possible with finite-focus lens.

Factors influencing detection efficiency of the x-ray detector were investigated with modeling methods. The x-ray detector used in the system was a modular scintillator-lens-mirror-CCD-camera tandem. The CCD incorporated in the detector was the e2v CCD230-42 (in the Apogee Imaging Alta U230). The mid-band (visible sensitive) CCD chip produces digital counts in response to light in the optical range. The efficiency of the CCD sensor varies depending on the wavelength. The number of photons of a particular

wavelength that are detected out of the total number of photons is a metric of detector efficiency. The detector's design had three critical components which controlled detection efficiency: The scintillator, the optical system, and the CCD. The optical system and the CCD had efficiency functions which depended on the wavelength of light being transferred or detected. The overall efficiency of the transfer of scintillated light to digital counts as a function of wavelength, $\eta_{optical}(\lambda)$, was modeled as

$$\eta_{optical}(\lambda) = \eta_{CCD}(\lambda) \cdot \eta_{window}(\lambda) \cdot \eta_{mirror}(\lambda) \cdot \eta_{lens}(\lambda)\ , \qquad (20)$$

where $\eta_{lens}(\lambda)$ is the transfer efficiency of the lens, $\eta_{mirror}(\lambda)$ is the transfer efficiency of optical light of the right-angle mirror, and $\eta_{window}(\lambda)$ is the efficiency of the MgF_2 CCD window, and $\eta_{CCD}(\lambda)$ is the CCD's quantum efficiency, all as a function of wavelength. The calculated resulting effective efficiency for the optical/CCD detector as a function of wavelength, from *Equation 19*, are plotted as the solid blue line in *Figure 6* using manufacturer data for the components used in this system's optical detector. The overall shape of the curve was a result of $\eta_{CCD}(\lambda)$, as the other loss functions were relatively negligible. The sharp edges in the curve were a result of efficiency data of limited wavelength range for the other optical components; between the sharp edges, the reduction was a result of optical losses considered for the mirror, lens and CCD window.

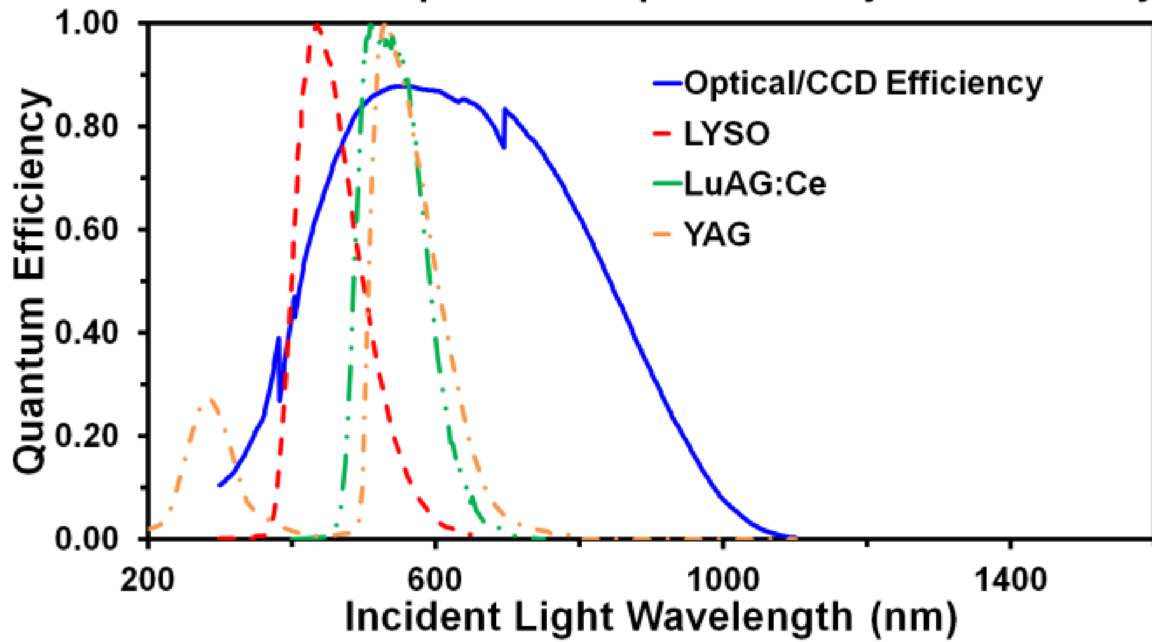

Figure 6. The Relative Emission Spectra of Three Scintillation Materials (y-axis not shown) of Relatively Good Fit with the Detector's Efficiency for the CCD/Optical System at Various Light Wavelengths

The effective scintillated–light-to-digital-counts conversion efficiency, $\eta_{\lambda/e}$, for three candidate scintillators as calculated in conjunction with the detailed optical light detector (*Figure 6*) are summarized in *Table 4*. The scintillated-light-to-digital-counts conversion efficiency was approximated with a single value based on the optical transfer efficiency spectrum of the detector at the wavelength of maximum scintillation intensity, using *Equation 21*:

$$\eta_{\lambda/e} \approx \eta_{optical}(\lambda(I_{scint}{}^{max})) \quad . \tag{21}$$

While *Table 4* provides a good understanding of the relative emission spectra, the absolute emission of each scintillator was also considered in order to get an absolute comparison of the detectors efficiency when coupled. This was computed by considering the light yield for each scintillator material. Also, the absorption efficiency of the scintillator must be considered (Koch *et al.*, 1998). Further, the light collection efficiency of the lens as a result of the numeric aperture must be considered (Koch *et al.*, 1998). Following A. Koch *et al.* (Koch *et al.*, 1998), these factors were modeled with *Equation 19*. The light to electron conversion efficiency is the solid blue line in *Figure 6* which is based on all losses in the conversion of optical light to electronic signal, but not considering the amount of light entering the system as a function of numeric aperture or light source. The collection efficiency is expressed as a function of the numeric aperture, *NA*, and the index of refraction of the scintillator, *n* (Koch *et al.*, 1998):

$$\eta_{coll} = (NA/n)^2/4 \, . \tag{22}$$

Table 4

The Effective X-Ray to Optical Light Conversion Efficiency, $\eta_{\lambda/e}$, Calculated for Various Scintillator Materials

Scintillator	Calculated $\eta_{\lambda/e}$ for Optical/CCD System at Scintillator Peak Emission
LuAG:Ce	0.8546
YAG	0.8723
LYSO	0.6278

The index of refraction for select scintillators is provided in *Table 5*. A high numeric aperture produces high light collection efficiency. The amount of light collected by the lens is also dependent on the x-ray absorption efficiency of the scintillator (Koch *et al.*, 1998). It can be seen in *Equation 19* that high absorption efficiency is desired. This is a function of thickness. As seen in *Equation 23*, the absorption efficiency, η_{abs}, is also a function of x-ray energy, because it is a function of the photoelectric absorption coefficient, $-\mu_{photo}(E^x)/\rho$. The absorption efficiency, $\eta_{abs}(E^x)$, is written as:

$$\eta_{abs}(E^x) = 1 - I/I_0 = 1 - e^{\left(-\mu_{photo}/\rho \cdot \rho \cdot t\right)}, \tag{23}$$

where I_0 is the initial x-ray intensity, I is the transmitted intensity as a function of x-ray energy, ρ is the density of the scintillator, and t is the thickness of the scintillator. The photoelectric absorption coefficients of the scintillators were calculated using the NIST X-COM calculator (NIST, 2014), and the total absorption was calculated for a scintillator compositions and thicknesses over the energy range of interest. The densities of select scintillators are provided in *Table 5*.

By assuming that the energy of light emitted by the scintillator is equal to the energy of the maximum output intensity, the light yield of the scintillator material, *LY*, in units of photons/energy of incident x-ray was taken as (Packham, 2010):

$$LY = \frac{\eta_{x/\lambda}}{E^{\lambda}} \ . \tag{24}$$

Table 5

Physical Properties for Various Scintillator Materials (Packham, 2010, Martin and Koch, 2006, Graafsma and Martin, 2008)

	LYSO	*LuAG:Ce*	*YAG*	*CsI:Tl*
Index of Refraction, n	1.81	1.85	1.82	1.80
Light Yield, LY (photons / keV x-ray)	32	20	40	65
Peak Wavelength (nm)	420	535	550	540
Density, ρ (g/cm^3)	7.1	6.73	4.57	4.52

The light yield for each material is provided in *Table 5* along with other various physical properties which were useful for the analysis of the scintillator detectors. *Equation 19* was evaluated in a more expanded form, using *Equation 23* and *Equation 24*, and using the reported light yield (*Table 5*) for the materials:

$$DQE = \left(1 - e^{-\mu_{photo}/\rho * \rho * t}\right) \cdot \left(1 + \frac{1 + 1/\eta_{\lambda/e}}{((NA/n)^2/4) \cdot E^x \cdot LY}\right)^{-1} . \tag{25}$$

In this representation, the term in the first set of parentheses is also a function of E^x. Thus, the x-ray detector efficiency was approximated as a function of x-ray energy. The results of these approximations are provided in *Figure 7* for three scintillator materials, modeled with a thickness of both 50µm and 250µm. *Figure 7* represents the efficiency of the detector in conjunction with a lens aperture at f/#2.8, the CCD efficiency, and the light transfer efficiency already detailed (see *Figure 6*).

Before consideration of the absorption efficiency, the YAG scintillator appeared the most efficient. By considering the whole range of x-ray energies (*Figure 7*), the LYSO crystal was calculated to be the most efficient combination with the optics and electronics of the detector. The anticipated performance of LuAG:Ce and LYSO were both improved due to their high density relative to that of YAG.

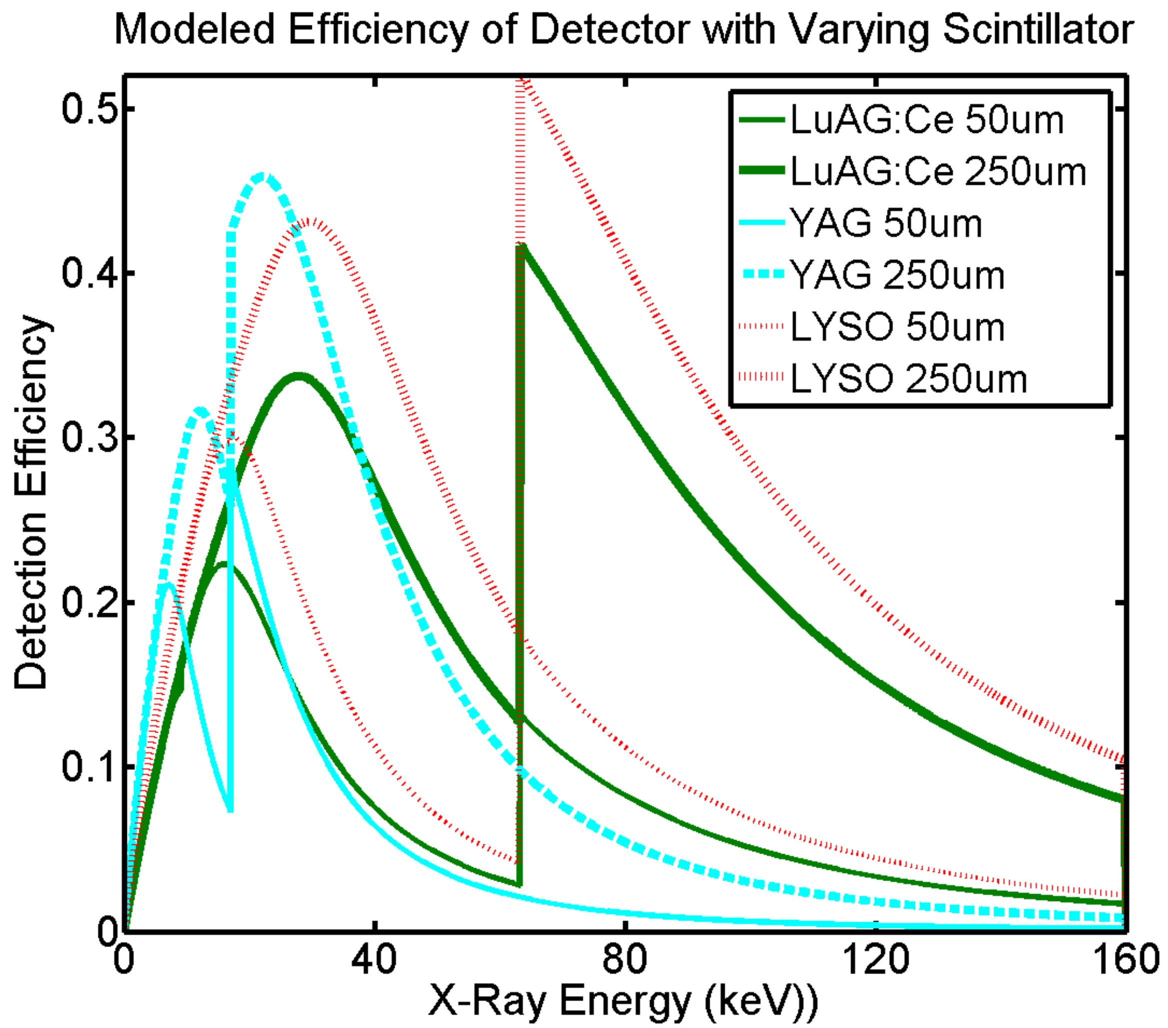

Figure 7. The Results of the *DQE* Model for the X-Ray Detector as a Function of X-Ray Energy using *Equation 25* Assuming Scintillator Emission Solely at the Wavelength of Maximum Intensity

4.3 MODELING A POLYCHROMATIC X-RAY OUTPUT USING A BREMSSTRAHLUNG APPROXIMATION

In practice, an energy sensitive detector is used to measure the signal from a polychromatic x-ray beam. The approach for modeling the x-ray detector used in this system has been discussed in the previous section. Several studies have looked at modeling the energy spectrum produced by vacuum-tube x-ray sources (de Paiva *et al.*, 1998, Krimmel *et al.*, 2005, Meng *et al.*, 2009, Imura *et al.*, 2012, Herman, 1979), primarily for alleviating beam hardening artifacts through deconvolution of x-ray attenuation values from a polychromatic x-ray beam, sometimes referred to as monotonization. A simple model was used for this study following the approach of S. Krimmel *et al.* (Krimmel *et al.*, 2005) in modeling the x-ray spectrum as a filtered linear function. The approach in this work to predict the absolute count rate as a function of energy was to model the number of x-rays being produced under varying accelerating voltage and target current, assume spherical emission, and use the solid angle of the detector and its detection efficiency as a function of x-ray energy. Although it is known that x-ray emission from the target is anisotropic, isotropic spherical emission was assumed for simplicity.

Only a small part of the energy being imparted to the target produces x-rays, much is converted to heat and other losses (Sprawls, 2014). The x-ray source being modeled is a solid tungsten target with atomic number Z=74. The number of x-rays produced depends on the efficiency of electron to x-ray conversion. The efficiency, $\eta_{e/x}$, of the process is approximately (Sprawls, 2014):

$$\eta_{e/x} = VZ \cdot 10^{-6} \, . \tag{26}$$

The total number of x-rays per second, N_x^T, was then calculated based on the target current, I_{target}, and the charge of the incident electrons, e:

$$N_x^T \approx \frac{I_{target}\, \eta_{e/x}}{e} \approx \frac{I_{target}\, VZ \cdot 10^{-6}}{e} \quad . \tag{27}$$

The total number of x-rays produced at a target current and voltage is approximated N_x^T, but an approximation of the energy spectrum was sought, that is, $N_x(E^x)$. In this work, a simple Bremsstrahlung model was used without characteristic x-ray spikes, even though it has been suggested that at high accelerating voltages, characteristic radiation can contribute up to 25% of the total radiation (Sprawls, 2014). At a given combination of I_{target} and V, the maximum x-ray energy expected is equal to the accelerating voltage in units of electrovolts (de Paiva *et al.*, 1998, Krimmel *et al.*, 2005, Meng *et al.*, 2009, Imura *et al.*, 2012). This process is very unlikely and many more x-rays are generated at low energy (de Paiva *et al.*, 1998, Krimmel *et al.*, 2005, Meng *et al.*, 2009, Imura *et al.*, 2012). The modeled number of x-rays as a function of accelerating voltage was set equal to zero at the maximum x-ray energy, as is shown in *Figure 8*. The area under the curve was taken as the total number of x-rays.

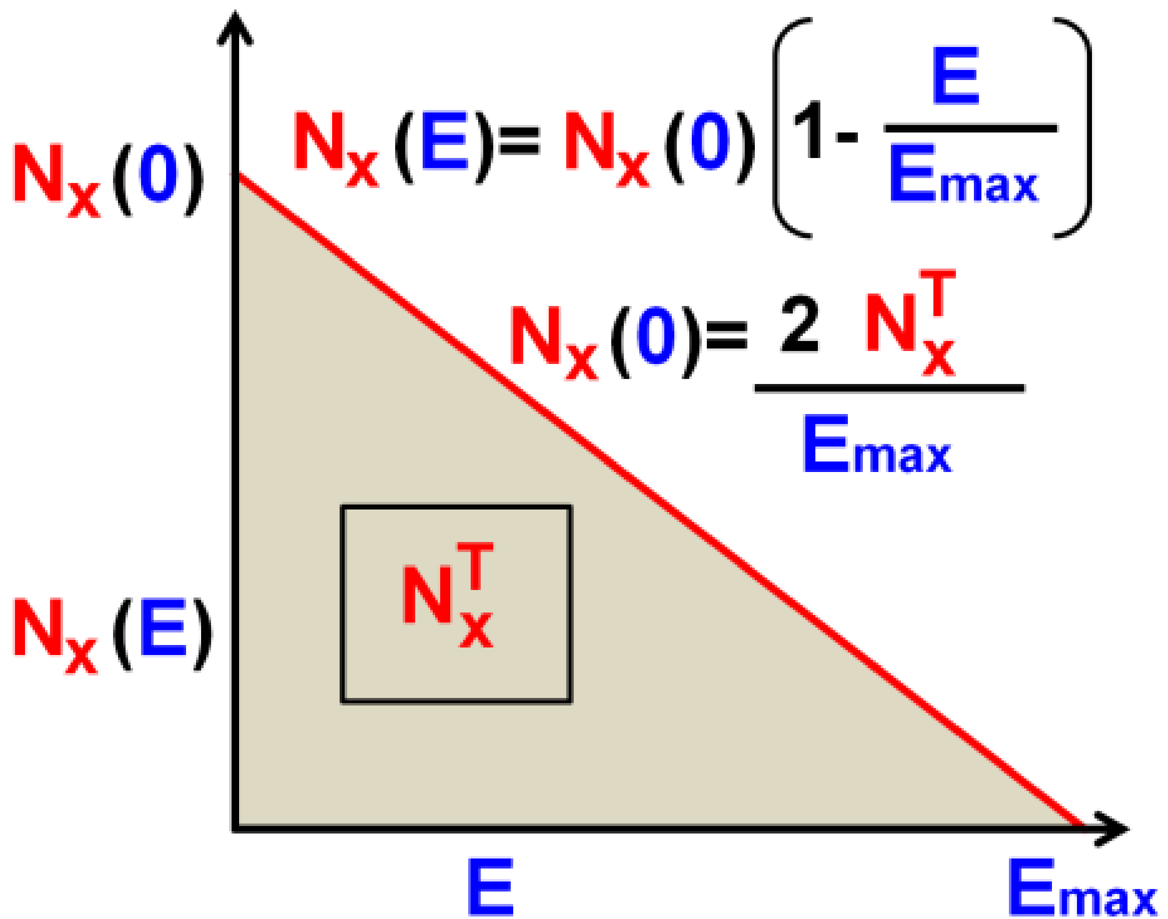

Figure 8. Diagram of the Model Used to Portray X-Ray Number-Energy Dependence on Accelerating Voltage and Target Power

The intercept of the y-axis in *Figure 8*, $N_x(E^x)$, was calculated using the slope of the line and the area under the curve (the total number of x-rays per second). The area under the curve, equal to N_x^T, was taken as:

$$N_x^T = \frac{1}{2} \cdot (N_x(0) \cdot E^x{}_{max}). \tag{28}$$

Rewriting *Equation 28*:

$$N_x(0) = \frac{2N_x^T}{E^x{}_{max}}. \tag{29}$$

Using *Equation 29* and the equation for the slope of a line, the slope was then written in terms of the total number of x-rays per second per maximum energy as:

$$slope = \frac{-N_x(0)}{E^x{}_{max}} = \frac{-2N_x^T}{(E^x{}_{max})^2}. \tag{30}$$

The intercept of the line was then expressed in terms of the total number of x-rays per second using *Equation 29*:

$$y\text{-}intercept = N_x(0) = \frac{2N_x^T}{E^x{}_{max}} \quad . \tag{31}$$

Thus, the model for the $N_x(E^x)$ line was taken as:

$$N_x(E^x) = \frac{2N_x^T}{E^x_{max}} - \frac{2N_x^T}{(E^x_{max})^2} E^x = \frac{2N_x^T}{E^x_{max}}\left(1 - \frac{E^x}{E^x_{max}}\right) = \frac{2\, I_{target}\, VZ\ 10^{-6}}{e\, E^x_{max}}\left(1 - \frac{E^x}{E^x_{max}}\right). \quad (32)$$

The line in *Equation 32* is shown qualitatively in *Figure 8*. The maximum energy was taken as the energy of the electron beam. The results of applying the model to various accelerating voltages at 150µA are shown in *Figure 9*, considering all emitted x-rays regardless of direction, and assuming filtering through 870µm of beryllium (the window of the x-ray source being modeled) and filtering through 380µm of iron (the thickness of the steel filter used for experimental measurement) by using small, discrete 1eV bins over the range of interest. This model is independent of the x-ray geometry and detector, and considers only x-rays being emitted by the target as a function of energy. That is, the x-ray-source-to-detector/scintillator-distance (*SDD*) was set to the theoretical zero. The accelerating voltage cancels out of the intercept value, leading to a common x-ray production rate near E^x=0 between all accelerating voltages (not obvious after filtering, as portrayed in *Figure 9*).

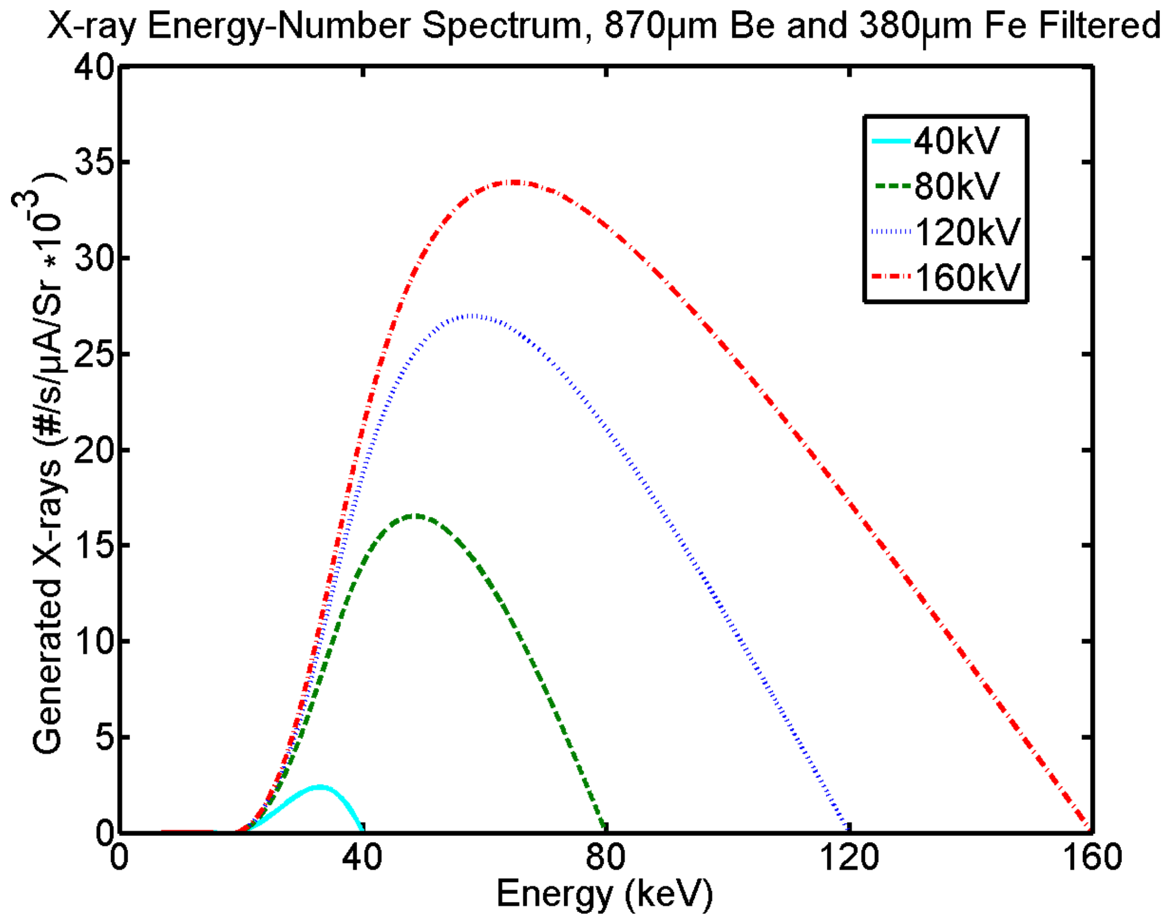

Figure 9. Modeled X-Ray Beam Spectra Transmitted Through the X-Ray Window and a Steel Filter as a Function of X-Ray Energy Using *Equation 32*

The adopted model for both x-ray production and x-ray detection as a function of energy were then combined. The number of theoretically detectable x-rays per second as a function of x-ray energy was calculated with the product of the spectrum of interest (*Figure 9*) with the *DQE* of the detector combination of interest (*Figure 7*). This is written as:

$$D^*(E^x) = N_x(E^x) \cdot DQE(E^x), \tag{33}$$

where $D^*(E^x)$ is the absolute detection count rate as a function of x-ray energy assuming all produced x-ray arrive at the detector. The result for the 50μm LuAG:Ce scintillator with the lens aperture at f/#2.8 is provided in *Figure 10* and is normalized to detector geometry and x-ray tube target current. The geometry of the x-ray detector will later be considered to calculate the total number of counts per pixel per second for the entire range of x-ray energy in the beam.

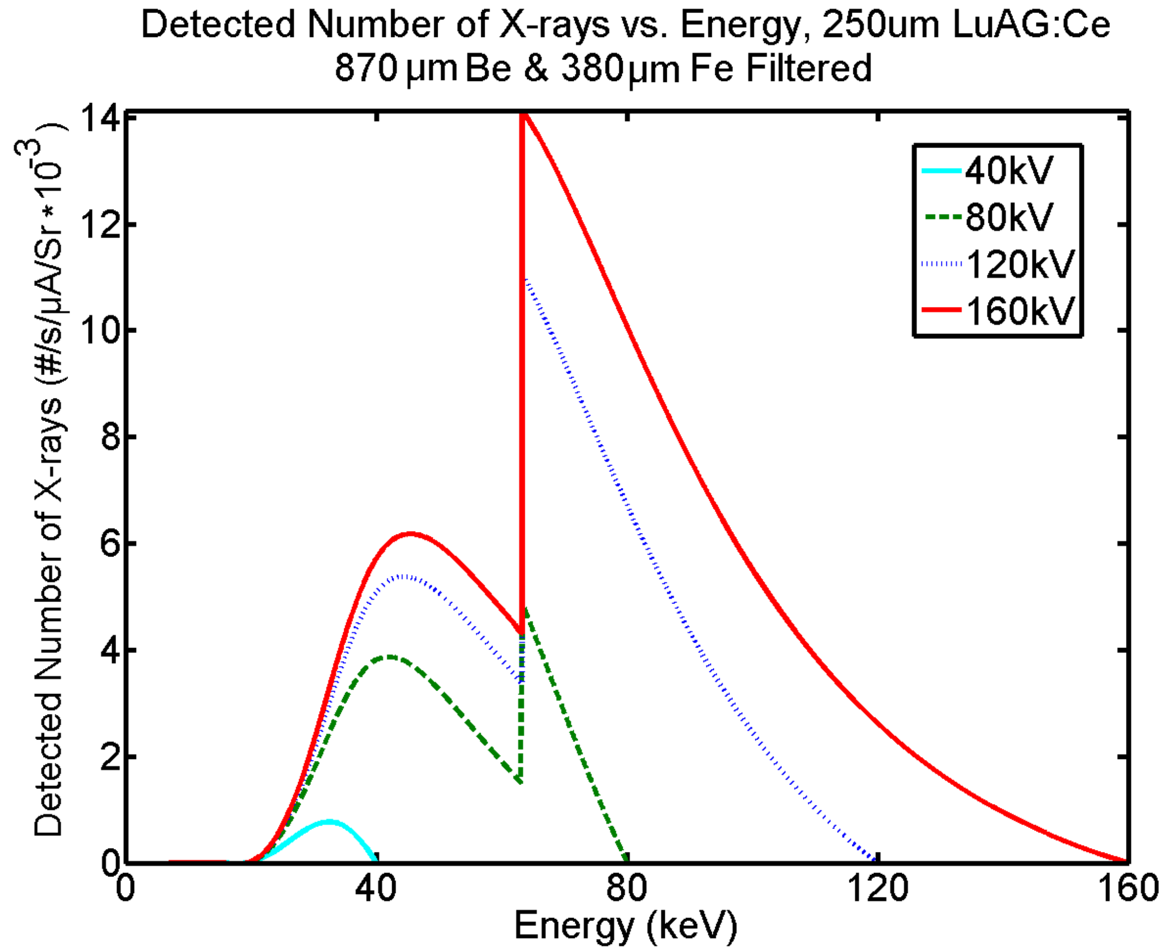

Figure 10. The Modeled Detected Signal Rate with a 250μm Thick LuAG:Ce Scintillator with 380μm Steel X-Ray Beam Filtering Based on *Equation 25* and *Equation 32*

Based on the modeled detectable x-ray spectra, several trends were observed. The number of x-rays at a particular energy increased with accelerating voltage. Low energy x-rays dominated the spectra with small amounts of filtering. The maximum x-ray energy in a spectrum was dependent on the accelerating voltage. To calculate the total number of x-rays detected per pixel per second, knowledge of the detection system was needed. Due to the divergent cone-beam, not all produced x-rays arrive at the detector. The solid angle, *SA*, of the detector element with the x-ray source was used to approximate the number of x-rays which arrived at each detector element per second. Essentially, the values of $D^*(E^x)$ were scaled down with the solid angle, to provide the absolute detection rate at the scintillator element. The absolute detection rate per scintillator element, $D\ (E^x)$ was modeled as

$$D\ (E^x, SDD, p) = SA(SDD, p) * D^*(E^x) = \frac{p^2}{4\pi SDD^2}\ N_x\ (E^x) \cdot DQE\ (E^x). \tag{34}$$

A pixel of size $p = (15\mu\text{m}/4\text{x})^2$ at the scintillator was modeled at an x-ray detector distance of 29.8mm to coincide with experimental conditions. The factor of four is due to the optical magnification of the scintillator onto the CCD elements. The total count rate, *C*, at the detector element was then approximated by integrating *Equation 34* over energy, taking:

$$C = \int_0^{E_{max}} D\ (E^x)\ \mathrm{d}E^x. \tag{35}$$

The model was applied to a small range of materials and thicknesses covering all of those which were available for experimental measurements. The model was applied to YAG, LuAG:Ce, and LYSO for thickness of 50μm and 250μm, although not all were available for experimental performance characterization. The results of the modeling predictions for the crystals are provided in *Figure 11*. Contrary to the measured performance, the model predicts a LYSO crystal to be slightly more efficient than a LuAG:Ce crystal of a given thickness when implemented in the detector. The measured yield with the LuAG:Ce scintillator were roughly twice that of LYSO.

4.4 MEASURED PERFORMANCE FOR MODEL ANALYSIS

The modeling predictions from **Section 4.3** were compared with measured values of absolute signal to evaluate the accuracy of the model. The x-ray source used in for this study was a microfocus 160XWT-SE from X-RAY WorX GmbH (Germany). The detector used in this study, and the complete imaging system, has been described in detail previously (Mertens *et al.*, 2014c, Mertens *et al.*, 2014a). Most notably, the detector consists of a CCD coupled to an interchangeable scintillator screen using a lens of adjustable magnification.

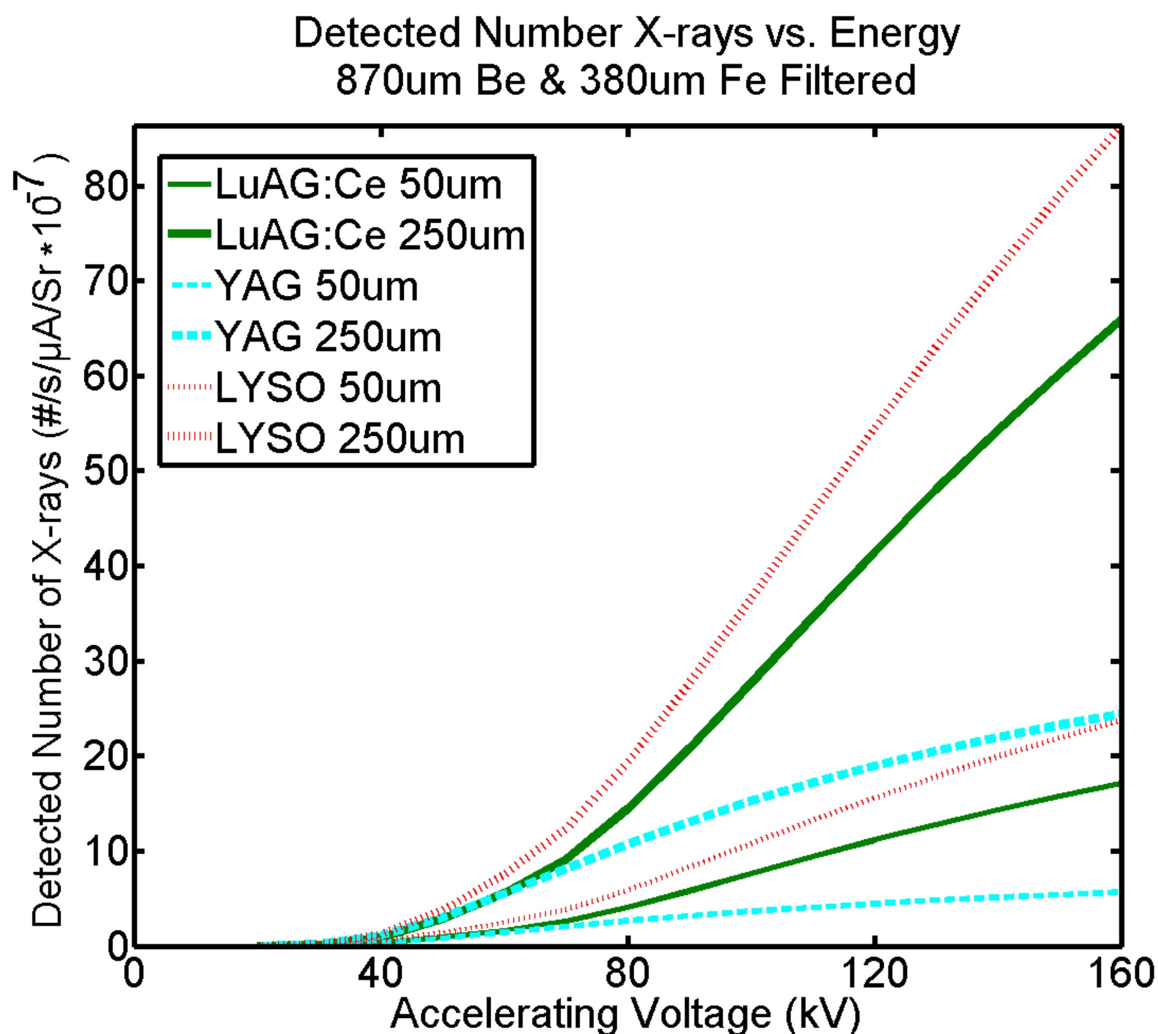

Figure 11. Modeled X-Ray System Count Rate Dependency on Scintillator Composition and Thickness as a Function of Accelerating Voltage Using *Equation 35* for 870μm Beryllium Window Filtering and 380μm Steel Filtering

X-ray images were acquired with no sample in place. The x-ray tube accelerating voltage was varied, but the beam current on the tungsten target was maintained at 150µA. The x-ray beam filtering was varied in the experiment between the intrinsic beryllium window of the x-ray tube and two thicknesses of steel filter. The magnification factor used in light transfer from the scintillator to the 15µm-pixel CCD was 4x, resulting in a detector element size of $(3.75\mu m)^2$ at the scintillators. The numeric aperture of the lens coupling the CCD-scintillator was maintained at f/#2.8. The scintillator composition and thickness used for the measurements was varied. An x-ray-target-to-scintillator distance of 28.9mm was used. The scintillators were centered and maintained perpendicular to the central axis of x-ray emission. Images of five second exposures were acquired under each studied condition for signal analysis. The CCD was cooled to -30.0°C, and a master dark frame was calculated using 10 dark frame exposures for CCD dark signal correction. The signal was analyzed using the mean value for the central 512 x 512 pixels of the 2048 x 2048 element detector under every condition to minimize the effect of optical lens vignetting. The measured count values were normalized in terms of the target current, exposure time, and the solid angle of the central detector elements with the x-ray source's focal spot.

The effect of the scintillator used in the x-ray detector on count rate was measured as a function of composition, thickness, and vendor for a select set of crystals as seen in *Figure 12*. With the exception of the '250µm LYSO Epic' data, which was gathered on a scintillator obtained from Epic Crystals Co. LTD (China), all data was gathered on scintillators from Crytur spol.s r.o. (Czech Republic). The CRY019 is understood to be somewhat proprietary, however, is also understood, based on physical properties, to be

primarily LYSO based, in composition. The effect of exposure time, target current, and the solid angle of the detector have been normalized out of the reported data, rendering it directly comparable to measurements made with other data. It can be seen that the thickest LuAG:Ce crystal is the most efficient. The LuAG:Ce crystal of one-fifth of the LYSO crystal's thickness had roughly one-half of the efficiency. Between the two vendors for crystals which were similar to LYSO, very little difference in efficiency was observed. Contrary to the measured performance, the model predicted LYSO crystal to be slightly brighter than LuAG:Ce. The measured signal with the LuAG:Ce scintillator was roughly twice that of LYSO, as shown in *Figure 12*.

X-ray beam filtering is typically applied during x-ray imaging in order to filter out low-energy x-rays from the generated x-ray spectra. In the medical industry this is often called a half-value-layer, the thickness of which is determined based on the material of the filter chosen such that the detected count rate is half that of the unfiltered beam. By preferentially filtering low energy x-rays, the polychromatic nature of the x-ray beam is reduced and it is sometimes said that the 'quality' of the x-ray beam is improved. Typical materials used for the filter are aluminum, or copper. For this study, steel filters were used. The measured effect of steel filtering is shown in *Figure 13*.

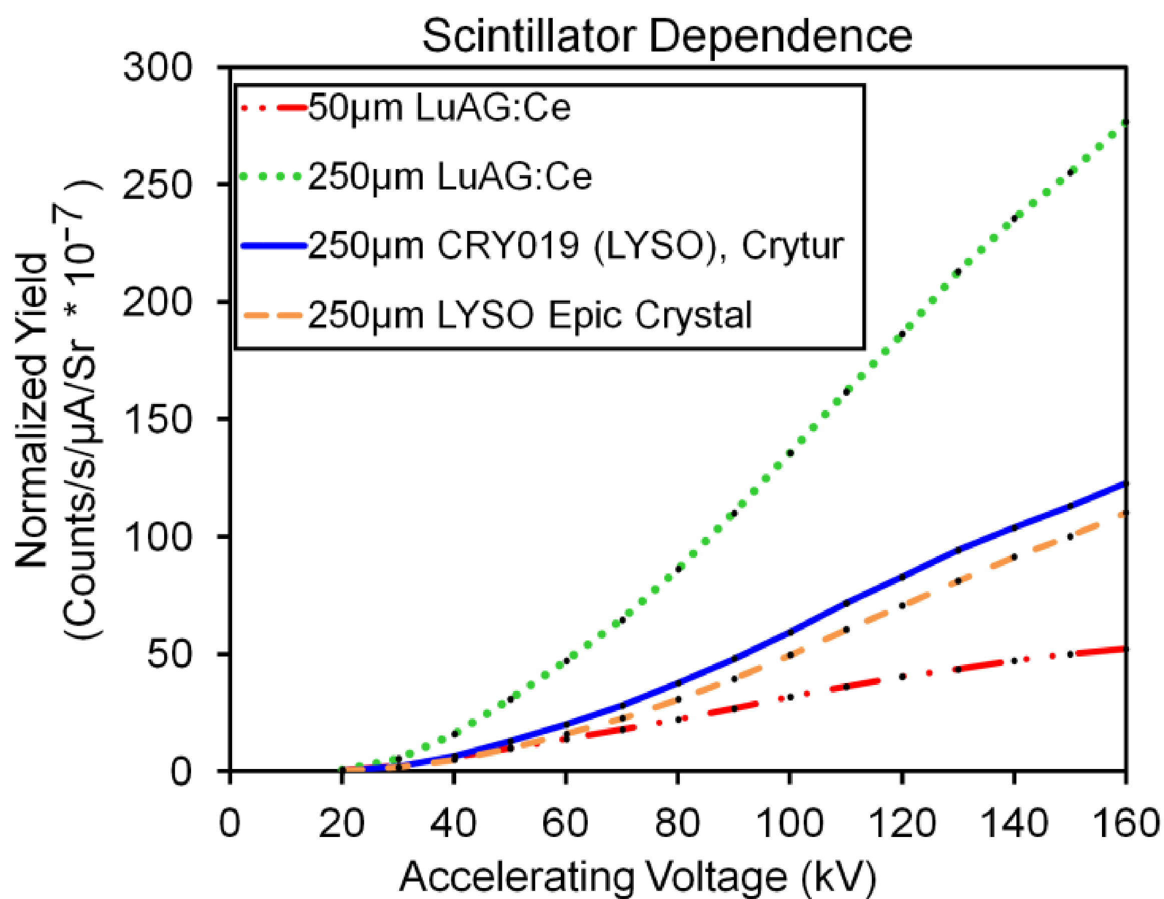

Figure 12. The Measured Effect of Accelerating Voltage and Scintillating Crystal Choice on the Normalized Signal Yield with No X-Ray Beam Filtering

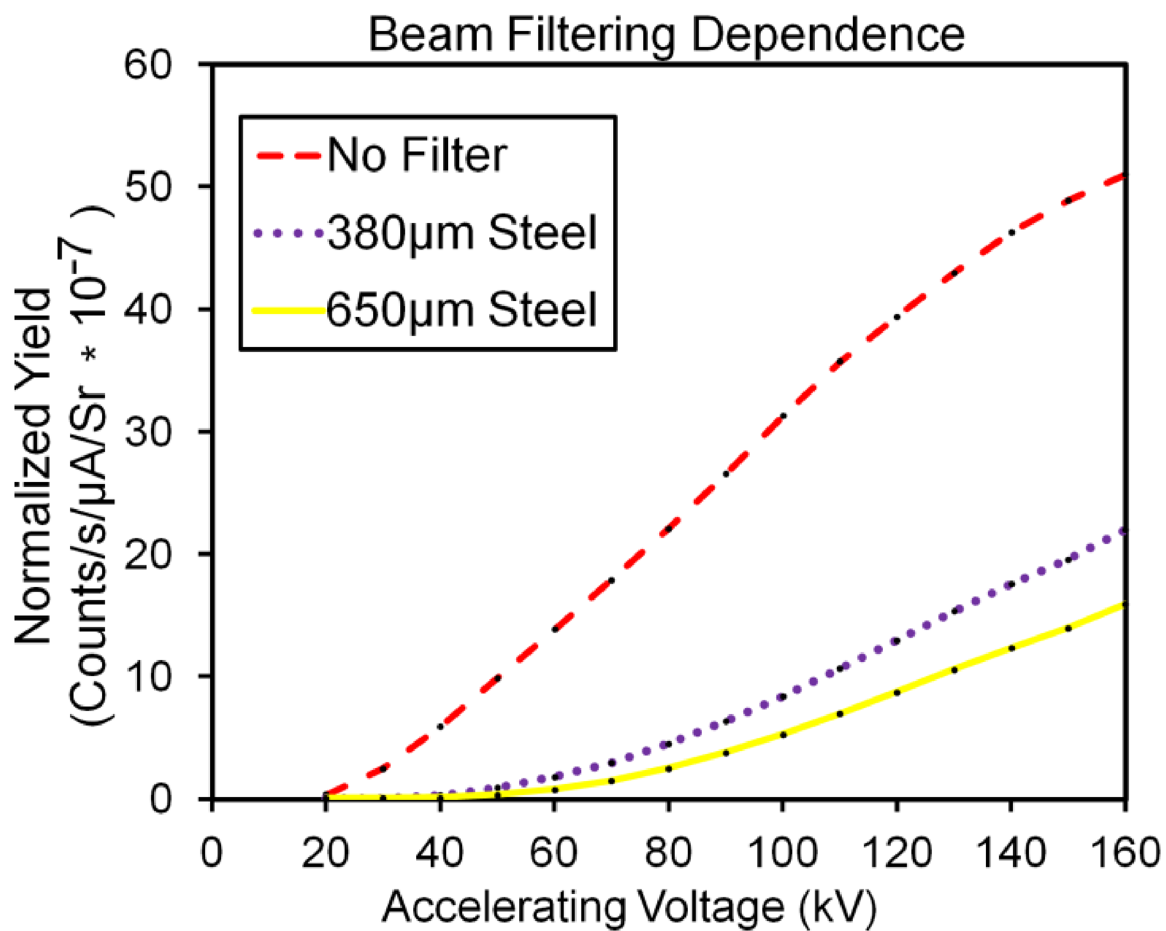

Figure 13. The Measured Effect of Steel Filtering on the Normalized Detection Count Rate for Varying Steel Filter Thickness and for Varying Accelerating Voltage as Measured with the 50µm LuAG:Ce Scintillator

The comparison of modeled versus measured values shown in *Figure 14* provides insight into the accuracy of the model in terms of accelerating voltage and x-ray beam filtering, using the 50µm LuAG:Ce f/#2.8 configuration. It can be seen that the model over predicts detection rates for the unfiltered (intrinsic Be filtering only) case, and underestimates the detection rate for most of the steel filtered case. One possible explanation is that the model does a better job predicting the absolute number of x-rays at high x-ray energy, and is probably over estimating the number of low energy x-rays. Nevertheless, the model reasonably predicts the absolute count rate of the x-ray system as a function of filtering, accelerating voltage, target power, and scintillator material. Three reasons this was unexpected was the lack of consideration of characteristic radiation, the accuracy of the efficiency coefficient used for calculating the total number of x-rays in *Equation 26*, and the assumption of spherical x-ray emission. The modeling efforts for predicting absolute count rates as a function of controllable x-ray source and detector characteristics were particularly accurate for the case of the 50µm LuAG:Ce crystal. A comparison between the measured and modeled detection signal rates as a function of accelerating voltage for the 50µm LuAG:Ce crystal is shown in *Figure 14* for two instances of x-ray beam filtering.

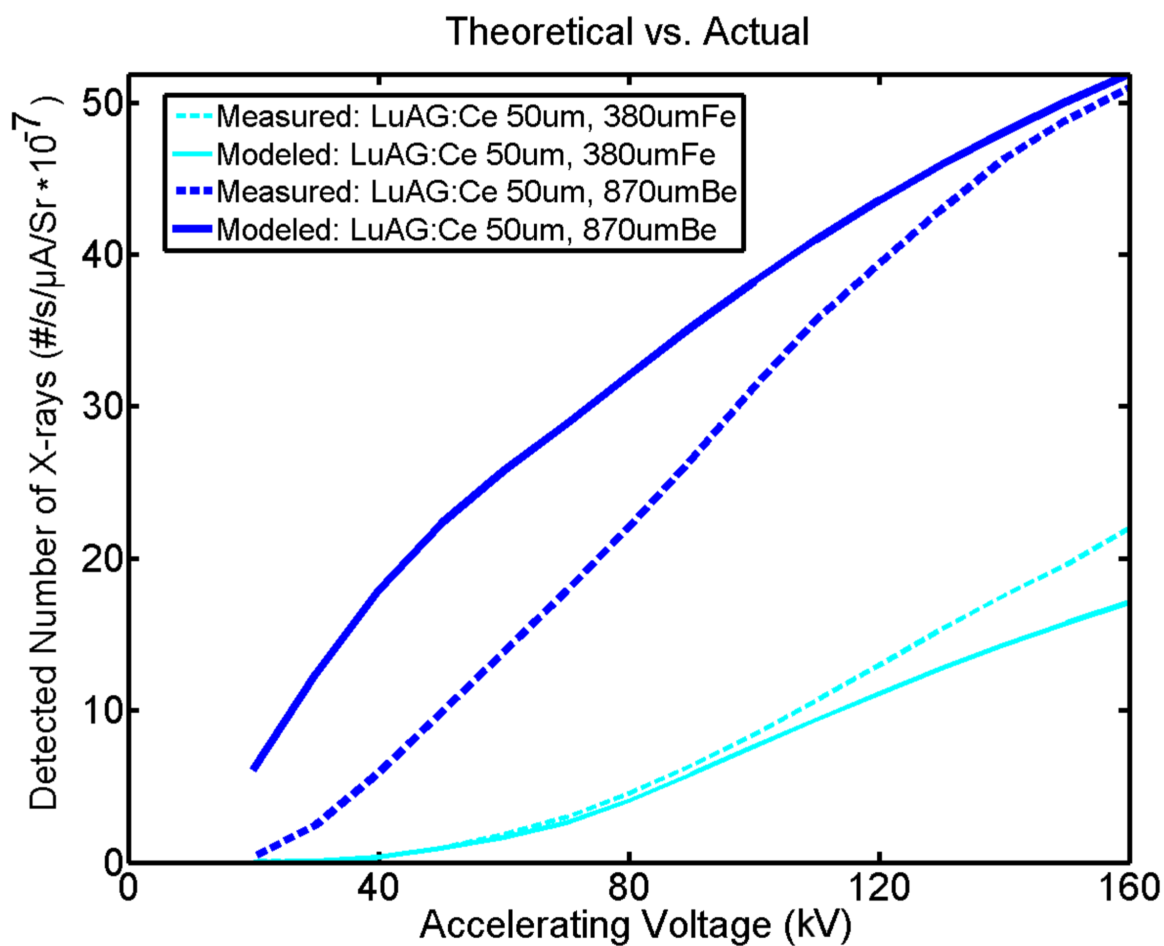

Figure 14. The Modeled and Measured Count Rates Independent of Target Current and Detector Geometry for the Steel Filtered and Unfiltered (Intrinsic Beryllium X-Ray Window Filtered) X-Ray Beam as a function of X-Ray Voltage

It might be that the exact thicknesses of the scintillators, which were unknown, were playing a role. The model appears to suffer from low energy overestimation. The lack of incorporating characteristic tungsten target x-ray radiation may be causing an underestimation at high accelerating voltages. The model has also made some simplifying assumptions along the way, including an isotropic x-ray emission and a linear x-ray number-energy generation without characteristics. The lack of incorporating characteristic tungsten target x-ray radiation may be causing an underestimation at high accelerating voltages. The filter absorption was modeled using pure elemental material without impurity. The experimental characterization might be used as a means to adjust the existing initial model for electron-to-x-ray efficiency, x-ray target directionality, accurate description of the low energy x-ray yield, and for characteristic x-ray influences. Nonetheless, the absolute signal at the CCD in practice was predicted reasonably well with the model.

4.5 SUMMARY

Modeling approaches have been demonstrated which predict the imaging count yield for varying x-ray generating conditions and x-ray detection configurations by modeling filtered polychromatic x-ray spectra interacting with an x-ray detector possessing energy-sensitive efficiency. Predictions have been compared with experimental measurements for several conditions of x-ray generation and detection which indicate reasonable accuracy. The models appear to suffer from overestimates of the number of low energy x-rays, suggested by better agreement with experimental data when filtering was applied and significant over estimates of count yield when it was not. Whereas the model has

predicted the LYSO crystal to be the most efficient, LuAG:Ce has provided higher count yield in practice (although exact crystal thicknesses were not taken into account). More accurate modeling of the x-ray source spectra may be possible by considering characteristic x-ray radiation. The importance of experimentally characterizing the physical scintillator performance is emphasized by the deviation of the LYSO materials performance from expectations for unknown reasons.

Coupled with models for x-ray source and detector resolution, the detection rate models and data will enable the optimization of x-ray efficiency with respect to a particular imaging resolution being targeted, by control over the scintillator composition and thickness, lens numeric aperture, and x-ray tube voltage, power, and filtering. The modular µXCT in this work has enabled full experimental control over these parameters. Quantitative descriptions of the system's resolution for varying detector parameters and x-ray generating conditions, and similarly the x-ray focal spot size at varying tube conditions, are still sought to directly compare the resolution/signal yield ratios at varying CT scan configurations.

The low flux resulting from x-ray tubes operating under high resolution conditions is an ongoing issue in lab-scale x-ray tomography. Improved detection efficiency is critical in the future of lab-scale x-ray microtomography, and the models given in this work will provide researchers performing broad-spectrum imaging a new tool predict the absolute detection count rate as dependent on scintillator composition, thickness, x-ray tube voltage, x-ray tube power, system geometry, the detector optics and the electronic sensor.

These models also provide good estimation of the relative x-ray number with x-ray energy, which is the most promising means of improving tomography reconstructions from polychromatic x-ray attenuation signals. Improved attenuation contrast in specific systems is also enabled through this contribution, as knowledge of the detected x-ray spectrum may be used to tailor imaging parameters to maximize detection over x-ray energy ranges of highest predicted feature-to-surrounding attenuation contrast.

CHAPTER 5

A METHOD FOR ZINGER ARTIFACT REDUCTION IN HIGH-ENERGY X-RAY COMPUTED TOMOGRAPHY

5.1 INTRODUCTION

In high energy x-ray computed tomography (XCT), the interaction of undesired stray x-rays with the imaging sensor causes a speckle type noise, or 'zingers', in the projection data. Untreated zingers in the projection data prior to volume reconstruction can yield dense, scratch-like features in the reconstruction planes. Presently, a reduction of these artifacts is achieved through detector design and the remaining zinger noise is treated with a new filtering algorithm. The prevalence of zinger noise is characterized under variations in the detector configuration, and for varying conditions of x-ray imaging. A standard method for zinger removal is known for filtering these artifacts but is shown to yield an alarming number of false positives and a large difference with the true signal over the entire image. A new approach was conceived which used a selective temporal frame averaging algorithm through which the random, speckle-like zinger noise is removed with a demonstrated drastic reduction in false positives. The accuracy of the temporal filtering approach is compared with a standard approach for zinger removal using simulated projections of the Shepp-Logan head phantom with a known artificial zinger density and location.

High energy x-ray computed tomography is an attractive technique for materials characterization, because of the ability to investigate the structure of dense or thick

samples in three dimensions (3D), at relatively high resolution (~1μm), and by non-destructive means (Stock, 2009). The process for obtaining 3D datasets is as follows. Several projection radiographs are acquired of the sample at unique angular positions throughout a full or half rotation. The sample's volume is then reconstructed in terms of the resolvable feature's average x-ray mass attenuation (across the cathode-tube derived x-ray energy-number spectrum) using any suitable reconstruction algorithm, such as algebraic reconstruction techniques (ART) (Mueller, 1998, Mueller *et al.*, 1999) or filtered back-projection (FBP) (Feldkamp *et al.*, 1984) techniques. The resulting reconstruction may contain any number of artifacts, depending on the x-ray source, x-ray detector, mechanical manipulation and sample characteristics (Bisogni *et al.*, 2007, Anas *et al.*, 2010, Anas *et al.*, 2011, Krumm *et al.*, 2008, Sasov *et al.*, 2008, Sasov *et al.*, 2010, Taylor and Lupton, 1986, De Man *et al.*, 1998, Hsieh, 1999, De Man *et al.*, 2000).

Erroneous signal from the direct interaction of incident or scattered x-rays with the CCD sensor elements can cause noise in the reconstruction (Rivers, 1998, Meng *et al.*, 2009). This effect has been studied and described for CCD sensors exposed to ionizing radiation in general, including cosmic rays and particles (Marshall and Marshall, 2003), gamma rays (Burke, 1986, Parish, 1990), and most relevant to this study, x-rays (Rivers, 1998, Meng *et al.*, 2006, Hopkinson, 1994). When a CCD element is exposed to ionizing radiation, electron-hole pairs can be generated which give rise to erroneously high signal, the magnitude of which can be related to the energy of the ionizing radiation and the electronic structure of the CCD element (Hopkinson, 1994). Pixels in the image array which exhibit the aforementioned erroneously high signal are sometimes called 'zingers'

(Rivers, 1998, Meng *et al.*, 2009). These zingers, when present in x-ray images, appear as straight, fine scratches in reconstructed images (Rivers, 1998). Thus, CCD sensors are sought which possess a high radiation hardness (Bosiers *et al.*, 2006), and approaches are needed for the omission of zingers to make use of the full data acquired (Marshall and Marshall, 2003).

In the application of cone-beam XCT for industrial research, higher x-ray energies and radiation doses are encountered (Mertens *et al.*, 2014b). Specific to high energy XCT, zinger prevalence needs be characterized with respect to operational parameters, including the nature of the x-ray beam and the design of the x-ray detector. In the current study, zingers are characterized with respect to XCT scanning conditions.

The methods currently suggested for the reduction or elimination of zinger artifacts were developed for a custom-built, lab-scale XCT system which uses a microfocus x-ray source and lens-coupled CCD-single-crystal-scintillator detector (Mertens *et al.*, 2014c, Mertens *et al.*, 2014a). Techniques and algorithms were developed for the removal of zinger artifacts in the projection stage of the XCT data processing. Although the data of interest is within the reconstruction volume, reconstruction artifacts can be treated prior to reconstruction in the projection stack, that is, the series of radiographic images acquired at fine rotational increment over some range.

It has been suggested that zingers are best removed by application of a temporal filter (Marshall and Marshall, 2003). Several solutions to zinger type noise were offered early

on (Parish, 1990) by using 'nominally matched signals from position correlated values' to perform what is described as 'gamma circumvention.' An optimal approach is identified which uses ten signals to perform intelligent averaging after throwing out any outliers, which the author describes as spike adaptive time delay integration (SATDI) (Parish, 1990): This is a form of a temporal filter which relies on 'identical' but unique samples. It has been suggested that unique but non-identical frames can also be used to perform temporal filtering for zinger removal, but may lead to blurring effects (Meng *et al.*, 2006). Rather than perform many identical and unique frame acquisitions (Parish, 1990), it has also been suggested that consecutive, unique frames may be used for zinger detection (Meng *et al.*, 2006). Another approach has been identified for zinger removal which does not rely on temporal filtering, but rather uses pixel statistics within a single frame to identify and treat zingers (Rivers, 1998, APS, 2015), though it has been suggested that by identifying zingers based on single-frame signal fluctuations may lead to many instances of faulty detection (Meng *et al.*, 2006).

In the newly put forth method for zinger removal, temporal filtering using as few as two 'identical' samples is shown to be more accurate than standard methods, particularly at low zinger density. The approach differs from previous temporal filtering approaches in that (at least) two samples are acquired under identical conditions. These can be used to efficiently detect zinger noise because the algorithm does not rely on in-frame statistics, yet do not lead to blurring when applied to static objects because nearly identical signal acquisition is practical for filtering and the zinger noise is random.

5.2 REDUCTION OF ZINGER NOISE

5.2.1 Zinger reduction through physical detector design.

It was noted in a custom XCT scanner that at high accelerating voltages of the x-ray source, a random 'speckle' noise of only bright pixels was present in the projections, where the number of pixels affected increased with accelerating voltage. The effect was attributed to the interaction of high energy x-rays with the imaging sensor (Rivers, 1998, Meng *et al.*, 2006, Burke, 1986, Parish, 1990, Hopkinson, 1994).

Three physical precautions have been made to minimize the extent of this noise, prior to employing image processing methods: 1) The camera lens incorporates a right-angle mirror to divert scintillated optical signal from the un-attenuated x-ray beam, 2) The camera lens tubing has x-ray attenuating, optically-transparent, leaded glass windows inserted both anterior and posterior to the right-angle mirror and 3) Pb-shielding is liberally applied wherever possible between the x-ray source and x-ray detector. After taking the previously mentioned physical precautions to the detection system, a great reduction in this effect was realized. Details on the detector design can be found elsewhere (Mertens *et al.*, 2014c, Mertens *et al.*, 2014a).The effects of the physical precautions taken are shown in *Figure 15*. Only ¼ of the image is shown for pixel clarity. *Figure 15.b* was acquired before the design detailed previously (Mertens *et al.*, 2014c, Mertens *et al.*, 2014a) was adopted, and noise of this type motivated the physical precautions taken, the effect of which is shown in *Figure 15.c-23.e*. *Figure 15.d-23.e* were taken with a slab of ¼" Pb draped over the x-ray source, with an aperture in the slab placed directly at the x-ray source, such that the x-ray beam emission angle is limited to

the detection medium, and were taken with no sample in the beam path as would be performed for a calibration or reference image. For *Figure 15.d*, the angle contains the entire scintillator crystal, whereas in *Figure 15.e*, the smaller aperture limits the angle to approximate ½ of the CCD's field of view at the scintillator crystal. *Figure 15.d* represents what is practically achievable in a typical XCT scan, using the detector configuration described previously (Mertens *et al.*, 2014c, Mertens *et al.*, 2014a).

The CCD used for all images and data in this study was a back illuminated e2v 230 with 2048x2048 pixel format cooled to -30.0°C. The x-ray source used was an X-RAY WorX XWT160SE tube with a reflection-style tungsten target capable of up to 160kV accelerating voltage and 280W target power. The scintillator used is a Crytur LuAG:Ce single crystal 50μm in thickness, coupled to the CCD with a 4x optical lens. The pixel size in the image plane was 3.75μm, and the x-ray target to scintillator distance was preserved at 58mm. For all data in **Section 5.2**, the x-ray beam was unfiltered, save intrinsically by the beryllium x-ray window and the target itself.

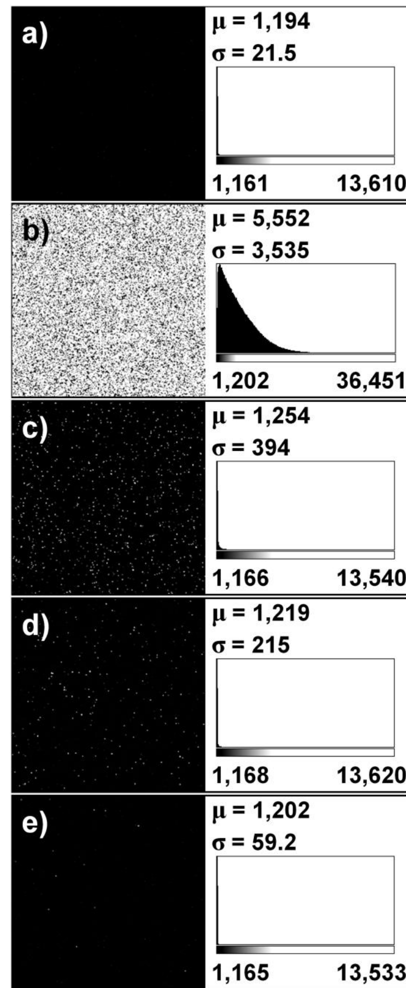

Figure 15. The Effect of Design Revisions on Zinger Noise from a 28 Second Dark Frame Exposure Image (Camera Shutter Closed) with the *a*) X-Ray Beam Off *b*) X-Ray Beam On, Before Taking Any Physical Precautions *c*) X-Ray Beam On, After Implementing Right-Angle Mirror Design *d*) Same as *Figure 15.c* Except with a 9mm Aperture in ¼" Pb In-Line with the Detector and *e*) Same as *Figure 15.d* Except the Hole Aperture is 2mm, all with the Corresponding Image Histogram with Minimum and Maximum Value, as Well as Mean Value, μ, and Standard Deviation, σ (For *Figure 15.b-23.e* the X-Ray Source was at 150kV and 160μA Target Current, Unfiltered and all Figures are Rendered with 1200 as Black and 4000 as White)

5.2.2 The effect of x-ray imaging parameters on zinger prevalence.

For the minimization of zingers in the raw data, an understanding of the zinger density as a function of XCT scan parameters is important in addition to the shielding design of the x-ray detector. The zinger noise has been observed to be additive to all other noise and signal. The probability, φ, that a given pixel is affected by zinger noise in a given exposure at a given distance from the radiation source at a particular accelerating voltage, target current, exposure length, and detector shielding configuration can be measured. The number of zingers present in an acquired image was explored as a function of exposure length (*Figure 16*), x-ray target current (*Figure 17*), and x-ray source accelerating voltage (*Figure 18*). The zinger count was determined by acquiring dark frame exposures (camera shutter closed, x-rays on) under the same conditions as the data in *Figure 15.c*. In order to count the zingers with the x-ray source on, statistics were acquired for dark frame exposures with the x-ray source off, and were used to determine a background. A pixel was said to be a zinger if the value of the pixel with the x-ray source on was greater than 2.5 standard deviations from the mean value of an exposure of the same length with the x-ray source off. Three frames were acquired for each type of exposure, and the average value of each was used. Further, a similar calculation was performed for the exposures with the x-ray source off, and this 'false zinger' count was subtracted to yield the final zinger count. A predictable number of 'false zingers' were counted in exposures where the x-ray source was off, thus known not to be zingers, and were attributed to extreme but predictable abnormality of CCD element response in dark exposure. As the number of pixels in the image array plays a role in the detectable

number of zingers, each count value has been normalized and displayed as an area fraction.

While absolute zinger count measurements may not be reproducible on another system due to complex contributions from geometry, detector design, and shielding, it is expected that this data is of quantitative use to researchers performing high energy XCT. A linear dependence has been observed for exposure and x-ray target current which is expected to extend to other systems. An exponential increase was observed with accelerating voltage. With the investigated detector, the zinger density becomes of increased concern over 100kV. The distance from the x-ray source to the sensor is also expected to have a significant effect, but was not varied in this investigation.

The intensity distribution of the zinger has not been explored in great detail. The zinger count rate measurements here presented are been based on zinger identification using a threshold intensity value. However, as shown in *Figure 15*, the zinger affected pixels have a distribution of intensity above the mean. The number of zingers with a particular increase in intensity from the mean falls off with increasing intensity, and upon first assessment, the distribution is roughly normal. The primary implication of such a distribution is that in real images suffering from heavy zinger noise, the low intensity zingers, although less detrimental to reconstruction, will be harder to identify than high intensity zinger, and may even fall into the noise level of the image.

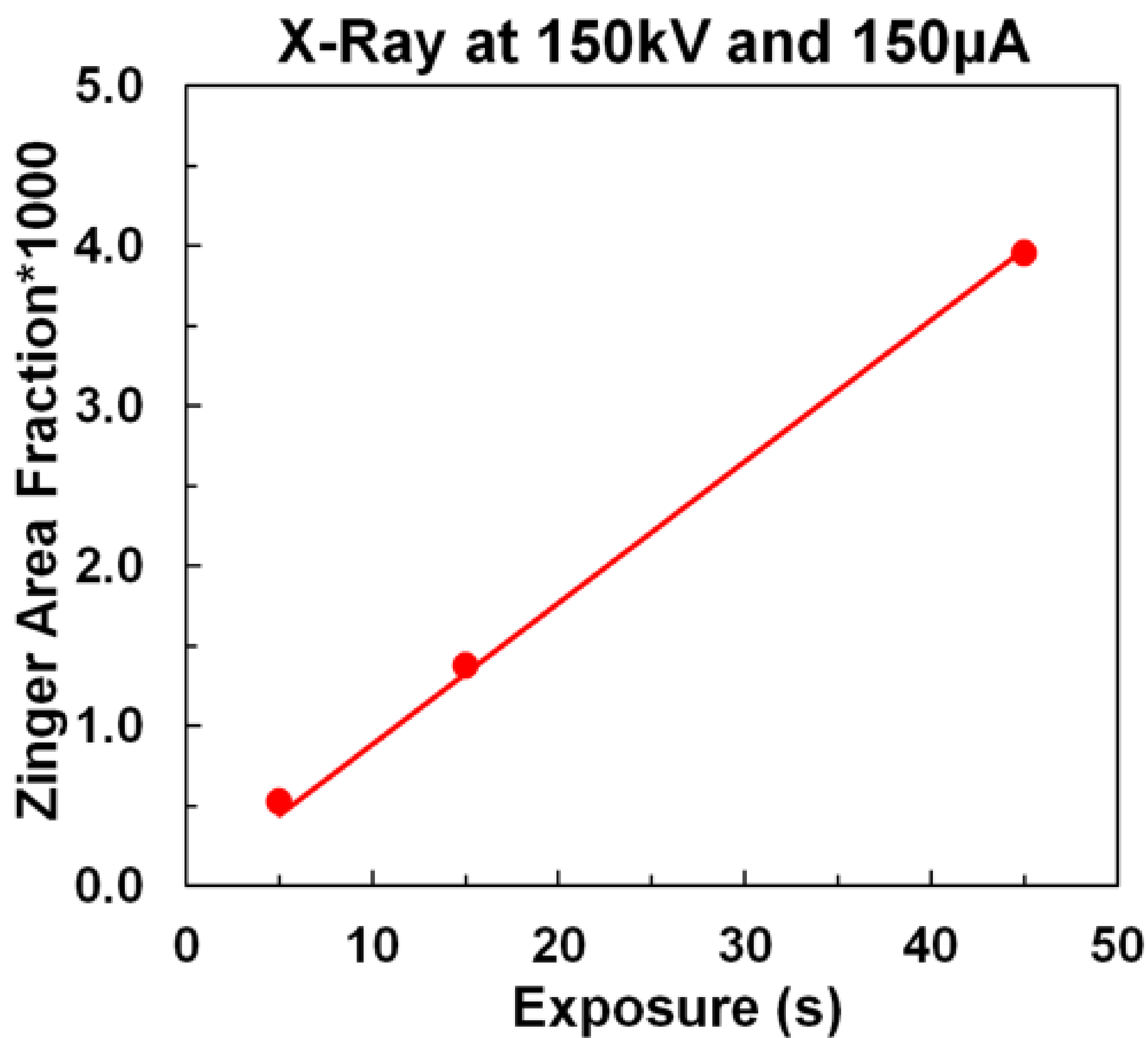

Figure 16. Area Fraction of the CCD Chip which is Corrupted by Zinger Noise at Different Exposures, with the X-Ray Source Unfiltered and Operating at 150kV and 150µA Target Current

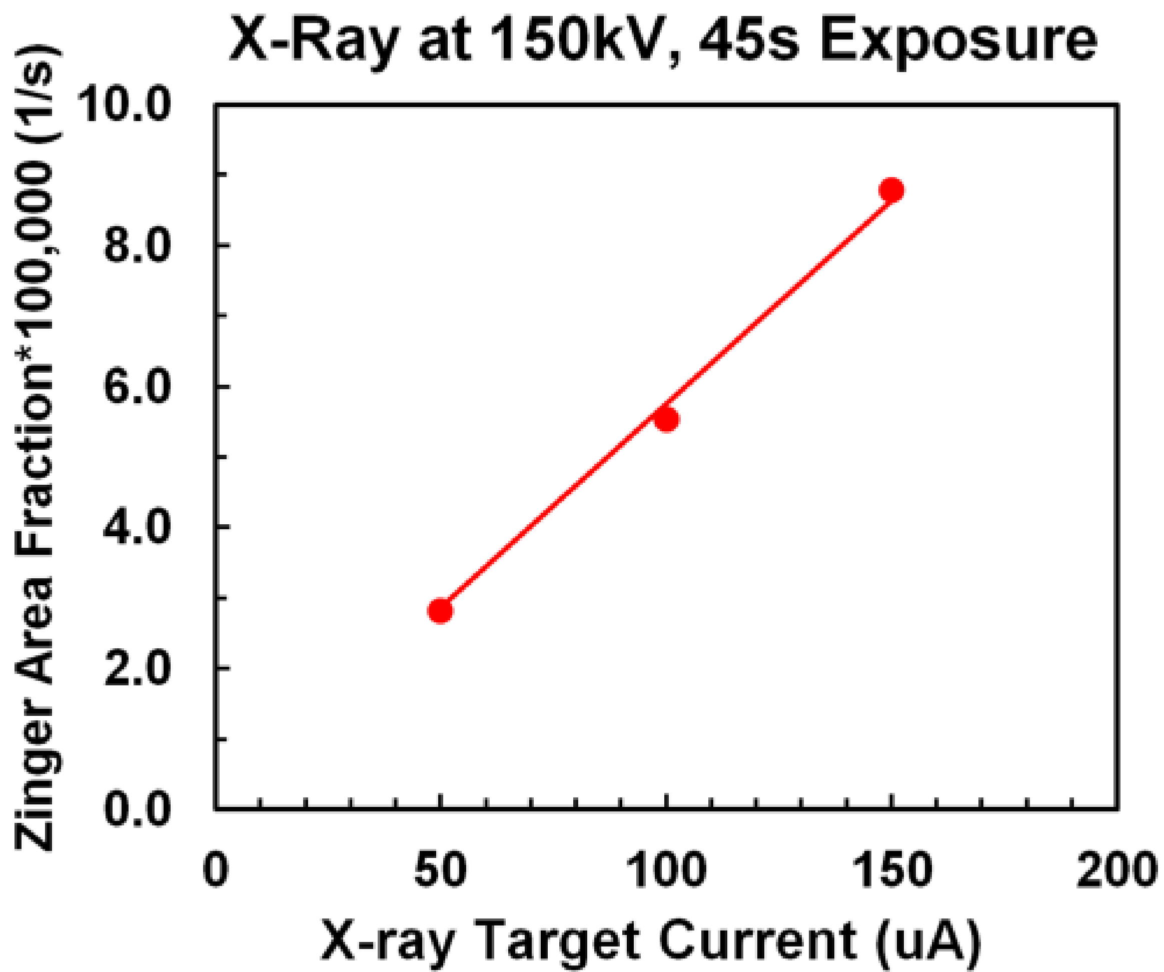

Figure 17. Area Fraction of the CCD Chip which is Corrupted by Zinger Noise at Different X-Ray Target Currents, with the X-Ray Source Unfiltered and Operating at 150kV with the Area Fraction Normalized by Exposure Time

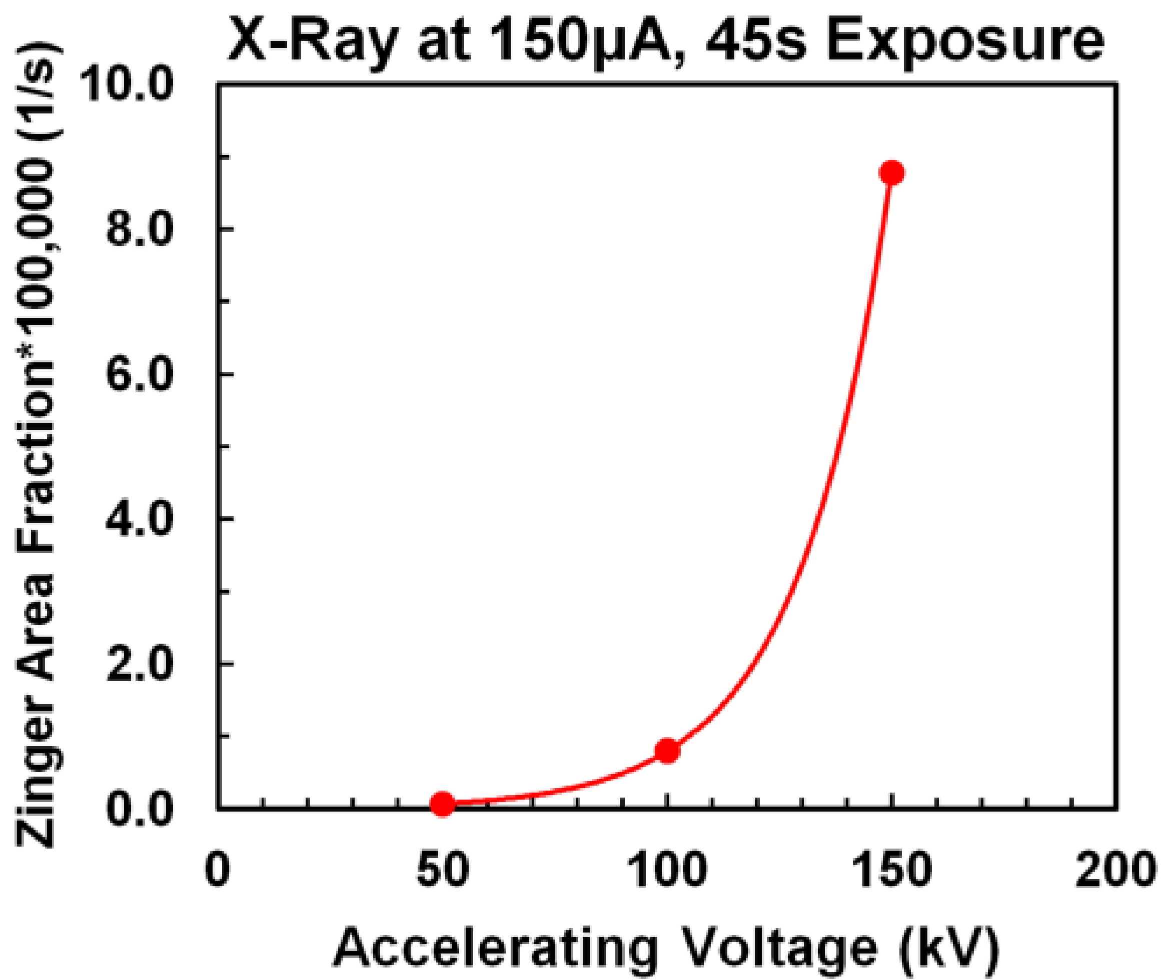

Figure 18. Area Fraction of the CCD Chip which is Corrupted by Zinger Noise at Different X-Ray Tube Accelerating Voltages, with the X-Ray Source Unfiltered and Operating at 150µA Target Current with the Area Fraction Normalized by Exposure Time

The explored parameters may be adjusted to minimize zinger density in the raw images; in general, the selection of these parameters is constrained by other imaging considerations. In practice, zinger noise can exist in raw images despite efforts to minimize their image density. Thus, an acquisition method and an accompanying algorithm were developed for their removal and are discussed in the next section.

5.3 DATA ACQUISITION AND PROCESSING

Although a two dimensional median filter, where each pixel value in an image is replaced by the median intensity value of a neighborhood of pixels centered around each pixel, is very powerful at removing 'speckle' or 'salt-and-pepper' noise, it also has the ramification of altering unaffected pixel values. Algorithms for selectively applying a median filter to only high frequency, high contrast features are commonly used on tomography data containing zingers (Rivers, 1998, APS, 2015). The algorithm used in the TomoPy package was selected as the standard for comparison with the newly put forth temporal selective frame averaging (SFA) algorithm. *Algorithm 1* was adapted from TomoPy to MATLAB for analysis, where *Pzing* is the dark-field-only corrected projection image containing zinger noise, Not(*x*) performs the logical '≠1' operation on array *x,* Median2D(*x*, *MedianWindow*) performs the two dimensional local neighborhood median filter on the array, *x,* using a square neighborhood centered about each pixel in array *x*, *Tolerance* is the relative increase in intensity chosen for zinger identification, *C* contains high frequency high contrast features of *Pzing*, *Zmap* is the generated map of zinger affected pixels, and *P* is the resulting zinger-filtered image. In this formulation, all

arithmetic is performed element-wise and logical operations are on an element by element basis.

Algorithm 1

Standard Zinger Removal Method

INPUT(*Pzing*, *MedianWindow*, *Tolerance*)

Pmed = Median2D (*Pzing*, *MedianWindow*)

$C = -(\ Pmed - Pzing\ ) / Data\ Med$

$Zmap\ (C > (1 + Tolerance)\ ) = 1$

$Zmap\ (C \leq (1 + Tolerance)\ ) = 0$

$P = Zmap * Pmed + \text{Not}\ (Zmap) * Pzing$

OUTPUT(p)

It was found upon application of this filter than many pixels in the image, in addition to the zinger affected pixels, were being altered to some extent. Thus, the accuracy of the filtered image was in question, and other means for zinger removal were sought.

Due to the random nature of the high-energy x-ray speckle noise, the following approach for data acquisition was adopted and the accompanying algorithm implemented to remove zinger noise by selectively replacing zinger affected pixel values with values from identical but unique exposures prior to frame averaging. Regardless of intensity, the

probability that a pixel is affected by a zinger can be expressed as φ, as was measured in **Section 5.2**. The probability that this same pixel is affected by a zinger in every one of a number, N, of identical exposures can be expressed as φ^N. The probability that the pixel is affected by zinger in none of a number, N, of exposures can similar be represented as $1-\varphi^N$.

During acquisition, multiple frames were obtained which were then used to identify zingers within the frames *before* averaging in order to reduce otherwise resulting artifacts in the reconstruction. Rather than take a single exposure of length t of the object's x-ray projection at a given orientation, at least two projections were acquired of the object at the same orientation of length t/N, where N is the number of projections acquired. Taking $N=2$ has yielded the satisfactory results, as will be demonstrated.

Using the newly implemented temporal selective frame averaging (SFA) algorithm, *Algorithm 2*, two dark-field-only corrected projections (with N=2), *P1* and *P2*, were then compared to determine which pixels, and in which projection, contained undesired x-ray noise (zingers). This was performed assuming, 1) zinger locations are unpredictable, 2) zingers are always significantly brighter than surrounding pixels, and 3) the imaging chip has a vast enough pixel count and zingers events are sparse enough to make the probability of a (random) x-ray interaction occurring in the same pixel between consecutive frames effectively zero. The correction was made using *Algorithm 2*, where C is a frame comparison image, *Tolerance* is the tolerated relative pixel variation between frames before replacing the pixel value with the value from another frame, and P

is the SFA zinger filtered projection. In this formulation, all arithmetic is performed element-wise and logical operations are on an element by element basis.

Algorithm 2

Temporal Selective Frame Averaging (SFA)

```
INPUT(P1,P2,Tolerance)
C = P1/P2;
P1 (C > (1+Tolerance) ) = P2
P2 (C < (1-Tolerance) ) = P1
P = ( (P1 + P2) / 2
OUTPUT(p)
```

The algorithm's approach in the application to zinger noise reduction in x-ray computed tomography radiographs was based on the fact that any pixel's value should only vary from one consecutive frame to the next due to random noise in the detection system or x-ray beam instability. As zingers cause a much greater variation in value from one frame to another, experience has suggested any tolerance value between 0.05 and 0.5 filters the observable majority of zingers, which is discussed in greater detail in the case study analysis in the next section. A tolerance of 0.1 has been used as a default in experimentally acquired radiographs. The last line of *Algorithm 2* is just an averaging of the two filtered projections.

With two frames being used (N=2), as embodied in *Algorithm 2*, the algorithm conceivably fails when a zinger occurs at the same detector element in both frames. For simplicity of analysis in this section, a zinger here is considered to be of a predictable constant value. Consider the exaggerated case of a long exposure of 60s at 160kV (the highest achievable by the tube measured in this system), at 50W target power (higher than practically used for the purposes of the high resolution system), the probability that a given pixel is affected by a zinger in a single exposure can be calculated as 1.1% using the data for the detector distance studied in **Section 5.2**. For the 2048^2 detector used in this study, this situation would result in over 47,000 zingers in the single image out of over 4 million. If instead, two images were acquired of half the length, the probability that the same pixel would be affected by zinger in both the initial and final exposure would be $(\varphi/2)^N$, or 1.2E-4, and thus 134 pixels would persist after the following algorithm due to zinger presence in those pixels in both exposures. The other roughly 47,000 pixels which were corrected for would suffer from a lower signal to noise ratio than the completely unaffected pixels, but would have intensity values representative of the object being imaged rather than zinger noise. In real imaging, where zinger affected pixels have a distribution of intensity, and other sources of noise in the image are present, the number of missed zingers is expected to increase.

To justify the choice of just two frames being acquired in practice using this method, consider the case of three frames being acquired. The acquisition of three frames of one-third the exposure length is similarly calculated to have 58 pixels remaining as zinger noise after the application of the approach in *Algorithm 2*, where zinger presence in two

of the frames is considered to be failure, because the algorithm would consider the unaffected pixel to be the outlier without any added sophistication. In addition to the small decrease in unfiltered zingers, the algorithm is also further complicated by the addition of comparisons of a pixel's value in one frame to the pixel's value more than one other frame. The additional cost of read-out time of the imaging sensor is another disadvantage of acquiring multiple exposures, which will vary from setup to setup. Furthermore, if one were to apply to the same approach to frames of unique orientation acquired consecutively during a scan wherein only an incremental change of the object being imaged is observed, using multiple frames would be disadvantageous. Yet, using a greater number of exposures of a static object does greatly improve the signal to noise ratio for zinger filtered pixels.

Algorithm 2 was applied in combination with a CCD dark field and flat field correction. In x-ray systems, the flat frame is simply taken by acquiring an image using the same equipment parameters as for the projections, but merely without the sample in place, and corrects for imaging system non-uniformity. A flat frame, *F*, was acquired by taking one flat frame both before and after acquisition of *P1* and *P2*. In practice, the XCT scan routine acquired one flat frame before and after imaging several sample orientations. The two flat frames, *F1* and *F2*, were then treated identically as the projections were (dark field correction followed by *Algorithm 2*) to remove speckle noise and arrive at a corrected average, *F*. Dark frames were acquired immediately preceding the XCT data acquisition and immediately following data acquisition, but with the x-ray source turned off, to capture dark noise without any zingers. A master dark frame, *MD*, was then

acquired by taking an average of the dark frames, and was subtracted from each raw flat image or raw projection image before being input to *Algorithm 2*. The flat frame correction was then performed to yield a calibrated radiograph image, R, for each orientation, with zinger noise removed. With this
approach, the calibrated radiograph R is then expressed as:

$$R = P / F, \tag{38}$$

where images P and F underwent dark field correction before high energy x-ray speckle noise removal, and the division is performed element-wise. Any background-corrected radiograph acquired under zinger generating conditions would have both bright and dark zingers, where the dark zingers would be caused by bright zinger pixels in the flat field background image. Rather than treat both bright and dark zingers in the background corrected image, bright zingers were treated in the object and background images separately.

The result of *Algorithm 2* in application to experimentally acquired projections and flat field images possessing zinger noise is provided qualitatively in *Figure 19*. The accuracy of the zinger identification and the similarity of the filtered images resulting from *Algorithm 1* and *Algorithm 2* are analyzed in the next section for artificial projection images.

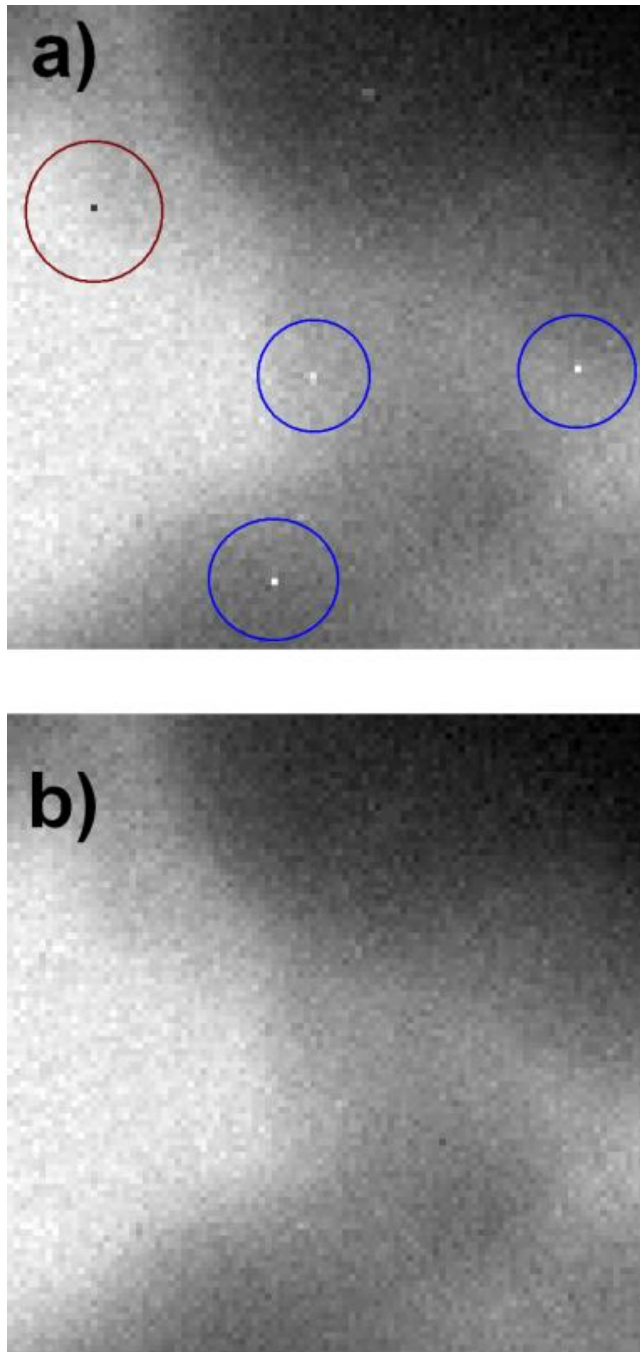

Figure 19. A Sub-Region of an Experimentally Acquired Flat and Dark Field Corrected Radiograph *a*) Without any Zinger Removal, and *b*) SFA Radiograph from Application of *Algorithm 2*

5.4 RESULTS AND ANALYSIS

In order to explore the performance of the newly adopted method over the standard method for zinger removal, a simulated dataset was generated. The dataset was generated based on the requirement for a known noise-free image which faint and strong features to which the filtered images could be compared, and also rooted in the need to know where each zinger affected pixel was located in the noise-containing filter input images. Because the new algorithm is intended for raw projection images in computed tomography, and the standard algorithm is suited for simulated projections, forward projections of the Shepp-Logan head phantom were selected as the test image. Due to the random nature of the zinger noise, a large number of images with varying features were required for the test. To apply the algorithms to the removal of zingers across many images, a full tomography scan of the Shepp-Logan phantom was selected as the input. The forward projections were generated using an open source cone beam forward projector with the digital Shepp-Logan head phantom (Kim, 2014). The default parameters were maintained yielding forward projection images with 100 rows (dimension i), 128 columns (dimension j), and 361 projections (dimension θ) corresponding to 1° increments over a full rotation. The 0° (θ=1) projection is shown in *Figure 20*. Then, artificial zinger noise was added to the projections.

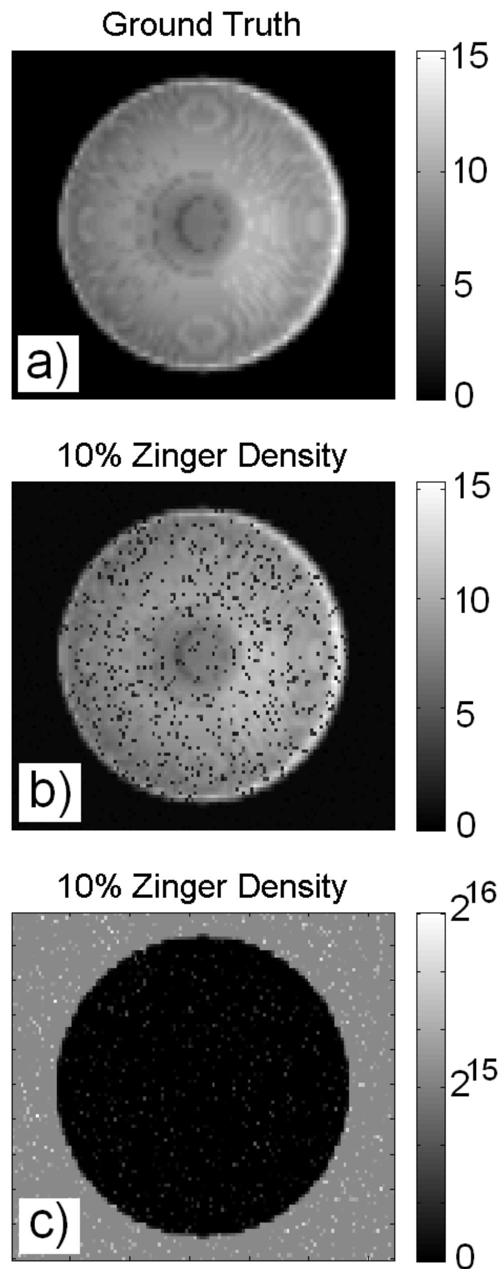

Figure 20. Simulated Forward Projections of the Shepp-Logan Phantom at 0° Showing *a*) the 'Perfect' Forward Projection of the Phantom *b*) With 10% Image Density Zzinger-Like Noise Added, and *c*) With 10% Image Density Zinger-Like Noise Added and Sscaled to Simulate the Experimental Projection Data

The zinger noise has been observed to be additive to all other noise and signal. The intensity value added to a particular pixel which is suffering from a zinger noise has been observed to follow a distribution, as shown in *Figure 15*. This distribution was modeled with positive integers from a normal distribution centered about zero and with a maximum value set to the count limit of a 16 bit sensor, 2^{16} -1$(G_{i,j,\theta}^{0\rightarrow 65536})$. The total number of zingers added to a particular projection was fixed by defining a random mask of pixels with a particular density, d^*, to be applied to each projection in the projection stack $M_{i,j,\theta}^{d_{i,j}=d^*}$. The zinger pixels are indicated in the mask $M_{i,j,\theta}^{d_{i,j}=d^*}$ by values one within a background of zeros. The zinger noise added to each projection, $Z_{i,j,\theta}^{d_{i,j}=d^*}$, was then calculated as:

$$Z_{i,j,\theta}^{d_{i,j}=d^*} = G_{i,j,\theta}^{0\rightarrow 65536} * M_{i,j,\theta}^{d_{i,j}=d^*}, \quad (39)$$

with element-wise multiplication. Before adding the zingers to the artificial projections, the projections were scaled in intensity to simulate a projection by restoring the transmission image and scaling the background value to one half of a 16 bit sensor, equal to 2^{15} -1. This image was considered to be the ground truth (*GT*) projection stack, with which the filtered images were eventually compared. The zinger-containing projections were then generated by adding the zinger noise mask with a particular zinger density to the ground truth image. This can be expressed as:

$$P_{i,j,\theta}^{d_{i,j}=d^*} = GT_{i,j,\theta} + Z_{i,j,\theta}^{d_{i,j}=d^*}. \quad (40)$$

where $P_{i,j,\theta}^{d_{i,j}=d^*}$ is the simulated projection with zinger density equal to d^* in the (i, j) domain and $GT_{i,j,\theta}$ is the ground truth forward projection image stack free of any zingers.

To compare the standard method which uses only one frame for zinger identification with the conceived method which uses two frames, three total stacks were generated for each simulated zinger density. One with the targeted zinger density, d^*, resulting from a simulated exposure, t, and two with a zinger density of $d^*/2$ resulting from two simulated exposures of length $t/2$. The two exposures of density $d^*/2$ (cumulatively a density of d^*) were used to study the temporal selective frame averaging (SFA) approach for zinger removal, and the single exposure with zinger density d^* was used to study the standard approach for zinger removal. For a more direct comparison between the two methods for zinger removal, the projection stacks were generated so that each projection in each stack had the same zinger noise, that is, such that the relationship,

$$Z(\text{Standard})_{i,j,\theta}^{\mathrm{d_{i,j}=d^*}} = Z(\text{SFA},1)_{i,j,\theta}^{\mathrm{d_{i,j}=d^*/2}} + Z(SFA,2)_{i,j,\theta}^{d_{i,j}=d^*/2}, \quad (41)$$

was satisfied for each set of projections for a given simulated zinger density. With this approach the same pixels for both methods were affected by zingers of the identical intensity, but each orientation contained a unique set of randomly affected zinger pixels.

The zinger densities which were evaluated for this study were 10%, 1.0%, and 0.1%. Thus for the frame averaging approach, for the 10% zinger density for example, two projection images were created which had 5% zinger density, which cumulative were identical to the single 10% zinger density projection used for the standard method. The intensity distribution of all the zingers for the 10% density study is portrayed in the histogram provided in *Figure 21*. The histogram shows that more low intensity zingers are present than high intensity zingers which, especially when added to image intensities, make the zingers a challenge to identify based on intensity value alone. Additionally, of course, the random nature of the zingers, both in the simulation and in reality, make zinger affected pixels impossible to identify based on position. A test vehicle for the newly constructed algorithm and the standard algorithm for zinger removal was in this way achieved. With the window size optimized for *Algorithm 1* for the test images in this study, *Algorithm 1* and *Algorithm 2* were directly compared as a function of the tolerance factor which both require. The comparison was made on the basis of true positive (T+) and false positive (F+) events relative to the known zinger affected pixels for a particular zinger density. The effect of tolerance factor on T+ and F+ for both algorithms in application to the 10% zinger density case is shown in *Figure 22* and *Figure 23*. It can be seen that the value of the tolerance factor has very similar effect on the obtained T+ rating for either algorithm, but that for increasing T+ rating using *Algorithm 1*, a significant increase in F+ instances is simultaneously achieved, undesirably. This is not the case for the newly constructed temporal averaging zinger removal method, *Algorithm 2*, as shown in *Figure 23*.

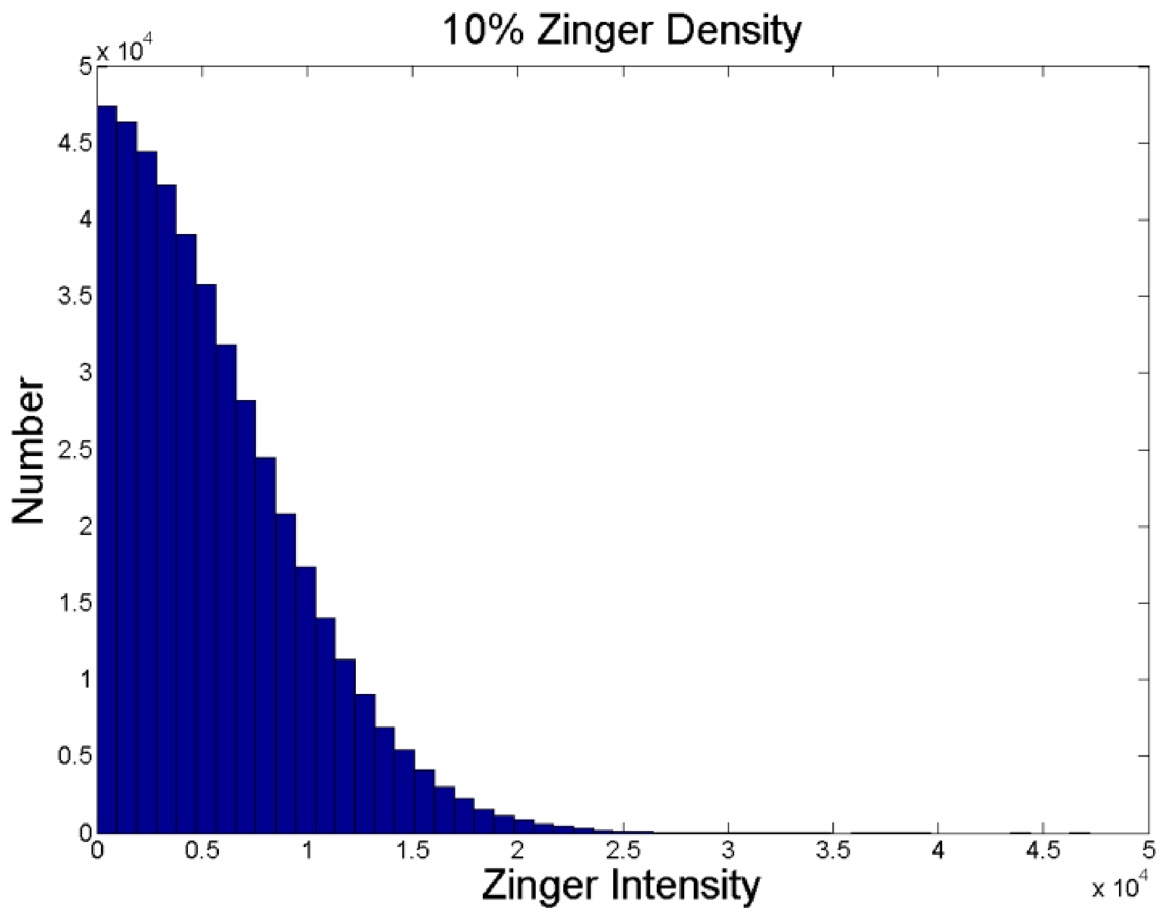

Figure 21. Histogram of Artificially Added and Randomly Positioned Zinger Pixels by Intensity Value in the Highest Zinger Density Implemented on the Simulated Shepp-Logan Phantom Forward Projection Stack where More Low than High Intensity Zingers are Used to Match Experimental Observation, Modeled here with a Normal Distribution

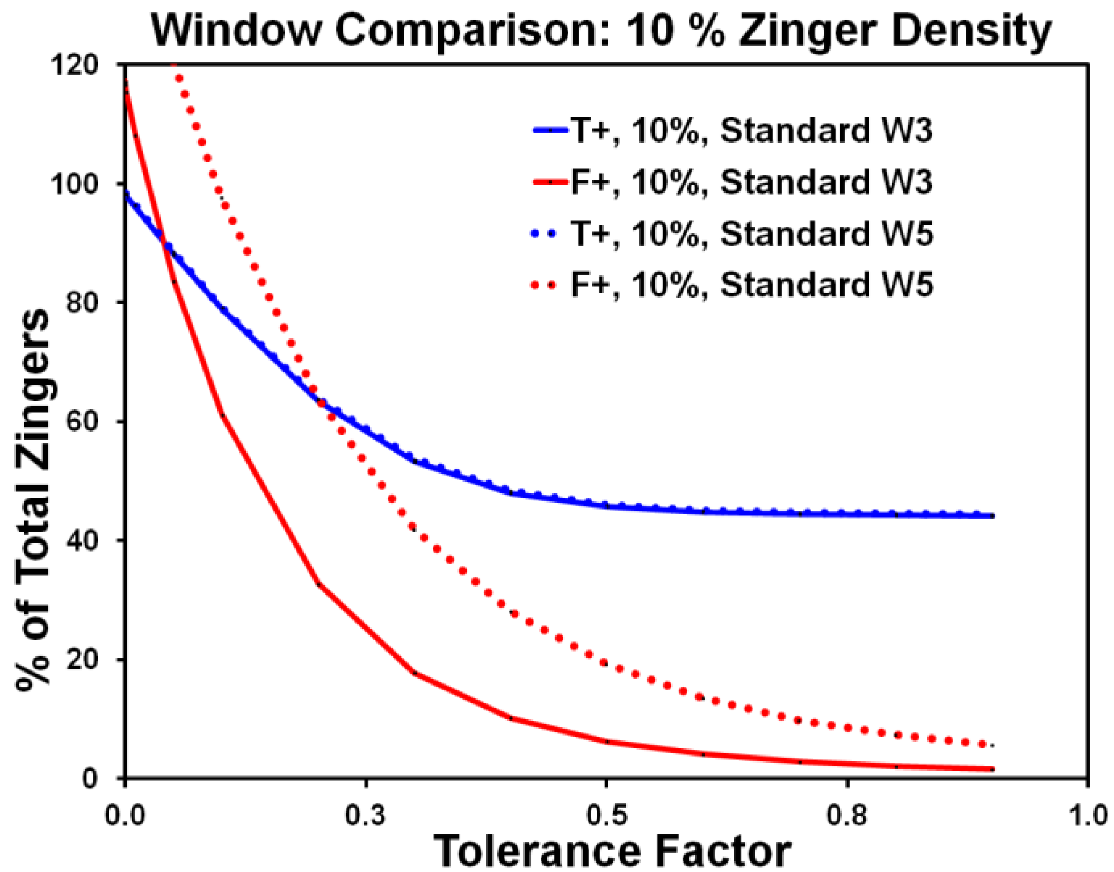

Figure 22. Comparison of Zinger Identification between the Standard Method of Varying Window Size as a Function of Tolerance Factor

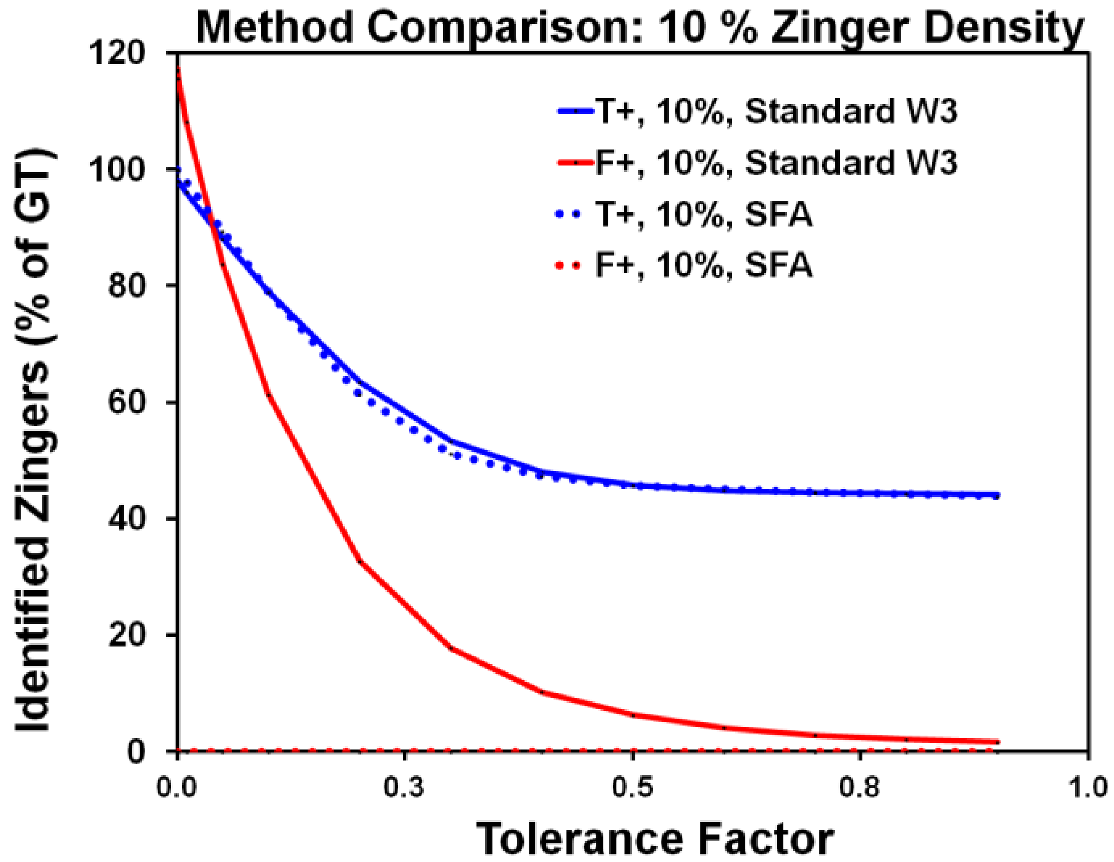

Figure 23. Comparison of Zinger Identification between the Standard Method with the Optimal Window Size and the Newly Constructed Selective Temporal Frame Averaging Approach as a Function of Tolerance Factor

The T+ and F+ ratings provided between both algorithms for the 10% zinger density case shown in *Figure 23* are for the entire projection stack and for varying tolerance factor input value. A tolerance factor of 0.01 was selected as optimal for both methods for all zinger densities based on a arbitrary criterion for a T+ rating of no less than 95%. By fixing the tolerance factor, and limiting the analysis to a single projection of the entire set of projections, the effect of zinger density and choice of algorithm on the accuracy of zinger identification can be more easily visualized. The zinger identification accuracy results for both algorithms with an optimal tolerance factor (0.01 in all cases), for each zinger density studied, are shown graphically for the θ=0° projection in *Figure 24*. As portrayed in *Figure 23*, no significant advantage in terms of T+ rating is realized upon using the new, selective frame averaging (SFA) approach. However, by observation of *Figure 24*, it can be seen that the new SFA algorithm offers extreme advantages in terms of F+ instances and in terms of false negative (F-) ratings. Even at a zinger density approaching null, the standard zinger removal algorithm falsely identifies zingers based on prevalent features in the image. The standard algorithm is also observed miss zinger affected pixels when the zinger occurs near a sharp edge, most obvious at higher zinger densities. The SFA algorithm is observed miss zinger pixels at higher zinger densities, due to the increasing probability of a zinger being present in the same pixel in both exposures of the same orientation at higher density. The SFA algorithm is not observed to generate false positive identifications, but conceivably would if the tolerance factor was low enough and the total noise in the image high enough.

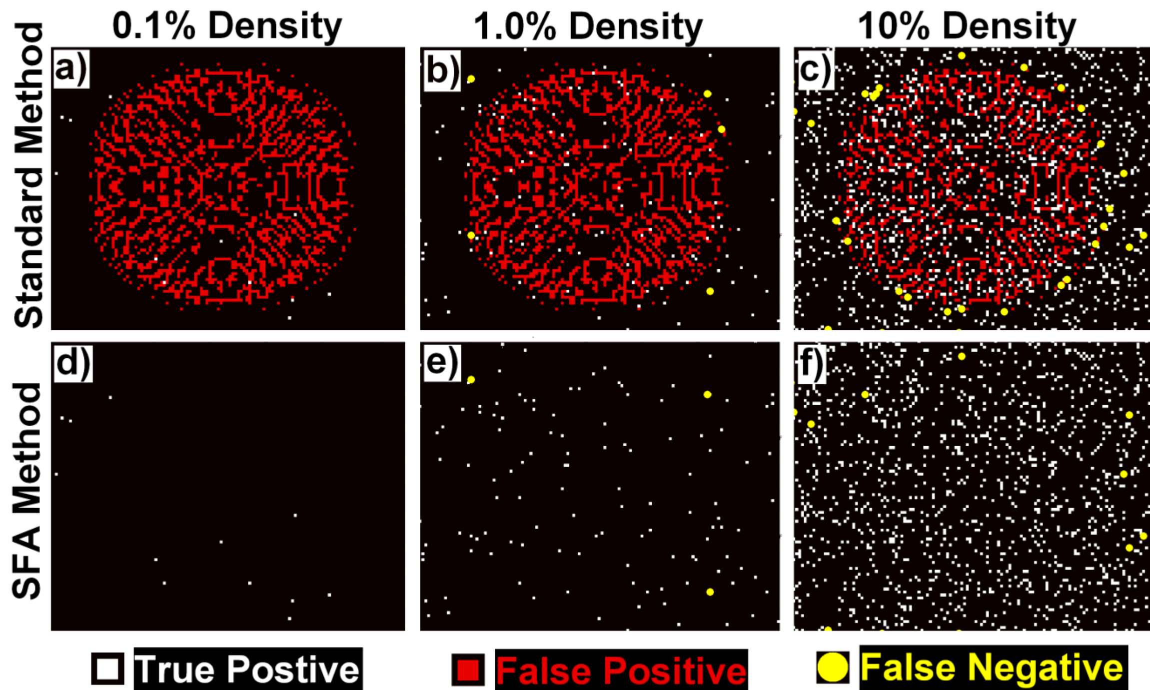

Figure 24. Comparison of Zinger Identification Between the Optimized (Tolerance Factor = 0.01) Standard and Selective Frame Averaging Methods for Zinger Removal with Correctly Identified Zingers Shown as White, Falsely Identified Zingers Shown as Red and the Yellow Circles are Centered on Zingers Missed by the Algorithms (Portraying the Accuracy of the Algorithm's Zinger Identification but Not the Accuracy of Filtering)

Apart from the capability to accurately identify zinger affected pixels, the algorithms were also compared on a basis of degree of restoration to the ground truth image, that is, in terms of the filtered images' similarity with the noise-free images. While one method may be superior in terms of zinger identification performance, a better restoration of the ground truth image data is not guaranteed. Along with the T+, F+, and F- rating, the average sum of the squared difference (*SSD*) per pixel of the filtered image compared to the ground truth was calculated. These ratings are tabulated for the standard zinger removal filter with a 3x3 window in *Table 6*, and for the presently constructed temporal frame averaging filter in *Table 7*. The mean *SSD* per pixel was calculated for both by considering all image pixels and only zinger affected pixels. For brevity, only the 10% zinger density and 3x3 pixel window cases are provided.

From *Table 6* and *Table 7*, it can be deduced that for the studied model, the temporal frame averaging filter outperforms the standard zinger removal approach in terms of true positives, false positives, false negatives, and sum of square differences with the ground truth image even at the highest analyzed zinger density of 10%. Apart from the sum of the square differences per pixel, the relative difference with the ground truth projections can be calculated for each filtered data set as another comparison. The relative difference 'volume' is calculated by subtracting the ground truth image from the filtered image and dividing the result element-wise by the ground truth image, for all 361 projection images analyzed. The results of this analysis are shown in *Figure 25* for the 0° projection. The results of *Algorithm 1* can be succinctly described as causing many small negative and positive deviations from the ground truth image, particularly where image features and

edges are present. The result of *Algorithm 2* can be described as very few pixels with deviation from the ground truth image, but those pixels that do differ from the ground truth have large positive deviations. The breakdown of the efficacy of *Algorithm 2* at extraordinarily high zinger density is a result of zinger overlap across both ‘exposures’ used for temporal averaging. The mean, standard deviation, and median value for the entire relative difference projection stack is also shown in *Figure 25*, overlaid with the associated 0° projection. Whereas the sum of the square differences enhances the many small negative and positive deviations from the ground truth image, and indicates superior results from *Algorithm 2* versus *Algorithm 1*, the relative difference is less convincing. The numerous small negative and positive deviations of the relative difference volume resulting from *Algorithm 1* result in a tight distribution and effectively cancel out resulting in a low standard deviation of the relative difference projections and a mean value of the relative difference projections near zero. The high intensity zingers missed by *Algorithm 2*, particularly at high zinger density, although few in number, result in relatively large positive mean and standard deviation values in the relative difference with the ground truth analysis.

Table 6

Tabulated Performance Data for the Standard Algorithm (Algorithm 1) with a 3x3 Window Operating on the Simulated Projection Stack at 10% Zinger Density

Tolerance Factor	T+ (% Zingers)	F+ (% Image)	F- (% Zingers)	SSD (Avg. per Image Pixel)	SSD (Avg. per Zinger Pixel)
1.0E-05	98.1	11.1	1.9	0.101	0.231
0.00010	98.0	11.1	2.0	0.101	0.231
0.0010	97.9	11.0	2.1	0.101	0.231
0.010	96.1	10.3	3.9	0.101	0.231
0.050	88.1	8.0	11.9	0.102	0.252
0.10	78.9	5.8	21.1	0.114	0.376
0.20	63.4	3.1	36.6	0.188	1.174
0.30	53.4	1.7	46.6	0.326	2.637
0.40	48.0	1.0	52.0	0.478	4.245
0.50	45.7	0.6	54.3	0.594	5.478
0.60	44.8	0.4	55.2	0.663	6.215
0.70	44.4	0.3	55.6	0.695	6.564
0.80	44.3	0.2	55.7	0.709	6.722
0.90	44.2	0.1	55.8	0.715	6.787
1	44.1	0.1	55.9	0.716	6.815

Table 7

Tabulated Performance Data for the Temporal Selective Frame Averaging Filter (Algorithm 2) Operating on the Simulated Projection Stack at 10% Zinger Density

Tolerance Factor	T+ (% Zingers)	F+ (% Image)	F- (% Zingers)	SSD (Avg. per Image Pixel)	SSD (Avg. per Zinger Pixel)
1.0E-05	99.9998	0	2.275E-04	1.684E-04	1.770E-03
0.00010	99.9800	0	2.002E-02	1.684E-04	1.770E-03
0.0010	99.7950	0	2.050E-01	1.684E-04	1.770E-03
0.010	97.92	0	2.1	1.684E-04	1.770E-03
0.050	89.36	0	10.6	1.685E-04	1.771E-03
0.10	78.9	0	21.1	1.690E-04	1.776E-03
0.20	61.3	0	38.7	1.707E-04	1.794E-03
0.30	51.2	0	48.8	1.724E-04	1.813E-03
0.40	47.3	0	52.7	1.783E-04	1.875E-03
0.50	45.7	0	54.3	1.836E-04	1.930E-03
0.60	45.0	0	55.0	1.925E-04	2.024E-03
0.70	44.6	0	55.4	1.981E-04	2.082E-03
0.80	44.3	0	55.7	2.072E-04	2.178E-03
0.90	43.9	0	56.1	2.226E-04	2.340E-03
1	22.4	0	77.6	2.512E-03	2.641E-02

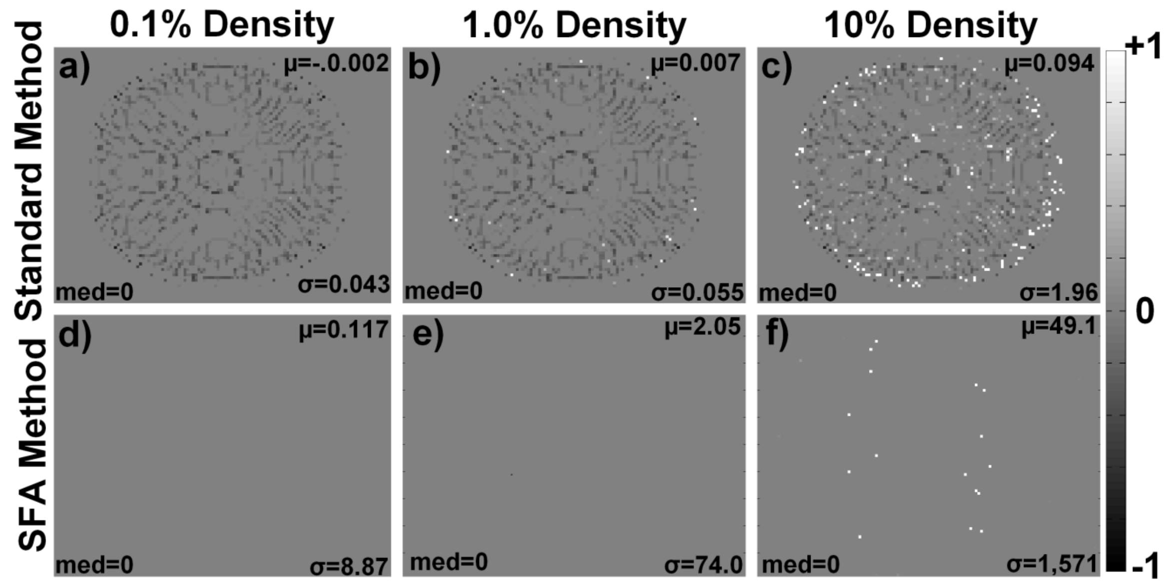

Figure 25. The Relative Difference Images Between the Ground Truth and the Zinger Filtered Images by Both the Optimized (Tolerance Factor = 0.01) Standard and Selective Frame Averaging Methods for the 0° Projection where a Value of Zero for a Pixel indicates No Deviation from the Ground Truth Image Portraying the Accuracy of the Filtering (The Mean (μ), Median (*med*), and Standard Deviation (σ) for Each Respective Stack of Projections are Inset in Each 0° Projection)

The effect of the selected tolerance factor in *Algorithm 1* or *Algorithm 2* on the filtered data's SSD with the ground truth can also be analyzed (Column 5 and Column 6 in *Table 6* and *Table 7*). For the 10% zinger density case, the average SSD value per pixel in the filtered projection data from *Algorithm 1* converges to roughly 0.1 at a tolerance factor of zero, as shown graphically in *Figure 26*. A tolerance factor of zero in *Algorithm 1*, however, resulted in a very large number of false positives.

The effect of either filter on the zinger affected pixels themselves was also analyzed. A histogram of the zinger affected pixels' noise intensity in the standard zinger filtered data using a window size of 3x3 and a tolerance factor of 0.01 is provided in *Figure 27.* The noise intensity was calculated by subtracting the ground truth pixel intensity from each zinger affected pixel in the filtered data.

Similarly, the histogram of the zinger pixels' noise intensity after applying the SFA filter is provided in *Figure 28*. For the standard filtered data, the number of zinger-affected pixels with small noise intensity increases drastically as a result of the filtering. For the SFA filtered data, the number of zinger affected pixels with low noise intensity does not increase, because in the simulated data the correct intensity value can be perfectly restored. In both cases, the number of high noise intensity zingers is effectively reduced as a result of the filtering process. It can also be visually observed in *Figure 27* and *Figure 28* that the number of zinger affected pixels with intermediate noise intensity in the filtered images is more greatly reduced by the application of *Algorithm 2* than *Algorithm 1*.

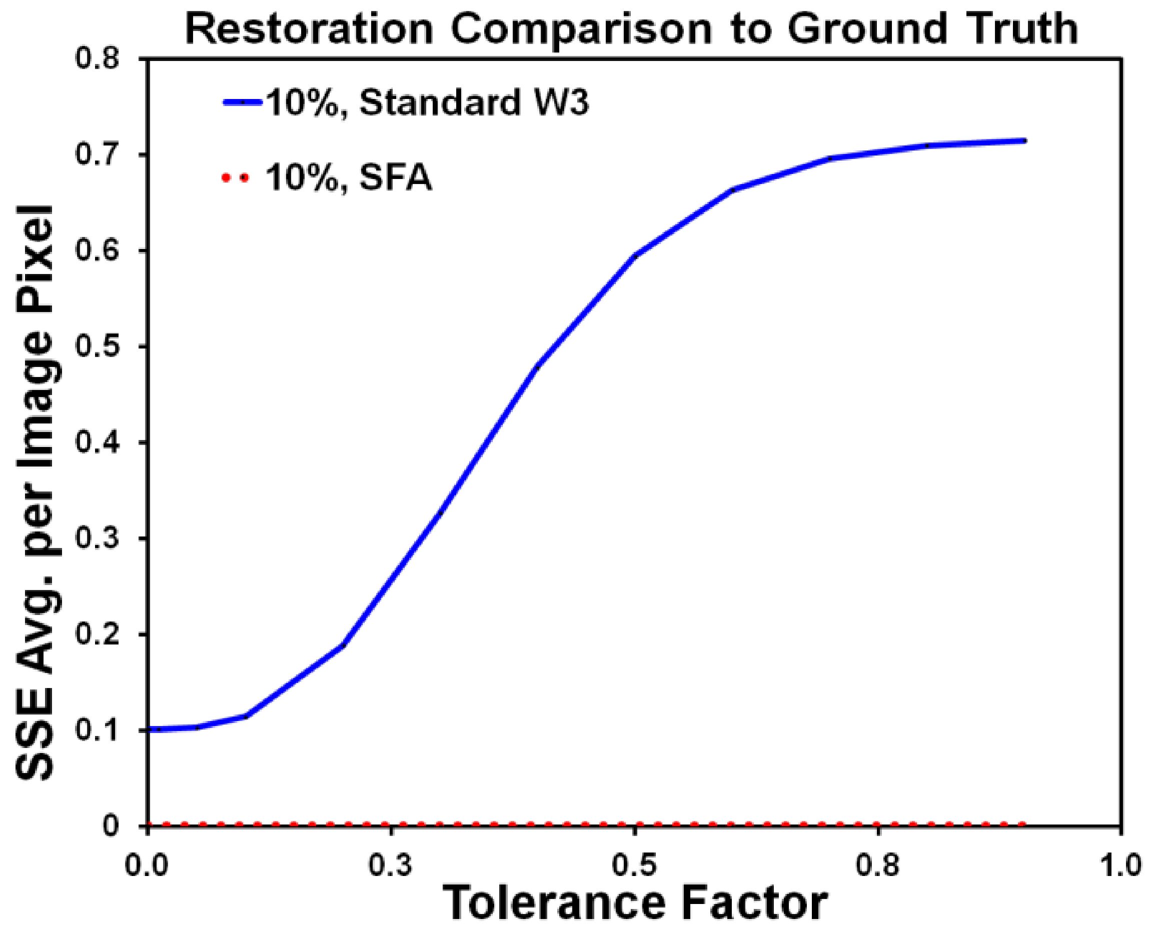

Figure 26. Comparison of Zinger Filtering Method as a Function of Tolerance Factor by Analyzing All Filtered Projections' Sum of Square Differences for All Projections and the Ground Truth Data for All Pixels

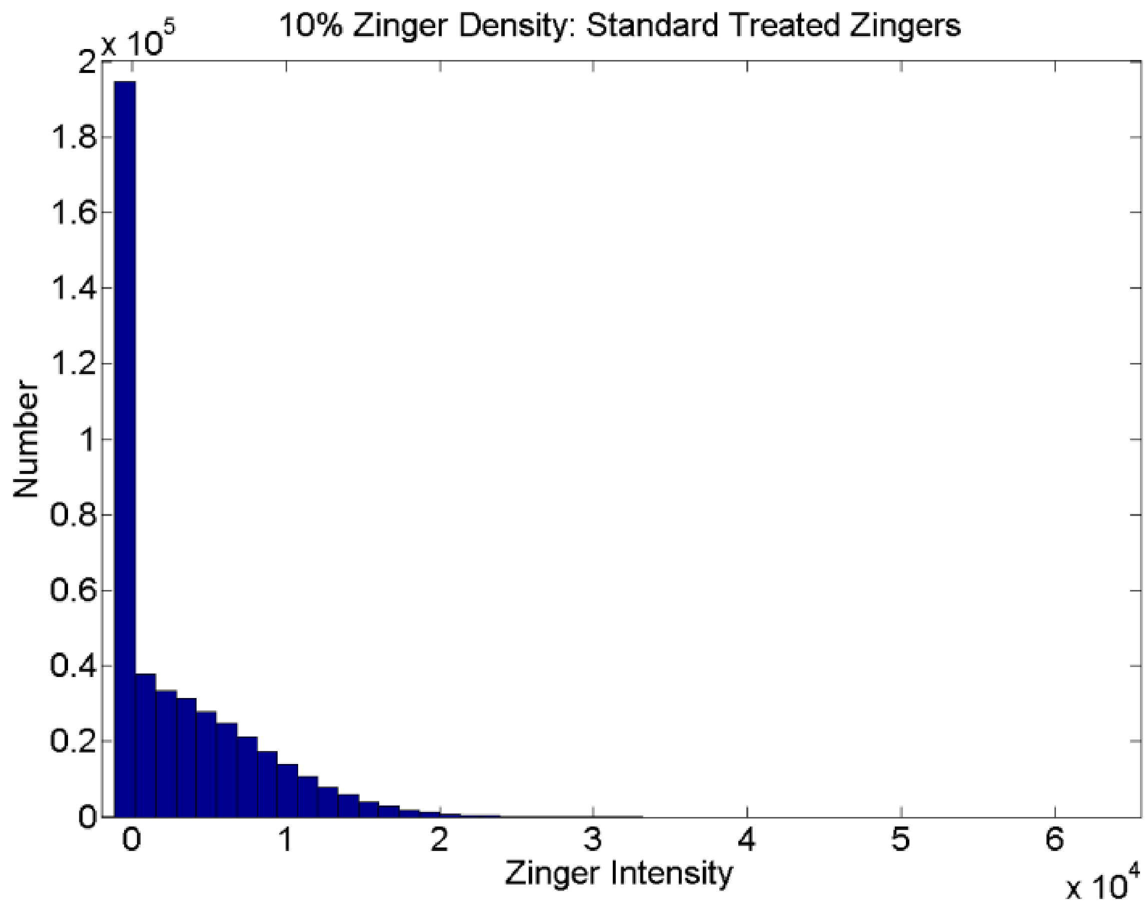

Figure 27. Histogram of Zinger Affected Pixel Intensity *above* the Ground Truth Intensity after Filtering the 10% Zinger Density Projection Stack Using the Standard Zinger Removal Method (*Algorithm 1*)

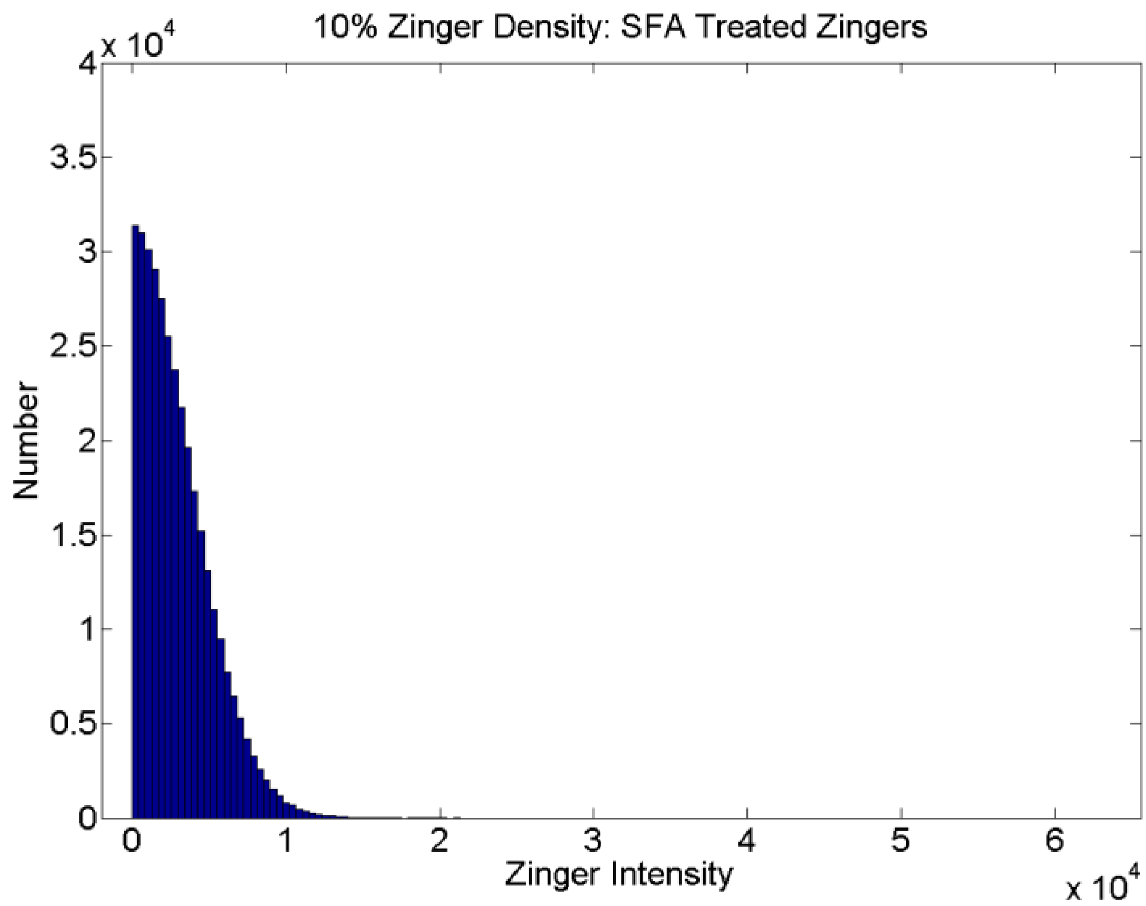

Figure 28. Histogram of Zinger Affected Pixel Intensity above the Ground Truth Intensity after Filtering the 10% Zinger Density Projection Stack Using the Newly Implemented SFA Method (*Algorithm 2*)

The last way in which the results of *Algorithm 1* and *Algorithm 2* were compared was through the tomographic reconstruction of the Shepp-Logan head phantom. To make the comparison, the cone beam reconstruction was first performed on the ground truth (free from zinger noise) projections, using the same geometric parameters as was used in the forward projection algorithm (Kim, 2014) to generate the projection, and using meshgrid based Shepp-Logan-filtered back projection. The same reconstruction method was then performed for the 1.0% zinger density projections filtered both by *Algorithm 1* with a 3x3 window and a tolerance factor of 0.01 and by *Algorithm 2* with a 0.01 tolerance factor. The sum of the squared difference for the entire reconstruction volume between each test volume and the ground truth reconstruction volume was calculated. The average SSD per pixel in the 128x128x100 reconstructions using the 1.0% zinger density projections filtered by *Algorithm 1* and *Algorithm 2* were 2.75E-5 and for 3.09E-6, respectively. An absolute difference image with the ground truth reconstruction is provided for the central slice (51 of 100) of the reconstruction volume, both for the results of *Algorithm 1* and *Algorithm 2*, in *Figure 29*. The absolute difference reconstruction plane in *Figure 29.a* is very representative of the entire difference volume. While the vast majority of the difference planes in the difference volume for the reconstruction from the projections processed with *Algorithm 2* look similar to that shown in *Figure 29.b*, the single plane does not represent the case of failure well. When *Algorithm 2* does fail in identifying a high noise intensity zinger, a very high contrast streak will occur through the reconstruction plane.

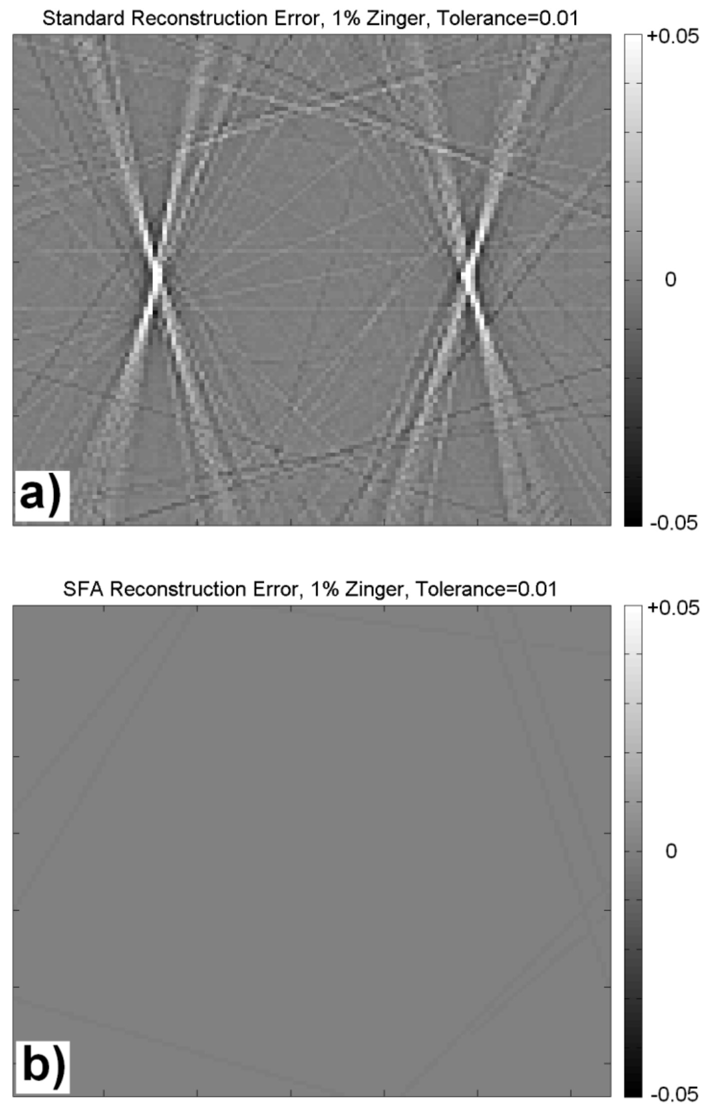

Figure 29. Difference Image of the Shepp-Logan-Filtered Back Projection Reconstructions of the Central (51 of 100) Reconstruction Plane *a*) Difference Between the Reconstruction from the Standard Zinger Removal Projections after 10% Zinger Density was Added and the Reconstruction Plane from the Ground Truth Projections, and *b*) The Difference Between the Reconstruction Plane from the Selective Frame Averaged Projections for Zinger Removal after 1.0% Zinger Density was Added and the Reconstruction Plane from the Ground Truth Projections

5.5 SUMMARY

An image acquisition processing method has been described for improved zinger reduction of a standard method. High energy x-ray noise, or zingers, can be attributed to erroneous signal from the interaction of x-rays with the image sensor. The number of zingers present was measured to be directly proportional to exposure time and x-ray tube target current, and increased more rapidly with increasing accelerating voltage. A temporal filtering algorithm was described, which hinged on the sparse and random nature of the zinger noise, to leverage frame averaging in which zinger-affected signal was replaced with signal from unique but separate data sets by using a user defined tolerance factor. In the event that very long exposures are required in imaging with high x-ray source voltage and target current, the zinger density is measured to increase, and the probability that a single imaging pixel is corrupted by a zinger in consecutive frames increases; in this case, the present SFA method begins to fail.

Sets of projections resulting from an artificial cone-beam x-ray CT scan of a digital Shepp-Logan head phantom were used as the basis for measuring the performance of the zinger filtering algorithms included in this study. Random additive zinger noise following a normal distribution in intensity was artificially added to the projections in varying density at known locations with known intensities. The zinger containing test projections of the Shepp-Logan head phantom used for each algorithm were kept cumulatively identical. The tolerance factor and window size of the standard existing algorithm for zinger removal was optimized in terms of the true positive zinger identification rate using the results from the entire set of test projections. The tolerance factor of the constructed

temporal filtering algorithm for zinger removal was optimized in terms of the true positive zinger identification rate using the results from the entire set of test projections. The optimized SFA method outperformed the optimized standard method in terms of true positive zinger identification rate, false positive zinger identification rate, false negative zinger identification rate, the sum of squared differences of the filtered projections with the noise-free projections, and the sum of squared differences of the reconstruction volume from the filtered projection with the reconstruction volume from the noise free projections for all of the zinger densities analyzed. The optimized standard method, did however, result in filtered projections which, when analyzed in terms of relative difference from the noise-free projections, had a mean value nearer to zero and a smaller standard deviation, thought to be the result of a median filtering a large number of point-like high contrast features. Most importantly, the results of this work indicate that the new SFA algorithm enables more accurate reconstructions of an object from projections containing zinger noise than the standard zinger filtering approach which was explored.

Future studies may include the effect of realistic imaging noise in the simulated projections, simulated projections of other phantoms, a detailed analysis of the zinger noise-intensity distribution, the possibility of combining the standard method and the newly constructed temporal filtering method, and the effect of using angularly separated tomographic projections for zinger identification with the new temporal filtering algorithm.

CHAPTER 6

A VOLUMETRIC MICROSTRUCTURE ANALYSIS OF A NEAR-EUTECTIC 63SN-37PB SOLDER

6.1 INTRODUCTION

A key challenge in the application of lab-scale x-ray computed tomography to the study of metallic alloys is achieving sufficient feature contrast and resolution for the segmentation between solid phases of similar composition and density at spatial length scales suitable to microstructure quantification. In the microelectronic packaging, value exists in the nondestructive evaluation of solder system microstructures resulting from varying compositional and processing factors. A near-eutectic 63Sn-37Pb butt-joint on copper was studied with a custom lab-scale micro-resolved x-ray computed tomography (μXCT) scanner with the goal of quantifying three dimensional (3D) microstructural constituents resulting from a reproducible reflow process. The 3D character of lead-rich dendrites resulting from non-equilibrium solidification was revealed. The quantification of the dendrite microstructure was made possible through a combination of data acquisition, data processing, and data segmentation techniques. The scanning parameter selection, with respect to the characterization task, is discussed. Data acquisition and processing methods which were determined to be beneficial for 3D microstructure characterization are detailed. A beam-hardening artifact reduction algorithm is provided, without which, microstructure quantification would not have been possible. The segmentation of the dendrite features, performed using a semi-automatic 3D region

growth method, is described. The segmented solder volume enabled quantitative description of the 3D dendrite microstructure and void content.

Lab-scale x-ray computed microtomography (μXCT) has recently been used to non-destructively quantify three-dimensional (3D) microstructures in small-scale solder joints (Teramoto *et al.*, 2007, Dudek *et al.*, 2010, Jiang *et al.*, 2011, Li *et al.*, 2012). Due to the non-destructive nature, and the accessibility of lab-scale tools, time-resolved four-dimensional (4D) studies have been performed which offer insight to solder interconnect failure mechanisms involving pores, voiding, and cracking (Tian *et al.*, 2011, Padilla *et al.*, 2012, Xie *et al.*, 2014). A secondary solid phase, inherently present in most alloys, serves as another means of quantifying the progression of damage in solder interconnects at a microstructural level. Although 3D imaging of solder alloys wherein (at least) two distinct solid phases are resolved has been demonstrated using μXCT beamlines at synchrotron storage ring facilities (Tsuritani *et al.*, 2007, Yazzie *et al.*, 2012a, Maleki *et al.*, 2014, Bertheau *et al.*, 2014b), it is understood that this has not been accomplished using lab-scale μXCT systems. One study is acknowledged wherein 4D μXCT data was acquired in which both phases of the 63Sn-37Pb eutectic microstructure was resolved but, here also, imaging was performed at the synchrotron facility and not performed using a lab-scale tool (Tsuritani *et al.*, 2011).

Several studies have been identified which have characterized 3D dendrite structures resulting from solidification processes using synchrotron μXCT (Mathiesen and Arnberg, 2005, Terzi *et al.*, 2010, Wang *et al.*, 2011, Tolnai *et al.*, 2012, Wang *et al.*, 2012, Friedli

et al., 2013, Wang *et al.*, 2014) , most of which also include segmentation of the dendrite from the 3D volume for quantification, but have not focused on alloys relevant to microelectronic soldering. Synchrotron x-ray imaging has also been a means for studying dendrite formation using 'real time' 2D imaging in the study of both non-solder alloys (Bogno *et al.*, 2013) and even in the solder relevant Lead-Tin system (Zhu *et al.*, 2012). One study which experimentally segmented and quantified the 3D Sn-dendrite structures resulting from solidification of a 80Sn-20Pb solder during reflow has been identified (Kammer and Voorhees, 2006), but has used destructive sectioning techniques to arrive at the three dimensional data. The Sn-dendrite secondary and tertiary arm spacing resulting in Sn-Pb alloys of 15% Pb, 20% Pb, 25%bPb, and 30% Pb have been reported for different cooling rates (Sá *et al.*, 2004). The secondary Sn-dendrite arm spacing for directionally solidified Sn-Pb alloys of 5%Pb, 15%Pb, and 20% Pb has also been studied (Souza *et al.*, 2005). The secondary Sn-dendrite arm spacing of a Sn-Ag alloy was measured as a function of cooling rate (Garcia *et al.*, 2011), and has been measured for rapid solidification of a Sn-Ag-Cu alloy (Lin *et al.*, 2006). Of most interest to the current study is previous work that has been performed on the characterization of Pb-dendrites forming from solidification in Pb-Sn alloys and, in particular, for the eutectic composition. The present understanding is that studies on the formation of lead dendrites in the eutectic lead-tin alloy have been scarce. Furthermore, it is believed that the complete definition of the dendrite structures within an entire reflowed solder volume has not yet been made for 63Sn-37Pb, nor for any solder alloy, whether with synchrotron or lab-scale μXCT.

Thus, an objective of this work is to characterize the 3D structure of lead dendrites in a near-eutectic composition 67Sn-37Pb formed by non-equilibrium solidification after joint reflow by application of lab-scale µXCT. A significant focus of this study regards data processing determined necessary for segmenting the µXCT resolved second phase. First, a beam-hardening artifact reduction algorithm was constructed which was used to de-convolute the signal of the targeted features from a cupping artifact caused by a beam-hardening effect common to reconstruction volumes from lab-scale CT scanners. Beam-hardening artifacts are manifested in the reconstruction plane, and are specific to polychromatic x-ray imaging, enhanced by imaging of heavily attenuating specimens. The 'intensity cupping' effect is the resulting artifact addressed in this work. Several solutions for performing a correction of the cupping effect have previously been reported, some relying on knowledge of the x-ray spectra (Herman, 1979, de Paiva *et al.*, 1998, Vedula and Munshi, 2008, Imura *et al.*, 2012, Bisogni *et al.*, 2007, Krimmel *et al.*, 2005) or sample (de Paiva *et al.*, 1998, Jian and Hongnian, 2006), some are performed in the projection stage (Herman, 1979, de Paiva *et al.*, 1998, Vedula and Munshi, 2008, Krimmel *et al.*, 2005, Krumm *et al.*, 2008, Menvielle *et al.*, 2005) , some during reconstruction (Imura *et al.*, 2012, Remeysen and Swennen, 2006), and some post-reconstruction (Menvielle *et al.*, 2005, Porter *et al.*, 1991). In the current study, a simple algorithm requiring no knowledge of the x-spectra is provided in detail, and proven effective on a multi-component system. The algorithm is applied with no knowledge of sample composition or geometry. In both approaches, the beam-hardening cupping effect is treated in post-reconstruction, in the reconstruction planes. Currently, a step-by-step

solution is provided, wherein a coarse, all-encompassing, sample segmentation and a Euclidean distance map was incorporated.

This study also aims to resolve inherently present second phase particles within a well-known solder alloy using a sub-millimeter butt-joint test vehicle by the application of lab-scale µXCT. In so doing, this study aims to serve as a step toward the application of digital volume correlation (DVC) algorithms to 4D lab-scale data for the quantification of damage and plastic strain at length scales relevant to the microstructural constituents in soldering alloys. In other words, interrupted *in situ* tensile testing of the classic lead-tin eutectic solder system is planned, wherein any microstructural feature's three-dimensional position is tracked over time, and thus the primary quantification sought is a plastic strain locally within the test specimen. The solder investigated is a near eutectic 63Sn-37Pb alloy, and the microstructure studied is a result of reflow of a <500µm joint on copper. The focus, at present, is thus the 3D segmentation and quantification of a dispersed second phase. It will be shown that Pb-rich dendrites resulting from non-equilibrium cooling serve as an attractive candidate for 3D quantification, and potentially even displacement tracking in future 4D studies.

A full sample volume description of the three dimensional dendrite structure of a sub-500µm diameter 63Sn-37Pb solder volume is achieved by acquiring x-ray tomography projection data in a custom lab-scale µXCT scanner (Mertens *et al.*, 2014c, Mertens *et al.*, 2014a), applying new data processing routines , and performing image segmentation using a semi-automatic volume region grow technique. The segmented microstructure

has enabled 3D characterization of the solder microstructure, and opens the door for future microelectronic packaging studies involving local strain mapping in 4D datasets using particle displacement tracking algorithms.

6.2 MATERIALS AND METHODS

Eutectic Lead-Tin butt joints were fabricated using a silicon v-groove process for joint alignment. A groove was etched into a Silicon waver which served to support the joint before reflow. The procedure for fabricating the Silicon v-groove support by photolithography and KOH etching has been previously described elsewhere (Xie *et al.*, 2014) . Copper wires (5N purity, ESPI Metals), initially 508µm in diameter, were straightened using an MTS Tytron 250 microforce mechanical testing system, cut to approximately 8mm lengths, and then polished perpendicular to their length axis at one end with the final step being a 0.05µm colloidal silica solution. The straightening was a result of plastic elongation by loading until failure, and a reduction in cross sectional area thus also occurred, resulting in copper wires of approximately 410-420µm in diameter away from the failure zone. The processing steps for the copper wire ‘substrates’ suited for sub-millimeter butt-joint fabrication are outlined with the flowchart shown in *Figure 30.*

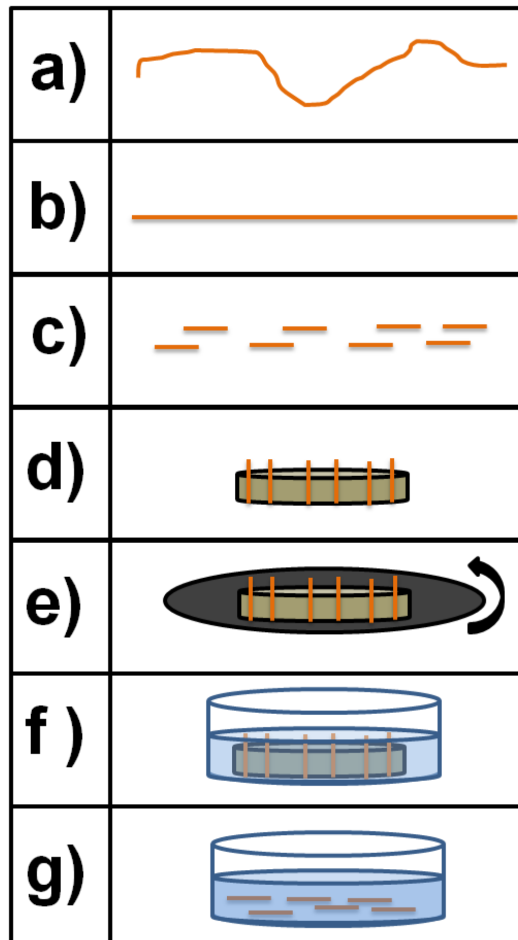

Figure 30. Processing Flow-Chart for the Preparation of Copper Wire 'Substrates' for Butt-Joint Fabrication *a*) Copper Wire (5N Purity, ESPI Metals) was Cut to Approximately 5cm Length *b*) The Copper Wire was Loaded in Tension with an MTS Tytron Microforce Testing System Until Failure and the Straightened Lengths were Removed *c*) The Straightened Wire Segments were Cut to Roughly Half of the Desired Butt-Joint Length *d*) The Straightened Segments were Super-Glued to Perpendicular Grooves Cut into an Epoxy Polishing Mount *e*) The Wires were Polished with a Final Step of 0.05μm Colloidal Silica *f*) The Epoxy-Wire Assembly was Placed in Epoxy to Free the Polished Wires *g*) The epoxy puck was Removed and the Wires were Cleaned Before Butt-Joint Fabrication

The polished ends of two wires were then coated with a rosin-mildly-activated (RMA) flux and placed facing one another within the Silicon V-groove but with a slight gap. A 63Sn-37Pb solder sphere (Indium Corp.) approximately 600μm in diameter was then similarly coated with flux and placed between the polished ends of the copper wire, also within the V-groove. The copper wires were then pushed gently towards one-another so as to contact the solder sphere firmly at both wires' polished surfaces. The silicon wafer, mounted to a copper plate, was then placed on programmable hot plate wherein a calibrated reflow profile was applied to the un-bonded solder assembly for the reflow of each joint. A thermocouple sensor was fixed to the solder end of one of the copper wires using Kapton tape to record the reflow profile for each joint. A schematic of the equipment and sample setup for reflow is provided in *Figure 31*.

The reflow process consisted of heating to an elevated temperature of 120°C for a 120s soak for flux activation, followed by a heating to 20°C above the solder melting point (T_m=183°C) where a 40s soak was performed, followed by cooling the joint and entire assembly in open air. A 1°C/s cooling rate was established. The reflow and cooling temperature profile is provided in *Figure 32* for a representative 63Sn-37Pb butt-joint on Cu using this process.

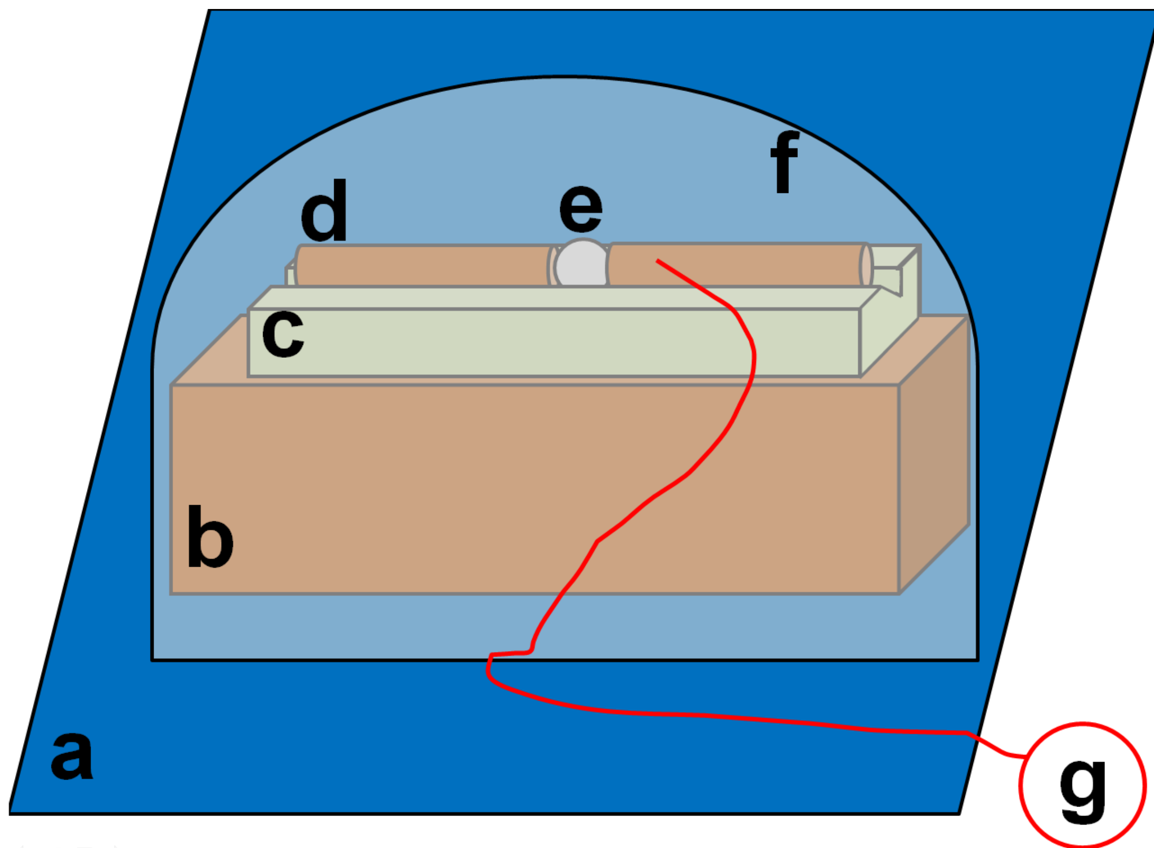

Figure 31. Schematic of Reflow Assembly Used for Sub-Millimeter Butt-Joint Fabrication *a*) Programmable Hotplate *b*) Copper Block *c*) Silicon with V-Grooves of Varying Depth *d*) Polished Copper Wires *e*) Solder Preform *f*) Aluminum Foil Convection Barrier *g*) Thermocouple, Signal Conditioner, and Data Acquisition PC

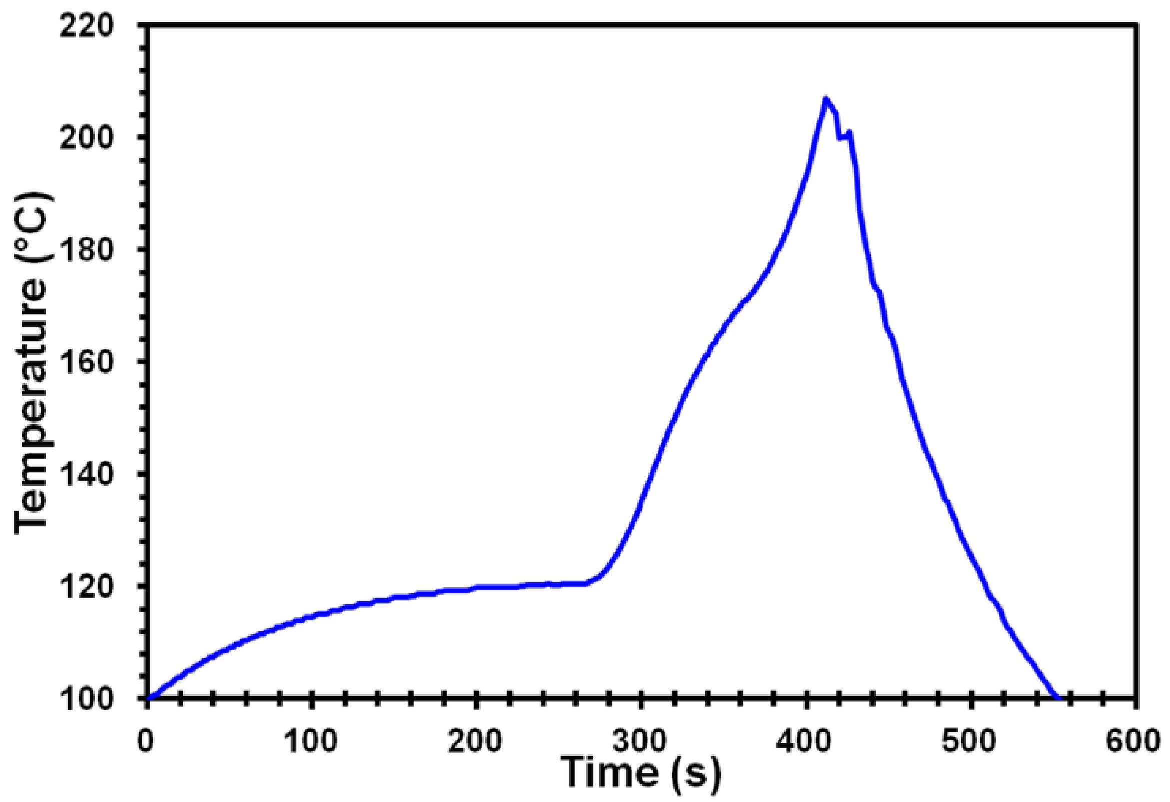

Figure 32. Reflow Profile for the 410µm Eutectic Pb-Sn Joint Used for XCT Imaging and Surface Microscopy

The established cooling rate (1°C/s) was determined to yield ideal microstructures for μXCT imaging, that is, a relatively large and well dispersed second phase possessing some x-ray attenuation contrast with that of the surrounding medium. After reflow, the solder joints were then removed from the v-groove and either mounted within slow-set epoxy for polishing and surface (optical) microscopy or mounted within the μXCT scanner for 3D x-ray imaging. *Figure 33* contains an optical micrograph of a eutectic Pb-Sn solder joint fabricated using this process. The temperature profile during the reflow and cooling process for the sample shown in *Figure 33* was nearly identical to that shown in *Figure 32*, but was not used for XCT imaging as it was mounted for polishing and surface microscopy. Lead dendrites of over 50μm in length in a fine eutectic matrix were observed using optical imaging in joints fabricated with this method, and were the targeted microstructural features in joints imaged using μXCT.

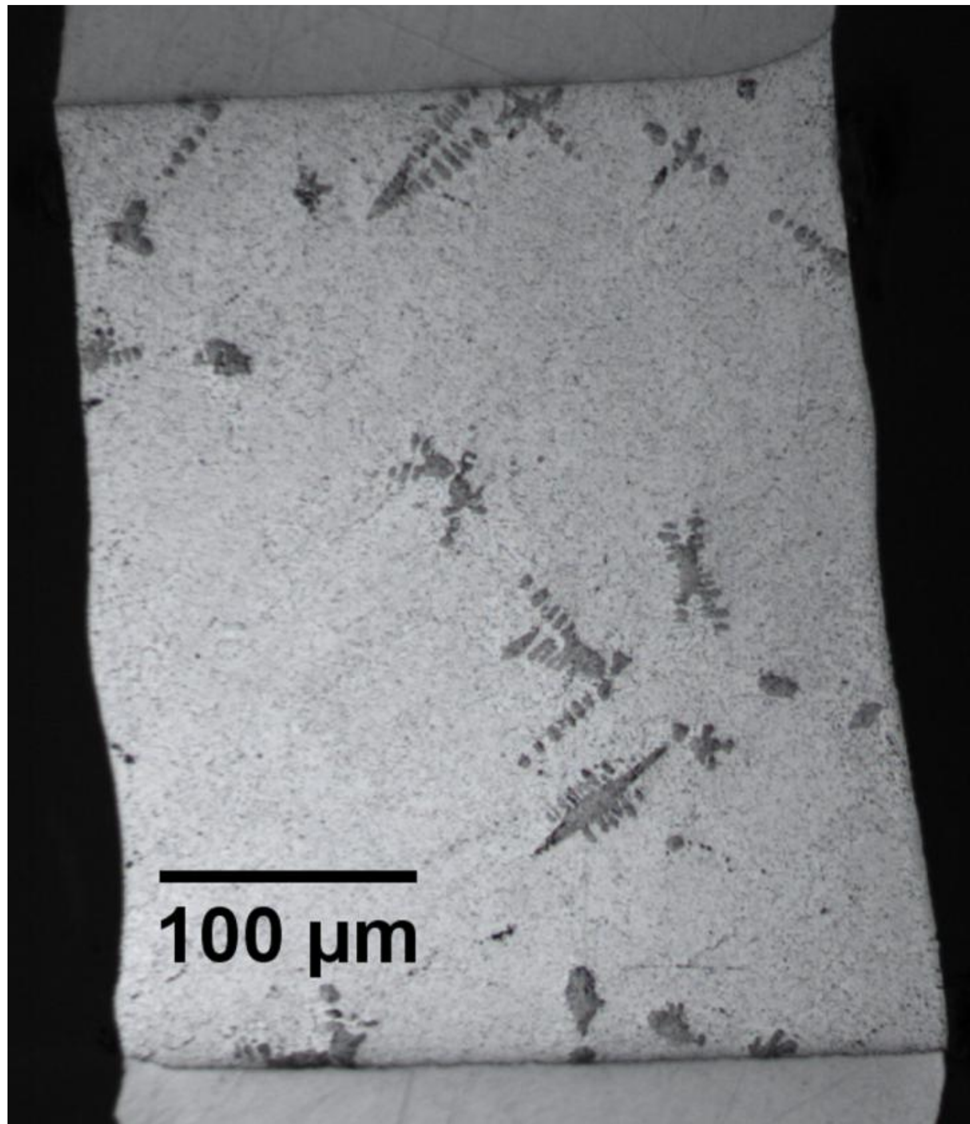

Figure 33. Optical Bright Field Micrograph of a Near-Eutectic Pb-Sn Butt-Joint Reflowed onto a Roughly 410μm Diameter Copper Wire with a Cooling Rate of Approximately 1°C/s where the Medium Toned Phases at the Top and Bottom of the Image are the Copper Wire Contacts of the Joint, the Light Phase is the Sn-Rich/Eutectic Phase of the Solder, and the Dark Phases are the Pb-Rich Phases (Primarily Dendrites) of the Solder

Dendrites are known to form as a result of heterogeneous nucleation during solidification and as a result of solidification in off-eutectic alloys (Kammer and Voorhees, 2006, Sá *et al.*, 2004, Souza *et al.*, 2005). The formation of dendrites in a two-phase eutectic system is interesting because eutectic microstructures are expected at equilibrium, and the dendrite formation can occur from the higher melting temperature component in a two phase system (Porter *et al.*, 1991). In the case of eutectic Pb-Sn, lead is the component with the higher melting temperature, and was thus expected to form dendrites in non-equilibrium solidification. As dendrites are typically single crystals, knowledge of lead's crystal structure can be used to predict the structure its dendrites. Lead is a cubic crystal solid at STP, and is thus known to grow dendrite arms along the ‹1 0 0› direction (Porter *et al.*, 1991). The cubic ‹1 0 0› pole figure is provided in *Figure 34* along with a schematic of the primary, secondary, and tertiary arm positions in the dendrite structure which possesses the symmetry of its cubic crystal structure.

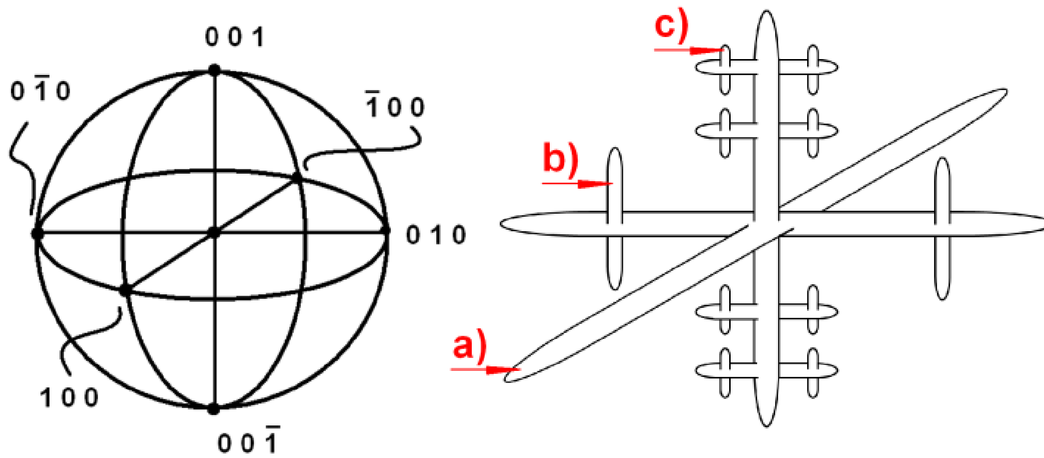

Figure 34. The [100] Pole Figure for Cubic Crystals and a Graphical Representation of Dendrite Growth Along the [100] Directions for Cubic Crystals Showing *a*) Primary Arms *b*) Secondary Arms, and *c*) Tertiary Arms of the Dendrite

X-ray microtomography was conducted on a custom-built system developed at Arizona State University. Details of the development and instrumentation for the system have been provided previously (Mertens *et al.*, 2014c, Mertens *et al.*, 2014a). To summarize, a microfocus x-ray tube (X-RAY WorX GmbH, Dresden, Germany) was used to emit x-rays through a solder joint seated on a precision rotation stage (Nelson Air Corp., CO USA) before being converted to visible light by an optical light scintillating crystal (Crytur, spols r.o., Turnov, Czech Republic), which was then detected by a CCD camera (Apogee Imaging Systems, CA USA) by means of a lens-mirror tandem. In the custom µXCT scanner a 2048^2 pixel CCD was used. Yet, for the heavily attenuating Pb-Sn samples, pixel binning (the grouping of multiple sensor elements into a single digital sensor) was found to be most beneficial in the optimization between resolution and feature signal during data acquisition. Filling the field of view using 2048 pixel resolution on a roughly 500µm wide sample had set the spatial sampling at roughly 0.25µm. However, operating the x-ray source at the low power condition required to meet this resolution was signal deprived for this sample. To achieve the required signal through the lead-tin specimen, but keeping in mind the spatial resolution required to capture the dendrite features, the scan was conducted with 2-by-2 pixel binning at a voxel size of 0.56µm. With the x-ray source operating at 140 kV and 140µm of target current (19.6W) on a bulk reflection-type tungsten target for reasonable signal level, the resolution was limited by the x-ray source. For the reduction of the beam-hardening effect, and to minimize low energy x-ray sensor saturation, a steel filter was used as a pre-hardening filter with a thickness of 0.70mm. The total magnification of the µXCT microscope was achieved using a lens magnification of approximately 4x and an x-ray magnification of

approximately 13.5x. The x-ray magnification was achieved with an x-ray-spot-to-sample distance of 125.106mm and an x-ray-spot-to-detector distance of 9.306mm. The phosphor used in this study was a 50μm thick LuAG:Ce (Lutetium Aluminum Garnet, Cerium doped) single crystal scintillator. Due to a relatively low incident x-ray flux from the x-ray source in microfocus mode, the heavily attenuating nature of the specimen, the large x-ray-to-detector distance, and a thinner-than-optimal scintillating crystal, very long exposures were acquired at each orientation: The total exposure time per unique sample position was 150s. A thicker (~250μm) LuAG:Ce scintillator which offered roughly a threefold gain in signal rate with no observed loss in resolution was unfortunately not available for this scan due to system maintenance. Ultimately, >3,000 counts were acquired through the thickest part of the specimen for each orientation. For the same region of the detector without the sample in place, approximately 10,000 counts were measured, indicating a maximum of roughly 70% x-ray attenuation by the sample. The x-ray scan was conducted over a 180° scan range using 1/4° steps, resulting in 721 orientations. The 721 projections were processed for noise reduction as is later detailed before being input to a cone-beam (Feldkamp-Davis-Kress, 'FDK') filtered back projection (FBP) algorithm using a Shepp-Logan filter to reconstruct the sample microstructure.

6.3 RESULTS AND DISCUSSION

After several post-reconstruction processing steps, the grayscale reconstruction appears as is shown for a reconstruction-plane in *Figure 35*. For a clear description of the reconstruction volume, *Figure 36.a* shows an orthogonal plane of the same reconstruction

where the copper contacts were also present, and *Figure 36.b* contain**s** a volume histogram labeled according to the visible phases in *Figure 36.a*. It is worth noting the overlap between the lead-rich phases and the surrounding solder in terms of gray-value, which can pose a challenge for volume segmentation relying on intensity values alone.

In working with 3D datasets, data is often represented using a 2D section of the dataset at a time. In taking such 2D sections of the 3D XCT volume of the lead-tin solder joint, there were observable similarities with identically processed samples imaged using 2D techniques. The Figure, *Figure 37.a***,** offers an optical micrograph of one sample mounted for optical microscopy (OM) compared against three 2D images from the 3D XCT dataset in *Figure 37.b*. Circled in solid blue in each image mode are instances where the secondary arms of a dendrite were coming out of the plane of the image, giving rise to an 'island chain' appearance. Circled in dashed red in both imaging modes are instances where the secondary arms were in the plane of the image and coinciding with a primary dendrite arm, giving rise to a 'rib cage' appearance. Qualitatively, this comparison increased confidence in the results of the μXCT reconstruction where similarities with optical imaging results were confirmed.

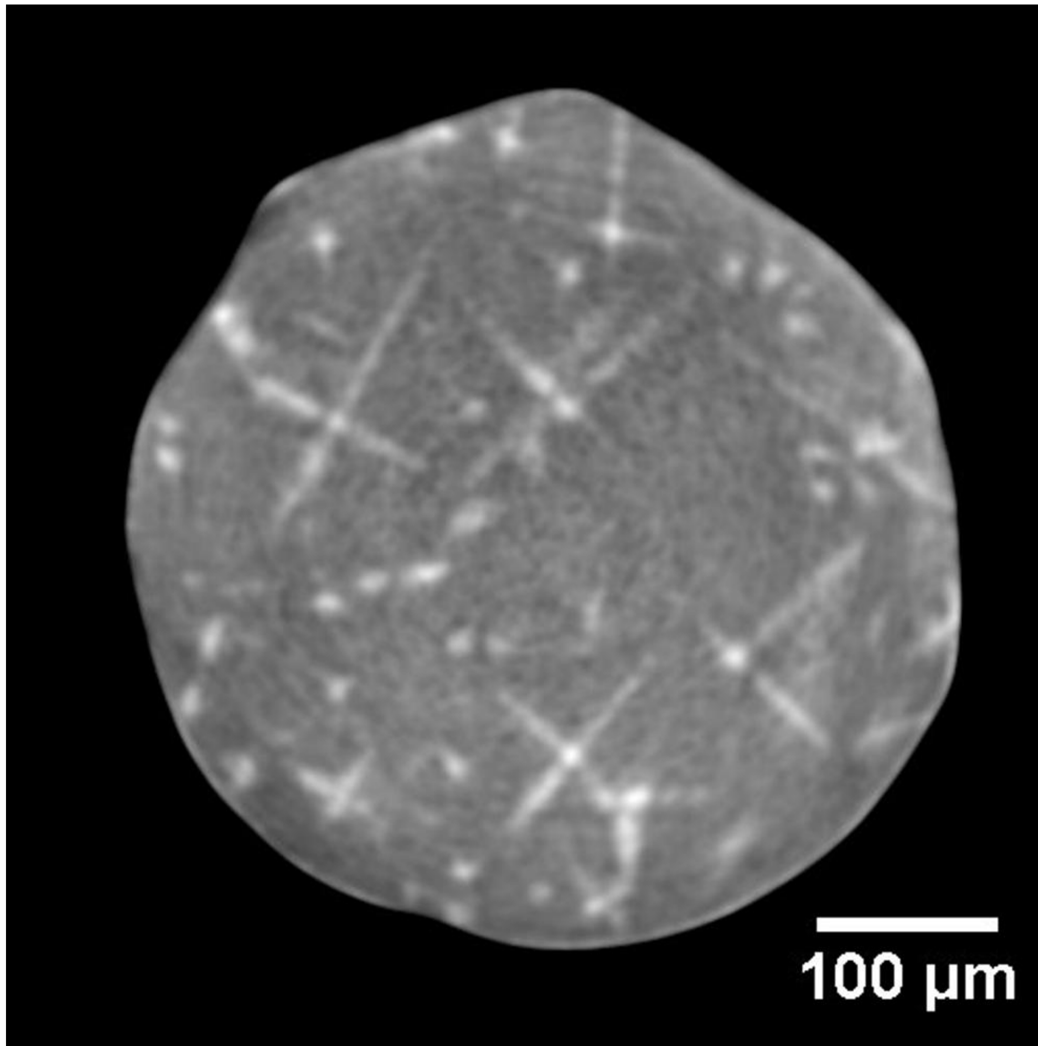

Figure 35. A Sample Cross Section (Reconstruction Plane Prior to Segmentation) of the Eutectic Pb-Sn Solder Joint Reconstruction Acquired via µXCT wherein the Light Phases are More Heavily Attenuating, the Black Phase is Air Surrounding the Sample, the Semicircular Blob is the Solder Itself wherein the Medium-Gray Phase is the Unresolved Eutectic Phase and the White Phases are Lead-Rich

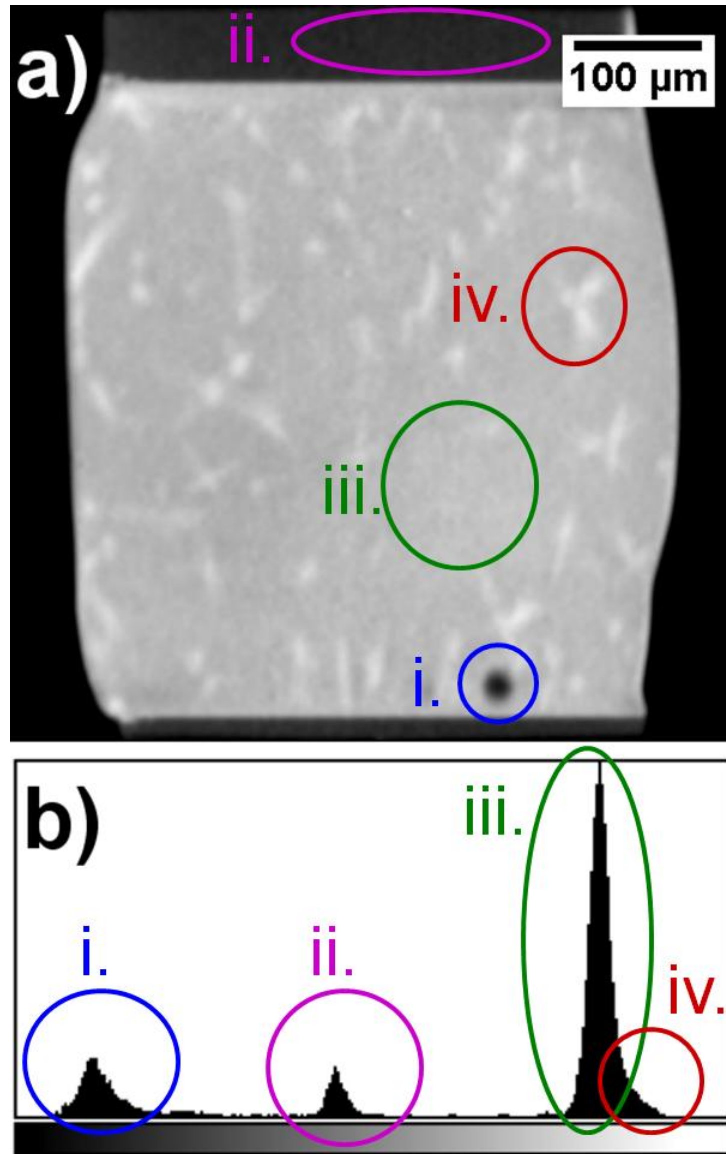

Figure 36. a) A Sample Cross Section of the Eutectic Pb-Sn Solder Joint Reconstruction Acquired via µXCT where the Vertical Direction is Parallel to the Rotation Axis, and Various Visible Phases are Labeled *b*) Volume Histogram of the Reconstruction Portraying Grayvalue Clustering of (i.) The Least Attenuating Phase, the Air/Voids (ii.) The Copper Phase (iii.) The Eutectic Phase and (iv.) The Most Attenuating, Lead-Rich Phase

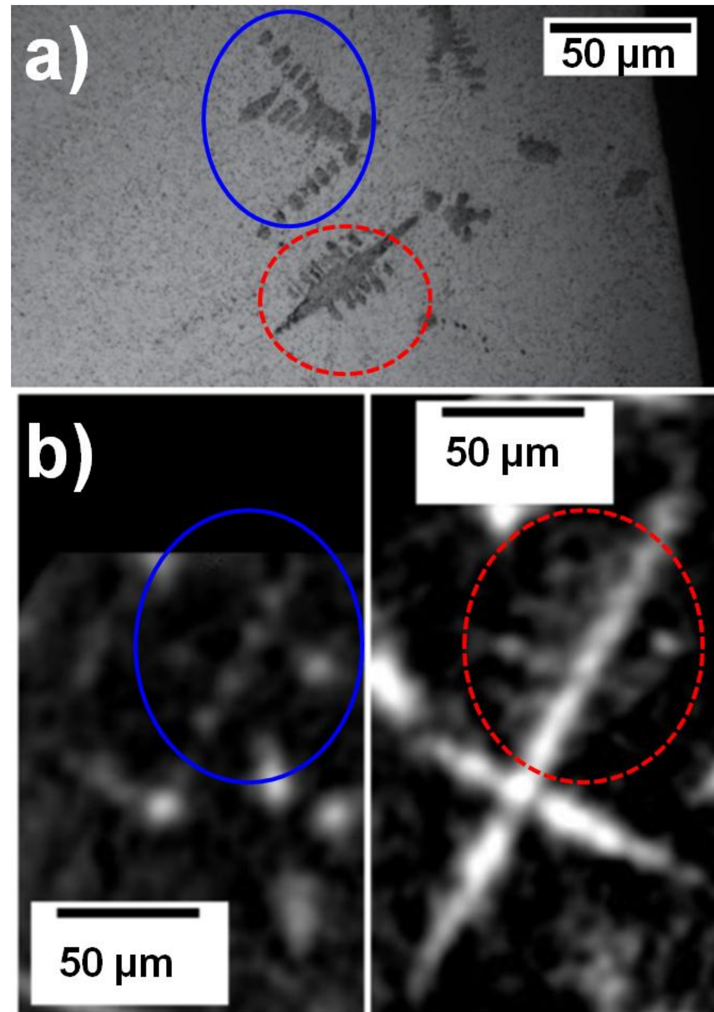

Figure 37. Comparison of Pb-Sn Microstructural Features Resolved in X-Ray CT and Optical Microscopy *a*) Optical Micrograph of a Eutectic Pb-Sn Solder Joint Showing Pb-Dendrites as Dark Phases *b*) 2D Sections of a Reconstructed 3D XCT Volume Showing Pb-Dendrites as Light Phases where Circled in Blue (Solid) for Both Imaging Modes are Cases where Secondary Arms are Nearly Perpendicular with the Plane of the Image Section, Giving Rise to an 'Island Chain' Appearance and Circled in Red (Dashed) for Both Imaging Modes are Cases where the Secondary Arms of the Pb-Dendrites are in the Plane of the Image and Coinciding with the Primary Arms of the Dendrite

Although the micrograph in *Figure 35* possesses all the desired image characteristics (contrast, resolution, noise level) for characterizing lead dendrite population's structure in three dimensions, it was found that the projection data acquisition and calibration approach, the projection processing, the reconstruction algorithm, and the post-reconstruction volume processing all were critical steps for arriving at this data. The following data processing steps were followed for achieving a segmented dataset of the low-contrast Pb-rich features from the solder volume's reconstruction. In general, some of the noise reduction steps taken may not be necessary depending on the particular scan conditions and sample characteristics. The first six steps dealt with improving the quality of the projections, and the last six steps regarded processing the reconstruction for volume analysis, and more specifically, for dendrite quantification. Due to the high degree of pixel processing that was performed, the first step was acquisition of the projection images in a higher format than necessary to preserve precision after downsizing the data to the true resolution. That is, the spatial resolution expected from the pixel size was set to be finer than necessarily expected possessed by the x-ray source for the conditions used in the scan. Projections for each orientation were acquired twice and averaged in an algorithm which corrects for the presence of zingers, while simultaneously performing the same treatment for reference images and performing the CCD image calibration. The projections were then corrected for any variation in the background intensity using air-normalization. The projections were then corrected for defects in the detector CCD, lens, and scintillator. Before reconstruction, the projections were aligned with one another in events where x-ray source beam refocusing was performed causing a slight shift in the projection data. The reconstruction was then

performed using a cone-beam FDK FBP algorithm on the entire volume after the rotation axis (RA) definition was optimized by tweaking the RA definition and evaluating the result on reconstruction images for the fan-beam plane of the sample only. As the resolution of the x-ray source was expected to be several micrometers at best given the relatively high target power, and the acquired pixel size was 0.56μm, the data was then downsized by volume binning in order to reduce the noise level without affecting the resolution of the data. The binning of 2^3 voxels to a single voxel resulted in an eighth of the data size and a doubling of the voxel size to roughly a 1.12μm edge length. A beam-hardening correction was then also performed, which will be further detailed. Smoothing the volume with a three dimensional Gaussian blurring kernel has also proven beneficial for feature segmentation. For the smoothing, a 3x3x3 kernel size was used.

6.4 BEAM HARDENING ARTIFACT REDUCTION

In order to segment dendritic features from the tomography volume, removing the beam-hardening artifact was critical. The basic observation of a beam-hardening cupping artifact is that an otherwise homogeneous object in the reconstruction image plane is perceived to have a brighter (more heavily attenuating) periphery, as shown in the upper portion of *Figure 38*. Beam-hardening arises due to energetically non-uniform attenuation of a polychromatic x-ray beam by an object, as contained in a radiographic projection. The effect is caused by a disproportionately high attenuation of lower energy x-rays relative to the total number of probing x-rays. As the polychromatic spectrum as a whole traverses some thickness of the sample, the low energy x-rays are effectively filtered by the sample, causing the beam to become higher in energy on average or

‘harder’ (lower portion of *Figure 38*). Hence after the polychromatic beam has passed through some unit thickness of the sample and is to some extent hardened, a lesser number of x-rays are attenuated through the next unit thickness. Effort can be taken to ‘pre-harden’ the beam by using a filter which the beam traverses prior to the sample, such as a so-called ‘half-value-layer’, but the artifact can still persist.

A method for beam hardening artifact reduction, post reconstruction, was constructed by Arizona State University research scientist Dr. Jason Williams, which has proven effective for cylinder-like specimens. Although the method has not been tested on samples with highly non-circular cross-section, the correction is expected to be less effective. The basic concept behind the developed algorithm, *Algorithm 3*, was that within the reconstruction plane image, for all reconstruction planes in the 3D stack, pixels at the periphery of the object which were exhibiting a cupping artifact affected intensity were scaled down relative to the intensity value at the center of the sample. This scaling was proportional to the pixel’s distance from the center, which was calculated using a Euclidean distance map (EDM). By thresholding the values corresponding to the sample, and filling the holes in the selection, a binary image was obtained for which an EDM was calculated. The original grayscale reconstructed image stack was then scaled down for each reconstruction image plane, using each reconstruction image plane’s EDM, yielding an image essentially free of the beam-hardening artifact originally observed. This process is shown visually in *Figure 38*. The algorithm was observed less effective on highly non-circular cross sections, through attempts to minimize beam hardening cupping in heavily attenuating specimens with rectangular cross section. The algorithm was not constructed

for minimizing beam-hardening occurring locally at sub-regions within the sample, for example in metal particles dispersed within a relatively lightly attenuating medium. Both short-comings can be attributed to the mechanism implemented by the algorithm for flattening the cupping artifact: The algorithm leverages large neighborhoods of pixels with similar values in the EDM for each slice for scaling attenuation values. The former can be attributed to counting statistics at the edge of the sample, where the number of pixels with a similar EDM value is lessened. Edge effects were observed to be minimal in cylindrical type specimens, whereas undesirable edge scaling is expected to increase in samples with non-circular cross sections. For instance, the corners of a square object are scaled based on values relatively deep into the sample based on the 'minimum pixel' criteria set by the user. The latter issue arises due to an assumption of global cupping. For example, local cupping artifacts at metallic spheres in a low density matrix would have to be individually treated with the algorithm by creating a EDM for each particle. It has, however, proven effective in a heterogeneous structure with roughly circular cross section wherein the primary beam-hardening is occurring globally, as will be demonstrated for a 63Sn-37Pb alloy.

Algorithm 3

Beam Hardening Correction

The algorithm takes a base volume within the reconstruction plane near the center of rotation to scale all values relative to, and uses the values of the EDM to perform the scaling from the center outward, for each reconstruction plane contained in the 3D reconstruction stack. The mean value for all pixels with a specific EDM value is

calculated, and all pixels in this group in the original reconstruction plane are scaled proportional to the group's calculated mean intensity relative to the mean intensity of a central base region. *PixelCount* is the number of pixels scaled with each iteration, corresponding to the number of pixels with a particular value within the thresholded region, determined using the histogram of the EDM. *DataBHC* is the corrected 3D reconstruction volume. As common with many instances of image processing, all multiplication and division of the image matrices in this work refer to the element-wise operation. To convey concepts, descriptive functions are used to the right of the equality, with the argument in parenthesis following the descriptive function. Italic face text is used to represent variables, typically arrays, which assume values before arriving at the corrected data. Matrix indexing, logical operators, and 'for' and 'while' loops are represented with syntax similar to that of MATLAB, as it is relatively intuitive.

Data = The reconstructed 3D volume

DataBHC = An array to contain corrected data

ThreshLevel= The value which selects phases containing sample with beam-hardening;

MinPixels=area of the 'ring' to be used in EDM scaling;

BaseSize = edge length of cube in

BasePixels = pixels representing 3D cube of size '*BaseSize'* at center of reconstructed sample volume

BaseValue = sum(*BasePixels*)

for *j* = 1:NumberOfReconstructionPlanes

```
  DataSlice = Data(: , : , j);
  DataThresh = Threshold(DataSlice, ThreshLevel);
  DataThreshfilled = FillHoles(DataThresh);
  DataEDMslice = BlkWhtEDM(DataThreshfilled);
  ScaleValues = Zeros(size(DataSlice));
  EDMmax = Max(DataEDMslice(:));
  EDMhist =…
  …Sum(Histogram(DataEDMslice,0:1:EDMmax),2);
  EDMhist=EDMhist(2:end);
    DataMean=0;
    i = EDMmax;
         while i >= 1
         i_end=i;
         PixelCount=EDMhisti);
         while PixelCount < MinPixels  & i_end>1
         i_end = i_end-1;
         PixelCount = PixelCount + EDMhist(i_end);
         end
         DataMask=
(DataEDMslice <= i) & (DataEDMslice >= i_end);
ScaleValues = ScaleValues + … …DataMask.*(Median(Nonzeros(DataMask.*…
…DataSlice)) - BaseValue);
             i = i_end - 1;
```

```
    end
DataBHC(: , : , j) = Data (: , : , j) - ScaleValues;
end
```

The results of the developed beam-hardening algorithm in application to the segmentation of the lead dendrites in the eutectic lead-tin μXCT solder reconstruction data can be visualized in *Figure 39*. Prior to the application of the beam-hardening correction algorithm, the ‘brightness’ of the lead rich dendrites was globally convoluted by the apparent ‘brightness’ caused by the beam-hardening effect (*Figure 39.a*). After the application of the beam-hardening algorithm, it was seen that the signal from the dendrites in the cross sections have been de-convoluted from the cupping effect (*Figure 39.b*). Thus, the application of the beam-hardening algorithm provided has facilitated the segmentation and thus quantification of the 3D lead dendrite structures.

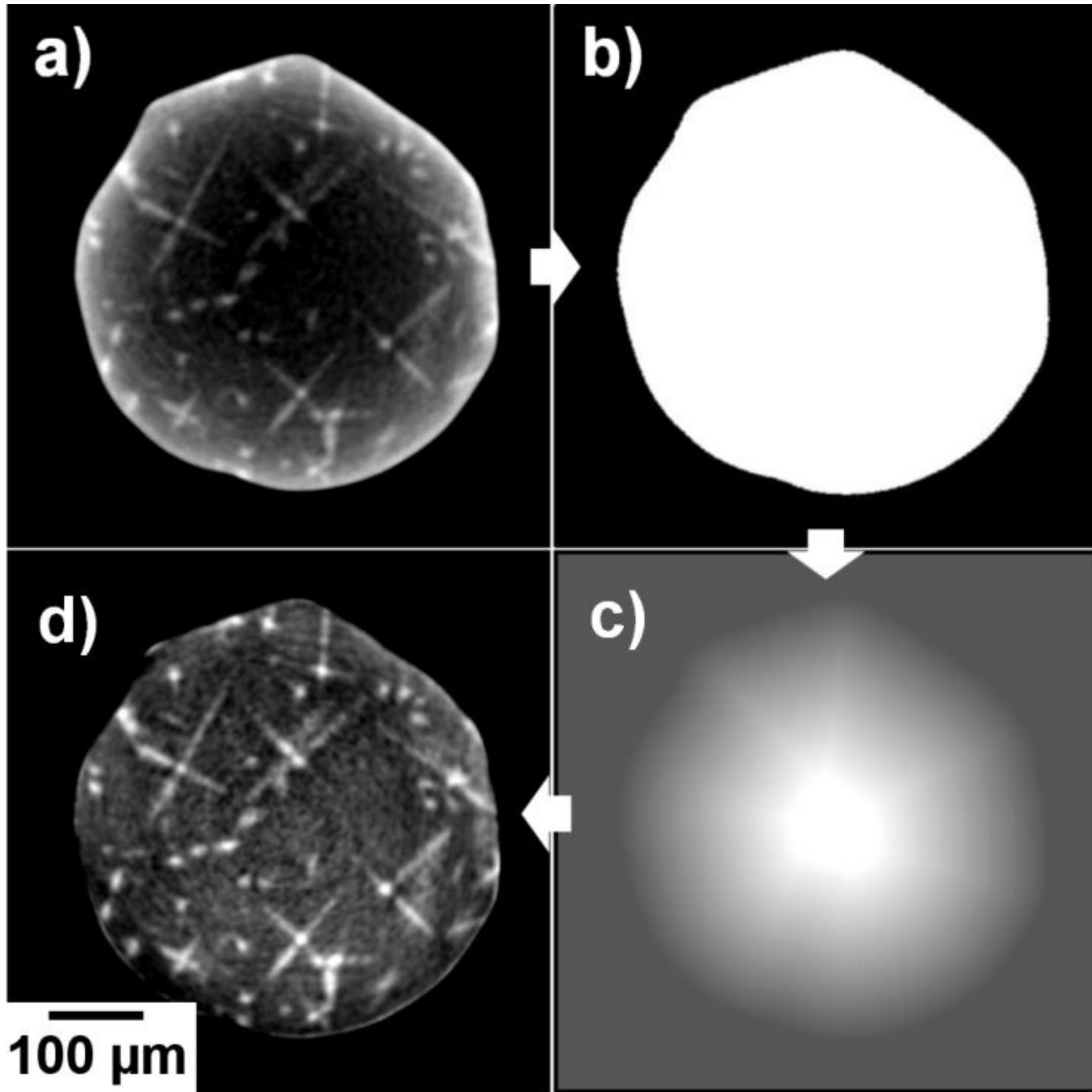

Figure 38. Beam-Hardening Cupping Reduction in a μXCT Reconstruction Plane *a*) Exhibiting a Beam-Hardening Intensity Cupping Artifact *b*) A Segmented Image of the Beam-Hardening Aaffected Phase Used for EDM Calculation *c*) EDM Calculated from *Figure 38.b*, and *d*) The Beam-Hardening Aartifact Corrected Plane Using *Algorithm 3*

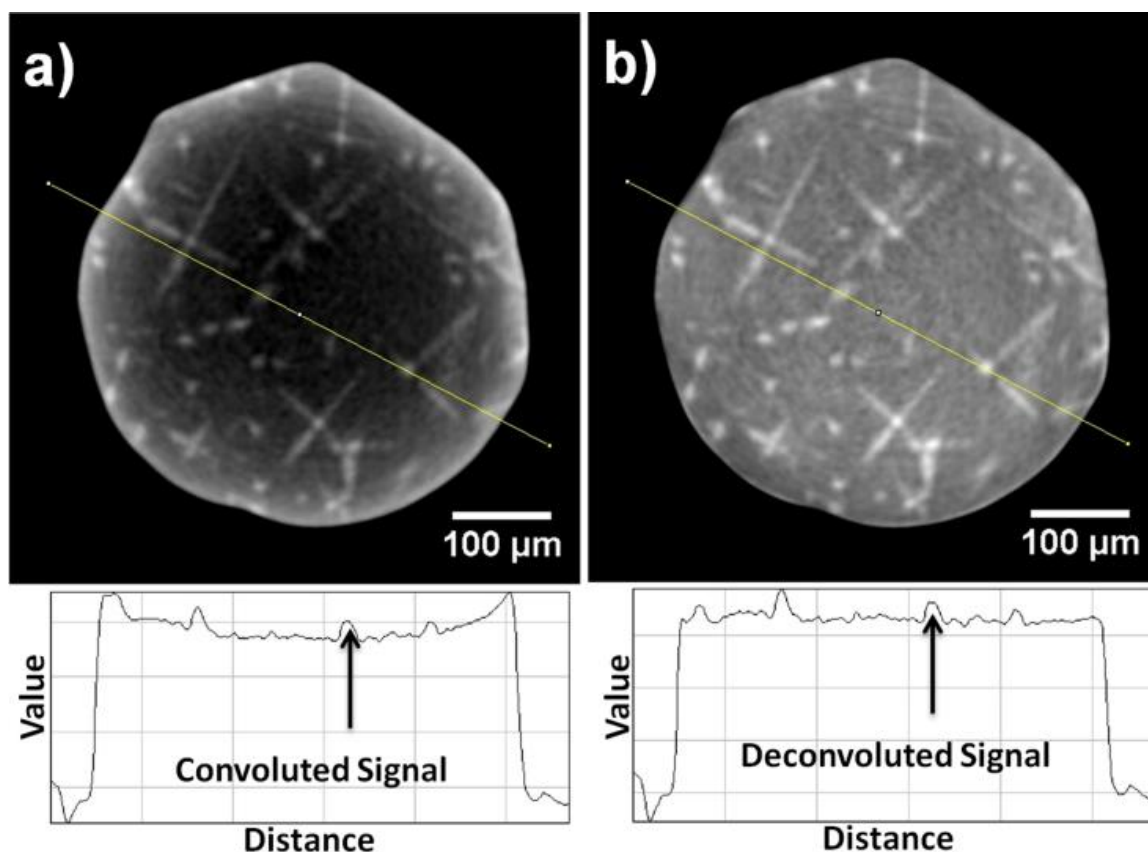

Figure 39. A Line Profile Across the Same μXCT Reconstruction Plane in *Figure 35*, but with *a*) The Original Reconstruction and *b*) The Beam-Hardening Corrected Reconstruction, where the Profile for the Line Shown is Portrayed Below Each Image

6.5 3D QUANTIFICATION OF LEAD-FREE DENDRITE STRUCTURES

Even after the beam-hardening artifact reduction, automatic segmentation techniques such as edge detection and global thresholding failed to accurately capture all the features than were apparently of the dendrite according to human inspection, as the gray-values of the finer features were still convoluted with the surrounding eutectic microstructure of the solder, which of course also contains a lead rich phase. Threshold, edge detection, and watershed based segmentation methods were attempted unsuccessfully due to what was determined to be insufficient contrast of the features of interest and reasonably high noise throughout the reconstruction volume. Thus, semi-automatic techniques for image segmentation were applied wherein manual intervention guided the segmentation locally at each feature. It was determined that a 3D region grow was suitable when applied from the center of each dendrite feature. As the lead dendrites were the features with the highest gray-value, selecting the dendrite's hub and allowing the selection to include connected pixels within a range of values from the maximum value of the datas*et al.*l the way to lower and lower values was found to grow the selection out into the surrounding dendrite. The lower limit of the region selection range was reduced until a limit value was selected which was so low that the selection expanded to include what were apparently separate dendrites or regions of the unresolved eutectic phase, indicating an overshoot of the optimal lower limit for the selection of single dendrite. The lower limit was accordingly increased until only an obviously interconnected feature was selected. In this way, the 3D region grow could be guided to segment the dendrite structures of the entire three dimensional μXCT dataset. This process is portrayed in *Figure 40*, wherein Figure progression corresponds to the reduction of the lower limit in the region growth selection.

Figure 40.a shows the selection limited to the highest values of the dataset, *Figure 40.d* shows the optimal selection and *Figure 40.e* shows the selected region when the lower limit of the selection has caused the selection to bleed out into the surrounding features of the dataset. The result of the limit selection process on a sample dendrite is shown in both two-dimensional grayscale data overlay and three-dimensional rendering of the selection in the upper and lower halves of *Figure 40*, respectively. It can be seen in the top half of *Figure 40.e* that even though only two of four visible secondary arms on the top side of the upper right primary arms have been captured in the segmentation, a surrounding dendrite had been included, and that the 3D region growth passed a threshold value which selected just a single (real) particle. In the selection shown in *Figure 40.d* it can be seen that only two of the four visible secondary arms were captured in the segmentation due to low feature contrast, but that these were adjacent arms because of a smooth intensity arc across the secondary arms collectively. The other resolved phases' high contrast made them well suited for segmentation by global threshold. All segmentation was performed using Avizo Fire, which proved to be extremely useful for the 3D region growth method (Magic Wand tool).

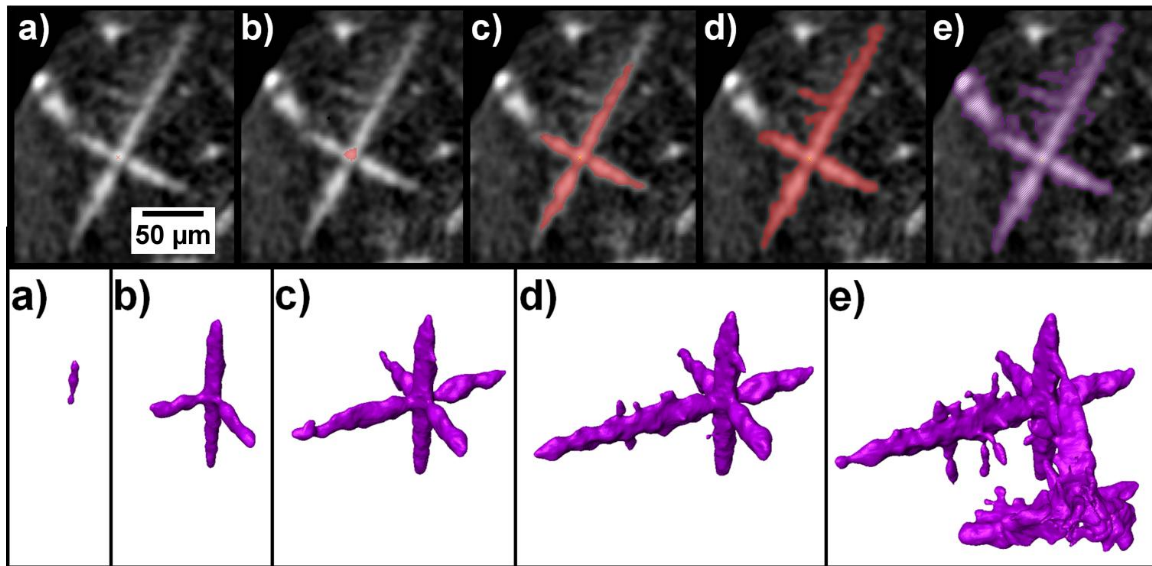

Figure 40. Demonstration of the 3D Region Growth Segmentation of a Single Lead-Rich Dendrite from the µXCT Dataset in 2D (Top) and 3D (Bottom) Representation, where the Dataset Has Been Scaled to a Minimum Value Corresponding to '0' and a Maximum Value of the Dataset Set to '1000' where the Selection Has Been Seeded at what was Perceived by the User to be the Hub of the Dendrite's Primary Arms and the Selection was Allowed to Include Connected Pixels with Values within a Range where the Maximum Value was 1000 and the Minimum Value was *a*) 800, *b*) 750, *c*) 740, *d*) 735, and *e*) 734, and finally, where the Poor Result of '*e*' Resulted in the Growth Stop at Condition '*d*'

The segmentation of four distinct phases was performed, being the copper, contained void, lead-rich and eutectic phases. After segmentation, the specimen could then be analyzed in terms of its 3D microstructure, and 3D quantification was performed. *Figure 41* contains a 3D rendering of the segmented dataset showing all four resolved phases. The dendrites are shown in green, interfacial voids in red, the unresolved Sn-rich eutectic phase as transparent gray, and the copper as dark opaque. Within the segmented volume the prevalence of the lead dendrites was overwhelming and omnipresent, showing no apparent clustering or preference for location or orientation within the joint. The dendrite features can be more easily visualized with the rendering presented in the right half of *Figure 42*, where all other phases are made transparent and the color coding is used to notate a single connected dendrite particle.

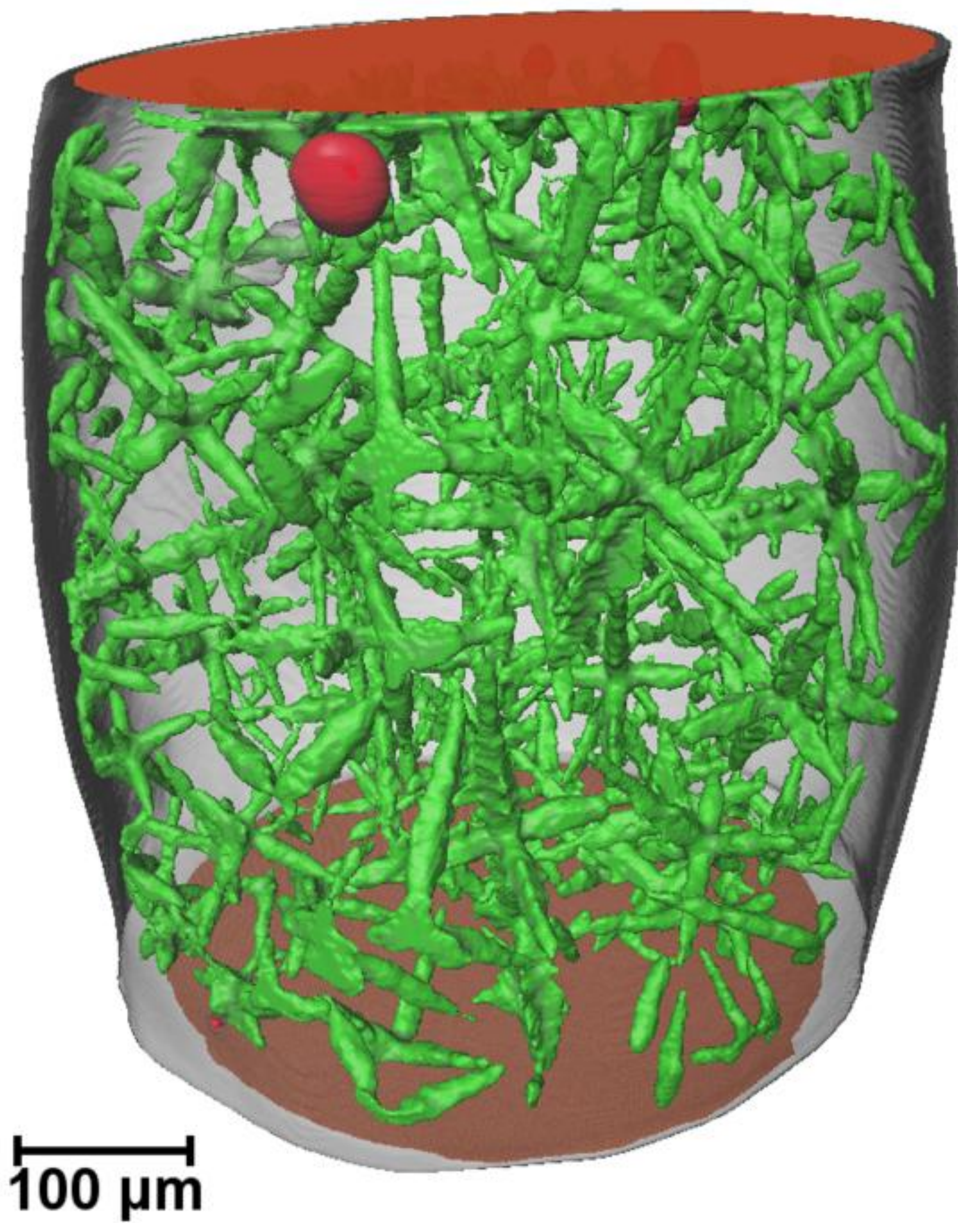

Figure 41. Segmented Microstructure of the Eutectic Pb-Sn Solder Joint Imaged Using µXCT, where the Green Phases Correspond to the Lead Rich Dendrites, the Transparent Phase Corresponds to the Tin Rich Eutectic, the Red Phases Correspond to Contained Voids, and the Copper Interface is Shown as Opaque at the Top and Bottom of the Volume

Figure 42. The Segmented Microstructure of the Eutectic Pb-Sn Solder Joint Using µXCT with Only Dendrite Features Shown and Connected Regions are Rendered in a Single Tone

The segmented microstructure allows for the independent and complete three-dimensional quantification of the resolved phases within the data volume. The data was conducive to the analysis of the solder as a whole, the interfacial or contained voiding, and even the lead dendrites that have formed during solidification. A brief analysis of the void volume and area content in the solder is provided in *Table 8*. Six total voids were resolved within the joint, five at one solder-copper interface and one void at the other. Four pores which were clustered at one interface are visualized in *Figure 43*, where a small fifth void is not visible. It was found that the void volume content was less than %0.1, however that the clustering of the voids resulted in a maximum measured pore area fraction of 1.58% which was more than one order of magnitude higher. The clustering of voids has obvious stress concentration implication in electrical or mechanical loading. Measurements were made on the equivalent diameter of the pores and are summarized in *Table 9*. The voids in this specimen were all less than 45μm, and were about half of this value on average.

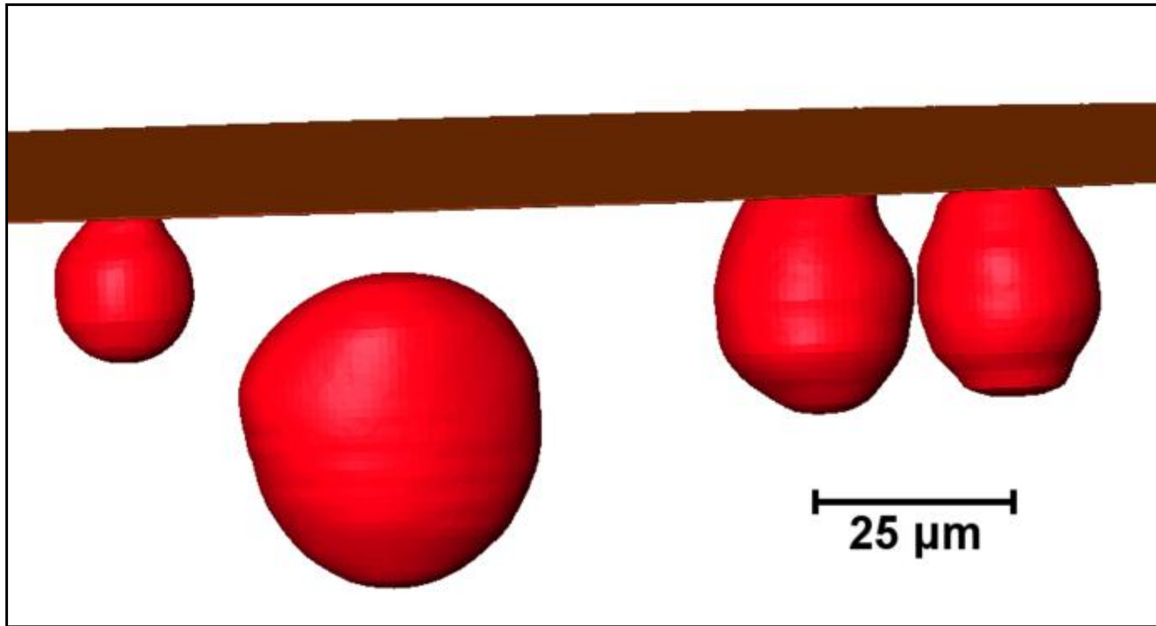

Figure 43. Voids Formed as a Result of the Flux Reactive Process During Solder Reflow with Voids Shown as Red (Light) Near the Copper Interface Shown as Brown (Dark) in the Segmented Data Volume

Table 8

Global Phase Analysis from the 3D Segmentation of Interfacial Pores and Lead Dendrites Formed as a Result of the Solder Reflow Process

Item	Measured Value
Pb-rich Dendrite Volume Fraction	3.60%
Porosity Volume Fraction	0.07%
Maximum Pore Area Fraction	1.58%

Table 9

Individual Particle Analysis from the 3D Segmentation of Interfacial Pores and Lead Dendrites Formed as a Result of the Solder Reflow Process

Measure	Sample Size	Mean	Min	Max	Standard Deviation
Secondary Dendrite Arm Spacing (μm)	21	17.0	12.3	22.6	2.82
Maximum Dendrite Length (μm)	207	88.5	13.5	222	41.8
Dendrite Primary Aspect Ratio	207	2.60	1.42	5.82	1.05
Pore Diameter (μm)	6	23.0	11.5	37.4	10.1

The dendrite features themselves were also characterized in terms of their three dimensional structure. In the solder joint, 207 distinct and separate dendrites were captured. The dendrite volume was measured less than 4%, and is detailed in *Table 8*. Analysis was also performed on the individual dendrites and their features, measurements of which are summarized in *Table 9*. Although visible in *Figure 41* and *Figure 42*, a higher magnification view of several of the largest dendrites is offered in *Figure 44*. The overall volume fraction of the dendrites in the solid phase was measured to be 3.6%. The average maximum dimension of the each dendrite feature was measured to be 89µm, and the largest dendrite was 222µm in length. A type of aspect ratio for the dendrites was measured, taking the ratio as the maximum 3D particle length over the maximum particle width orthogonal to the length direction. In other words, a bounding ellipsoid of the dendrites has on average an aspect ratio of approximately 2-to-1.

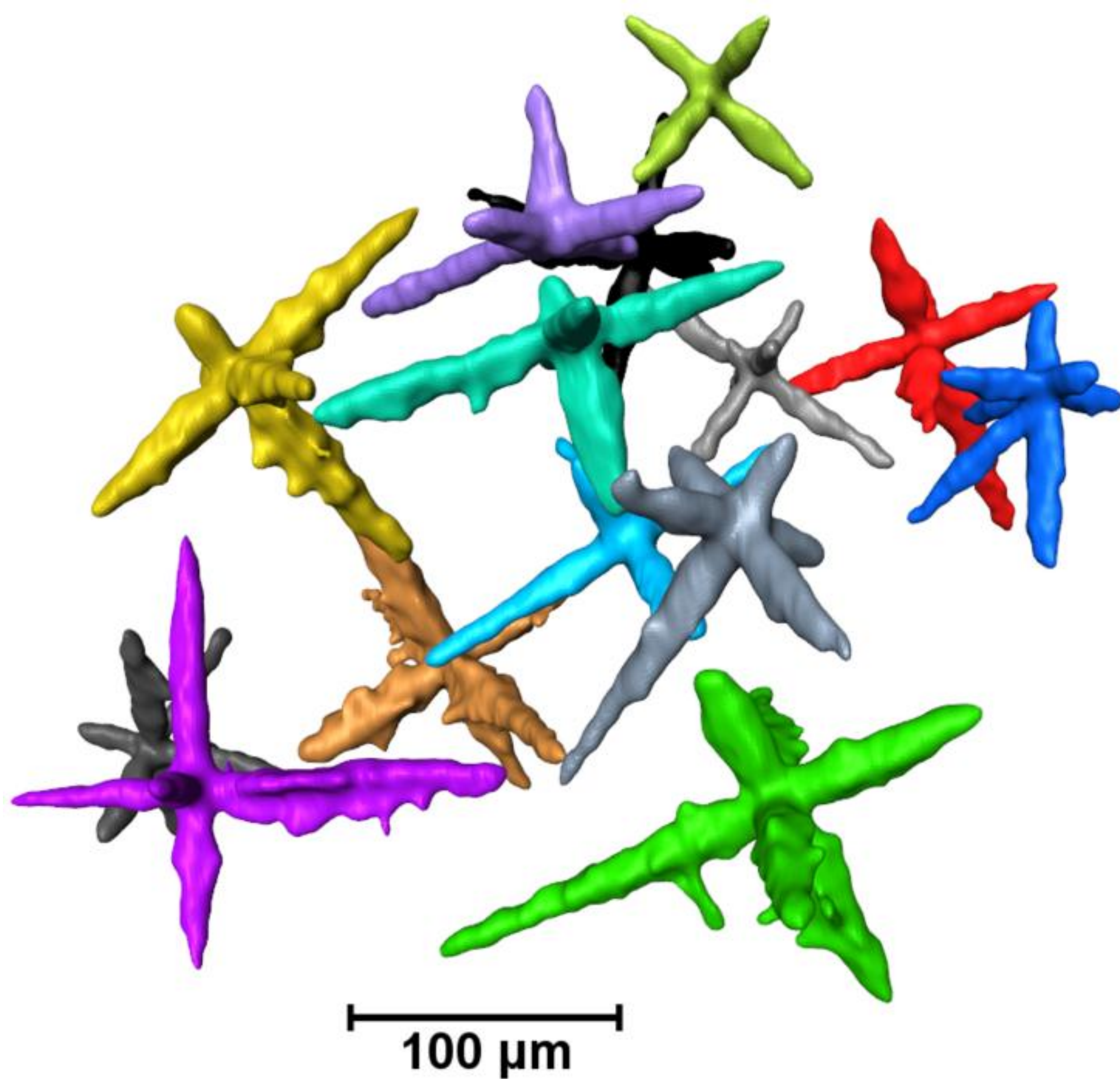

Figure 44. Selected Neighboring Dendrites from the Segmented Population Rendered in Separate Colors for Distinction

In most of the dendrites contained within the reconstruction, the provided segmentation technique has resulted in the complete inclusion of primary dendrite arms which were apparent in the gray scale reconstruction volume. For the secondary arms for individual dendrites, however, the regions included with the described segmentation technique have resulted in protruding nodules at the base of the primary arm at best, visible in *Figure 44*. On inspection of the gray scale volume, it can be seen that the contrast and resolution of the raw data prohibits the segmentation of these fine features, as demonstrated in *Figure 40*. It was believed that the length of the tertiary arms protruding from the secondary arms was greatest near the axis of the secondary arm, and for this reason, a contrast difference was observed enabling segmentation of the base of the secondary arms.

Two approaches have been adopted to measure the separation distance of the lead dendrites secondary arms resulting from a 1°C/s cooling rate using µXCT data. As the secondary arms were not easily captured by semi-automatic segmentation approached attempted, the first technique for measuring the arm spacing analyzed the grayscale data of the dendrite features. Necessarily, a two-dimensional image of the grayscale volume was taken such that two of the primary arms of one of the larger dendrites in the sample were parallel with the image plane, as shown in *Figure 45.a*. Although surface imaging techniques allow for similar 2D measurements with superior image quality, the surface being imaged is not as easily manipulated to be coincident with two of the three primary dendrite arms in order to measure the secondary arm spacing accurately. A line intensity profile was taken across the secondary arms of the dendrite in the location indicated by the red line in *Figure 45.a*. The intensity profile itself is provided in *Figure 45.b*. The

intensity plot confirms what was observed by human observation, which was the presence four heavily attenuating masses protruding from the primary dendrite arms, believed to be secondary arms. The signal from the four lead-rich arms was detected as the four peaks in *Figure 45.b*, and the spatial separation of the peaks was used to measure the secondary arm spacing. With this approach, the spacing was measured to be 16μm.

The second approach used to measure the secondary arm spacing was to use the segmented data, which was more practically suited to structural measurements. As noted, the secondary arms were not satisfactorily captured in the segmented dendrite structures, but in the larger of the dendrites present nodule protrusions can be seen as an effect of the secondary arms. As demonstrated in *Figure 40*, the captured nodules have been confirmed to be typically adjacent secondary arms, implying a measurement of the nodule spacing would be direct measurement of the secondary dendrite arm spacing. Five of the largest segmented dendrite features were used for measuring arm spacing, renderings of three of these are provided in *Figure 46*. This approach produced 21 spacing measurements. The average secondary arm spacing was measured to be 17.0μm, with a standard deviation of 2.8μm. These measurements are summarized in *Table 9*. In the case of the secondary arm spacing measurement, the sample size stated in *Table 9* refers to the number of measurements, which were spread across 5 dendrites, whereas for the other measurements the sample size refers to the number of particles.

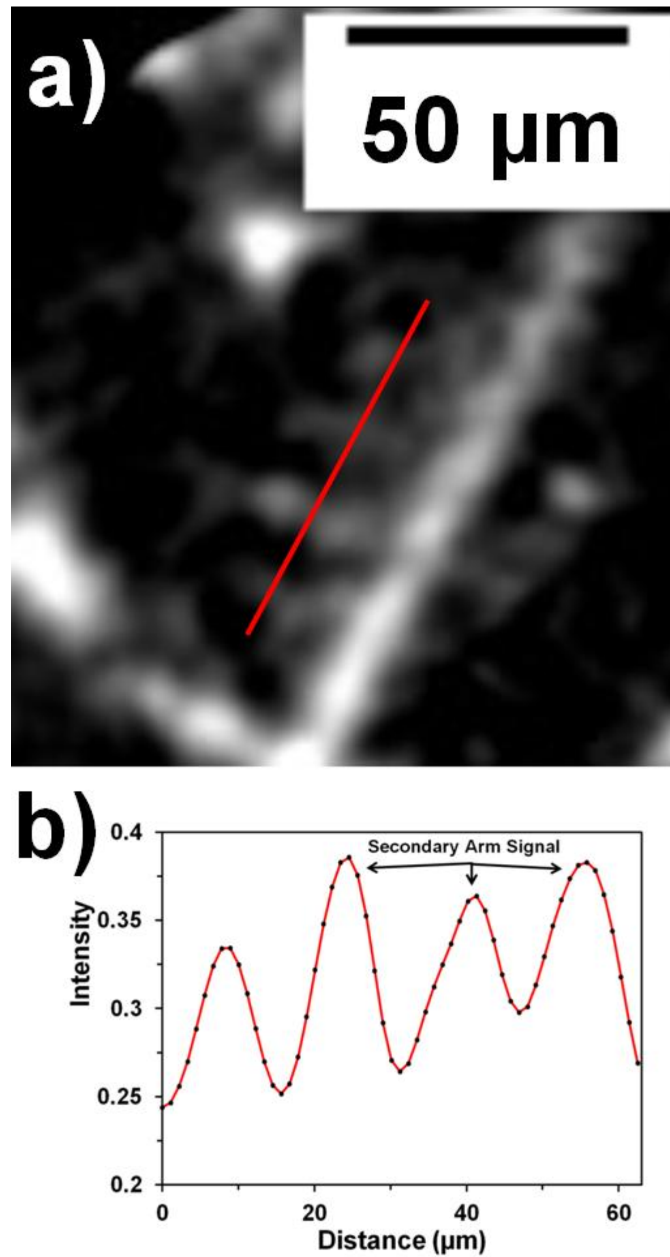

Figure 45. Measurement of Secondary Dendrite Arms Spacing from Grayscale Data *a*) A 2D Cross Section of the 3D µXCT Reconstruction Volume containing a Lead Dendrite Feature with Pronounced Secondary Arm Features for which an Intensity Profile was Taken as Indicated by the Solid Line *b*) The Average Secondary Arm Spacing of this Dendrite was Measured to be 16µm Using the Intensity Profile

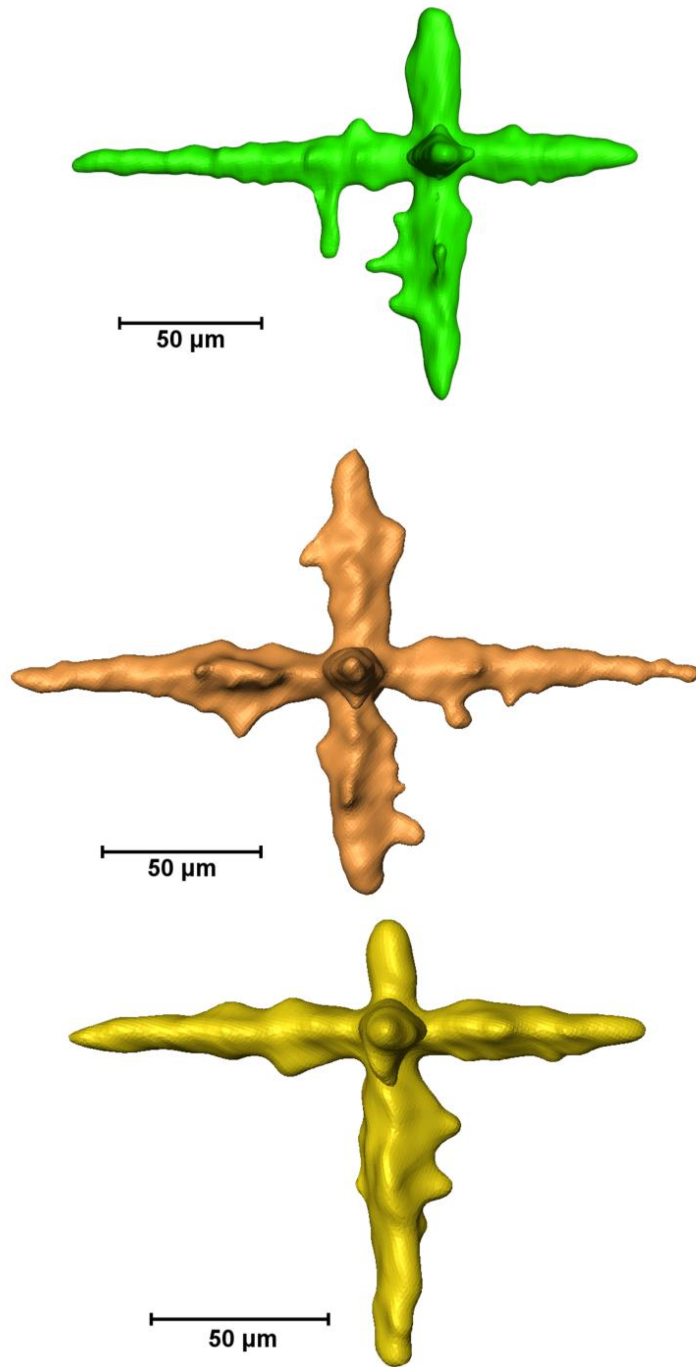

Figure 46. Segmented Renderings from Lab-Scale µXCT Showing Three of the Lead Dendrites which had Distinct Nodules from the Base of the Secondary Arms Enabling Secondary Arm Spacing Measurement

Several other observations were made of the dendrite structure via the segmented μXCT data. Based on the cubic structure of lead, and what has been by and large observed in tomography, lead dendrites were expected to grow primary arms along the six ‹100› directions. However, in rare cases, the dendrites have been observed to form with seven apparent primary arms, as demonstrated for a representative segmented dendrite exhibiting this structure in *Figure 47.a*. Although it would be challenging to say for certain without any crystallographic analysis, the seventh arm of the dendrite shown in *Figure 47.a* appears to be growing equidistant from the main primary arms, along a ‹111› direction relative to the other arms. Whether this was the result of a grain boundary at the base of the seventh arm and a preference for growth away from the main primary arms, or indeed dendrite growth on a ‹111› crystal axis, is uncertain.

Other instances of atypical primary arm structures have been observed for dendrites. In *Figure 47.b*, two separate dendrites are shown which have formed adjacent to one another in the solder volume. Apart from being very close to one another, the primary arm directions were also more or less targeted toward one another. The primary arms which were observed to be growing toward the neighboring dendrite are much shorter in length than the other primary arms. It was believed that these crystals had impeding one another's growth. Whether this obstruction was caused by their very presence or due to a mutual consumption of lead species from the near-eutectic melt was unknown.

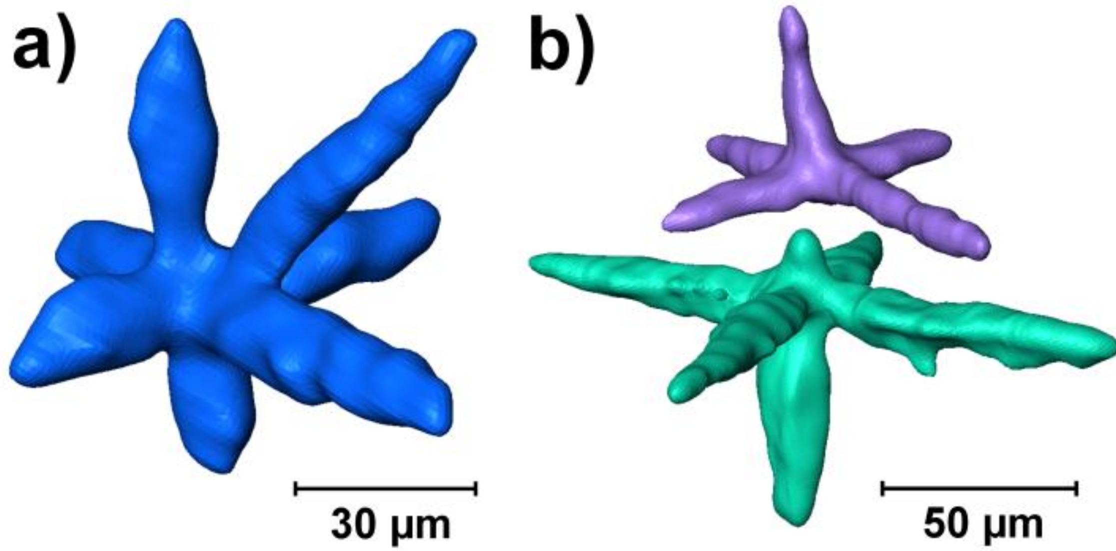

Figure 47. Abnormally Structured Segmented Dendrites *a*) A Lead Dendrite which is Observed to Possess an Anomalous Seventh Primary Arm in Nearly the “[1 1 1]” Type of Direction *b*) Segmented Dendrites which have Formed in Near Proximity to One-Another and have Apparently Mutually Impeded the Growth of Primary Arms

It has also been observed that dendrites forming at the solder surface of the copper interface generally have less than four dendrite arms. This was expected as the dendrites had nucleated at a surface and were thus restricted to roughly one half of the ‹100› growth directions along which they might grow. A collection of segmented dendrites which have apparently nucleated at the copper interface are provided in *Figure 48*, where structures with one, two, and three primary arms can be observed. In *Figure 48*, the dendrites have less than six arms due to surface nucleation whereas for *Figure 47.b* the arm reduction was attributed to growth interference.

Lab-scale μXCT has shown that heterogeneous solidification processes even in eutectic alloys can result in microstructures which contain a high dendrite density, nearly 4% of the solder volume, and well dispersed. Three dimensional quantification of the dendrite population has shown that the dendrites in the studied specimen were typically greater than 20% of the joint's diameter in length and in rare cases more than 50%. Although the dendrites did form along three orthogonal directions, it was observed that one of these directions typically dominated by more than a factor of two according to statistical analysis. In the five lead dendrites that were probed throughout the eutectic Pb-Sn solder volume, the secondary arm spacing was relatively constant, measured to be 15-20μm at a ~1°C/s solidification cooling rate. Interaction between the dendrite particles during growth was suggested by neighboring structures.

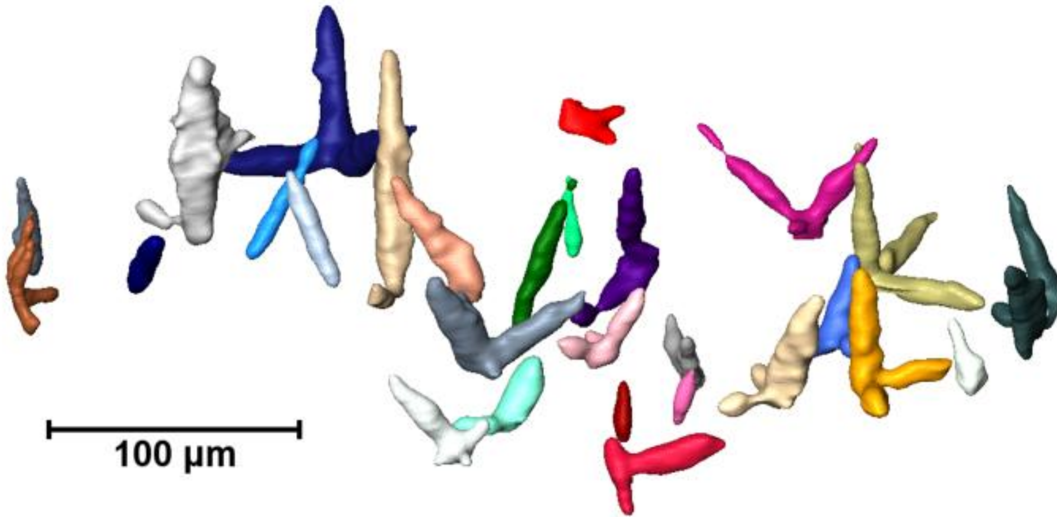

Figure 48. Segmented Dendrites which have Formed at the Copper Substrate Interface and Possessing at Most Three Primary Arms due to the Dendrite Hub Nucleating Heterogeneously at the Interface (similarly observed for dendrites forming at the solder surface)

6.6 ACQUISITION OF 4D 63SN-37PB RESPONSE TO TENSILE STRESS

The three dimensional features of a eutectic 63Sn-37Pb solder joint as segmented via μXCT data volumes have been provided. These features, present throughout the solder joint, might serve as an attractive means for tracking 3D strain field evolution under stimulus. Digital Volume Correlation, or DVC, is a semi-automatic technique which essentially determines the 3D strain field within a volume in comparison to a similar reference volume (Smith *et al.*, 2002, Smith *et al.*, 2002, Smith *et al.*, 2002, Smith *et al.*, 2002, Smith *et al.*, 2002). However, this technique typically requires high contrast, point-like, well dispersed features. The 63Sn-37Pb joint, discussed in the previous section, was removed from the x-ray imager and loaded within a pneumatic microforce tester (MTS Tytron), wherein a load was applied to the sample until strain of approximately +10% was induced. Following tensile straining, the specimen was introduced to the μXCT microscope and again subjected to a CT scan under the same imaging conditions, yielding an as-processed reference sample volume and a deformed sample volume.

For visualization of the strain induced on the sample, and the subsequent evolution of the microstructural features captured in the CT imaging, *Figure 49* is provided. Here, a cross section with the vertical direction parallel to the rotation axis is provided before and after deformation, where the vertical direction also corresponds to the loading axis of the solder joint. In *Figure 49.a,* a cross section is shown for the as-processed sample, prior to application of a plastic strain. *Figure 49.b* offers cross section through the same plane of sample, although after the application of the strain. The orange color at the bottom of the image is the copper bar contact masked off for visual clarity. It is worth noting the

relative displacement between the visible lead dendrites, as well as the shape and size change associated with the interfacial pores. The tomography volumes for this system may therefore be conducive to volumetric strain quantification via feature tracking.

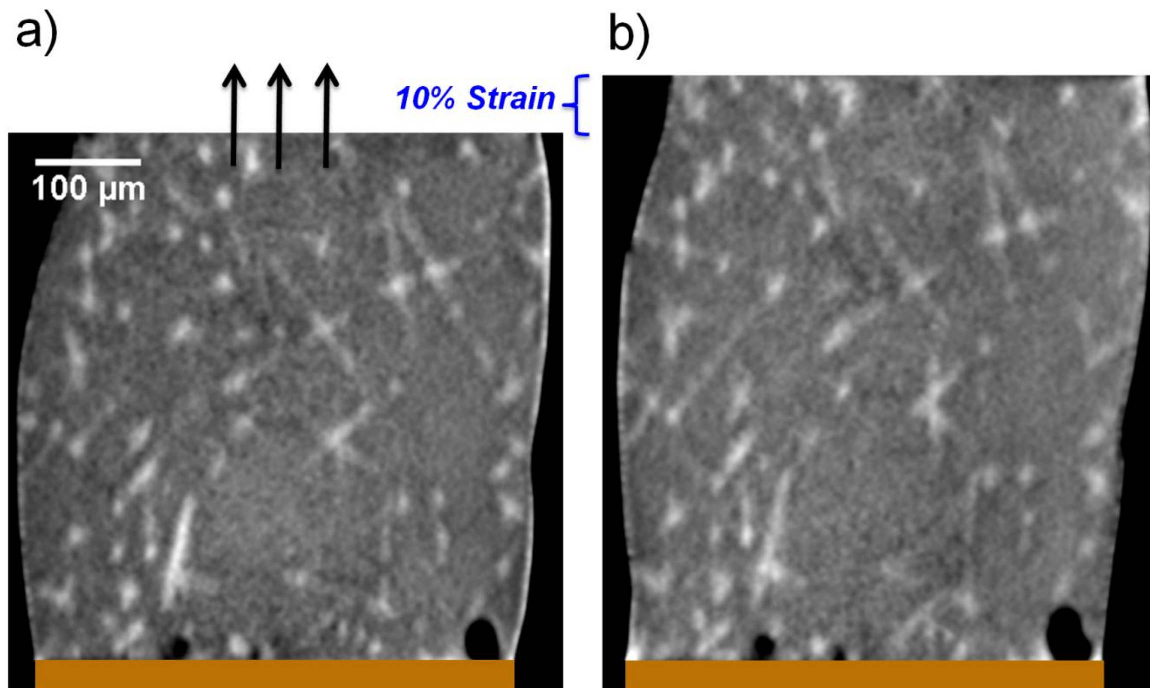

Figure 49. Qualitative Strain Response of a 63Sn-37Pb Solder Joint in a Tomography Section through the Grayscale CT Volume in Both the *a*) Un-Deformed Specimen and *b*) The Specimen after a Tensile Strain was Applied

6.7 SUMMARY

A three dimensional structural characterization of the lead dendrite phase in a <500μm diameter 63Sn-37Pb solder has been provided in the form of a segmented attenuation contrast reconstruction volume, accomplished through application of lab-scale μXCT microscopy. The eutectic Pb-Sn solder system was chosen for 3D x-ray attenuation imaging based on expectations of high feature contrast regarding lead-rich phases dispersed in a tin-rich eutectic matrix. The solder joint fabrication approach and processing parameters were selected based on experimentally determined reproducible microstructure, specifically regarding the size and spacing of lead-rich dendrites. The μXCT x-ray scan parameters were established based on signal requirements for the technique in conjunction with the heavily attenuating nature of the solder system, but with the counter-influencing requirements for spatial resolution considered. A beam-hardening cupping artifact reduction algorithm was constructed to enable segmentation of low-contrast microstructural features and has been provided in full detail. A semi-automatic 3D region grown was used for segmenting the Pb-dendrites from the surrounding eutectic microstructure and has been described. The segmented solder joint microstructure volume has enabled quantification of lead dendrite particles and reflow porosity contained in the solder joint. Within the joint, 207 Pb-dendrites were segmented with an average maximum dimension of roughly 90μm. The dendrites on average had a maximum width of almost half of their maximum length. All considered, the dendrite volume content in the solder joint was measured to be almost 4%. Both approaches for measuring the lead dendrite secondary arm spacing via tomography data were consistent, and was determined to be 16μm -17μm. The observed 3D structure of the dendrites

indicates that the dendrites interact with one another and can affect each other's structure. The number of primary dendrite arms per dendrite was observed to depend on location. Heterogeneously nucleated voids, seen at the solder surface or copper substrate, had three or less primary arms from their nucleus. Dendrites nucleated within the solder volume were typically observed to have 6 primary arms extending from their nucleus. In rare cases, anomalous seventh arms were observed, possibly grown along a ‹111› crystal direction. The symmetry of the dendrites observed in the segmented volume matched the symmetry of the expected ‹100› system for a cubic crystal such as lead. Only 6 total voids were observed in the joint as a result of flux reactive processes during joint fabrication, although 5 of the 6 were observed localized in one cross section of the butt-joint at one of the substrate interfaces resulting in an maximum area fraction parallel to the copper interface of 1.58%. The maximum pore observed had a diameter of less than 40µm, and the total pore content by volume was measured to be less than a tenth of a percent of the total joint. Both the nondestructive 3D quantification of a second metallic phase in a solder alloy using lab-scale equipment and the segmentation of an entire dendrite population for a full solder volume were believed to be new achievements in the realm of solder microstructure characterization efforts relevant to modern microelectronic packaging.

CHAPTER 7

ELECTROMIGRATION DAMAGE IN A FREE-SURFACE SN-0.7CU SOLDER

7.1 INTRODUCTION

Preliminary electromigration experiments in Sn-0.7Cu have been performed using the μXCT characterization apparatus described in the previous chapters. Due to the non-destructive nature, and the accessibility of lab-scale tools, time-resolved 3D (4D) studies have been performed which offer insight to failure mechanisms in solder interconnect structures through voiding and cracking (Tian *et al.*, 2011, Xie *et al.*, 2014, Tsuritani *et al.*, 2011). A secondary solid phase, inherently present in most alloys, may also be of interest. Second phase resolution might also serve as another means of quantifying the progression of damage in solder interconnects at a microstructural level. 3D imaging of solder alloys where at least two distinct solid phases are resolved has been demonstrated using μXCT beamlines at synchrotron storage ring facilities (Bertheau *et al.*, 2014b, Yazzie *et al.*, 2012a, Maleki *et al.*, 2014, Tsuritani *et al.*, 2007, Tsuritani *et al.*, 2011). Three studies are known in which 4D μXCT data was acquired in which both phases of the 63Sn-37Pb eutectic microstructure was resolved, but here also, imaging was performed at the synchrotron facility and not performed using a lab-scale tool (Yazzie *et al.*, 2012a, Tsuritani *et al.*, 2007, Tsuritani *et al.*, 2011). Just recently is there evidence of the resolution of microstructural phases within micro-scale solder joints using lab-scale μXCT, but where the composition was lead containing (Mertens *et al.*, 2014b).

This study implemented a lab-scale µXCT tool to characterize microstructural evolution in a Pb-free Sn-0.7Cu alloy subjected to accelerated electromigration (EM) testing. This study was preliminary for follow up experimentation with more joints. The sample geometry used was a <250µm diameter butt-joint on <250µm copper wire substrates. The sample microstructure is characterized in 3D via µXCT before accelerated testing, and again after failure. The attenuation contrast in the sample enabled quantification of the migrating species by measurement of the substrate volume, solder volume, and the formation of reactant products.

7.2 MATERIALS AND METHODS

A custom *in situ* jig was constructed for containing a tin-copper solder joint during electromigration (EM) testing and during µXCT. The <250µm tin-copper solder joint was fabricated by reflow in a silicon v-groove hot plate assembly (Mertens *et al.*, 2014b). To reiterate the basics of the procedure, a groove was etched into a silicon wafer which served to support and align the joint before and during soldering. Copper wires (ESPI Metals, 5N purity), initially 254µm in diameter, were straightened using an MTS Tytron microforce tester, cut to approximately 8mm lengths, and then polished perpendicular to their length axis at one end.

Butt-joints used in this study were fabricated using the silicon v-groove technique (as discussed for the tin-lead system in **Chapter 6**), but with a different sample composition and joint size. To reiterate the basics of the procedure, a groove was etched into a Silicon wafer which served to support and aligns the joint before reflow. Copper wires (5N

purity, ESPI), initially 254μm in diameter, were straightened using an MTS Tytron microforce tester, cut to approximately 8mm lengths, and then polished perpendicular to their length axis at one end. The polished ends of two wires were then coated with a Rosin-Mildly-Activated (RMA) flux and placed facing one another within the Silicon V-groove but with a slight gap. The primary difference for the fabrication procedure in this study was that an additional step was required in order to achieve spherical solder preforms of the desired volume, due to a larger in-stock solder sphere diameter than desired. In order to fabricate the preforms, the as-received preforms (Indium Corp.) were cut down, coated with flux, and re-melted to achieve a smaller, spherical preform. The Sn-0.7Cu solder, approximately 300μm in diameter was then similarly coated with RMA flux (Indium Corp.) and placed between the polished ends of the copper wire, also within the V-groove. The copper wires were then pushed gently towards one-another so as to contact the solder preform firmly at both wires' polished surfaces. The silicon wafer, mounted to a copper block, was then placed on programmable hot plate wherein a calibrated reflow profile was applied to the un-bonded assembly for the reflow of each joint. After reflow, the solder joints were then removed from the V-groove and either mounted within slow-set epoxy for polishing and surface (optical and scanning electron) microscopy or mounted within the μXCT scanner for 3D x-ray imaging. A special approach was adopted for performing both polishing and mounting within the XCT scanner, as will be discussed.

The reflow process consisted of a rapid heating to approximately 170°C for a 120s soak for flux activation, followed by a rapid heating to 20°C above the solder melting point

(~250°C) where a 40s soak was performed, followed by cooling of the joint and entire assembly in open air. A 1°C/s rate was established and measured. The enhance the suitability of the realized microstructure for second phase resolution in the µXCT reconstructions of the solder joints, an aging was performed at 190°C for 24 hours. This aging recipe was determined experimentally to yield ideal microstructures for µXCT and DVC studies, that is, a relatively large and well dispersed second phase. The reflow profile of a Sn-0.7Cu joint is portrayed in *Figure 50*, was determined to be stable and reproducible, and was used for the Sn-0.7Cu joints discussed in this work.

The reflowed Sn-0.7Cu microstructure was initially characterized with surface microscopy techniques. *Figure 51* provides a bright field OM micrograph of a polished Sn-0.7Cu butt-joint fabricated by reflow onto <500µm diameter copper wire. After reflow, the joint was aged for 24 hours at 190°C for intermetallic coarsening. The medium gray phase at the top and bottom of the image is the copper wire, the lightest continuous central phase is tin-rich, and the dispersed medium gray phase within the light phase possessing dark and well defined boundaries is the Cu_6Sn_5 intermetallic. Cu_6Sn_5 and Cu_6Sn_5 were both observed at the copper-solder interface.

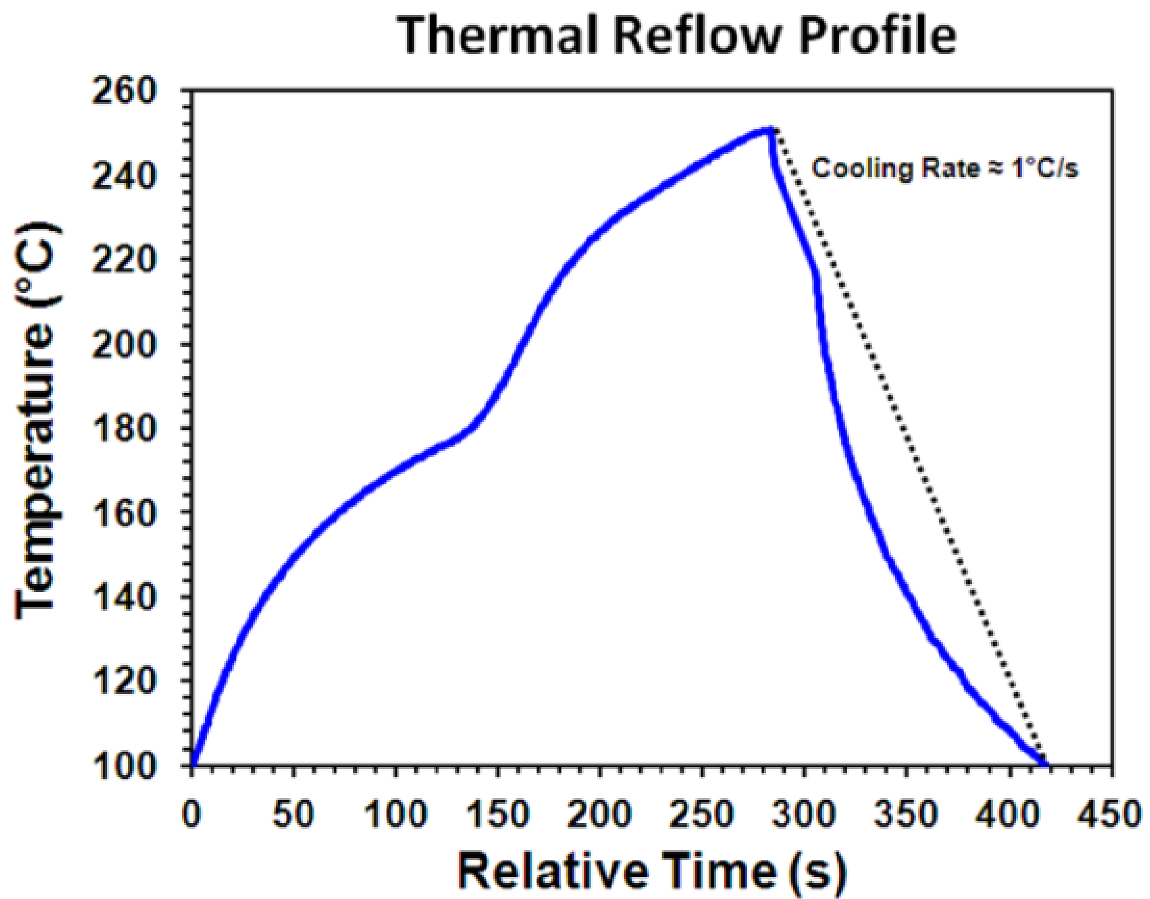

Figure 50. The Reflow Profile Applied to All Sn-0.7Cu Solder Joints for Fabrication in this Study, Containing a 170°C Soak for 120s for Flux Activation Followed by a Rapid Heating to250°C for 40s Before Cooling at 1°C/s

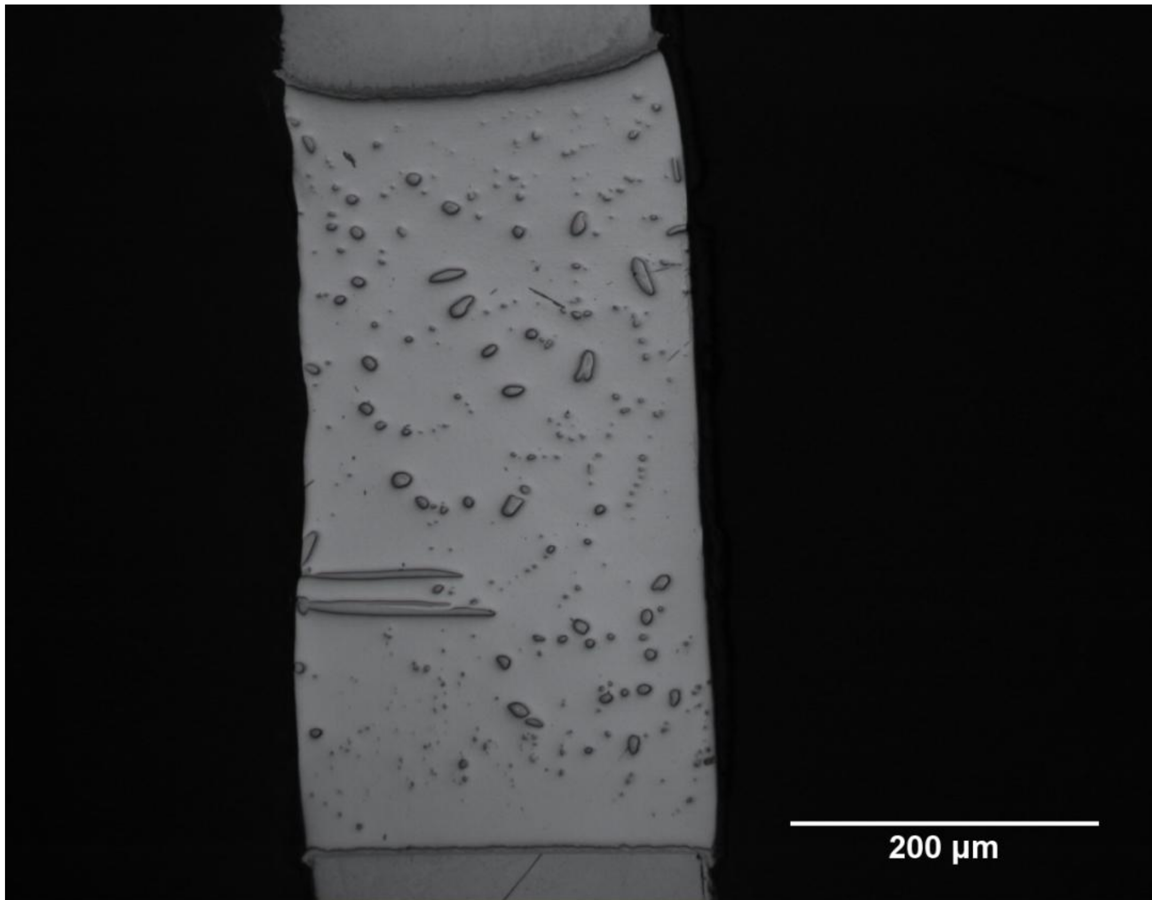

Figure 51. A Bright Field OM Micrograph of a Polished Sn-0.7Cu Butt-Joint Fabricated by Reflow onto <500µm Diameter Copper Wires and Aged 24 Hours at 190°C after Reflow

While the presence of the Cu_6Sn_5 intermetallic was confirmed from surface microscopy of the processed Sn-0.7Cu joints, as demonstrated in *Figure 51*, an x-ray attenuation contrast is required in between the surrounding tin-rich phase and the dispersed Cu_6Sn_5 phase in the acquired x-ray projections in order for these features to be distinguished in the μXCT reconstructed volume. Although the resolution of voids in a densely attenuating medium, such as solder compositions is all but guaranteed because of a high x-ray attenuation contrast with one another, this is certainly not necessarily the case between two solid metallic phases of similar composition and density. To determine the expectable x-ray attenuation contrast using a polychromatic x-ray source in tandem with a polychromatic x-ray detector, both with energy sensitivity, a simple modeling approach was adopted. The model for the CT system was arrived at using the approach outlined in **Chapter 4**. An approximation for the expectable contrast of Cu_6Sn_5 in a Sn-rich medium was made. X-ray mass attenuation data for tin as a function of x-ray energy (NIST, 2014), and composition weighted calculations of the same for Cu_6Sn_5, x-ray attenuation contrast was calculated between the two phases of unit thickness after taking into account their relative density (approximated as 7.31 g/cm³ for tin and 8.37 g/cm³ for Cu_6Sn_5) by using Beer's Law. The matrix was thus modeled as pure tin. The contrast was calculated for every x-ray energy of interest, limited by the x-ray tube's accelerating voltage. In *Figure 52*, the blue line represents the result of this model. As the x-ray CT system is capable of producing x-ray of up to 160kV, a range of 0-160kV was of most interest. In *Figure 52*, the y-axis represents positive contrast between tin and Cu_6Sn_5 intermetallic. A positive value at a particular x-ray energy indicates that the pure tin phase is more heavily attenuating than the intermetallic, although being of lower density, due to a higher

effective atomic number. A negative value on the y-axis indicates the exact opposite, and is only the case for x-ray energies up to about 4keV and roughly between 8keV and 28keV. The primary implication of this model is that although x-ray attenuation contrast is low between the two phases of interest, it is predictably greater than 10-15% for photons roughly between 30-160keV. The contrast was expected to decrease as a result of copper alloying in the tin surrounding, as in the eutectic composition.

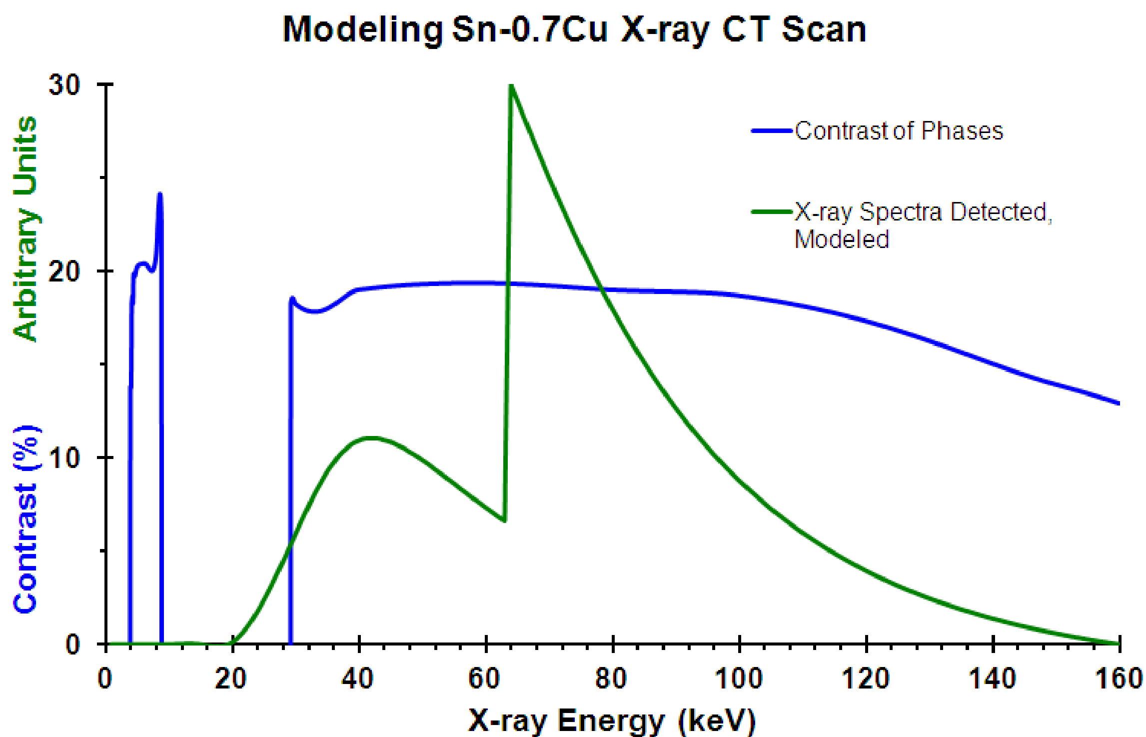

Figure 52. Modeling X-Ray Mass Attenuation Contrast between Pure Sn and Cu_6Sn_5 of Unit Thickness as a Function of X-Ray Energy (Dark/Blue) and Modeling the Relative Detected X-Ray Energy Spectrum (Light/Green)

Unfortunately with polychromatic lab-scale XCT systems, the x-ray flux is usually too low to make monochromatic studies possible, even at characteristic energies of the target material. That is, typically x-ray radiographs used for CT reconstruction contain contrast resulting from a range of x-ray energies that are present within the x-ray energy spectrum of emission. Although characteristic spikes in x-ray energy occur near the band gap energy of the x-ray tube target material, a significant portion of the x-rays produced are 'braking' x-rays, or Bremsstrahlung radiation. Braking x-rays result from the continuum of possible interaction and scattering processes that the electron beam may experience with the target material before producing an energy conserving x-ray. Essentially, a continuum of x-ray energy is created all the way from the maximum energy equal to that of the incident electron beam all the way down to near-zero. Upon exiting the window of the x-ray tube (Beryllium), a disproportional amount of low-energy x-rays are attenuated by the window while high energy x-rays by and large pass through the window in what is called filtering. Additional filtering of low-energy x-ray may be performed by the application of an additional filter, sometimes in the form of what is called a 'half value layer', placed between the x-ray target and the object being imaged. The filter composition and thickness provide a means of tailoring the low-energy end of emitted x-rays and the accelerating voltage of the x-ray tube's electron beam provides means of controlling the high energy limit of emitted x-rays. Unfortunately, the number of x-rays emitted at the high energy limit approaches zero as the energy limit is approached due to the mechanism of Bremsstrahlung x-ray generation. For this model the Bremsstrahlung continuum was considered and the characteristic spikes of the x-ray emission were ignored for simplicity. The interaction of the emitted x-ray spectrum with the energy

sensitivity of the detector produces what is shown in *Figure 52* as the green line, when considering x-ray generated from 160kV electron beam and 0.355mm of iron for low-energy filtering. The large spike in detection efficiency at around 64keV is due to the absorption edge of the scintillation medium used in this model (and in the real x-ray detector): Cerium-doped Lutetium Aluminum Garnet (LuAG:Ce). The accelerating voltage and filtering resulting in the detection spectrum line shown (*Figure 52*, green) were selected in order to optimize contrast between the tin-rich and Cu_6Sn_5 phases known to exist in the solder system of interest. The primary result of the model was the determination of optimal x-ray generating parameters for 3D µXCT characterization of the Sn-0.7Cu system's microstructure.

Accordingly, the µXCT scan parameters for detection of both phases in a ~230µm diameter Sn-0.7Cu system were selected. An x-ray accelerating voltage of 160kV was adopted with a pre-sample low-energy x-ray filter composed of 0.355mm of steel, resulting approximately in the relative detected x-ray number vs. x-ray energy spectrum shown in green in *Figure 52*. The x-rays were generated using a bulk (reflection type) Tungsten target, with a target current of 30µA, resulting in approximately 3-4µm x-ray resolution. Projections were acquired at 1/4 ° steps over a 185° rotation range, resulting in 741 projections with unique perspective. At each orientation, two 45s exposures were acquired before averaging with a zinger detection filter as detailed in **Chapter 5**. The projections were acquired in a 512 x 512 pixel format with a 1.22µm effective pixel size, resulting from the 3.8x optical magnification and 13x x-ray magnification acting on the 60µm CCD pixel. For the ~230µm diameter specimen, the 512 format under the stated

magnification factors resulted in approximately 210 pixels across the entire sample. The scintillator onto which the CCD's lens was focused was a single crystal LuAG:Ce scintillator of 250μm thickness, with a field of view of roughly 8mm x 8mm on the 25.4mm diameter crystal. The sample volume was reconstructed using the cone beam (Feldkamp-Davis-Kress) filtered back projection (FBP) algorithm with application of the Shepp-Logan filter function.

A single projection of the 741 projection stack used for reconstruction of a Sn-0.7Cu solder volume is provided in *Figure 53*. Shown with a blue inset frame is the approximate region-of-interest to which the projection volume was cropped prior to reconstruction. The apparent 'bright circle' in the image which is in some places cut off by the field of view was the result of a beam aperture in a ¼" lead shielding in order to minimize zinger noise in the projections. The central, dark (most heavily attenuating) phase in the projection shown in *Figure 53* is that of the solder itself, bounded on top and bottom by the copper wire contacts onto which the joint was reflowed. Visible at the lower copper-solder interface is the presence of a large pore, resulting from gaseous flux reaction products. The lead into which the aperture was placed appears less attenuating than the solder because the image has been reference image corrected, taken without the sample in place, but containing also the lead shielding with the aperture. The visibility of the aperture and its periphery are thought to remain after background normalization due to x-ray scattering effects.

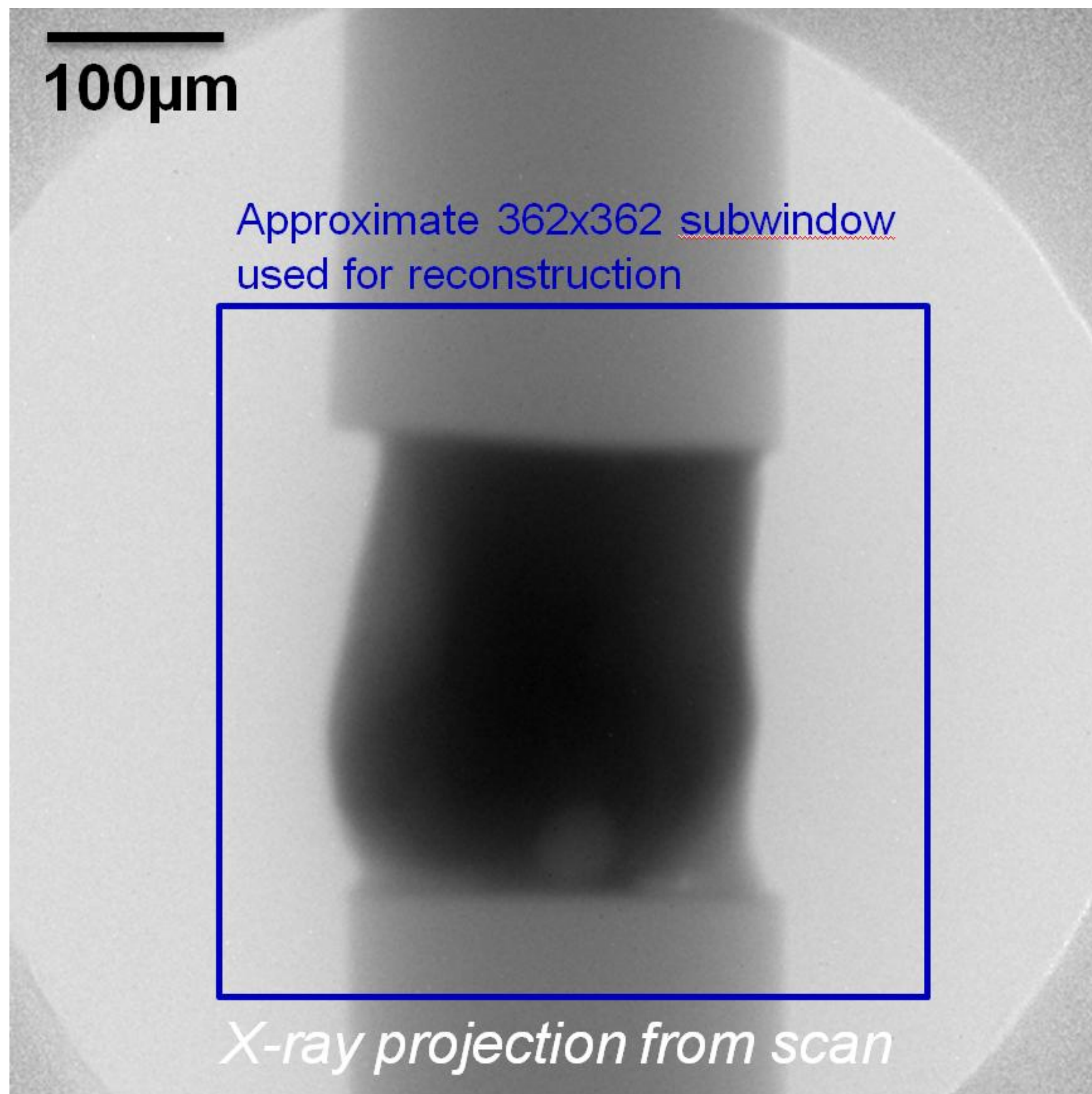

Figure 53. One Projection of the 741 Projection Stack that Results from Data Processing after XCT Data Acquisition where the Sample (Sn-0.7Cu Solder Joining ~230µm Diameter Copper Wires) Region of Interest is Highlighted with a Blue Inset

The results of the filtered back projection reconstruction are shown in *Figure 54* for the sample whose projection is shown in *Figure 53*. Four phases have been detected in the reconstruction: Air/Void, Copper, the tin-rich phase, and Cu_6Sn_5. In *Figure 54*, two different images are provided of the same cross section for optimal phase visualization. *Figure 54.a* is provided with maximum viewing contrast between the solder phase and the surrounding medium, air. *Figure 54.a* is provided with maximum viewing contrast between the primary and secondary solid solder phases, in other words, the tin-rich phase and *Figure 54.a*. Although sufficient contrast and spatial resolution was present in the volume for the 3D segmentation of the copper, solder, and void phases, the contrast difference between the tin-rich phase and *Figure 54.a* was approaching the level of noise in this region of the volume posing a challenge for intermetallic segmentation from the tin-rich volume. Nevertheless, using the x-ray parameters determined with simple modeling approaches for enhancing pure tin contrast with Cu_6Sn_5, reconstructions were obtained with resolution of the spatial distribution of, at least, the largest Cu_6Sn_5 particles.

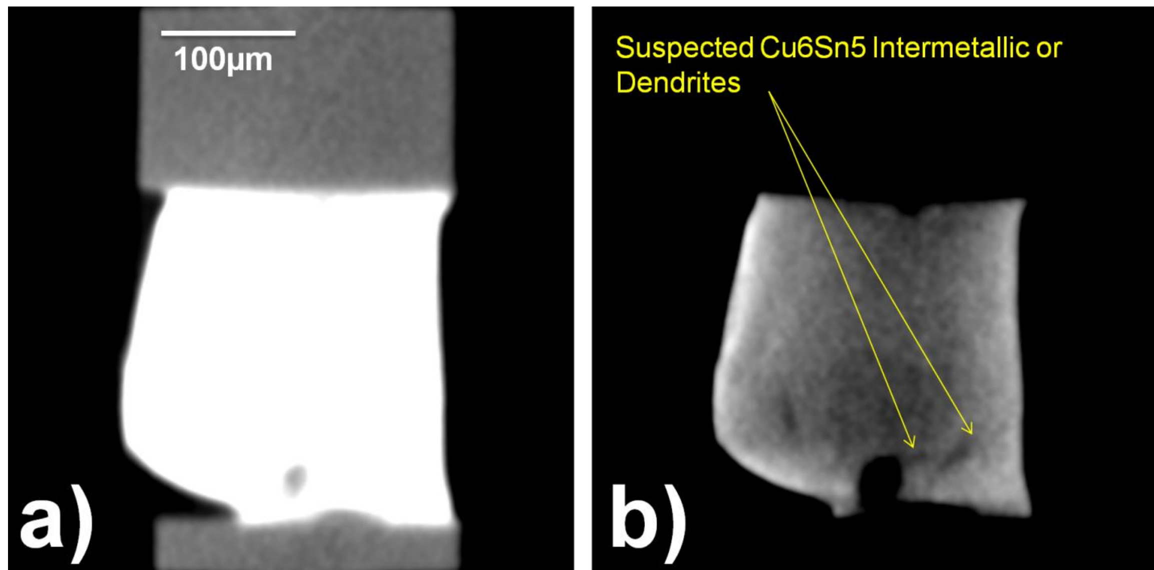

Figure 54. Cross Sections Parallel to the Rotation Axis of an XCT Reconstruction Volume for a Sn-0.7Cu Solder Bonded to ~230μm Copper Wires Under Different Intensity Scaling to Accentuate the Contrast between Different Sets of Phases *a*) Adjusted for High Contrast Between Solder (White), Copper (Gray), and Air (Black) and *b*) Adjusted for Highest Contrast Between the Eutectic Phase and the Cu_6Sn_5 phase (Dark)

The most general description of electromigration damage is the migration of solid material under an applied electric field which leaves a void in the material. Parameters that can be related to void nucleation and growth rate include the current density the sample experiences, the temperature of the sample, the degree of joule heating experienced, the sample composition, the surface composition of the contacting material, and the mechanical constraint of the material during current loading. Historically, the role of these parameters has been studies using two-dimensional imaging techniques. Two obvious approaches exist for two-dimension characterization of electromigration in three-dimensional specimens. One may perform testing on a large number of samples and characterize the sample microstructure by systematically destructively imaging the interior of the specimens at various points during the duration of the test, thus making it impossible to study the evolution of a single representative microstructure. The addition of serial sectioning to this approach introduces three-dimensional structure information; however, no single 3D microstructure may then be witnessed under evolution. Alternatively, non-volumetrically, one can perform testing on a sample which has had at least one surface created in the sample for continual monitoring of the microstructure of that specific cross section throughout the duration of the test, thus making it impossible to study the un-sectioned specimen in the as-processed geometry. Neither approach allows for the determination of the minimum current bearing cross section before imaging, thus occluding the possibility of accurately applying a precise current density in the specimen. The issues associated with these two methods are negated under the application of non-destructive, volumetric imaging enabled with x-ray CT.

A primary advantage of x-ray CT in the study of electromigration in solder joints is the accuracy with which the current density can be controlled. For the case of a 250μm diameter solder joint, a simple cylinder model can be used to determine the minimum current bearing cross sectional area. With this area known, a current magnitude can be determined that must be applied to achieve any arbitrary current density within the sample. This assessment is summarized in *Table 10* for the roughly 250μm diameter solder joint of interest. In the case of the simple cylinder model, this circular cross section was uniform throughout the sample. In real solder joints, however, geometric variations in the cross section due to processing give rise to a particular cross section in the sample which is smaller than any other, and the solder may not fully wet the cathode. Furthermore, microstructural variations within the joint, such as the presence of reflow interfacial porosity, can also give rise to cross sectional area variation through the joint, and result in a unique minimum cross sectional area existing in the joint. With any given two dimensional section of the joint, it is challenging to accurately measure the minimum cross sectional area, and therefore also a challenge to determine an applied current to the sample that would result in a precise targeted current density. With the method of x-ray CT, the joint's three dimensional structure can be non-destructive analyzed before application of current to the sample, and thus a current can be determined which will result in a particular current density when applied to the sample.

Table 10

Calculated Current Density through an Ideal 250µm Diameter Solder Joint (Shown in Figure 50) From Various Applied Current Magnitudes Achievable with the Employed Power Supply (Agilent E3633A)

Applied Current (A)	Maximum Current Density (A/cm²)
0.5	1×10^3
2.5	5×10^3
5.0	1×10^4
10	2×10^4
15	3×10^4
20	4×10^4

The values shown in *Table 10* are for a structurally homogeneous specimen. It was expected that the presence of any concavity of the solder structure after reflow, or the presence of any porosity in the specimen, would effectively decrease the area of the current bearing cross section, and that the current required to achieve a particular current density in the solder joint may thus decrease accordingly. For a real sample, the values shown in *Table 10* for 'Maximum Current Density' are underestimates of the actual current density for any corresponding 'Applied Current.' Two cross sections from an X-ray CT reconstruction volume of a ~230μm diameter Sn-0.7Cu solder joint are provided in *Figure 55*, where the cross sections shown are within the solder volume and immediately adjacent to the contact interface, in this case, copper wires of the same diameter. The two cross sections correspond to the top (*Figure 55.a*) and the bottom (*Figure 55.b*) relative to the orientation of the sample during the XCT scan. Although the top interface possessed a high degree of solder wetting/coverage on the copper contact, the bottom interface was seen to cover, roughly, only 55% of contact interface. In the event that testing this specimen at particular current density is desired, the ideal values in *Table 10* for applied current must be scaled down according to the true minimum observed cross section before selecting a current to apply during testing.

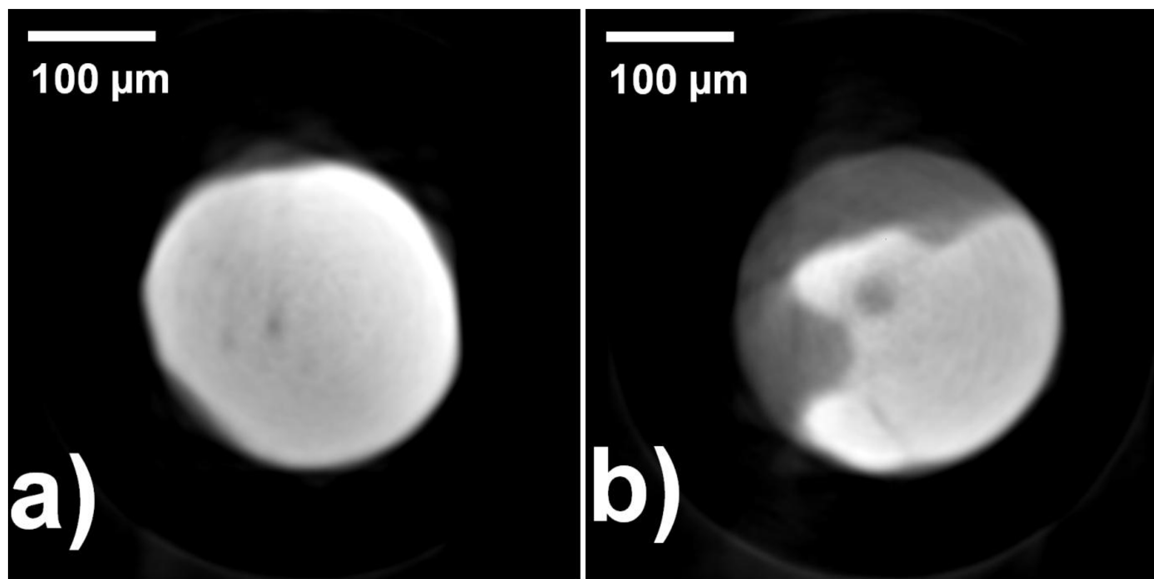

Figure 55. Cross Sections of a XCT reconstruction Volume of a Sn-0.7Cu Solder (Light) Bonded to ~230µm Copper Wires (Medium) Showing the Degree of Solder Coverage on the Contact *a*) The Top Interface has a High Degree of Solder Coverage and *b*) The Bottom Interface Possesses a Lesser Extent of Solder Coverage (The Black Phase is the Surrounding Air)

While it was possible to determine the initial minimum current bearing cross sectional area with XCT imaging, it was understood that as electromigration occurs in the specimen, voiding occurs in the solder, and the minimum cross sectional area in the joint would be decreased. Therefore, if the goal of electromigration lifetime experimentation involved understanding the effect of current density, it would be ideal to apply a constant voltage across the solder volume in order to keep this parameter approximately constant while damage progresses. Previous electromigration studies published in open literature have been run in both constant voltage and constant current settings, although the latter is the more common approach (Zhang *et al.*, 2013, Xie *et al.*, 2014). It has been said that actual solder interconnects may experience either condition in modern chip circuitry (Zhang *et al.*, 2013). In order to apply a constant voltage to the solder volume, it has been found that a very steady and predictable resistance in the power leads and sample fixture is required. Accordingly, a firm understanding of the temperature increase as a result of joule heating and the resulting resistance increase as a function of temperature in the system and the sample is required to be known as a function of current. In the case of accelerated testing at high temperature, the resistance increase in the elevated temperature range must also be known for the application of a constant voltage across the solder volume. Hence, many researchers have used the constant current approach, but careful note of the method used should be made when using current density exponent values from the literature in lifetime modeling.

In the present *in situ* μXCT study of electromigration in the Sn-0.7Cu system, a constant current approach was adopted. Prior to the application of an electric field to the reflowed

solder volume, the sample was subjected to µXCT imaging. Therein, the current bearing cross section was determined, and a current value was determined which, when applied to the sample, results in a pre-determined targeted current density within the sample. In this study, the current density targeted for initial studies was $1.0x10^4$ A/cm². This current was then run through the sample for a predetermined time, before again subjecting the sample to 3D µXCT imaging of the solder microstructure with particular interest in void and crack formation. The current applied to the solder volume can then be adjusted (decreased) to maintain the initial current density within the sample, or the same initial current value can be reapplied to the sample. For initial studies, the latter approach was adopted, although damage will occur more rapidly near the end of the solder's lifetime. The primary drawback with the experimental approach adopted was the deviation of the current density which the sample experiences from the initially applied and targeted value as time, and thus damage, progressed. Initially, at a time of zero, the initial current density was set with the aid of XCT to the targeted value.

A fixture was needed for mechanically supporting single butt joints 125-500µm in diameter, electrically facilitating connection with a power supply, providing thermal control of the test, and providing x-ray transparency of the system for *in situ* µXCT imaging. A design was conceived for the study of electromigration damage in single-butt-joint solder volumes at elevated temperature using *in situ* µXCT. *Figure 56* provides a rendering of the 3D CAD model used for the design and the machining of a custom sample fixture, and also highlights some of the key design features which were mandatorily incorporated. The design included two aluminum blocks into which each

half of the butt joint was affixed, and a Zerodur glass rod which fixed the aluminum blocks with respect to one another. Heating was achieved with the use of a side-mounting resistive ceramic heater, discussed further on in more detail. Aluminum was chosen for the conductive blocks because of an ideal combination of stiffness, strength, electrical and thermal conductivity. The butt joint was placed into each block through 500μm electric discharge machined hole-punch machined cylinders. The solder contacts, in this case the copper wire, were fixed to the aluminum block using set screws nearest the joint on the block. A Zerodur glass rod 1.5mm in diameter was similarly placed between the two aluminum halves, using a machined cylindrical port and set screw. The Zerodur rod provided mechanical connection and support between the aluminum blocks, but does not provide an electrical connection limiting current pathways between the aluminum halves to within the solder joint itself. The Zerodur material was chosen for this rod because of its thermal and electrical properties, with a near zero thermal expansion coefficient and near zero conductivity. As the joint was mounted at ambient room temperature, and the electromigration testing was performed at elevated temperature, minimal thermal stress on the solder volume due to fixture expansion was desired. Although a brittle mechanical member, the strength of the rod was sufficient to couple the fixture halves. Another desirable characteristic possessed by the glass rod was a high degree of x-ray transparency, especially so at high x-ray energy, as the rod entered the field-of-view and affected the data acquired during x-ray CT scanning. Each aluminum block half also had a connection terminal for either the positive or negative lead to the power supply. The bottom aluminum block was also designed to facilitate a post to support the fixture,

particularly during XCT data acquisition, and the top block had a connection for a side-mounting plate heater.

The mechanism for heating the specimen for achieving accelerated electromigration results is shown in *Figure 57*. A ceramic resistive heater 8mm x 8mm square (Watlow) capable of up to 200°C was used to conductively heat the fixture and ultimately the sample. The high thermal conductivity of aluminum and copper aided in the efficient transfer of heat from the ceramic plate to the solder volume. In order to perform XCT imaging, the heater plate was removed from the fixture after terminating any applied electric field. The heater itself contained a feedback thermocouple in order to control the power to the heater and ultimately the temperature at the heater. In addition to the applied system temperature, measurement of the temperature at the joint due to environmental heating as well as Joule heating was needed.

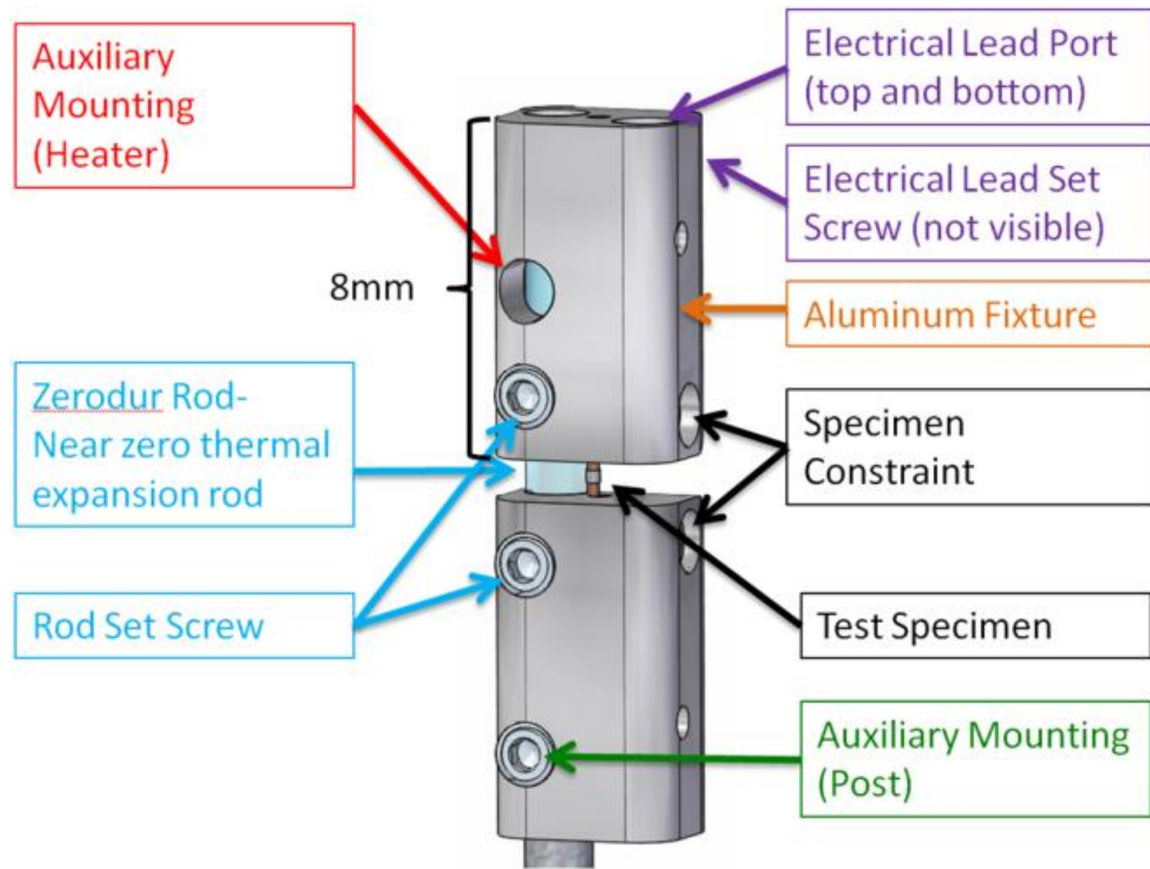

Figure 56. CAD Model Representation of the EM Fixture Designed for *in situ* μXCT Imaging with Each Primary Component Labeled with a Description of the Function that it was Designed to Accomplish

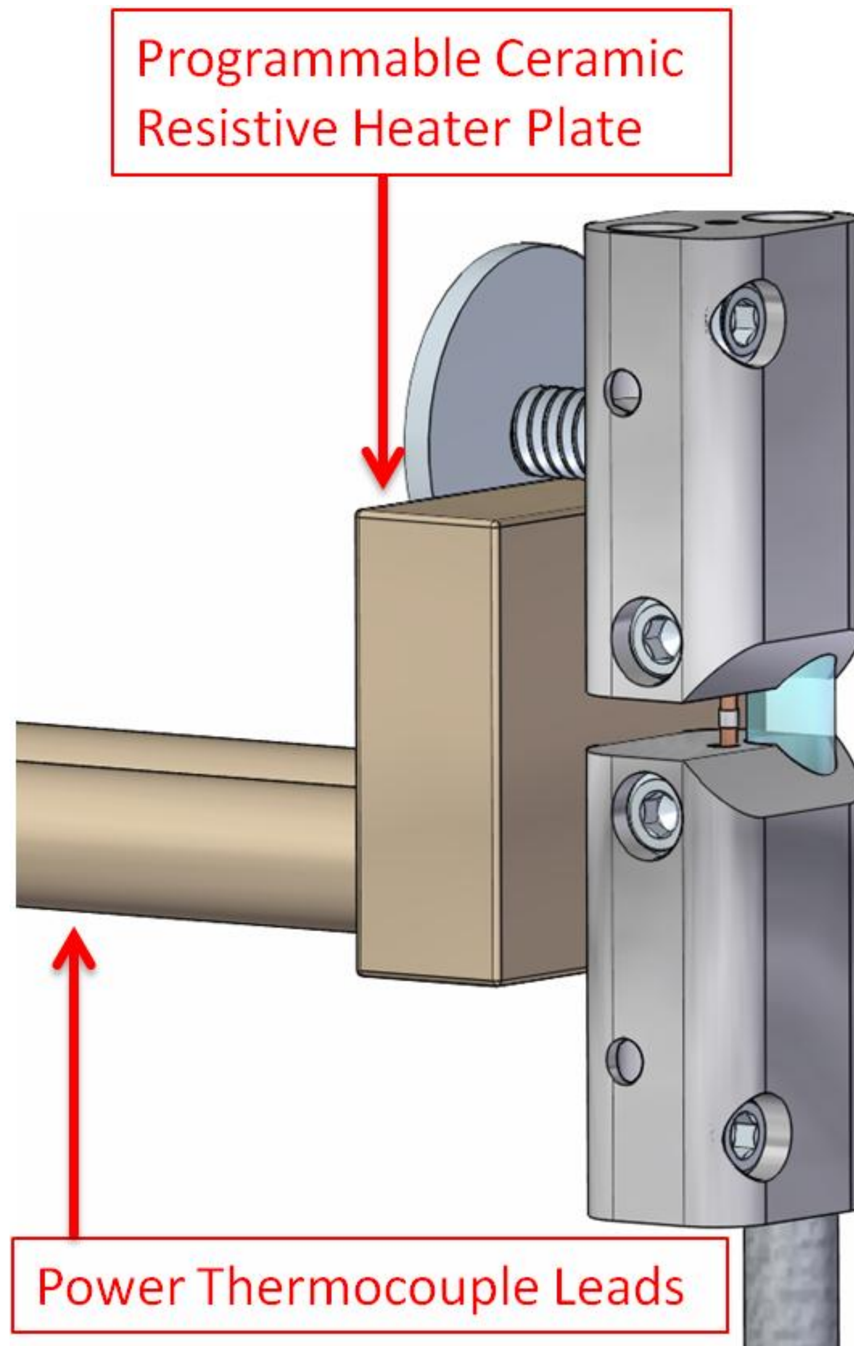

Figure 57. A CAD Rendering of the Electromigration Fixture for *in situ* µXCT Shown with a Ceramic Resistive Heater for Conductively Heating the Solder Volume and Performing Accelerated Testing

To monitor the temperature of the solder during electromigration, a thermocouple was fed through the chamber containing the solder joint until the joint's copper wire was contacted with the couple. *Figure 58* provides a CAD rendering of the fixture and heater design assembled for *in situ* XCT, with simple renditions of the thermocouple wires and power supply lead wires. Also contained in this figure is a schematic of the post design for mounting the sample to the rotation stage of the tomography system. Due to electrical shorting concerns, the rotation stage was isolated from the electromigration circuit using an isolating polytetrafluoroethylene (PTFE) block. For performing x-ray tomography scanning, the upper power supply lead, the thermocouple leads, and the heater assembly were removed before acquiring radiographic projections at many orientations. To continue the electromigration process after x-ray CT scanning, the electrical lead, thermocouple, and heater assembly were reattached to the fixture.

The *in situ* μXCT electromigration fixture possessed control over sample temperature and provided mechanical restraint in order to perform electromigration testing with sufficient control over lifetime influencing parameters.

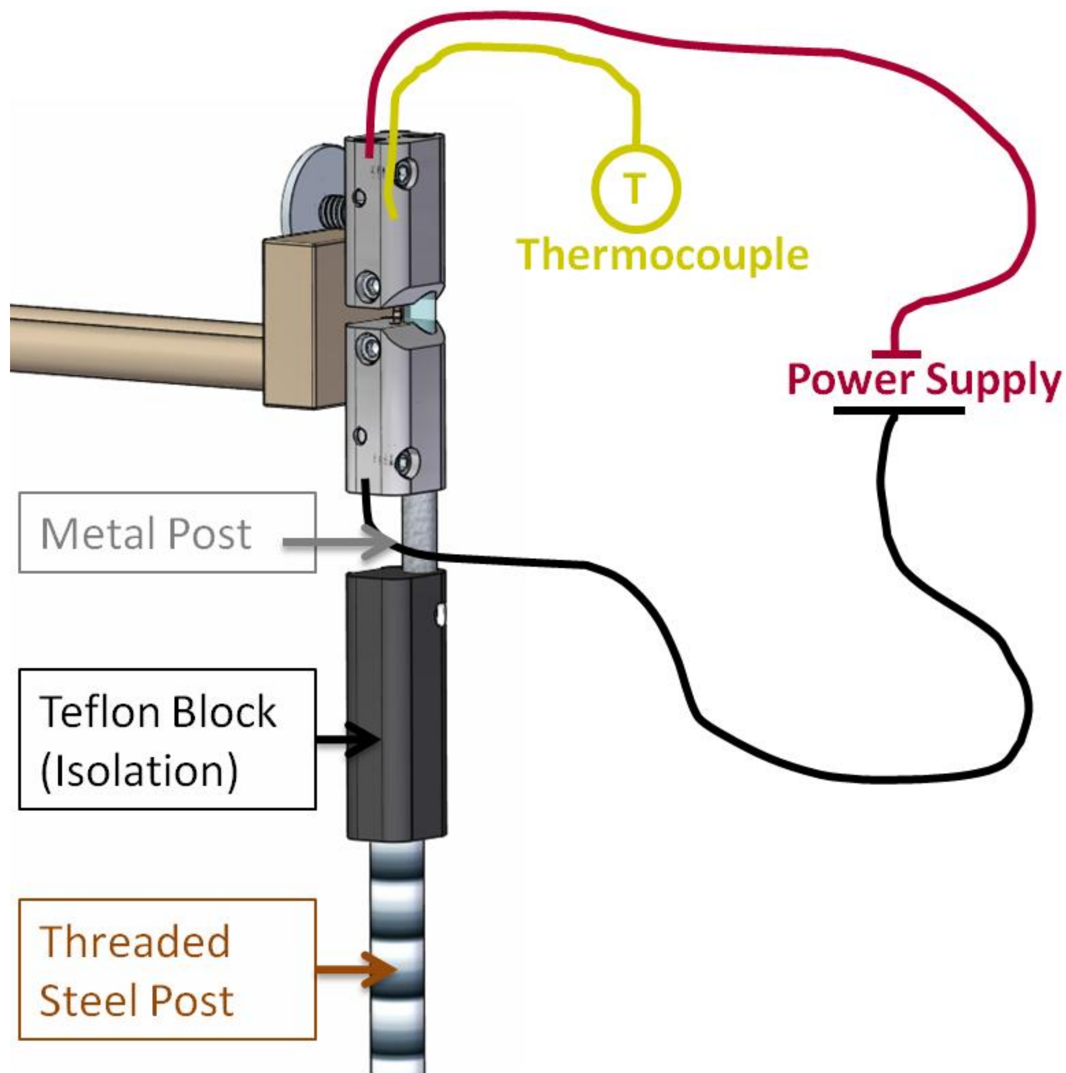

Figure 58. A CAD Rendering of the Electromigration Fixture Configured for *in situ* μXCT Experimentation where the Post Assembly (Bottom-Left) Facilitates X-Ray CT, the Thermocouple (Simple Representation, Yellow, Top) Enables Temperature Monitoring of the Solder Volume, the Power Supply (Simple Representation, Right) Enables the Application of Current to the Ssample, and the Heater Assembly (Brown, Upper Left) is used for Performing Accelerated Testing

The technique of μXCT provides complimentary 3D structural information to more traditional techniques of 2D surface optical microscopy (OM) and scanning electron microscopy (SEM). However, in most cases, OM and SEM techniques can provide better spatial resolution and feature contrast for a single surface. This considered, the approach used in the initial testing was to polish a facet into the (roughly) cylindrical butt joint, with a depth of up to half of the copper wires' diameter. Once the joint had been inserted into the electromigration fixture, the polished surface was used for making contact with the fixing set screw, providing a larger contact area and also preventing rotation inside the sample chamber. The process used for polishing a facet into the roughly 230μm butt-joint without any residual mounting is to first fix the un-faceted butt-joint with super-glue into an epoxy puck's groove, polish the joint, and then release the joint by exposure to acetone. Once affixed to the jig, the specimen was then subjected to electromigration testing, analyzed with μXCT, OM, and SEM.

OM and SEM images of a particular Sn-0.7Cu butt joint on ~230μm diameter (before polishing) copper wire substrates, Sample '03202014JointD', both before and after mounting into the electromigration testing jig, are provided in *Figure 59*. The joint can be seen in true-bright field contrast in *Figure 59.a* before being fixed to the aluminum blocks, where the tin-rich and Cu_6Sn_5 phases of the solder were seen as light and dark phases, respectively, between the copper wire contacts. In *Figure 59.b*, the sample was again imaged with bright field OM, but now after being mechanically fixed into the jig. The apparent dark lines in this micrograph were thought to have arisen from dark-field effects when imaging the joint in a deep valley formed by the aluminum jig, rather than

by deformation. This was reinforced by the back-scattered electron (*Figure 59.c*) and secondary electron (*Figure 59.d*) images, wherein the copper-tin intermetallics appeared darker than the tin-rich phases and some contrast between tin grains was observed. A side view of the sectioned, but free-surface, joint mounted within the fixture is provided in *Figure 60*, where the upper surface is the polished surface. Good alignment between the copper wires was observed.

The fixture's gap between the aluminum blocks for this sample was set at approximately 1.2mm to minimize the length which was free to expand thermally upon heating. The 1.2mm gap distance was set with the intention of minimizing the length of the joint which was allowed to expand freely and ultimately to minimize the compressive stress in the solder arising there from.

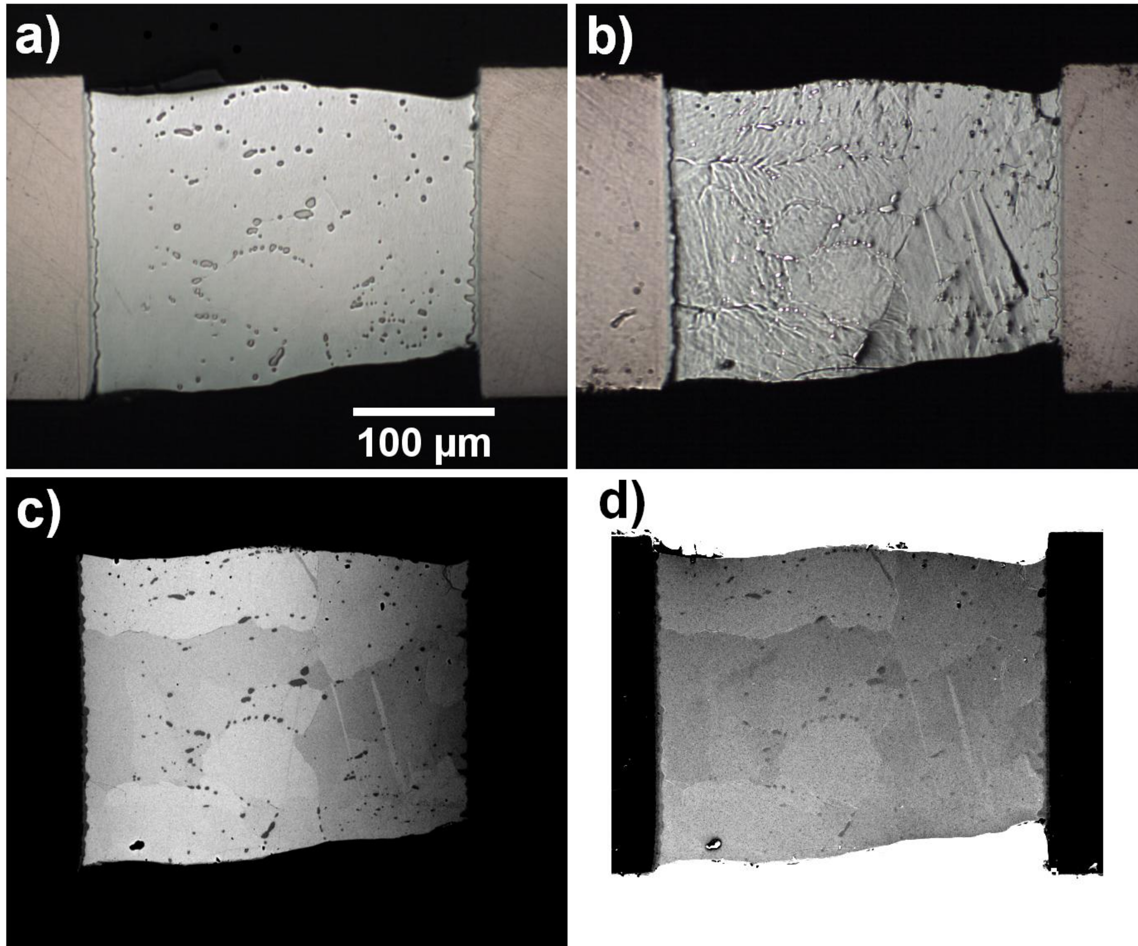

Figure 59. Mounting of a Sn-0.7Cu Butt-Joint 'Sample 03202014JointD' in the EM Test Fixture after Polishing to a Depth of approximately ½ of the Joint's Diameter *a*) Bright-Field Optical Micrograph Before Mounting *b*) Bright-Field Optical Micrograph After Mounting *c*) Back-Scattered Electron Micrograph After Mounting *d*) Secondary Electron Micrograph After Mounting

Figure 60. Bright-Field Optical Micrograph with a Side View of ‘Sample 03202014JointD’ Mounted within the EM Fixture before Testing with the Approximate Polished Surface Normal in the Up Direction

3D resolution of the copper-tin intermetallic phases within the solder and at the interface before and after EM using µXCT was targeted. Prior to conducting accelerated EM testing, x-ray computed tomography was performed on the as-processed butt-joint, mounted within an *in situ* EM fixture, in order to determine the minimum cross section of the solder conduction path. The cross sectional current-bearing area was critical to measure accurately, to determine the current necessary to achieve a targeted current density. The current density targeted in this experiment was 1.0×10^4 A/cm^2. X-ray computed tomography scans were performed using the custom lab-scale µXCT system already detailed. The x-ray projections were acquired every ¼ ° over a 200° scan range, yielding 801 orientations. Projections were acquired in 1024^2 pixel format (i.e. binning of 2 for the x-ray detector used). The physical pixel size of the CCD was $(15\mu m)^2$, but with 2x2-pixel binning during acquisition, a digital size of $(30\mu m)^2$ was realized. The optical magnification of the x-ray detector was configured at 3.80x. An x-ray magnification of 16.7x was achieved with an x-ray target to rotation-axis distance of 8.04mm and a target to scintillator distance of 134mm. Hence, the resulting voxel size of the tomography data was 0.473µm, and the resulting maximum out-of-fan-plane angle used for tomography was calculated as 1.8°. To improve signal and reduce noise, and to align the voxel size closer with the resolution of the x-ray source during the tomography scan, the data was further downsized by a factor of two, resulting in a voxel size of roughly 0.947µm and thus approximately 250 voxels across the polished edge of the copper wire cross section in the final tomography volume used for segmentation and quantification. Still the resolution was thought to be limited by other factors than the voxel size, specifically the focal spot size.

The sample reconstruction volume was calculated using a custom algorithm based on the open-source, cone-beam, Feldkamp-Davis-Kress (FDK), Filtered Back Projection (FBP) code, OSCaR, implemented in MATLAB and made available by N. Rezvani *et al.* (Rezvani *et al.*, 2007), including additions in GPU acceleration, improvements in memory allocation, improvements in mathematical implementation for speed, and added user functionality. The reconstruction was performed with Shepp-Logan filtering. Three 2D orthogonal views of the solder joint reconstruction volume are provided in *Figure 61*. The grayvalues in the reconstruction volume represent the average x-ray attenuation determined for that voxel based on 801 unique projections. The most heavily attenuating phases are brightest in this figure. The darkest phase is that of air or void, the medium gray phase is the copper volume, and the brightest phase is that of the solder volume.

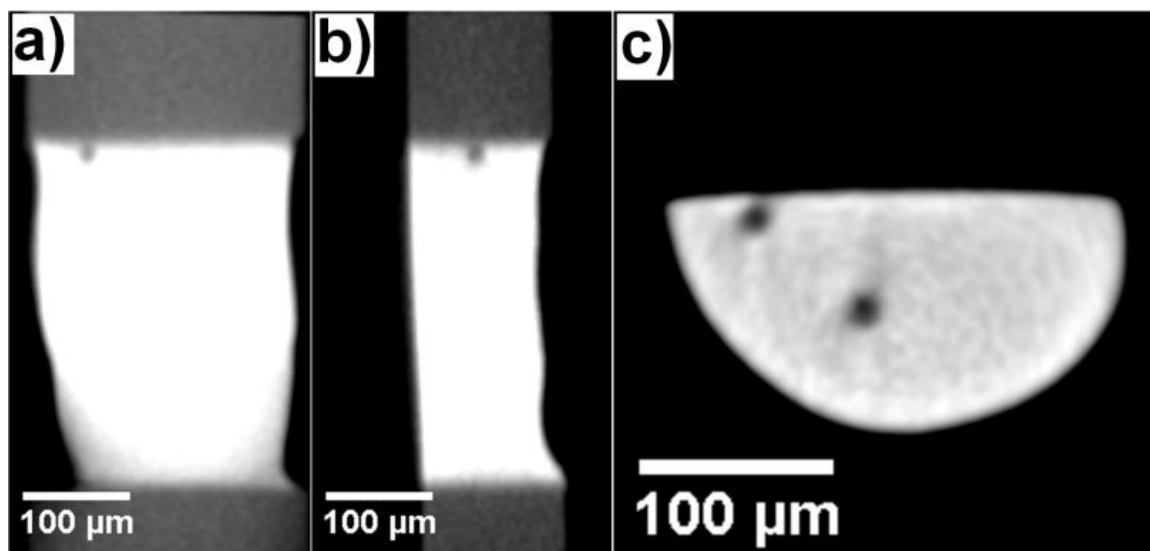

Figure 61. Three 2D Orthogonal Views of the 3D Reconstruction Volume of the Sn-0.7Cu solder 'Sample 03202014JointD' Prior to Accelerated EM Testing *a*) Near the Polished Surface of the Joint Showing Anode and Cathode *b*) Orthogonal to the Polished Surface Showing Anode and Cathode *c*) Orthogonal to Both '*a*' and '*b*' and Near the Cathode

Before conducting accelerated EM testing, μXCT was used to measure the minimum solder cross section parallel to the solder interfaces. In order to calculate the minimum cross section of the solder conductor, it was necessary to first perform a segmentation of the volume. Within the pre-EM volume, the grayvalue differences between copper and solder make the segmentation possible to perform with simple thresholding. For calculating the minimum cross section, this is all that was needed. However, segmenting the solder joint was most challenging in terms of the copper/ copper-tin intermetallic/ tin-copper alloy interface. Even without the presence of any interfacial intermetallic, there was expected to be a gradual variation in gray value of the cross sections in the transition from copper-to-solder from the reconstruction algorithm approximations and the finite spatial resolution realized in the tomography data. Although the presence of intermetallic at the interface and within the alloy was known from optical imaging of identically processed joints, no intermetallic phase was observed. Even away from the interface, and intermetallic particles were not clearly visible.

Coupled with the high-level knowledge that a copper-tin intermetallics exist at the interface, the actual gray value transition was thus acknowledged to be a convolution of contrast-resolution of the tomography and the attenuation transition between a pure copper phase, a Cu_3Sn phase, a Cu_6Sn_5 phase, and a copper-saturated tin-rich alloy. The intermetallic was set using a local threshold in transition planes of intermediate grayvalue where the deviation from the mean solder or copper gray value was large. The interfacial porosity was also segmented using local thresholds. For demonstration of the

segmentation results, a comparison of the segmented microstructure with that of the grayscale volume is provided in *Figure 62*.

The segmented volume was used for quantifying copper and tin-rich solder migration with the eventual post-electromigration tomography volume, but before conducting accelerated EM testing, was also used for measuring the minimum solder cross section parallel to the solder interfaces. For this sample, the minimum conductor cross section was found to be near the lower interface portrayed in *Figure 62*. This cross section was measured, and a 1.51A current was calculated, as demonstrated in *Table 11*.

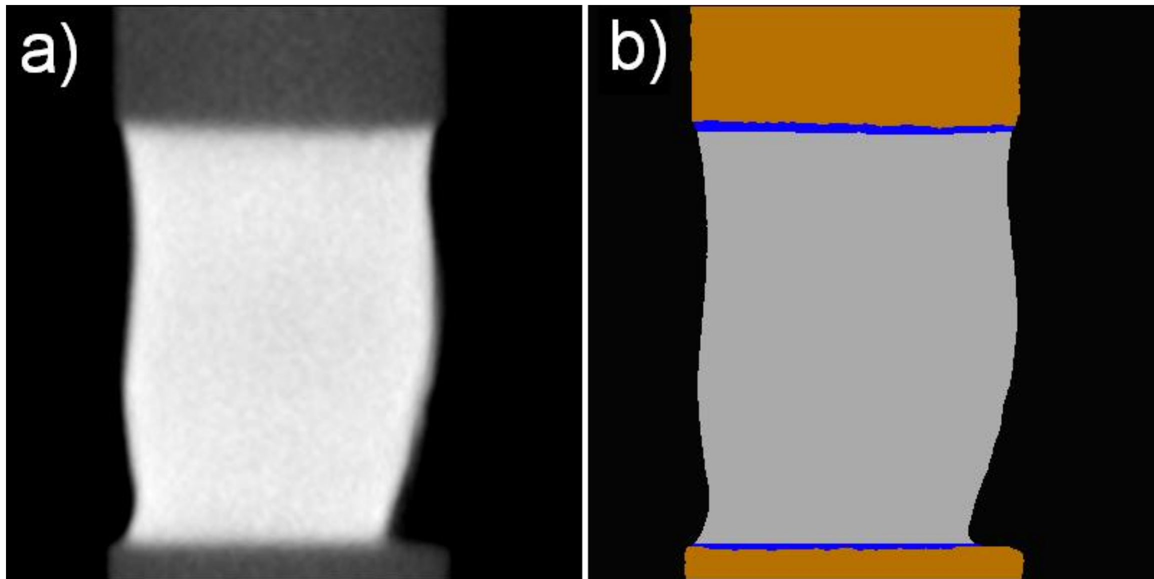

Figure 62. Segmentation Visualization of the Sn-0.7Cu Solder Joint 'Sample 03202014JointD' Tomography Volume Prior to Accelerated Electromigration Testing *a*) The Grayscale Reconstruction Volume *b*) The Segmented Volume with Copper Shown as Orange, Solder as Gray, and the Interfacial Phase as Blue Likely Corresponding to Regions of High Intermetallic Density

Table 11

Measured Conductor Cross Section, Targeted Current density, and Calculated Current for Accelerated Electromigration Testing Using Tomography Data for the Pre-Electromigration Sn-0.7Cu Joint, 'Sample 03202014JointD'

Minimum Cross Section	1.51E-04cm²
Targeted Current Density	1E+04 A/cm²
Applied Current	1.51A

The accelerated EM testing was performed with the top copper conductor shown in *Figure 61* acting as the cathode at a current of 1.51A and an applied temperature of 100°C before any Joule heating was observed. The electron wind force vector was thus directed from the cathode toward the anode, or from top to bottom as portrayed. The effects of the un-encapsulated free solder surface, pre-existing voids at the cathode, the minimum conductor cross section being near the anode, and the varying current density in the joint expected (and thus also varying joule heating) as a result of constant-current (CC) testing were expected to have ramifications on the observed solder joint lifetime and volume/microstructure evolution during testing/failure, but these effects were not explored. During testing, a maximum observed joule heating of $\Delta T \approx +35$°C was observed near the end of the test at an applied temperature of 100°C and an applied current density of 1.0×10^4A/cm², similar to what's been reported in the literature (Xie *et al.*, 2014, Yang *et al.*, 2008b). Of course, the current density was only expected to be exactly 1.0×10^4A/cm² at the beginning of the test. Ultimate failure was reached at approximately 220 hours of testing.

For EM testing here discussed, interrupted *in situ* imaging was performed at various time steps, for which the application of heat and current was necessarily paused. For this test µXCT was performed at time *t*=0h and at time *t*=220h, corresponding to the states of as-processed and after EM failure. At times *t*=100h, t=150h, and t=200h, optical imaging of the polished surface and a side-view of the joint was performed for monitoring damage prior to failure. Although µXCT characterization is most desirable during interruption, optical microscopy was used in this preliminary study for simplicity.

In general, literature shows that the resistance of the EM tests structures are very steady with minor gradual increase in resistance for the majority of the test duration, but begins to rapidly increase near the end of the experiment when voiding near the cathode becomes more rapid as current density becomes larger and larger in a cyclic process (Basaran *et al.*, 2009, Yamanaka *et al.*, 2010, Zhang *et al.*, 2013). With the Joule heating known to be proportional to I^2R (Chen and Chen, 2001), ignoring any temperature dependent heat loss rate, the relative increase in sample temperature from joule heating can be expected to closely follow the relative increase in resistance during the test. It was therefore expected that the resistance increase of the joint was steady and small initially; the increase in temperature due to joule heating was expected be steady and relatively low, initially. It was thus expected that as electromigration caused conductor atoms to migrate away from the cathode, and voiding would begin to form at the cathode, the resistance would begin to rapidly increase and thus also would the temperature resulting from Joule heating, with the highest absolute solder joint temperature of the test realized, at least locally, near failure.

7.3 RESULTS

Ultimate failure was reached at approximately 220 hours of testing. After 100 hours of testing, the application of current and heat was briefly interrupted to perform optical imaging of the damage state. For this purpose, as previously mentioned, a polished surface was prepared prior to testing through which solder evolution could easily be monitored. Due to the un-encapsulated geometry, the joint's structure could also be satisfactorily imaged from other orientations of the joint, which although not polished or

even flat, were not obscured by epoxy 'underfill' or some other encapsulating agent. Characterization of the joint at 100 hours is provided in *Figure 63*. The cathode is shown at the right side of these micrographs; at 100 hours, oxidation was obvious on the copper cathode. A large dark spot was also apparent at the cathode in the right half of *Figure 63.a* which had a pit-like appearance; this dark spot however was determined to be not a pit, but rather a nodule growing out of the surface, which was not obvious from *Figure 63.a*. This nodule growth can be observed in *Figure 63.b*, which offers a side view. In *Figure 63.a*, darkening of the polished surface was seen, likely caused by shadowing from damaged grains, whether shifted rotated or extruded through grain boundary diffusion or alternatively caused by the presence of voids either at the cathode or granular interfaces. The anode remained relatively unaltered. The presence of damage or voiding at the cathode was expected, as copper and tin atoms were expected to migrate in the direction of the electron wind force leaving voids in their wake. What was not expected from results of EM testing in the literature was the formation of solder nodules or reaction products at the cathode interface, which is generally observed to occur near the cathode (Chen and Chen, 2001, Gan and Tu, 2002, Liang *et al.*, 2010). This was thought to be an effect of the free, un-constrained, joint surface as is later discussed in more detail.

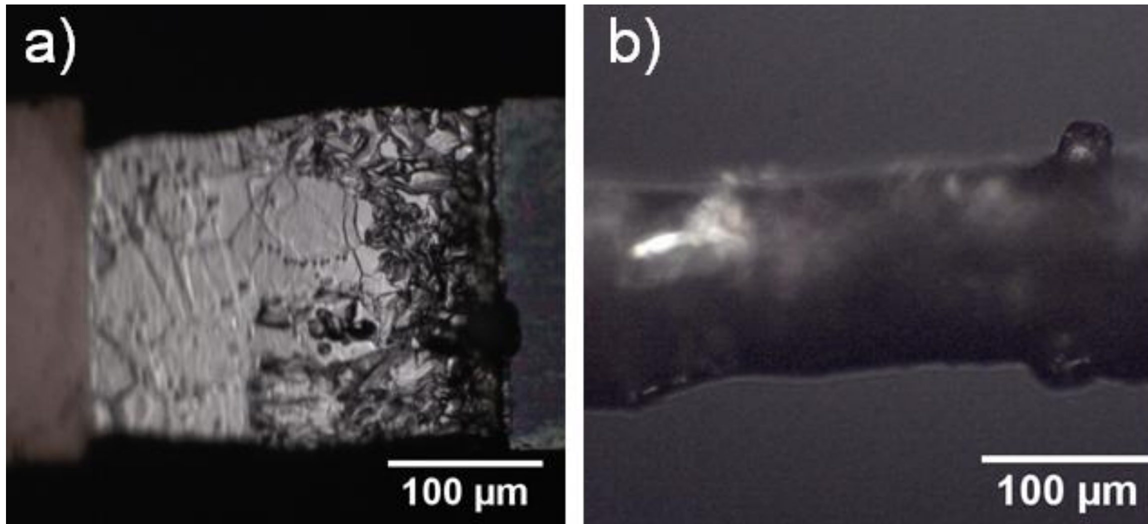

Figure 63. Bright Field Optical Micrographs of Sample '03202014JointD' after 100 Hours of Electromigration at 10^4A/cm² and 100°C, Still Contained within the Electromigration Fixture with the Cathode at Right and the Anode at Left *a*) Top View of the 'Polished' Surface with Damage Obvious at the Cathode *b*) Side-View Relative to the Polished Surface Showing the Formation of Solder Nodules Protruding from the Cathode Interface

After the first round of interrupted imaging, the test vehicle was again subjected to accelerated EM testing under identical conditions. The testing was again interrupted, this time, after only 50 hours of additional testing, that is, after 150 hours of total testing. At 150 hours of accelerated EM, an obvious degradation of the copper cathode was observed at the interface: What was initially a flat, polished surface had developed an apparently tortuous nature. This, as will be discussed in greater detail, was attributed to the rapid electromigration of copper atoms into the tin-rich solder alloy. At 150 hours, some significant voiding was seen at the free surface of the cathode interface opposite the polished surface. After 220 hours of total testing time, the joint experienced total failure in the form of an open conductor circuit. At this point, the test structure was subjected to optical microscopy (OM) (*Figure 64.a – Figure 64.f*), scanning electron microscopy (SEM) (*Figure 64.g* - *Figure 64.h*), and 3D x-ray computed tomography microstructural characterization. The micrographs in *Figure 64.a* - *Figure 64.d* and *Figure 64.g* - *Figure 64.h* are of the originally polished surface of the failed joint. The complex topography of the final structure made it challenging to image the entire structure due to the high surface roughness and low depth-of-field, even at low numeric aperture. Near the anode, the originally polished surface was seen relatively unaltered after failure. The central portion of the joint viewed from this orientation contains a large 'valley', and near the cathode, material has deviated in the opposite direction, out of plane of the image. By changing the location of the focal plane in OM, structure of the formations near the cathode were studied as shown in *Figure 64.c* and *Figure 64.d*. In this orientation two large primarily spherical structures were seen growing away from the joint. The larger of the structures had a tin-like luster, whereas the smaller structure appeared to have a

copper-like color. To characterize the height of these structures, the sample was viewed from the both sides (*Figure 64.e* and *Figure 64.f*). Viewing the failed solder joint from an orthogonal perspective to that of the (originally) polished surface normal provided additional insight. The two spheroids present in *Figure 64.a* through *Figure 64.d* were also seen in the side view, shown in the right half of *Figure 64.e* and *Figure 64.f.* A new spheroid was also observed near the bottom side of the cathode. A fourth, even smaller, spheroid was seen at the cathode interface, and is provided in the right half of *Figure 64.f.* Even through leveraging three separate viewing orientations in OM, it was not possible to acquire a clear picture of the actual voided cathode which was only partially observed. The micrographs also provide another perspective of the jagged sub-growths on the largest spheroid shown in *Figure 64.d*. The non-planar structures were better studied through SEM imaging with a much larger depth of field, as in *Figure 64.e* and *Figure 64.f*, where a more clear picture of the failure void was observed. *Figure 64.e* and *Figure 64.f* correspond to Secondary Electron (SE) and Back Scattered Electron (BSE) contrast modes, respectively.

The sphere-like 'growth' structures at the cathode were unexpected. The initial growth nodules near the cathode, observed for example in *Figure 63*, might be explained by the relative high diffusivity of atoms on a free surface. While it is known that a sphere is low energy structure due to a low surface area, reports of spheroids are not known, and nodules or whisker reports are much more common (Chen and Chen, 2001, Gan and Tu, 2002, Liang *et al.*, 2010). It might be speculated based on an apparent history of bridging that the last part of the solder joint to fail completely was near the lower end of the

cathode with respect to *Figure 64.g*. It might be further speculated that the current density was at a maximum near failure. Conceivably, the current density would be an order of magnitude larger than initially established if/when the current-bearing cross sectional area was reduced to 1/10 of the initial; the resistance would be expected to be approximately ten times greater at that moment, and the degree of joule heating would similarly be expected to be one hundred times greater. One possible reason for the sphere-like formations is that local temperatures near the 'growth' structures approached the melting temperature of the tin-copper alloy immediately preceding joint failure. This was not confirmed with the temperature measurements during the test.

The challenge of accurately characterizing the failed solder volume in 2D was demonstrated in *Figure 63* and *Figure 64*. The ideal characterization tool would provide non-destructive, volumetric quantification of the consumption of the copper cathode, migration of tin, and the formation of copper-tin reaction products. The custom lab-scale μXCT system was been applied to the sample of interest prior to electromigration, in order to quantify the minimum solder cross sectional current bearing area. The *in situ* fixture, containing both the anode-half and the cathode-half of the failed butt joint, allowed for reinvestigation of the solder volume using x-ray computed tomography. The sample was subjected to μXCT post-mortem, under the same scan conditions as the as-processed sample volume. Two slices from the failure volume are presented in *Figure 65* under two display settings for each. The void coalescence is seen near the cathode in *Figure 65.a* and *Figure 65.b* along with the formation of solder structures near the surface. The sample was actually completely open, but is held in place from the top and

bottom respectively by sample clamps of the in-situ testing fixture. Although no copper-tin reaction product was observed in the pre-EM µXCT volume away from the interface, the reaction products, formed as a result of accelerated EM, were indeed detectable to high degree using µXCT. The presence of copper-tin reaction products within the failed solder joint is not obvious in *Figure 65.a* and *Figure 65.b* with the portrayed brightness and contrast settings due to the relatively low difference in grayvalue between the intermetallic and the solder in the reconstruction volume. The black phase present in *Figure 65.c* and *Figure 65.d* then also included the copper as well as the surrounding air, the bright phase corresponds to tin-rich phases, and the dark gray values correspond to the copper-tin intermetallic as detected with µXCT. A simple description of the intermetallic phase observed in the volume was a large, connected intermetallic structure branching from the anode interface to a large central island via a narrow channel. The large central island is seen in *Figure 65.c*, and *Figure 65.d* portrays a section containing growths down to the anode, which were all connected in 3D. In *Figure 65.a* and *Figure 65.b*, the brightness and contrast settings for visualizing the tomography data have been adjusted for best contrast of the copper, solder, and surrounding air. The brightest portions indicate solder, the medium gray indicates copper, and the black portions correspond to the surrounding air. The display settings for the volume were also adjusted for better visualization of the intermetallic phase that had formed within the volume, as shown in *Figure 65.c* and *Figure 65.d*.

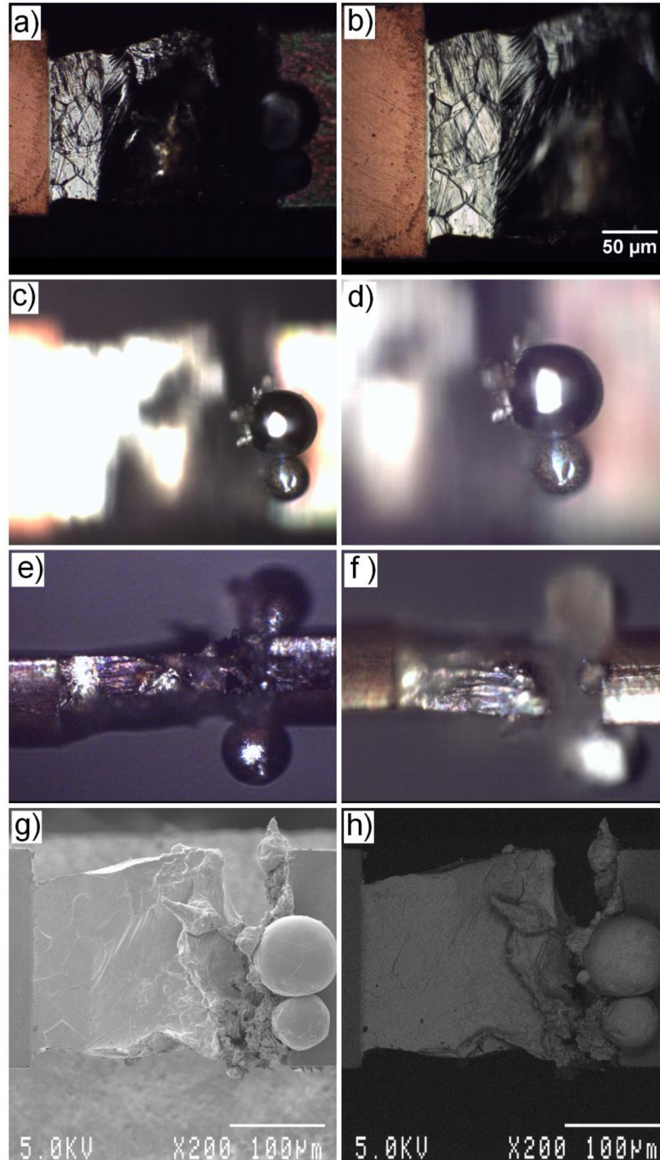

Figure 64. Surface Images of Failed Sn-0.7Cu 'Sample 03202014JointD' after 220 Hours of Electromigration at 10^4A/cm² and 100°C, Still Contained within the Electromigration Fixture with the Cathode at Right and the Anode at Left *a-b*) Bright Field Optical Micrographs of the Anode *c-d*) Bright Field Optical Micrographs of the Growth Nodule at the Anode *e-f*) Bright Field Optical Micrographs with Side-Views *g*) SEM Micrograph in SE Mode *h*) SEM Micrograph in BSE Mode

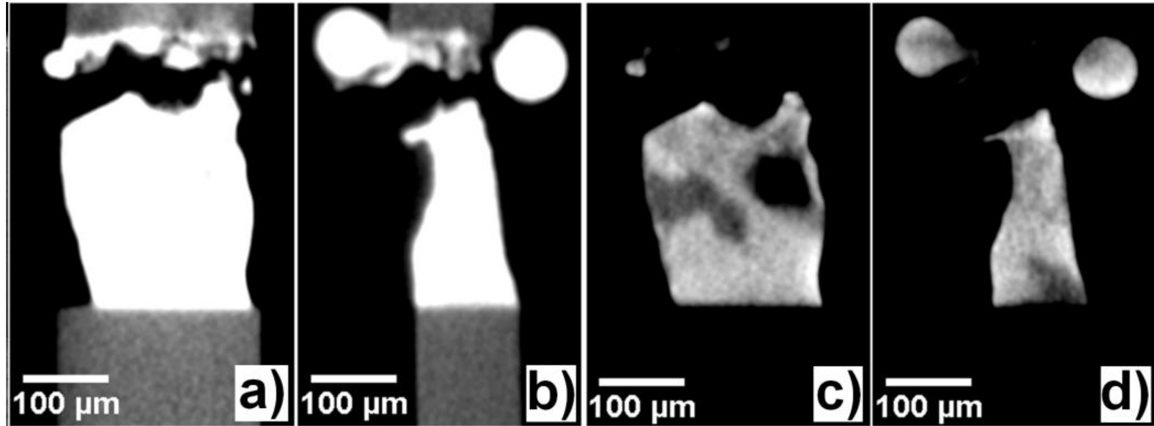

Figure 65. Three 2D Orthogonal Views of the 3D Reconstruction Volume of the Sn-0.7Cu solder 'Sample 03202014JointD' After Accelerated EM Testing *a*) Near the Polished Surface of the Joint Showing Anode and Cathode with Brightness and Contrast Adjusted for Solder/Copper Contrast with the Brightest Phase as the Solder, the Medium Phase as the Copper , and the Black Phase as the Surrounding Air *b*) The same as '*a*' but Orthogonal to the Polished Surface *c*) The Same Plane as '*a*' but with the Viewing Window Adjusted for Solder/Intermetallic Contrast where the Black Phases are Copper and Air, the Dark Gray Phase is the Intermetallic, and the Lightest Phase is the Tin Rich Solder *d*) The Same Viewing Settings as '*c*' but for the Plane Shown in '*b*'

X-ray computed tomography applied post-mortem provided a better description of the failed joint's structure than SEM imaging. In order to quantify the migration of tin, copper, and the formation of intermetallic reaction products, the post-EM reconstruction volume was segmented into the phases of best description, according to gray value. It was found that 3D anisotropic diffusion filtering was beneficial in enhancing the uniformity of the grayvalue within the intermetallic phase of the reconstruction. To quantify the migration of tin, copper, and the formation of intermetallic reaction products, it was necessary to segment to post-EM reconstruction volume into the phases of best description, according to gray value. The post-EM volume was segmented into copper, tin-rich, intermetallic, surrounding air, and contained void phases using a combination of grayscale volume filtering, global threshold, local threshold, 2D region grow, and 3D region grow algorithms. Global threshold was used to capture the tin-rich solder volume, including the faint contained intermetallic phases. The copper phase was then captured using a solder-restrictive global threshold. No porosity was detected after failure. The copper-tin intermetallic was then captured using consecutive and cumulative 2D and 3D region grow implementations across all three planes and within the volume, however, this was performed using a gray volume which had first been filtered using 3D anisotropic diffusion which had been established to give the best results using trial-and-error. The results of the segmentation process are provided visually in *Figure 66.c*, where a segmented slice of the segmented volume is compared with an identically positioned slice of the volume without anisotropic diffusion filtering (*Figure 66.a*) and the anisotropic diffusion filtered grayscale volume (*Figure 66.b*).

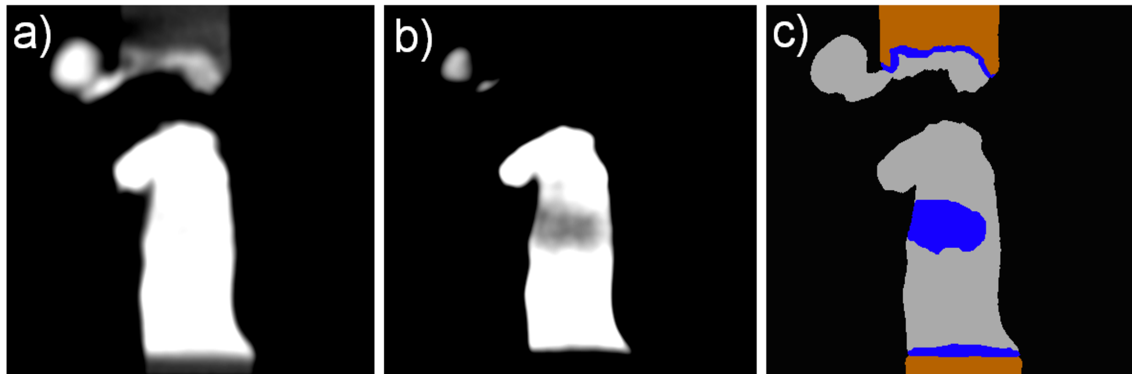

Figure 66. Visualization of CT Volume Phase Segmentation for EM Failed 'Sample 03202014JointD' through Three Identically Positioned Slices *a*) Original Grayscale Volume with Some Smoothing, Showing Copper and Solder contrast *b*) 3D Anisotropic Diffusion Filtered Volume Adjusted for Intermetallic/Solder Contrast *c*) Segmented Volume with Copper Colored Orange, Tin-Rich Solder Colored Gray, and Intermetallic Colored Blue

The segmented volume was rendered in 3D to provide a better picture of the phase evolution resulting from electromigration. The solder is rendered transparent to view the internal intermetallic (blue), and the surfaces were smoothed, as is provided in *Figure 67*. Two orthogonal views are given. The anode intermetallic was found to be connected with the large central island of intermetallic that had formed in the joint.

Optical surface microscopy was used to verify the accuracy of the segmentation. The sample was mounted and destructively sectioned for optical characterization after EM failure to compare the observed microstructure with the μXCT results. A view of the verification is provided in *Figure 68*. The upper OM micrograph in *Figure 68.a* portrays the tortuous cathode interface after copper migration. The lower OM micrograph in *Figure 68.a* shows a large Cu_6Sn_5 island separated from the Cu_6Sn_5 interfacial intermetallic at the anode by a tin-rich phase, as was similarly observed in the corresponding section of the tomography volume. What is visible in this micrograph, not observed in the segmented volume (*Figure 68.b*), is the accumulation of fine intermetallic precipitates at the grain boundaries ahead of the large intermetallic island. The intermetallic captured in the segmentation, rendered as blue, was confirmed to be Cu_6Sn_5.

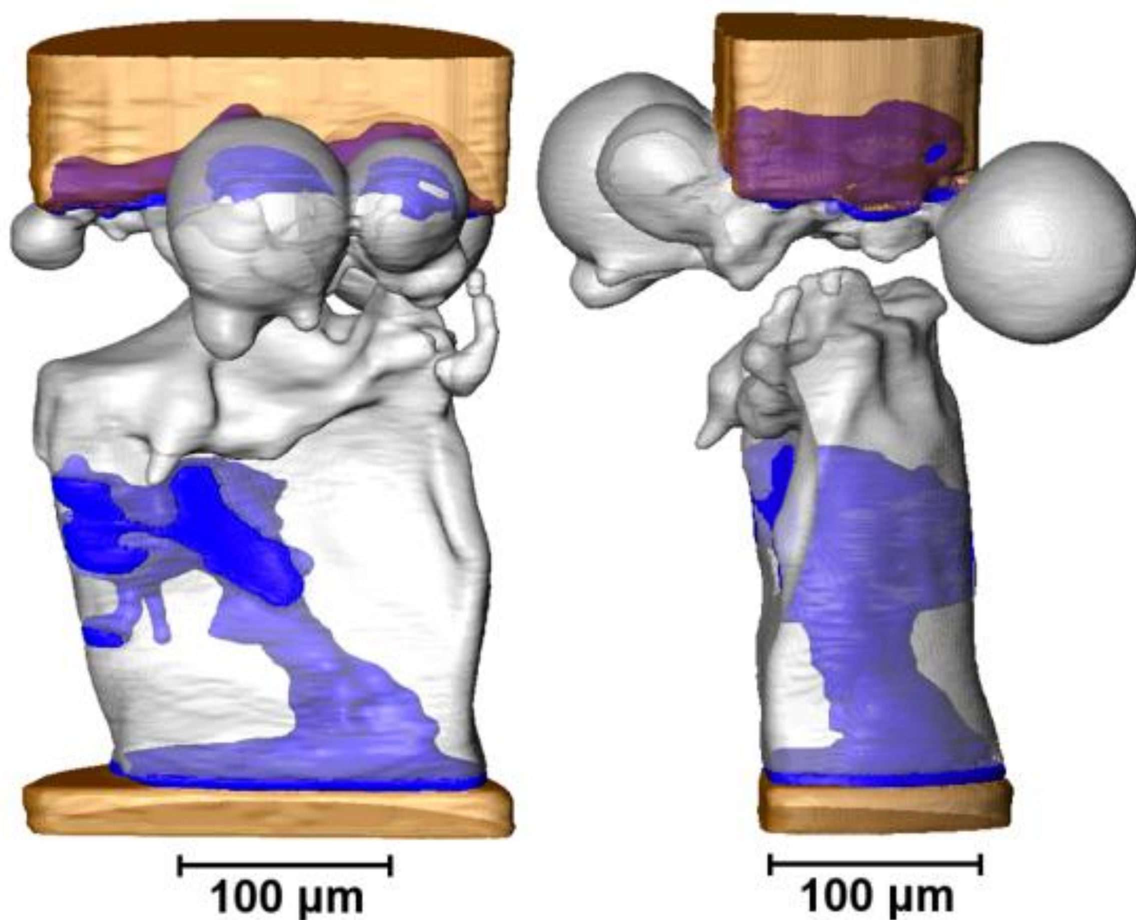

Figure 67. Volume Rendering of the Post-EM Segmentation for 'Sample 03202014JointD', Showing Copper (Orange Transparent), Tin-Rich Solder (Gray Transparent), and Intermetallic (Blue) Portraying the Large, Connected Intermetallic Structure Branching Down to the Anode Interface

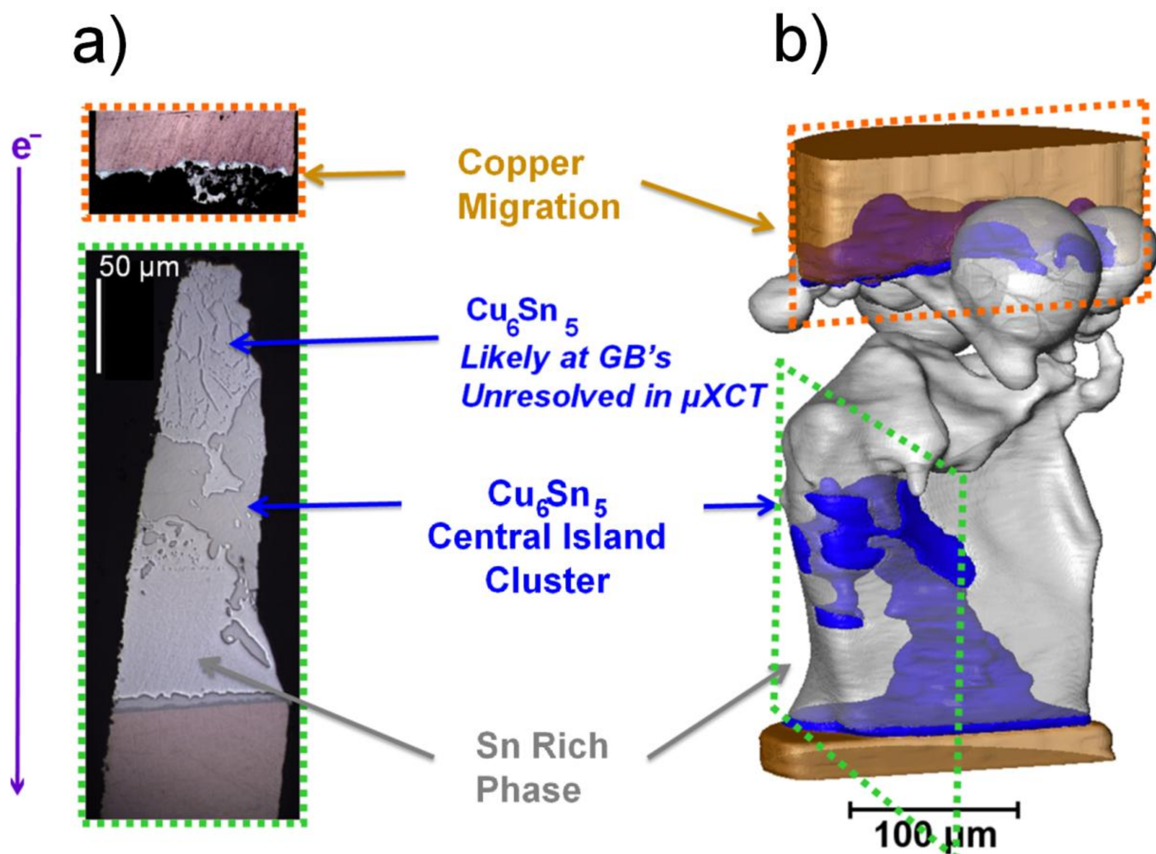

Figure 68. Comparison of the Post-EM Volume Segmentation with Destructive Surface Imaging Observations *a*) OM Bright Field Micrographs of the Cathode and Anode Halves After Failure *b*) Segmented Volume of the Post-EM Microstructure

A summary of the total volume of the resolved material phases is presented in *Table 12*. The tin-rich phase was observed to deplete during EM, whereas the copper-tin intermetallic phase was observed to increase. The copper volume near the cathode was also observed to deplete as a result of EM until failure. The total measured depleted copper volume and the total depleted tin-rich volume are summarized in *Table 13*. Also included in this table are the measured intermetallic volume increase and the total change in the joint volume with intermetallic considered as 'joint'.

From measurement of the tin-rich volume prior to electromigration and after electromigration, the total number of 'lost' tin atoms can be approximated. Using the physical properties for density and molar mass of tin and Cu_6Sn_5 (*Table 14*), the maximum volume of intermetallic expected to form can be calculated.

To summarize, the highly deformed joint failure was rather surprising. Unexpected growth structures were observed at the cathode during testing, which are not typically reported in microbump electromigration experiments. The observed void coalescence at the cathode is typical; however, growth structures at the cathode are not. It is generally found that growth structures occur at the anode, but typically this is reported with encapsulated test vehicles. One possible explanation is that these structures were a result of the free surface testing structure, and that migration to the surface was followed by melting caused by large amounts of joule heating during the circuit opening event, but would require more data from a follow-up experiment to confirm.

Table 12

Measured Tin-Rich and Copper-Tin Intermetallic Volume Prior to and After Failure by 220 Hours of 1x10^{4}A/cm² at 100°C in 'Sample 03202014JointD'

Phase	Volume Pre-EM (μm³ /10^6)	Volume Post-EM (μm³ /10^6)
Tin-Rich	4.6	4.1
Cu-Sn Intermetallic	0.17	0.81

Table 13

Measured Phase Volume Change by 220 Hours of Electromigration in 'Sample 03202014JointD' at 1x10 ^{4} A/cm² and 100°C

Electromigration Result	Volume (μm³ /10^5)
Copper Depletion (from localized calc.)	-3.5
Tin-rich Alloy Depletion	-5.2
Joint Gain	+1.1
Gained Intermetallic	+6.3

Table 14

Physical Properties of Copper, Tin, and Cu_6Sn_5 at STP

Electromigration Result	Value
Copper Molar Mass	63.546 gram/mole
Copper Density	8.96 gram/cm^3
Tin Molar Mass	118.71 gram/mole
Tin Density	7.31 gram/cm^3
Cu_6Sn_5 Molar Mass	88.621 gram/mole
Cu_6Sn_5 Density	8.37 gram/cm^3

Similarly, with the lost copper volume at the cathode, the expected volume of Cu_6Sn_5 to form can be determined assuming the copper all reacts to form the intermetallic. The results of this analysis are shown in *Table 15*, and compared with the measured Cu_6Sn_5 volume gain of 6.29E+05μm³. It is worth noting that both calculations gave overestimates. This is expectable, as it was observed that not all copper-tin intermetallic was captured in the segmentation, particularly any fine particles below the resolution limit with the observed contrast. Apart from segmentation errors, the difference between the two calculations may be speculatively attributed to copper consumption elsewhere, such as the formation of Cu_3Sn intermetallic products, or super saturation in the tin-rich phase.

Table 15

Calculated Expected Cu_6Sn_5 Reaction Product Volume Based on Measured Changes in Tin-Rich Volume and Copper Volume Loss and the Deviation from the Measured Value of Intermetallic Volume by Assuming Complete Reaction and Complete Resolution of the Intermetallic

Basis	Expected Volume of Cu_6Sn_5 (μm^3)	Difference from Measured
Tin-rich Depletion	7.75E+05	+23%
Copper Depletion	9.52E+05	+51%

7.4 ANALYSIS AND DISCUSSION

Previous studies have provided insight into the diffusion of copper and tin during electromigration (Ke *et al.*, 2011). The electron wind force causes both the migration of copper and tin away from the cathode toward the anode. Copper atoms are present as interstitials in tin solid solutions, and thus the diffusion of copper in tin has a lesser temperature dependence than that of tin substitutional self diffusion which has a strong temperature dependence due to vacancy dependent mechanisms. Tin is tetragonal at room temperature up to its melting point, and diffusion is highly anisotropic, with varying diffusion rates along the a- or c-axis for both tin self diffusion and copper interstitial diffusion. Following the analysis of Ke *et al.* (Ke *et al.*, 2011), focusing on diffusion rates along the a-axis which have been more widely studied, the diffusion rates of copper and tin were compared for different temperatures. In the electromigration test for 'Sample 03202014D', a maximum temperature of 135°C was observed. At this temperature, the ratio of copper diffusivity along the a-axis in tin relative to tin self diffusivity is approximately 4E+05; in other words copper diffusion is about one-half-of-a-million times greater. A visualization of the diffusivity of copper in tin and tin self diffusion is provided in *Figure 69*, as adapted from Ke *et al.* (Ke *et al.*, 2011).

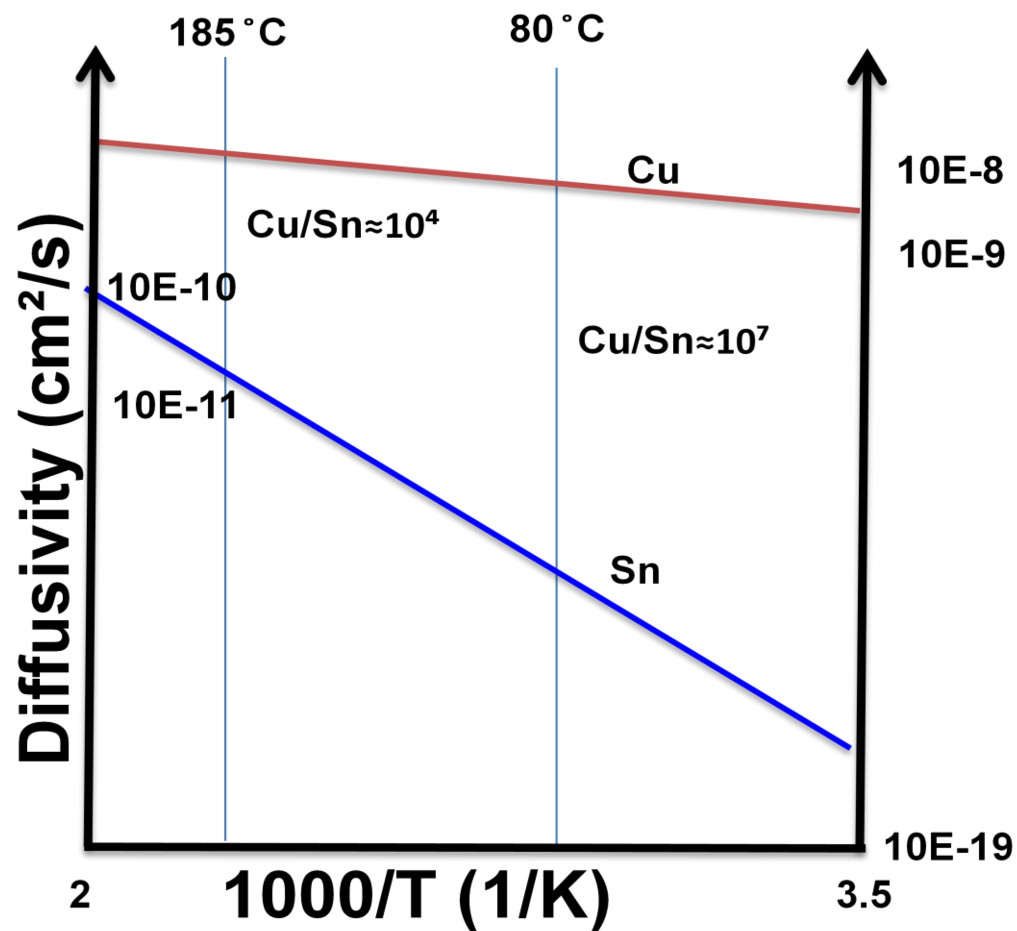

Figure 69. The Diffusion of Copper and Tin Along the A-Axis of Tetragonal Tin as a Function of Temperature (Ke *et al.*, 2011)

However, despite the massive difference in diffusivity between copper and tin in tin, the flux of copper atoms is limited by the saturation limit of copper in tin, which is also a function of temperature. The saturation limit of copper in tin, X_{Cu}, which is assumed to be reached, is a function of temperature, T. As shown by Ke *et al.* (Ke *et al.*, 2011), this is given as:

$$X_{Cu} \approx 0.9e^{\frac{-37.5\text{kJ/mol}}{RT}}. \quad (42)$$

For the case of 100°C applied, and ~35°C temperature increase at the interconnect due to Joule heating, *Equation 42* can be used to determine the saturation limit in tin:

$$X_{Cu}(135°\text{C}) \approx 1.4*10^{-5}\ . \quad (43)$$

The ratio of the atomic flux of copper, J_{Cu}, to that of tin, J_{Sn}, along the a-axis in tin is given as:

$$\frac{J_{Cu}}{J_{Sn}} \approx X_{Cu}\frac{D_{Cu}}{D_{Sn}}, \quad \frac{J_{Cu}}{J_{Sn}}(135°\text{C}) \approx 7. \quad (44)$$

Therefore, assuming this same proportionality of diffusion between components along the c-axis, one can expect copper migration to dominate over that of tin by a factor of approximately seven.

The electromigration resistance is often quantified using *Equation 45*, assuming no compressive stress build up in the solder (Gan and Tu, 2002, Gan and Tu, 2002), where J_A^{EM} is the flux of component 'A' in the host lattice, C_A is the concentration of component 'A' in the host lattice, $\widetilde{D}_A$ is the effective diffusivity of component '*A*' in the host lattice, kT is the thermal energy, Z_A^* is the effective charge of component '*A*' during electromigration, e is the fundamental charge, ρ is the resistivity, and j is the current density:

$$J_A^{EM} = C_A \frac{\widetilde{D}_A}{kT} Z_A^* e\rho j \, . \tag{45}$$

Of most interest is the diffusivity term, as this value has implications on the active mechanism of diffusion during electromigration. Although literature values have been reported for the effective charge of tin during electromigration testing in tin based alloys (Gan and Tu, 2002, Gan and Tu, 2002), similar reports for the effective charge of copper in copper or copper in tin haven't been identified. Accordingly and as is commonly performed in studies in the relevant literature, the term sought herein to be calculated was the product of diffusivity and effective charge for components of interest, that is, $\widetilde{D}_{Cu} Z_{Cu}^*$ and $\widetilde{D}_{Sn} Z_{Sn}^*$, which is a useful metric for electromigration tolerance. This value can be expressed as:

$$\widetilde{D}_A Z_A^* = \frac{J_A^{EM} kT}{C_A e\rho j} \, . \tag{46}$$

Hence, the value which need be known for accurate determination of the diffusivity-charge product quantity is the flux of the component due to electromigration. The flux is defined as the number of species to traverse a unit area per unit time. Thus, the flux of a species can be expressed using *Equation 47* where N is the number of atoms which have migrated through a cross section of area, A, within a time, t, of electromigration:

$$J_A^{EM} = \frac{N}{A \cdot t}. \tag{47}$$

With the application of μXCT, the number of tin atoms and copper atoms which have migrated, and the initial cross sectional areas of each conductor, can be easily calculated. For the case of Sample 03202014D, the volume of copper which has migrated from the cathode is reported in *Table 6* and visible in *Figure 67*. Using the values in *Table 6*, the number of copper atoms which have migrated was approximated. The initial cross section of the copper conductor was measured to be 2.0E-04cm², and over 220 hours of migration, the atomic flux of copper was approximated as:

$$J_{Cu}^{EM} = \frac{\text{2.95E16 Cu Atoms}}{(\text{2.0E-04cm}^2 \cdot \text{792E+03s})} = \text{1.83E+14 Cu atoms cm}^{-2}\text{s}^{-1}. \tag{48}$$

With a measure of the atomic flux of copper, the product of copper's effective diffusivity in the tin-copper alloy can be approximated as:

$$\widetilde{D}_{Cu} Z^*_{Cu} = \frac{J^{EM}_{Cu} kT}{C_{Cu} e \rho j} \approx 4.619\text{E-05} \frac{\text{cm}^2}{\text{s}} \ . \tag{49}$$

Of course, the temperature and resistance were not constant during electromigration, and the values used in the above calculations were approximations. The current density used for approximation was also an estimate, more specifically an underestimate, as this value corresponds to the initial minimum cross section of the solder. The product of the effective charge and diffusivity can be similarly calculated for the tin component. Whereas the copper migration was easily visualized by the resulting tortuous cathode interface, the migration of tin atoms can be monitored though the evolution of the tin-rich solder phase. The solder flow beyond the original volume can be visualized in *Figure 70*. In *Figure 70.a*, the tin-rich solder volume which has flown beyond the original volume is rendered in red coloring. This volume was calculated using the segmented tomography volume, and was used for approximation of tin atom migration during accelerating electromigration testing. In *Figure 70.b*, the original solder joint volume is portrayed as transparent and blue, and the post mortem volume can be seen overlain with opaque rendering. In this representation, the flow of solder can be visualized as the gray solid beyond that of the transparent volume.

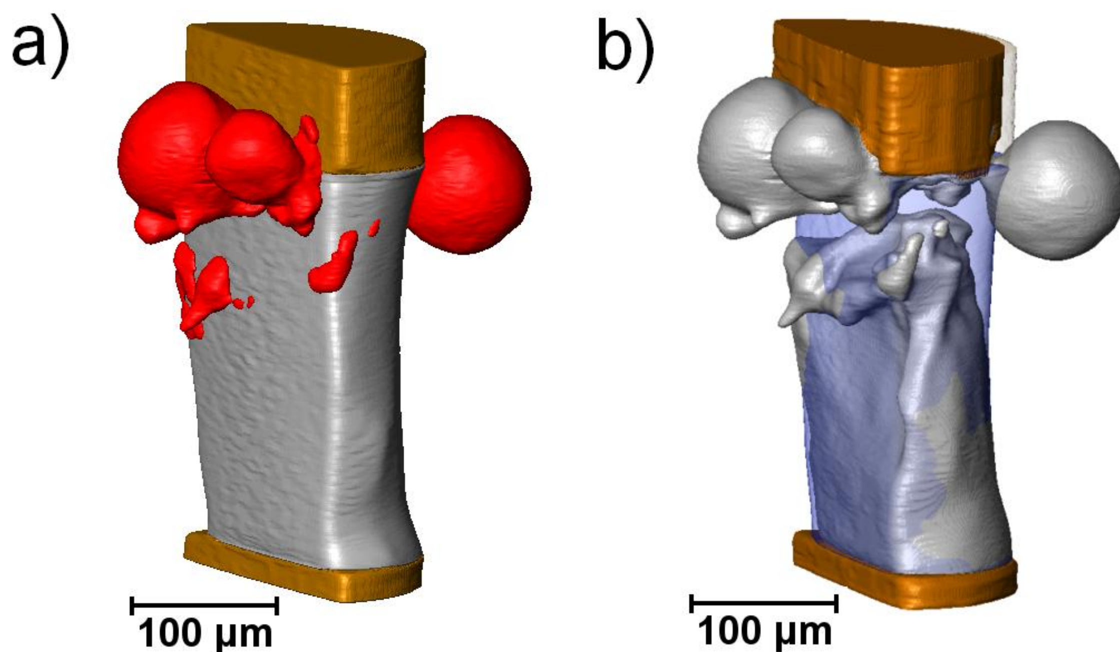

Figure 70. Segmented Rendering Overlay of the Post-EM Solder Volume with that of the As-Processed Solder Volume Highlighting the Mass Transport of the Tin-Rich Solder Phase *a*) Original Volume Shown as Opaque Gray and the Final Volume Shown as Red *b*) Original Volume Shown as Transparent Blue and the Final Volume Shown as Opaque Gray

Similar to as was performed for the copper analysis, the flux of tin due to electromigration can be calculated as:

$$J_{Sn}^{EM} = \frac{\text{5.39E16 Cu Atoms}}{(\text{1.51E-04cm}^2 \cdot \text{792E+03 s})} = \text{4.5E+14 Sn atoms cm}^{-2}\text{s}^{-1}. \tag{50}$$

The flux of tin was then used for determination of the product of the effective diffusivity and effective charge:

$$\widetilde{D}_{Sn} Z_{Sn}^{*} = \frac{J_{Sn}^{EM} kT}{C_{Sn} e \rho j} \approx \text{4.25E-10} \frac{\text{cm}^2}{\text{s}} . \tag{51}$$

Before a discussion of the calculated $\widetilde{D}Z^{*}$ values, it is worth investigating the relative magnitudes of copper and tin flux which were calculated relative to what is expected at the active temperature based on tin a-axis diffusion. From tomography measurements:

$$\frac{J_{Cu}}{J_{Sn}} \approx \frac{\text{1.83E+14 Cu atoms cm}^{-2}\text{s}^{-1}}{\text{4.5E+14 Sn atoms cm}^{-2}\text{s}^{-1}} \approx 0.4 . \tag{52}$$

This ratio was roughly 18 times lower than was expected from the thermal migration considering diffusion along the a-axis in tin. It thus appeared that with surface diffusion, grain boundary diffusion, c-axis diffusion, and dislocation core diffusion that the diffusion of tin is tipped toward being the dominant migrating species by a factor or roughly 2.5 times over that over copper at the temperature investigated.

Regarding the product of diffusivity and effective charge for each species, some assessments were made to glean the underlying mechanisms for electromigration. One literature study reports an effective charge of tin in a tin-based alloy to be Z^*_{Sn} = 18 in electromigration observed near 10^4A/cm² and 100°C (Gan and Tu, 2002, Gan and Tu, 2002). Using this value, $\widetilde{D}^{EM}_{Sn}$ was compared with $D^{a\text{-}axis}_{Sn}$:

$$\frac{\widetilde{D}^{EM}_{Sn}}{D^{a\text{-}axis}_{Sn}} \approx \frac{(4.25\text{E-}10\text{cm}^2/\text{s})\ /\ 18}{3.16\text{E-}13\text{cm}^2/\text{s}} \approx 75\ . \tag{53}$$

In other words, the active diffusion mechanism through which tin atoms appear have migrated is roughly 75 times greater than is expected from substitutional self diffusion of tin along the a-axis. As mentioned, this may have been an effect of the c-axis diffusion, grain boundary diffusion, or free surface diffusion, or could also be related to shortcomings in the tomography feature resolution. The calculated values for $\widetilde{D}_{Sn}Z^*_{Sn}$ and $\widetilde{D}_{Cu}Z^*_{Cu}$ were also compared in a relative sense to the expected thermal migration contributions from considerations of bulk diffusion of copper and tin along the a-axis in a tin lattice. This was expressed as:

$$\frac{\widetilde{D}_{Cu}Z^*_{Cu}}{\widetilde{D}_{Sn}Z^*_{Sn}} \approx 1.1\text{E}5, \text{ and, } \qquad \frac{D^{a\text{-}axis}_{Cu}}{D^{a\text{-}axis}_{Sn}} \approx 4.0\text{E}5\ . \tag{54}$$

As it was expected that the effective charge for tin and copper should be on the same order of magnitude, it was a reassurance to the reasonability of the above analysis that the two above ratios were of the same order. If it were assumed that the active diffusion mechanisms during

electromigration possessed the same copper-to-tin diffusivity-ratio as that of the a-axis migration in thermal diffusion, than the above relation would indicate that the effective charge of tin is roughly four times greater than that of copper, that is, taking $Z^*_{Sn} = 18$, $Z^*_{Cu} \approx 5$.

The preliminary application of a custom lab-scale x-ray computed tomography system and an *in situ* testing fixture built for the study of microelectronic packaging alloys has proven to be a useful tool for quantifying electromigration induced damage, evolution of microstructure, and migration of atomic constituents under accelerated testing of a eutectic Sn-0.7Cu butt joint. The formation of a copper-tin intermetallic reaction product has been resolved non-destructively in 3D using lab-scale μXCT, confirmed to be Cu_6Sn_5 with optical imaging, and the measured volume has been used as a check against the measured copper migration into the solder joint at the cathode in the form of cathode dissolution, and also as a check against the measured loss of tin-rich phase as a result of electromigration and the formation of the copper-tin intermetallic. The atomic flux of copper and tin during electromigration has been quantified using 4D μXCT. A summary of the quantification of the electromigration of tin and copper is provided in *Table 16*. Unexpected growth structures have been observed at the cathode during testing; it was hypothesized that these structures were a result of the free surface testing structure.

Table 16

Summary of Atomic Flux Analysis of Tin and Copper Due to Electromigration, and the Resulting Calculations of the Product of Effective Diffusivity and Effective Charge and a Comparison of the Values Between Tin and Copper

Parameter	Tomography Measured Value
J_{Cu}^{EM} (atoms $cm^{-2}s^{-1}$)	1.8E+14
J_{Sn}^{EM} (atoms $cm^{-2}s^{-1}$)	4.5E+14
$J_{Cu}^{EM} / J_{Sn}^{EM}$	0.40
$\widetilde{D}_{Sn}Z_{Sn}^{*}$ (cm²/s)	4.6E-05
$\widetilde{D}_{Cu}Z_{Cu}^{*}$ (cm²/s)	4.2E-10
$\widetilde{D}_{Cu}Z_{Cu}^{*} / \widetilde{D}_{Sn}Z_{Sn}^{*}$	41.1E5
$\widetilde{D}_{Sn}^{EM} / D_{Sn}^{Sn,\ a\text{-}axis}$	80
$\widetilde{D}_{Sn}$ ($Z_{Sn=18}^{*}$) (cm²/s)	2.3E-11

7.5 SUMMARY

In a Sn-0.7Cu microscale butt-joint on a copper substrate subjected to accelerated electromigration, the migration of copper and tin species, as well as the formation of copper-tin intermetallic, has been observed and quantified in 3D using lab-scale μXCT. The quantification was enabled by the design of a miniature fixture for mechanically constraining microscale specimens, applying high current densities, high temperature, and while enabling imaging of the specimen. The custom μXCT system has demonstrated capability to resolve micro-scale low-contrast features in a Pb-free solder system. The finer intermetallic phases were not resolved, as expected from considering the mass balance in the segmented volumes before and after electromigration. This work has demonstrated the potential of the *in situ* fixture and the μXCT system to characterize microstructural evolution in response to applied electric fields at elevated temperatures.

CHAPTER 8

ELECTROMIGRATION DAMAGE IN SURFACE ENCAPSULATED SN-0.7CU SOLDERS

8.1 INTRODUCTION

In **Chapter 7**, a preliminary study on the migration of copper and tin in a microscale Sn-0.7Cu solder on Copper substrate using interrupted µXCT was described. More specifically, the capabilities of µXCT for the volumetric quantification of material phase evolution were demonstrated in a faceted butt joint on ~250µm copper wire substrates. The material phases which were observed, and in which evolution was quantified, included a tin-rich solder phase and voiding therein, a pure copper cathode, and intermetallic compound between tin and copper. In that study, an approach was outlined for quantifying the $\widetilde{D}Z^*$ parameter for both copper and tin based on extracting specie flux values from observed phase volume evolution during accelerated EM testing, and by implementing *Equation 42*, *Equation 46*, and *Equation 47*. The failure process at 150°C appears to be neither dominated by solder voiding nor cathode consumption.

Although a proof of concept was achieved for the data acquisition, processing, and analysis, several flaws were identified in the preliminary study described in **Chapter 7** which made the analysis potentially unreliable. The first issue identified was associated with the free-surface joint geometry implemented in conjunction with reexamination of the test specimen only after total failure. These factors led to only a rough estimation of the cross sectional area through which species were migrating during the test, conceivable affecting the measured flux for copper

and tin. The free surface also made it difficult to analyze specie migration with respect to bulk diffusion. Imaging the sample after failure had also made it challenging to analyze specie migration with respect to solid state diffusion processes, as the most-portem specimen appeared to have suffered from melting processes preceding inspection conceivably as a result of high joule heating through the final solder joint ligaments. The experimental setup also resulted in high and unstable electrical resistance realized across the test volume, due to the lengthy lead connections to the power supply in order to test the specimen within the CT chamber, combined with very low gauge leads at the testing fixture in order to minimize mechanical forces acting on the test volume during CT scanning which could yield motion artifacts in the CT reconstruction. The high and unstable lead/specimen resistance led to a questionable specimen temperature during the test as a result of unpredictable and significant joule heating. The approach for heating the specimen during testing was also determined non-ideal. The experimental approach for heating the sample during current stressing with a side-mounting miniature hot plate conceivably resulted in high temperature gradients across the test fixture and the sample. Also, heating the specimen in open air was thought to have resulted in a large thermal gradient between the specimen and the air surrounding the specimen.

The following study was conducted with the intent of eliminating or reducing the aspects of the preliminary study which were deemed analytically problematic. The experimental setup was adjusted to instill minimal and stable joule heating induced temperature increase within the test volumes, to minimize thermal gradients across the testing fixture and in the test volumes, and to reduce surface diffusion. Additionally, the samples in the following study were reexamined after testing before failure had occurred to observe microstructural evolution with minimal change in

the test volumes' cross section and to reduce the potential for liquid state specie migration prior to volumetric imaging. Test specimens were scanned tomographically prior to accelerated EM testing and after >200h of current stressing at high temperature. The specimen testing conditions cover a narrow range of temperature and current density in order to understand the effect of testing parameters on copper and tin diffusion mechanisms and the competition between both failure modes as a result of either specie dominating the migration process.

8.2 MATERIALS AND METHODS

The solder systems tested were all of the same size and composition, adopting the Sn-0.7Cu system in a butt-joint configuration on ~250µm copper wire substrates. In this study, the solder volumes were not faceted, but were instead encapsulated in an epoxy overcoat. After cleaning the solder surface in a bath of isopropyl alcohol, and then in acetone, an epoxy encapsulation was applied to the test solder volumes at ~110°C using a hot plate to rid the solder surface of any moisture. An optical image of an encapsulated solder joint is provided in *Figure 71*. The test joints were then mounted within the containment fixture described in **Chapter 7** (*Figure 56*). Prior to EM testing, the fixture-mounted test specimens were scanned using the lab-scale µXCT system described in the previous chapters. The scans were conducted under the x-ray generation and detection conditions modeled in *Figure 52* in order to strive for maximum contrast of the Cu_6Sn_5 intermetallic within a tin-rich surrounding. The scans, both before and after EM testing for all specimens, were conducted with the x-ray source operating at 160kV and 35µA (5.6W) on a tungsten transmission-style target with a maximum target power rating of 10W. The x-ray source was operated under high-power mode. A steel x-ray beam filter with 0.31mm thickness was used to improve the x-ray beam quality.

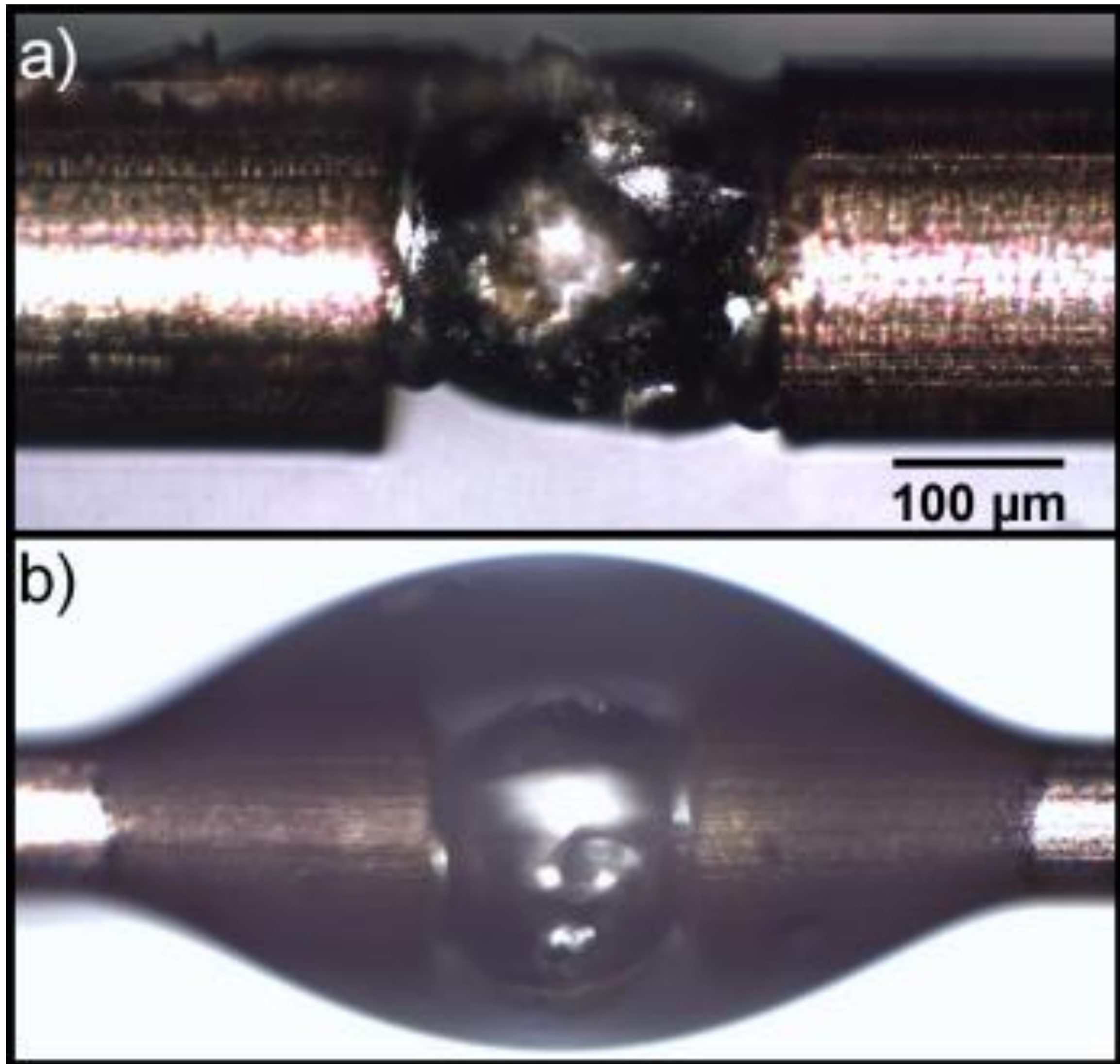

Figure 71. A Sn-0.7Cu Solder on <250µm Copper Wire Butt-Joint Test Specimen Used for Accelerated Electromigration Testing a) After Reflow b) After Epoxy Surface Encapsulation

The x-ray detector consisted of a 250µm LuAG:Ce scintillator coupled to a CCD sensor/camera which has been described in the previous chapters (*Figure 3* and *Figure 4*) using an optical lens at a magnification of 4.186x. The x-ray target to rotation axis distance was approximately 7mm, and an x-ray geometric magnification of 15.5x was used resulting in a field of view roughly twice the joint diameter and a voxel size of 0.4628µm after acquiring x-ray projections in 1024^2 format (Bin 2). Projections were acquired by averaging two 60s exposures using the frame averaging approach described in **Chapter 5** for zinger noise reduction, resulting in approximately 20k background counts. Tomography scanning was performed by acquiring projections over 350° of rotation with a 0.35° angular increment, resulting in 1001 unique x-ray projections for reconstruction. Reconstruction was conducted in MATLAB using an FDK (Feldkamp et al., 1984) cone-beam weighted Shepp-Logan-filtered back-projection algorithm discussed in the previous chapters.

Prior to performing accelerated EM testing at elevated temperature, the cross sectional area of the solder volumes at the cathode interface was measured to determine the necessary applied current to achieve a targeted current density. The fixture-mounted specimens were then placed within a convection furnace, and connected to a power supply using ~2 ft. long 16 AWG lead wires. A thermocouple was also mounted within the fixture as near the test volume as possible to measure the temperature at the test volume which was a product of both applied temperature and joule heating and was monitored throughout the test. The furnace was then heated to the applied temperature and allowed to stabilize for about 10 minutes before a voltage was applied across the sample. The power supply was operated in current control mode, and EM testing was performed using a constant-current condition. The applied temperature and electrical current were held

constant throughout the test for a duration of over 200 hours in each sample. The setup for the electromigration testing is shown in *Figure 72*. The resistance was monitored for a 10% increase as a stop condition for the test, but was not reached in any sample, leading the stop condition in all samples to be based on the testing time. During the test, the applied voltage, applied current, fixture temperature, and test time were monitored using a custom LabVIEW (National Instruments) program. After the duration of the test was reached, the applied current was terminated, and then the heating, allowing the sample to cool to room temperature with no current applied. The test volumes were then again subjected to x-ray computed tomography imaging in order to characterize the microstructural evolution as a result of electromigration induced tin and copper migration in the volumes.

Ultimately, three samples were tested in order to understand the effect of current density and temperature on the observed specie migration. Two were tested at 150°C, and one at 100°C applied temperature. Two samples were tested at ~3.5E4 A/cm², and one at ~1E5 A/cm². The sample testing matrix and testing data is provided in *Table 17*. The recorded applied current, measured test resistance, and measured temperature at the fixture for all three tests are provided in *Figure 73 – Figure 78*.

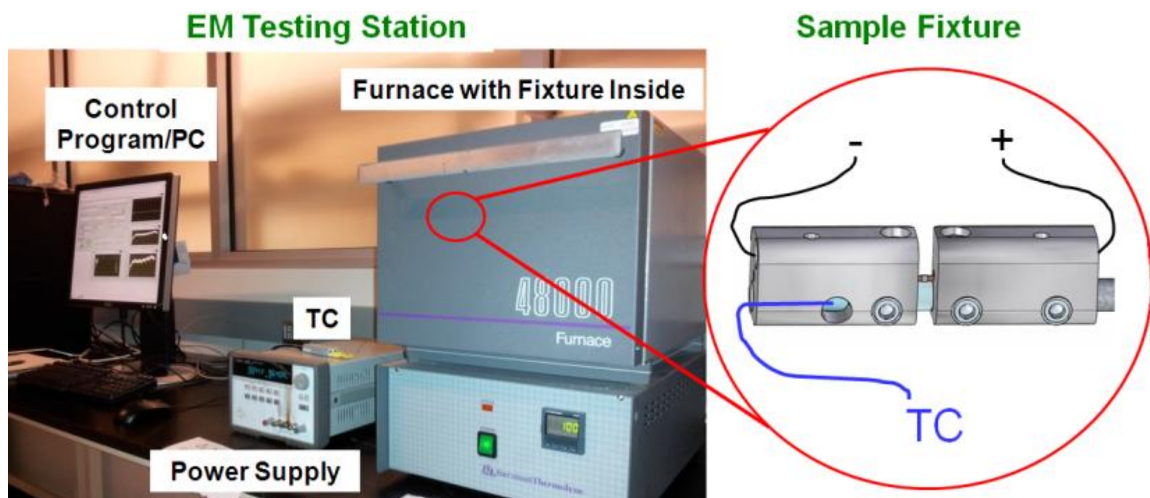

Figure 72. Experimental Setup for Electromigration Testing Including a Testing Fixture, Convection Furnace, Electrical Power Supply, Thermocouple, and Control Station

Table 17

Test Sample Identification Codes and Accelerated Electromigration Testing Conditions and Observed Response for Surface Encapsulated Sn-0.7Cu Solder Butt-Joints on <250μm Diameter Copper Wire Substrates

Sample	92414	101014	120214
Surface Encapsulation	Yes	Yes	Yes
Heating Configuration	Furnace	Furnace	Furnace
T Applied (°C)	150	150	100
Average T (°C)	152.4	150.6	101.1
Average Resistance (mΩ)	4.64	4.49	4.3
Cathode Area (cm^2)	1.89 E-4	2.82 E-4	3.08 E-4
Current Density (A/cm^2)	1.06 E5	4.14 E4	3.13 E4
Current (A)	20	11.7	9.64
Test Duration (h)	215	238	210

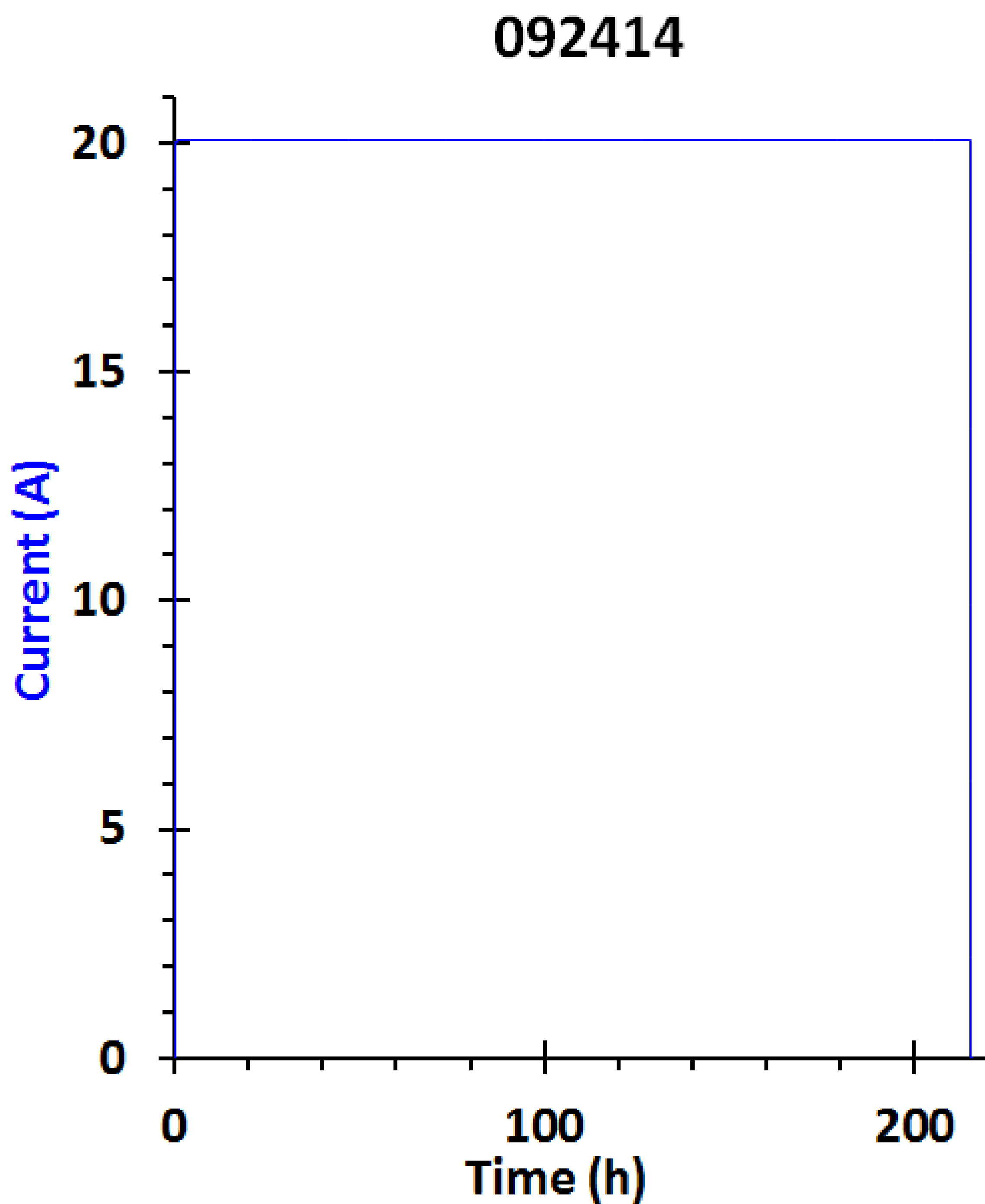

Figure 73. Recorded Electrical Current Applied Versus Recorded Time in Electromigration Testing of Sample 092414, Where the Calculated Initial Current Density in this Sample was 1.06E5 A/cm^2 and the Recorded Test Duration was 215h

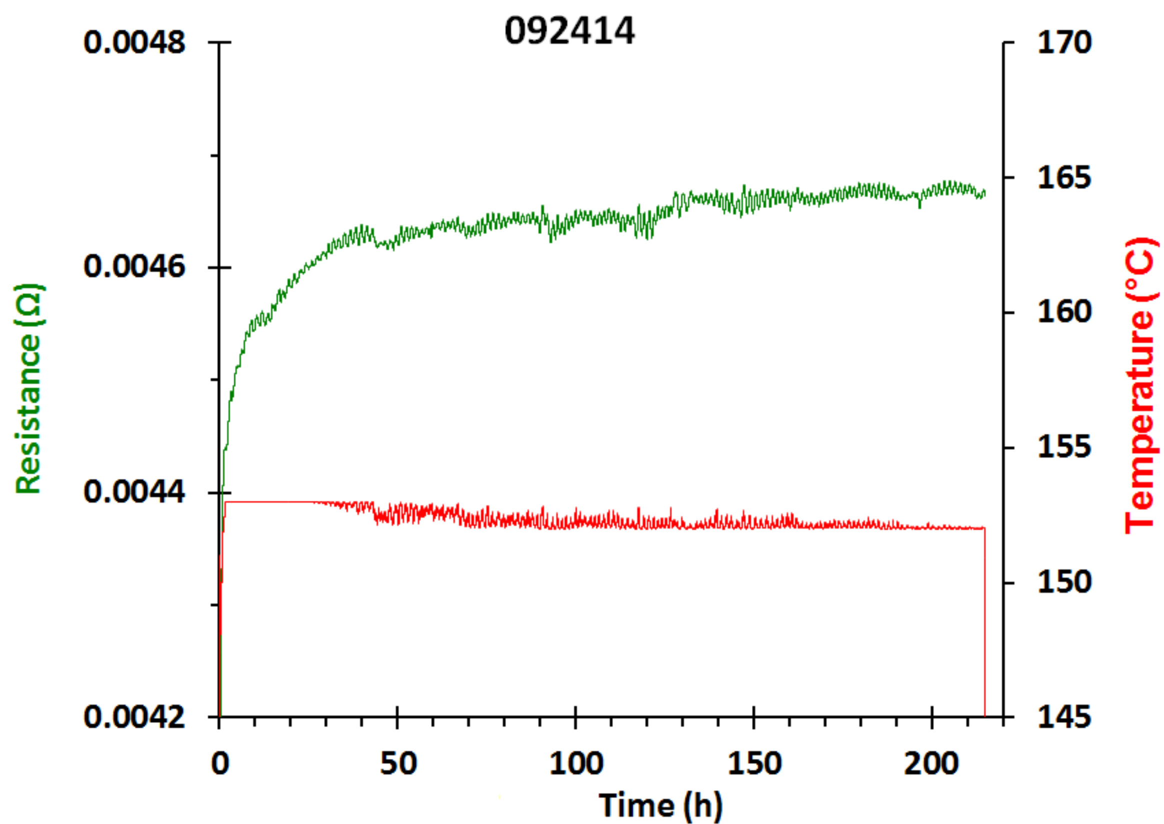

Figure 74. Recorded Test Resistance and Temperature Versus Recorded Time in Electromigration Testing of Sample 092414, Where the Average Recorded Resistance During Testing was 4.64 mΩ and the Average Recorded Test Temperature was 152.4°C, and the Applied Temperature was 150°C

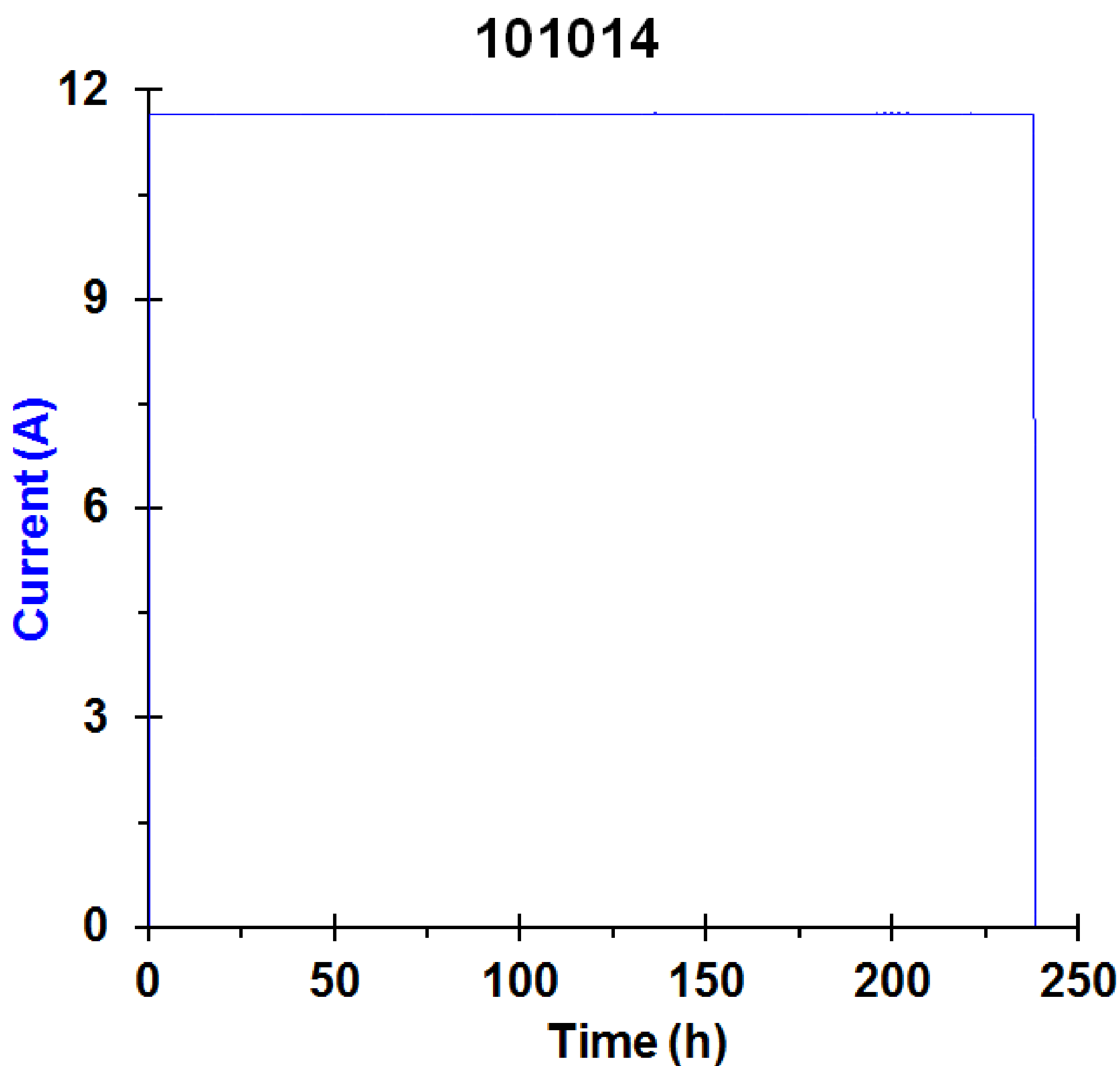

Figure 75. Recorded Electrical Current Applied Versus Recorded Time in Electromigration Testing of Sample 101014, Where the Calculated Initial Current Density in this Sample was 4.14E4 A/cm^2 and the Recorded Test Duration was 238h

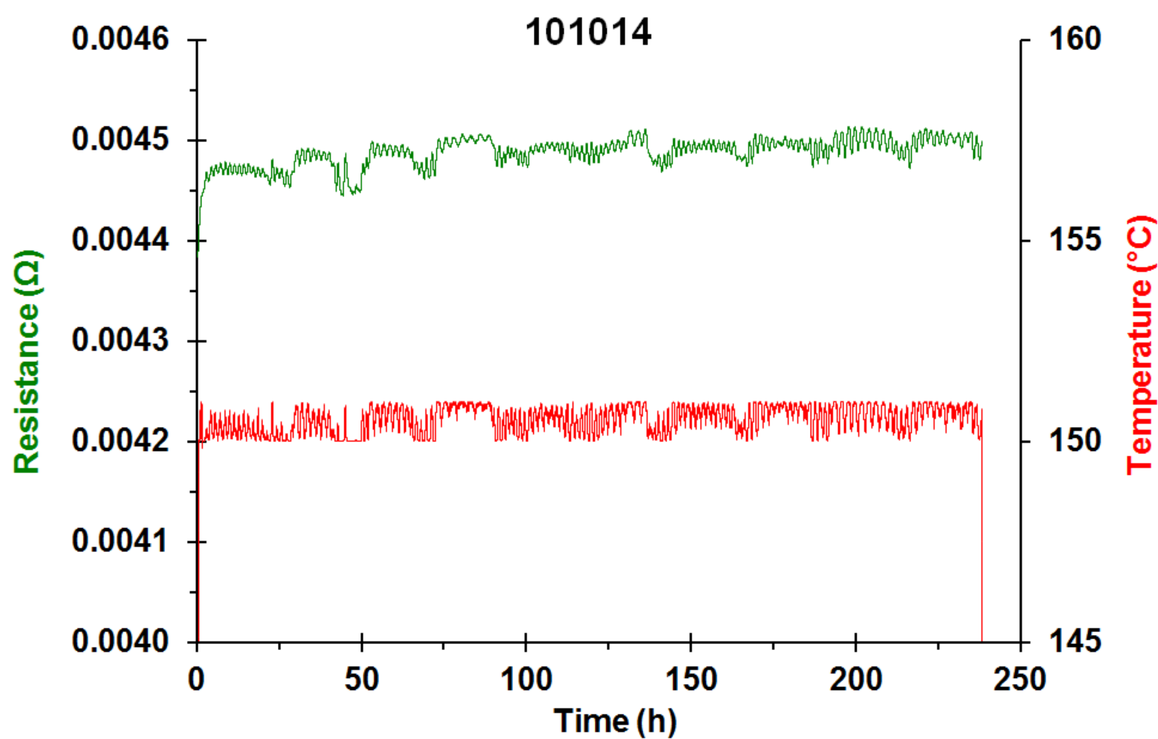

Figure 76. Recorded Test Resistance and Temperature Versus Recorded Time in Electromigration Testing of Sample 101014, Where The Average Recorded Resistance During Testing was 4.49 mΩ and the Average Recorded Test Temperature was 150.6°C, and the Applied Temperature was 150°C

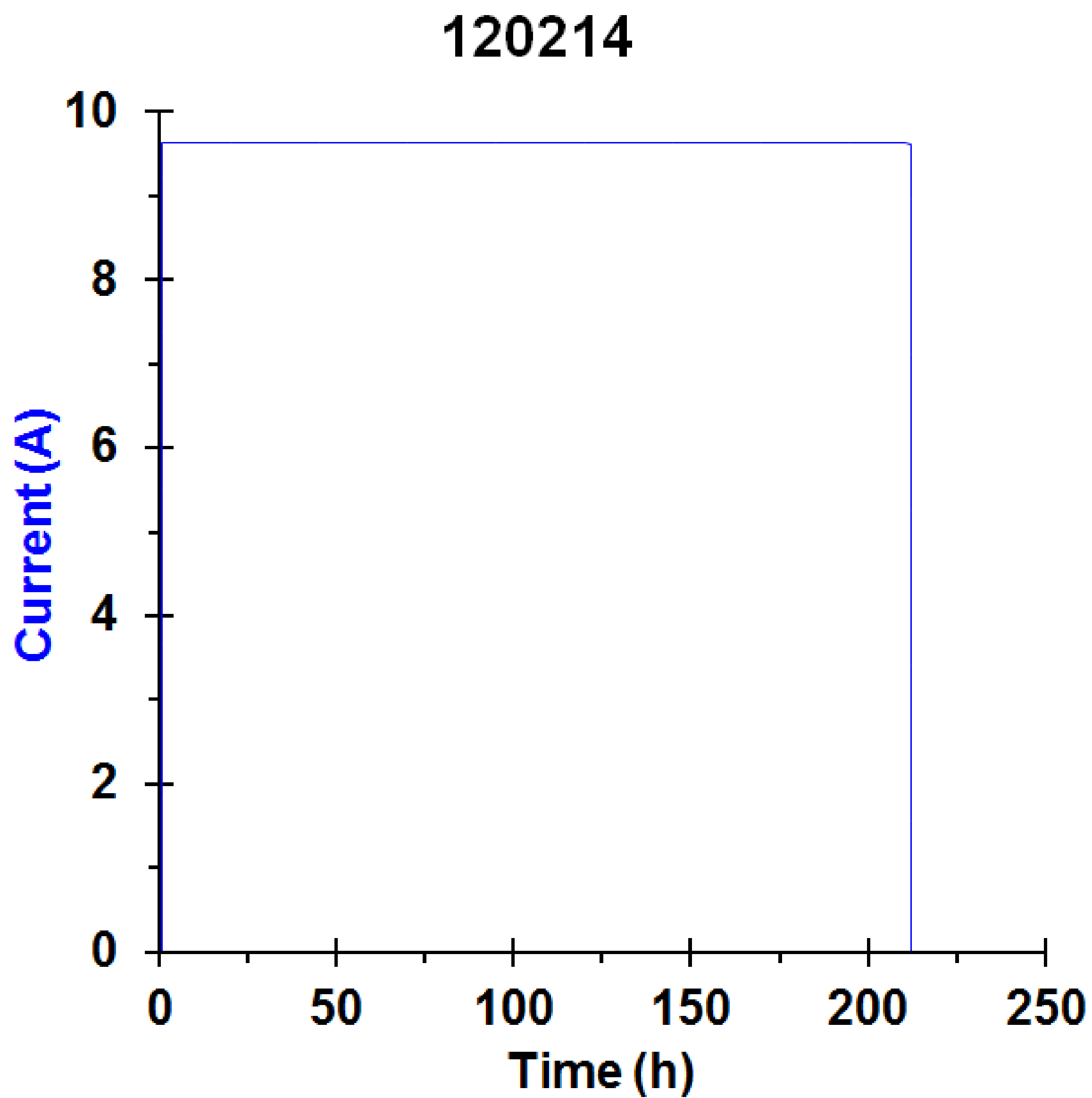

Figure 77. Recorded Electrical Current Applied Versus Recorded Time in Electromigration Testing of Sample 120214, Where the Calculated Initial Current Density in this Sample was 3.13E4 A/cm^2 and the Recorded Test Duration was 210h

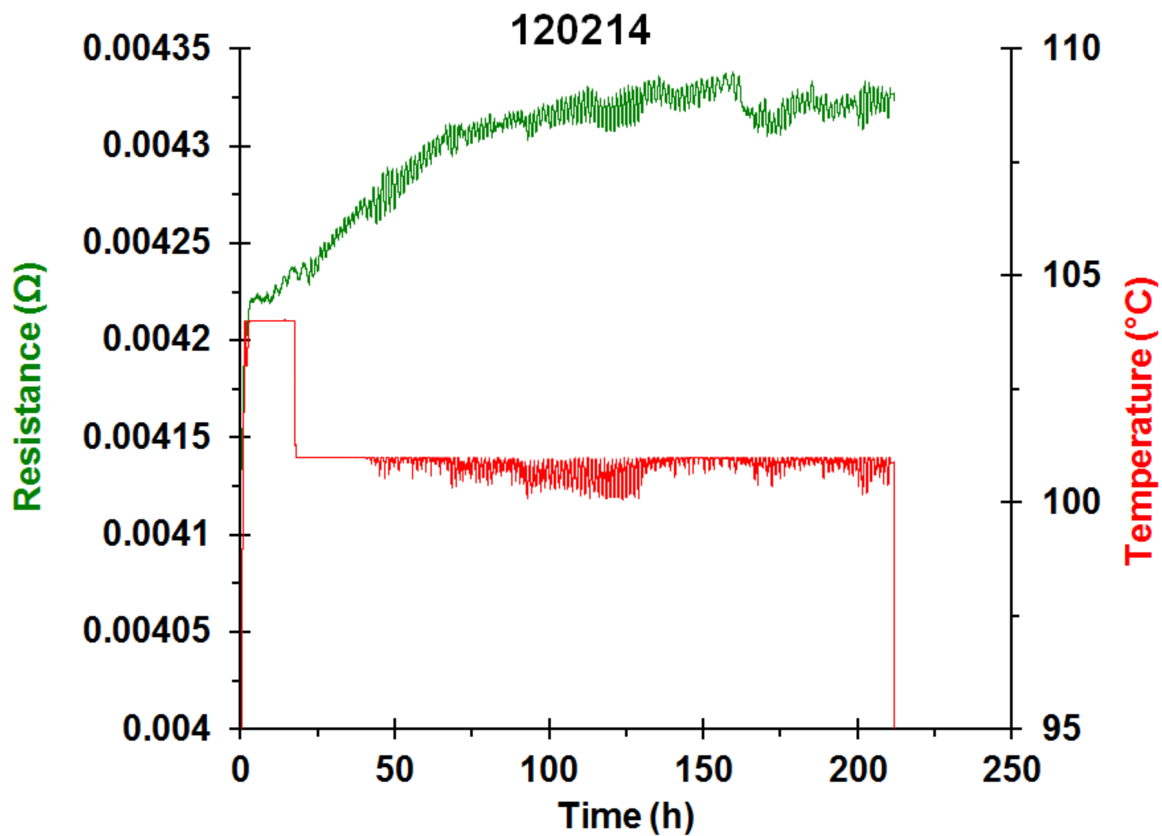

Figure 78. Recorded Test Resistance and Temperature Versus Recorded Time in Electromigration Testing of Sample 120214, Where the Average Recorded Resistance During Testing was 4.30 mΩ and the Average Recorded Test Temperature was 101.1°C, and the Applied Temperature was 100°C

For analysis of microstructure evolution through tomography imaging, it was found ideal to first align the tomography reconstructions (shown schematically in *Figure 79*). This was performed by first performing rotational alignment such that the cathode interface was parallel to the plane of the data volumes which originally had contained the reconstruction planes and the x-ray fan plane. Then, the data sets were again aligned rotationally to one-another, but in the plane containing the cathode interface. After rotational alignment, the datasets were translation-aligned in the 'vertical direction', along the axis of the copper wire lengths, and the translation-aligned in the plane of the cathode interface, effectively completing the alignment process. Before cropping the reconstruction volumes, which spanned roughly twice the required length in any direction to encompass the solder volumes, to minimize the data size and aid in image segmentation, a 4x downsizing step was applied to minimize the noise in the data and bring the voxel size nearer to the anticipated resolution of the CT scan, limited by the penumbra effect of the x-ray target focal spot. As the voxel size in the as-reconstructed data had a size of 0.4628µm, the 4x downsizing of the volume resulted in a voxel size of 1.810µm, by averaging neighboring 4x4x4 voxel cube's intensity values into a single voxel. Finally, the data was cropped so as to encompass the entire solder volume and 20 voxels of the copper substrate past the copper-solder interface of both the anode and the cathode.

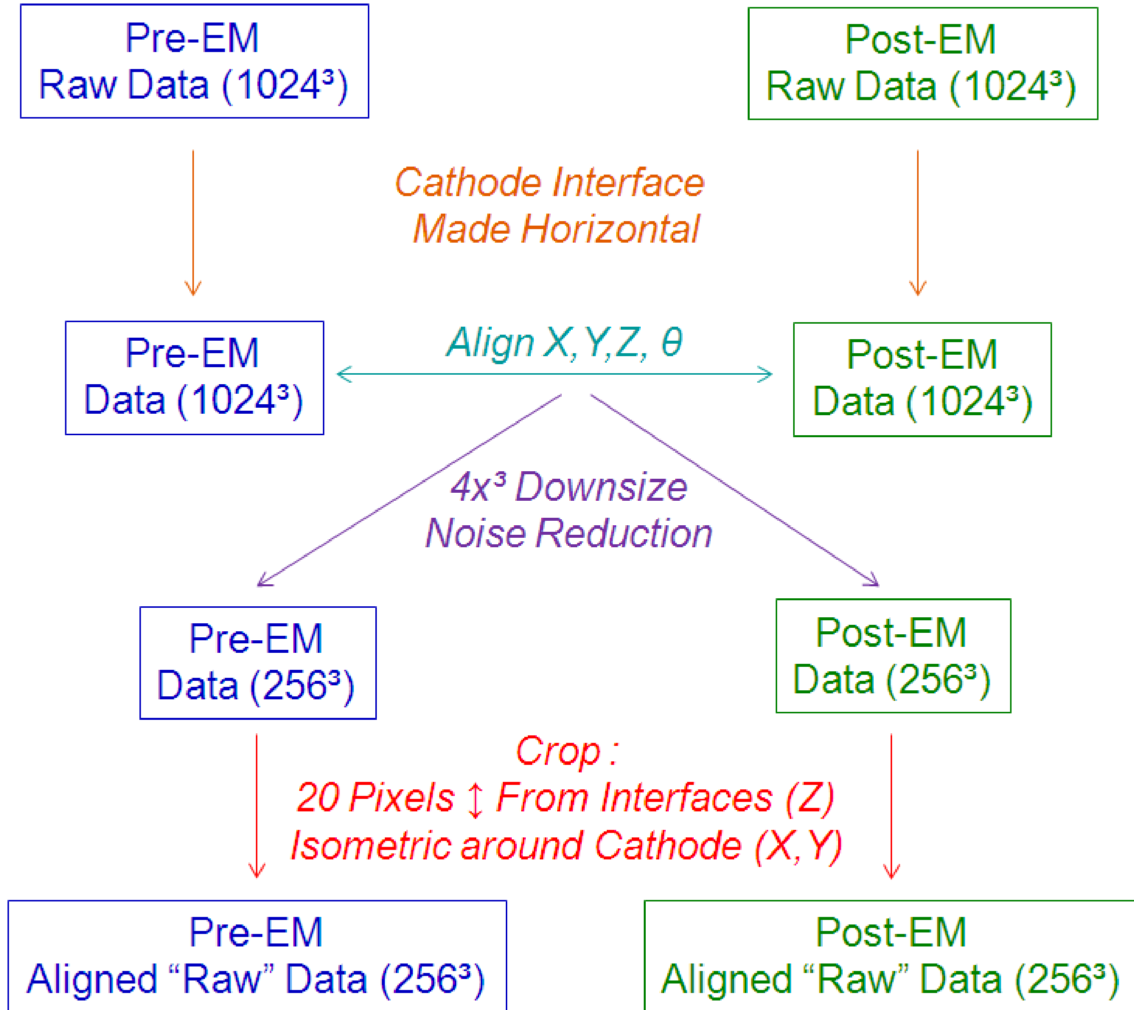

Figure 79. Data Processing Flowchart for Analysis of Four-Dimensional Imaging Data Containing Electromigration Induced Structural Evolution

After the pre and post electromigration datasets of each sample were aligned in this fashion, the datasets were processed for feature segmentation. A wide range of filtering processes were used in order to enhance the effectiveness of segmentation techniques and depending on the phase being targeted for segmentation. Essentially, the segmentation for a particular phase was performed on the volume noise-filtered in a particular way, and combined with the segmentation of another phase deriving from a version of the original volume noise-filtered in a different manner. Four phases were targeted for segmentation: Sn-rich solder, Cu substrate, Cu-Sn intermetallic compound, and contained void (apart from the 'exterior'). All filtering and segmentation was performed using the Avizo Fire software package. The implemented filtering routine was determined by trial-and-error results in attempting to elucidate the phase of interest from the very noisy raw data. For void segmentation, a 3D Gaussian filtering with a sigma of 0.5 and a 3^3 kernel was applied before using local thresholding to capture the observed voids. The Sn-rich and Cu phases were obtained by then following with a 2D adaptive Non-Local Means filtering in the planes perpendicular to the cathode interface with a search window of 61, a local neighborhood of 3, a similarity value of 0.6. Using this method, global and local thresholding were used to capture the Sn-rich solder and copper phases. Capturing the IMC phases required further effort. A primary artifact which inhibited IMC segmentation in the raw data was the beam-hardening induced intensity cupping seen across the sample cross sections. The cupping artifact is described as voxels near the periphery of the sample possessing higher intensity values on average than voxels at the interior of the sample, even if sampling material of the same density and composition, as described in **Chapter 6**. A beam-hardening cupping correction has been constructed (Mertens et al., 2014b) and has already been described in **Chapter 6**. The correction method requires a segmentation (or mask) of the phase exhibiting intensity cupping.

For this purpose, the mask of the solder phase obtained using the segmentation method described above was used as an input. The grayscale data input into the algorithm was the raw (aligned and downsized only) reconstruction volume. The beam hardening corrected data was then filtered using a SNN filter with a kernel size of 3^3 voxels, followed by a 2D adaptive Non-Local Means filtering with a search window of 5 and a local neighborhood of 3, and anisotropic diffusion filtering with 5 iterations using the maximum contrast threshold. Finally with this method, the interior intermetallic was possible to segment using local thresholding. The interfacial intermetallic, when sought, was also captured using local thresholding, but instead, on the raw data which has only been 3D Gaussian filtered as discussed above, which was the same volume from which voids were extracted if present. This entire processing and segmentation approach was performed on all sample reconstructions in both the as-processed and post-EM conditions. The data processing and segmentation approach for a given reconstruction volume is provided schematically in *Figure 80*. The filtered grayscale datasets and the ensuing segmented volumes were found to yield reasonable results in line with the grayscale data intensity values and the high-level knowledge of the material system. A comparison of a particular slice of the filtered reconstruction for copper/solder compared with the same slice of the same reconstruction though filtered for IMC segmentation and the same slice of the segmented reconstruction for one of the samples after electromigration testing is provided in *Figure 81*.

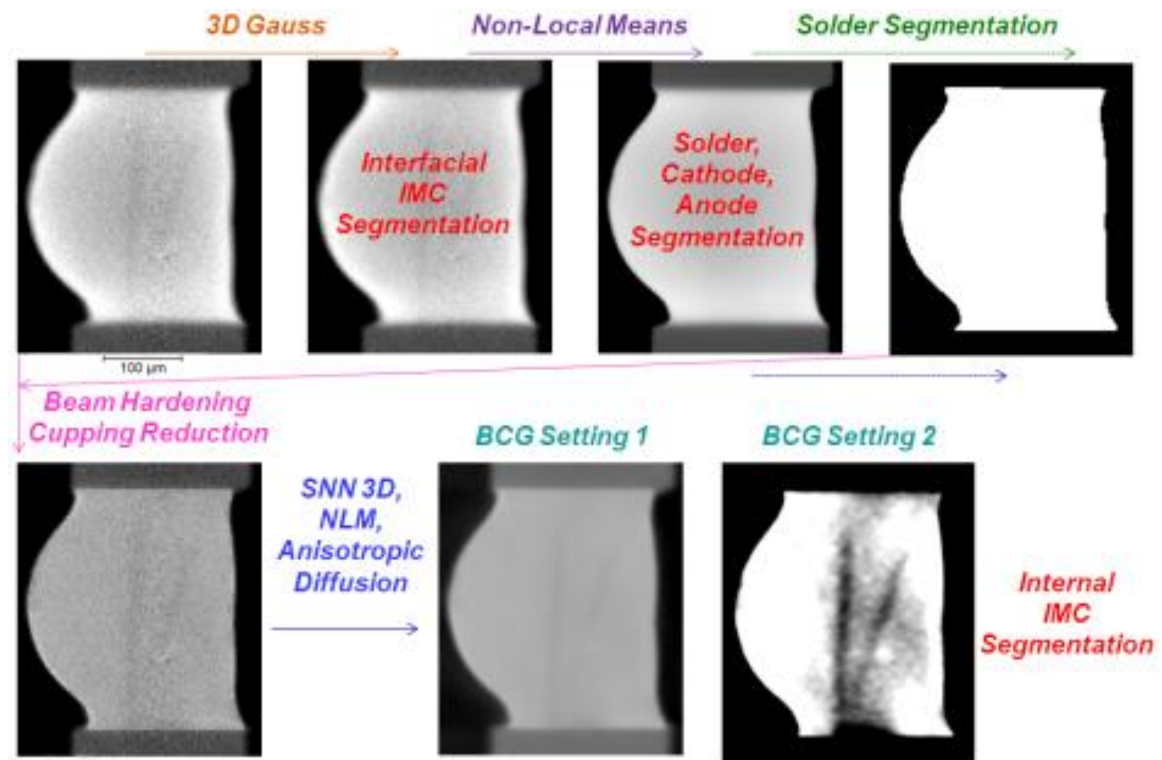

Figure 80. Data Processing Flowchart for Analysis of Four-Dimensional Imaging Data Containing Electromigration Induced Structural Evolution

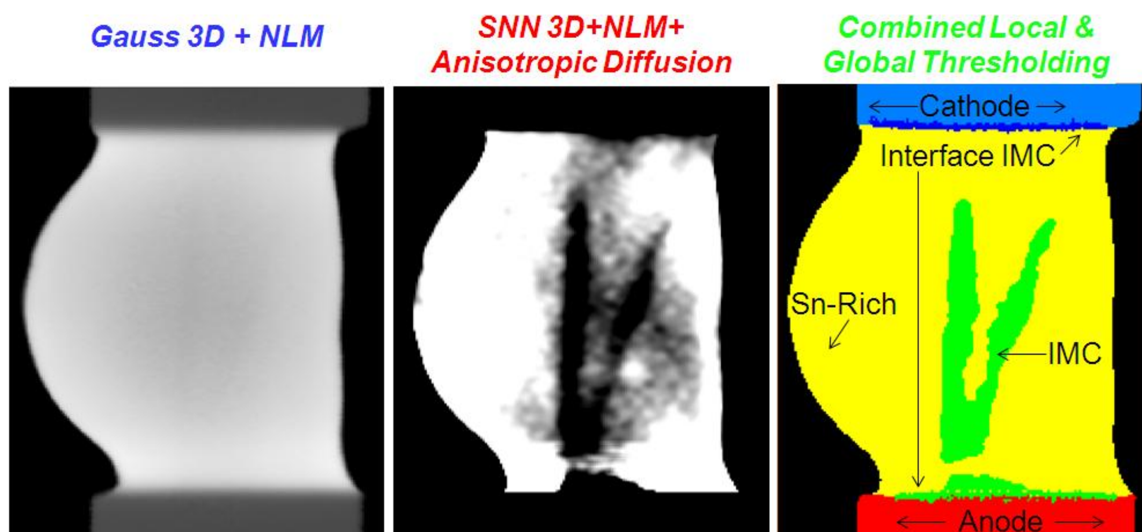

Figure 81. A Single and Identical Tomography Slice of the 101014 Sample Volume Imaged After Current Stressing Compared Between the Filtered State for Copper/Solder Segmentation, the Filtered State for IMC Segmentation, and the Full Segmentation

8.3 RESULTS

The segmented x-ray tomography reconstruction volumes of each sample before and after imaging are provided in both volumetric and two dimensional representations in *Figure 82 – Figure 84*. In each volume, measurement of the phase volumes was performed. The difference between the measured volumes before and after electromigration was used to calculate the atomic flux for copper and tin by considering the phase density, molar mass, and stoichiometry, cathode cross sectional area, and the temporal duration of current stressing. The segmented IMC was assumed to be Cu_6Sn_5 in all cases, which is known to be an oversimplification, particularly at the copper-solder interface where Cu_3Sn is known to form, although no Cu_3Sn has been observed at the interior of any samples of the same composition with the same processing applied, which is a reasonable observation considering the tin-rich nature away from the copper wire substrates.

During electromigration testing at elevated temperature, some compression of the joint is conceivable as a result of thermal expansion in the copper wires which are both much longer and stiffer than the solder volume. However, after cooling back to room temperature, it would be expected that any compression of the joint would be alleviated, that is, no change is the solder joint bridge length was expected upon reexamination of the test volume after EM testing. In this case of the 101014 sample tested at 150°C, this expectation was met. However, in the 120214 sample tested at 100°C, a compression of 9.4% was observed and measured. Even more unexplainable, in the 092414 sample tested at 150°C, a 10.4% elongation was observed and measured. Several factors may influence this result. Firstly, during electromigration testing, compressive stresses are expected to form in the solder volume as a result of tin migration

toward the anode, which could conceivably affect the solder volume and the overall change in bridge length. Secondly, the formation of intermetallic compound within the solder volume as a result of cathode consumption could conceivably affect the joint bridge length, both due to change in the joint's density and volume as well as a result of the migration of the interface during cathode consumption. Furthermore, the epoxy encapsulation may not be stable at temperatures above 100°C, and could change in stiffness before and after testing, and the expansion of the epoxy itself could apply some mechanical forces on the solder joint. For example, if the epoxy between the cathode and anode expands significantly, it could cause a tensile elongation of the solder bridge length, and if it were to then decompose, it may not release the tensile load upon cooling, which could be an explanation for the observed elongation in the 092414 specimen. Alternatively, if the epoxy were to undergo shrinkage as a result of decomposition at elevated temperature, as reduction in the bridge length might be possible, as was observed in the 120214 sample. However, the lack of any observed change in solder bridge length in the 101014 sample, tested at 150°C, does not support these scenarios, and the lack of consistency across the samples in the nature of the bridge length change makes it challenging to explain the cause of the change in bridge length. Variation in the holding force of the specimen constraining fixture screws, or variation in surface friction, could also have led to variation in the slippage of the joint in the fixture at elevated temperature. Finally, mishandling of the miniature samples is another possibility, which seems unlikely, as they were secured within the testing fixture. Without further investigation, no sound explanation can be suggested. In the ensuing analysis, the change in the bridge length is neglected, and only the volume change of the various segmented phases is considered.

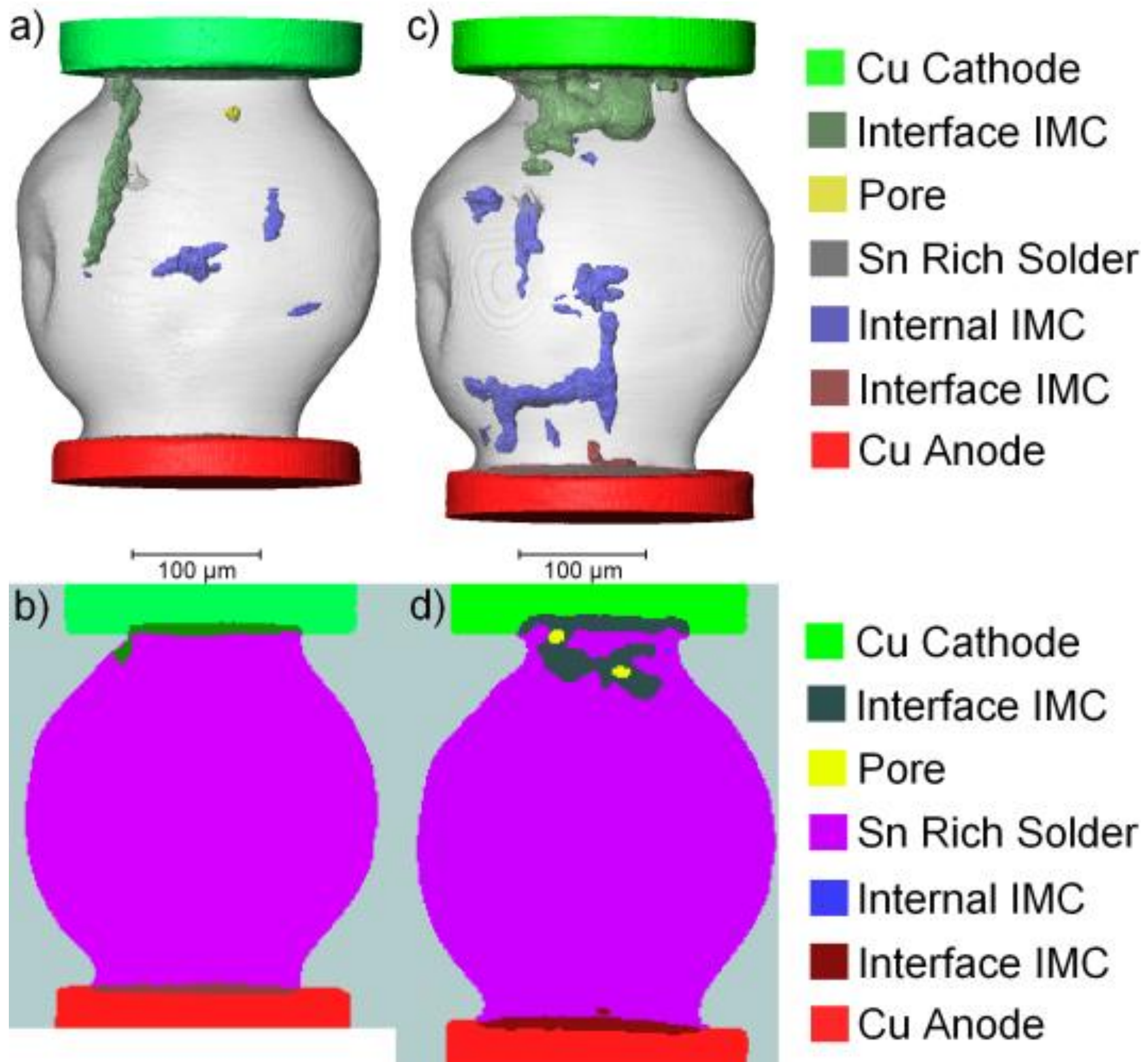

Figure 82. Segmented X-Ray Computed Tomography Representations of Electromigration Induced Microstructural Evolution in Sample 092414 a) As-Processed, Volume Rendering b) As Processed, 2D Section c) After Current Stressing, Volume Rendering d) After Current Stressing, 2D Section

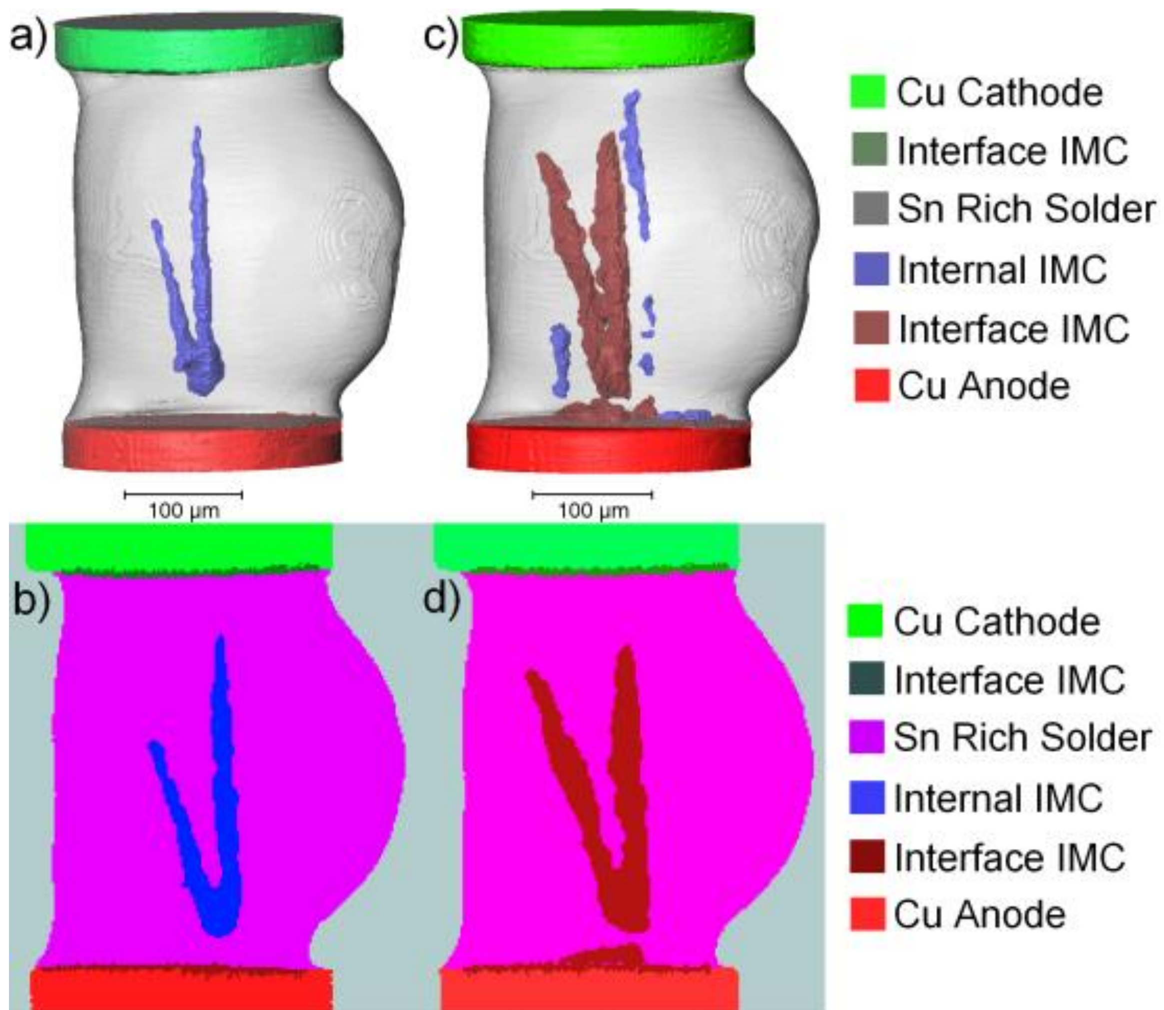

Figure 83. Segmented X-Ray Computed Tomography Representations of Electromigration Induced Microstructural Evolution in Sample 101014 a) As-Processed, Volume Rendering b) As Processed, 2D Section c) After Current Stressing, Volume Rendering d) After Current Stressing, 2D Section

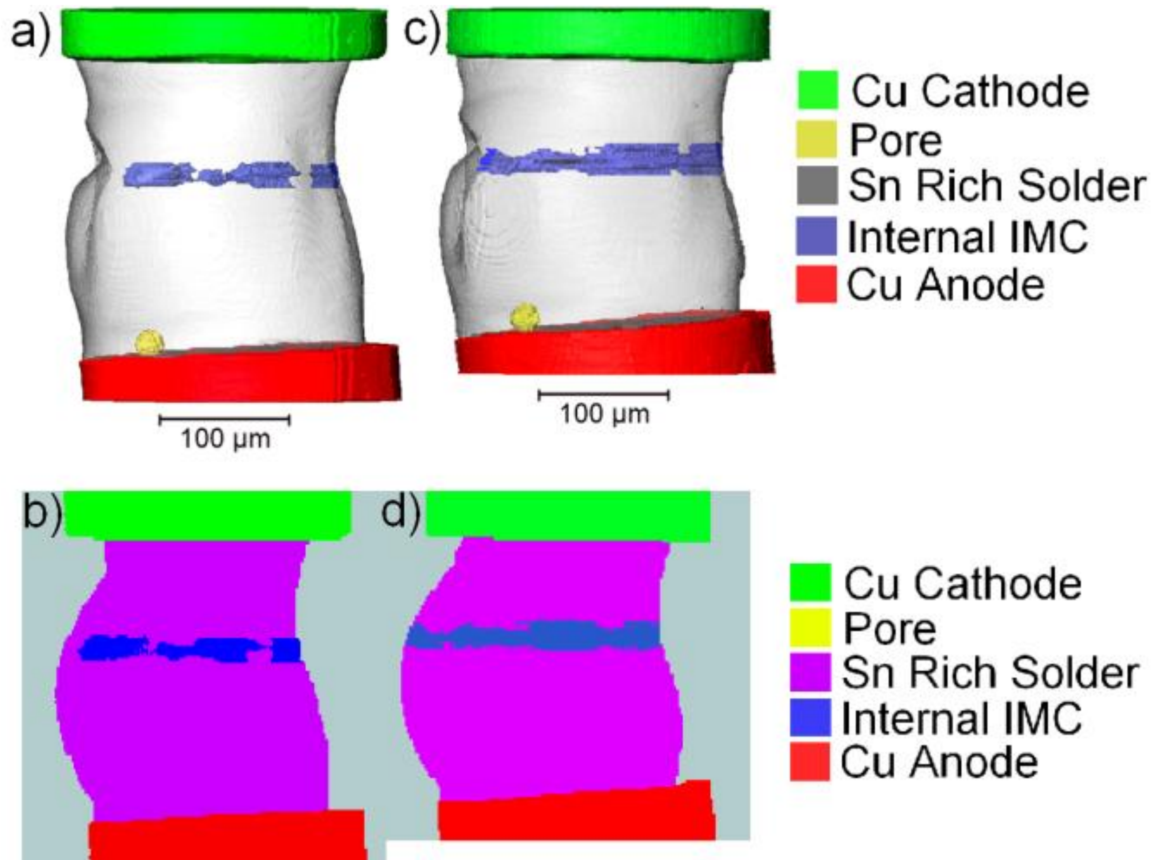

Figure 84. Segmented X-Ray Computed Tomography Representations of Electromigration Induced Microstructural Evolution in Sample 120214 a) As-Processed, Volume Rendering b) As Processed, 2D Section c) After Current Stressing, Volume Rendering d) After Current Stressing, 2D Section

8.4 ANALYSIS AND DISCUSSION

The measured temperature during testing, solder cross sectional area at the cathode interface, current density, and current stressing time are reiterated in *Table 18* along with the expected values for the copper saturation limit in tin (*X*) according to *Equation 42*, the diffusivity of copper along the a-axis of tin, the diffusivity of tin along the a-axis of tin, and the ratio of the copper/tin a-axis diffusivity in tin corresponding to the testing conditions. Based on the measured phase volume change, provided in *Table 19*, and the physical properties of copper, tin, and Cu_6Sn_5 (given in *Table 14*), the change in the number of the copper and tin atoms in each phase before and after testing, ΔN, was estimated. Based on the measured change in the number of copper and tin atoms in each phase, the cross sectional area of the sample at the cathode, and the time duration of current stressing, the atomic flux of copper and tin were calculated based on each of the five relevant phases which were analyzed (also provided in *Table 19*) using *Equation 47*. Based on the measured atomic flux values, the product of the effective diffusivity and the effective charge of the ion in electromigration testing, $\widetilde{D}Z^*$, was calculated according to *Equation 46* and is also included in *Table 19*. The $\widetilde{D}Z^*$ parameter measured at 150°C for copper is roughly 55,000 times greater that of tin (*Table 19*), and from knowledge of bulk diffusion rates (Ke et al., 2011) is likely dominated by the difference in the diffusivity of interstitial copper relative to substitutional diffusivity of tin, which is about 21,000 times greater for copper than tin along the a-axis of tin (*Table 18*).

Table 18

Testing Conditions, Expected Copper Saturation Limit in Tin, X, and The Expected Diffusivity Value, D, Along the a-axis of Tin for Copper and Tin for the Samples Tested in Accelerated Electromigration

Sample ID	092414	101014	120214
Time, *t* (h)	214.9	237.9	210.2
Current Density, *j* [A/cm²]	1.06E+05	4.14E+04	3.13E+04
Temperature, *T* [°C]	152.4	150.6	101.1
Area, *A* [cm²]	1.89E-04	2.82E-04	3.08E-04
X (Cu in Sn) [# Fraction]	2.24E-05	2.14E-05	5.25E-06
D (Cu) [Sn a-axis]	2.07E-07	1.99E-07	5.75E-08
D (Sn) [Sn a-axis]	1.01E-12	8.82E-13	1.50E-14
D(Cu)/D(Sn) [Sn a-axis]	2.06E+05	2.26E+05	2.26E+05

Table 19

Measured Values from Electromigration Tests via Segmented X-Ray Tomography Data

Sample ID	092414	101014	120214
ΔV (Cathode) [cm³]	-1.63E-08	-7.88E-08	-2.65E-08
ΔV (Anode) [cm³]	1.46E-07	2.79E-08	-4.27E-08
ΔV (Total IMC) [cm³]	3.11E-07	1.38E-07	1.27E-08
ΔV (Void) [cm³]	6.52E-09	0	2.79E-10
ΔV (Sn-Rich) [cm³]	2.23E-07	-7.52E-08	6.79E-08
ΔV (Joint+IMC) [cm³]	5.35E-07	6.29E-08	8.07E-08
ΔN (Cu, IMC) [# Atoms]	8.44E+15	3.74E+15	3.45E+14
ΔN (Cu, Cathode) [# Atoms]	-1.39E+15	-6.69E+15	-2.25E+15
ΔN (Sn, Sn-Rich) [# Atoms]	8.28E+15	-2.79E+15	2.52E+15
ΔN (Sn, Void) [# Atoms]	2.42E+14	0	1.03E+13
ΔN (Sn, IMC) [# Atoms]	7.03E+15	3.12E+15	2.87E+14
Δ ΔN (Cu, IMC to Cathode) [%]	84	-79	-553
Δ ΔN (Sn, IMC to Sn-Rich) [%]	218	11	977
J (Cu, IMC) [atoms/cm²s]	5.78E+13	1.55E+13	1.48E+12
J (Cu, Cathode) [atoms/cm²s]	9.48E+12	2.78E+13	9.66E+12
J (Sn, Sn-Rich) [atoms/cm²s]	5.67E+13	1.16E+13	1.08E+13
J (Sn, Void) [atoms/cm²s]	1.66E+12	0	4.44E+10
J (Sn, IMC) [atoms/cm²s]	4.81E+13	1.29E+13	1.23E+12
$\widetilde{D}Z^*$(Cu, IMC) [cm²/s]	9.11E-07	6.54E-07	2.98E-07
$\widetilde{D}Z^*$ (Cu, Cathode) [cm²/s]	1.50E-07	1.17E-06	1.94E-06
$\widetilde{D}Z^*$ (Sn, Sn-Rich) [cm²/s]	2.01E-11	1.05E-11	1.14E-11
$\widetilde{D}Z^*$ (Sn, Void) [cm²/s]	5.86E-13	0.00E+00	4.69E-14
$\widetilde{D}Z^*$ (Sn, IMC) [cm²/s]	1.70E-11	1.17E-11	1.30E-12
$\widetilde{D}Z^*$(Cu, IMC)/DZ*(Sn, Sn-Rich)	4.54E+04	6.26E+04	2.61E+04
$\widetilde{D}Z^*$(Cu, Cathode)/DZ*(Sn, Sn-Rich)	7.46E+03	1.12E+05	1.70E+05
$\widetilde{D}Z^*$(Cu, IMC)/DZ*(Sn, Void)	1.56E+06	0	6.35E+06
$\widetilde{D}Z^*$(Cu, Cathode)/DZ*(Sn, Void)	2.56E+05	0	4.15E+07
$\widetilde{D}Z^*$(Cu,IMC)/DZ*(Sn, IMC)	5.35E+04	5.60E+04	2.29E+05
$\widetilde{D}Z^*$(Cu, Cathode)/DZ*(Sn, IMC)	8.79E+03	1.00E+05	1.49E+06

Upon analysis of the results provided in *Table 19*, the measurements for $\widetilde{D}Z^*$ for copper and tin in this system appear to most reasonable from quantification of the IMC phase. Voiding was not seen in all samples, and was therefore an unreliable means to quantify tin diffusion. Although one void was observed in sample 120214, the void was present after reflow (known as reflow porosity), and was actually intentionally made to be at the anode (to avoid pre existing voids at the cathode) where voids are not expected to grow or form as a result of electromigration. In sample 101014, no reflow porosity was observed, nor was any voiding as a result of electromigration. Sample 092414, experiencing both the higher of the two temperatures and the higher of the two current densities, was the only sample in which voiding near the cathode was observed as a result of current stressing. The volume of the tin rich phase is suspected to be an unreasonable means for quantifying tin flux, as compressive stresses are thought to arise as a result of electromigration, and thus quantifying tin flux based on the density would be conceivably erroneous. The cathode phase, although observed to be consumed in the preliminary test sample in **Chapter 8**, and in sample 092414, is thought to be an unreliable means for copper flux measurement because the cathode wire extended approximately 8mm above the cathode interface, and had experienced high temperature and current density all along the length of the wire, and therefore the entire copper wire cathode may act as a source of copper in electromigration, and might even 'replenish' the cathode interface following its consumption into the solder volume. For these reasons, measurements from the IMC phase were suspected to be the most reliable, and were preferred in the ensuing analysis of $\widetilde{D}Z^*$ for copper and tin, and the effect of temperature and current density on this parameter.

As no significant change in the microstructure of the 120214 sample was observed (which was tested at the lower of the two temperatures and the lower of the two targeted values for current density across all three samples) the results from this sample were suspected to be flawed. Due to the low confidence in the analysis of the 120214 sample, an analysis on the effect of temperature on the $\widetilde{D}Z^*$ parameter was not performed.

While the analysis from the IMC phase change measurements were suspected the most trustworthy for quantifying the $\widetilde{D}Z^*$ parameter, and the sample 120214 provided poor results, measured values from all five phases and for all three samples are provided in *Table 18* through *Table 20* which upon analysis can support both claims. Using literature reported values for the diffusion of copper and tin along the a-axis of tin (Ke et al., 2011), inferred values for the effective charge of tin and copper are provided in *Table 20*, assuming predominant migration along the a-axis of tin. Also provided in *Table 20* are the effective charge ratios of copper to tin as was extracted through measurements of the various material phases for all the tested samples. The effective diffusivity of tin during the test can also be inferred from literature reported values of the effective charge of tin under electromigration inducing conditions (Gan and Tu, 2002), and these inferred values for the effective diffusivity of tin in the tested samples are also provided in *Table 20*. It can be seen that values for inferred values of Z^* from IMC phase measurements are in the best agreement with one another, and for the case of tin, are in best agreement with literature reported values (Gan and Tu, 2002).

Table 20

Effective Charge Values for Copper and Tin Inferred from Literature Values for a-axis Diffusivity Along the a-axis of Tin, the Effective Charge Ratios of Copper to Tin, and the Effective Diffusivity of Tin as Inferred from Literature Reported Values for the Effective Charge of Tin in Electromigration, as Measured Through the Observed Phases

Sample ID	092414	101014	120214
Z^* (Cu, IMC) if $\widetilde{D} = D$ (Sn a-axis)	4.4	3.3	5.2
Z^* (Cu, Cathode) if $\widetilde{D} = D$ (Sn a-axis)	0.72	5.9	34
Z^* (Sn, Sn-Rich) if $\widetilde{D} = D$ (Sn a-axis)	20	12	758
Z^* (Sn, Void) if $\widetilde{D} = D$ (Sn a-axis)	0.58	0	3.1
Z^* (Sn, IMC) if $\widetilde{D} = D$ (Sn a-axis)	17	13	86
Z^*(Cu, IMC)/Z^*(Sn, Sn-Rich) if $\widetilde{D} = D$ (Sn a-axis)	0.22	0.28	0.0068
Z^*(Cu, Cathode)/Z^*(Sn, Sn-Rich) if $\widetilde{D} = D$ (Sn a-axis)	0.036	0.50	0.045
Z^*(Cu, IMC)/Z^*(Sn, Void) if if $\widetilde{D} = D$ (Sn a-axis)	7.5	0	1.7
Z^*(Cu, Cathode)/Z^*(Sn, Void) if if $\widetilde{D} = D$ (Sn a-axis)	1.2	0	10.8
Z^*(Cu,IMC)/Z^*(Sn, IMC) if $\widetilde{D} = D$ (Sn a-axis)	0.26	0.25	0.060
Z^*(Cu, Cathode)/Z^*(Sn, IMC) if $\widetilde{D} = D$ (Sn a-axis)	0.043	0.44	0.39
$\widetilde{D}$ (Sn, Sn-Rich) if Z^*=18	1.11E-12	5.81E-13	6.34E-13
$\widetilde{D}$ (Sn, Void) if Z^*=18	3.25E-14	0	2.60E-15
$\widetilde{D}$ (Sn, IMC) if Z^*=18	9.46E-13	6.49E-13	7.23E-14

Taking literature reported values for Z^* of tin (Gan and Tu, 2002), the value of $\widetilde{D}$ can be inferred from the measure $\widetilde{D}Z^*$ values. Using this approach, inferred values of $\widetilde{D}$ from the IMC phases are most reasonable when compared with calculated diffusivity values of either species along the a-axis of tin (Ke et al., 2011) given in *Table 18*, as is sown in *Table 20*. Measurements of $\widetilde{D}Z^*$ taken from the other phases imply effective diffusivities of tin an order of magnitude above or below the a-axis diffusivity and are even less consistent between the three tested volumes.

The two samples which yield reasonable values across the board (092414 and 101014), both in terms of the $\widetilde{D}Z^*$ value of each specie and the ratio fo the same paramter between the species as compared with other reports in the literature were both tested at 150°C, and therefore an effect of testing temperature was not enabled by the current results. However, as the testing conditions for each sample employed much different applied current density magnitudes, an analysis of the effect of current density on the $\widetilde{D}Z^*$ parameter was performed. Based on measured values of the change in the IMC content, the effect of current density on the $\widetilde{D}Z^*$ for copper is provided in *Figure 85*, and the effect of current density on $\widetilde{D}Z^*$ for tin is provided in *Figure 86*. The plotted values are also given in *Table 19*. Based on this analysis, it can be seen that the $\widetilde{D}Z^*$ increased with current density between these two samples, either as a result of a higher $\widetilde{D}$ in the sample at higher current density, which would conceivable only be based on microstructural differences such as grain size and orientation, or as a result of the Z^* parameter, which would be a result of a greater interaction of the ions with the electron wind force at higher current density. As both samples had the same processing, the latter seems more probable.

As previously discussed, the effective charge of either species can be deconvoluted from the effective diffusivity with approximation of the effective diffusivity values. The value of Z^* which would result from diffusion predominantly along the a-axis of tin is provided in *Figure 87*, as is similarly provided in *Table 19*. It can be seen in *Figure 87* that the applied current density has a similar influence on the effective charge of tin in this system as on the effective charge of copper in this system. It was also observed that if the diffusion mechanism in these samples was predominantly a-axis, although copper has a higher diffusivity along the a-axis in tin than tin itself (Ke et al., 2011), the tin specie has a greater effective charge in electromigration, and that $Z^*(Sn) \approx 4 \cdot Z^*(Cu)$.

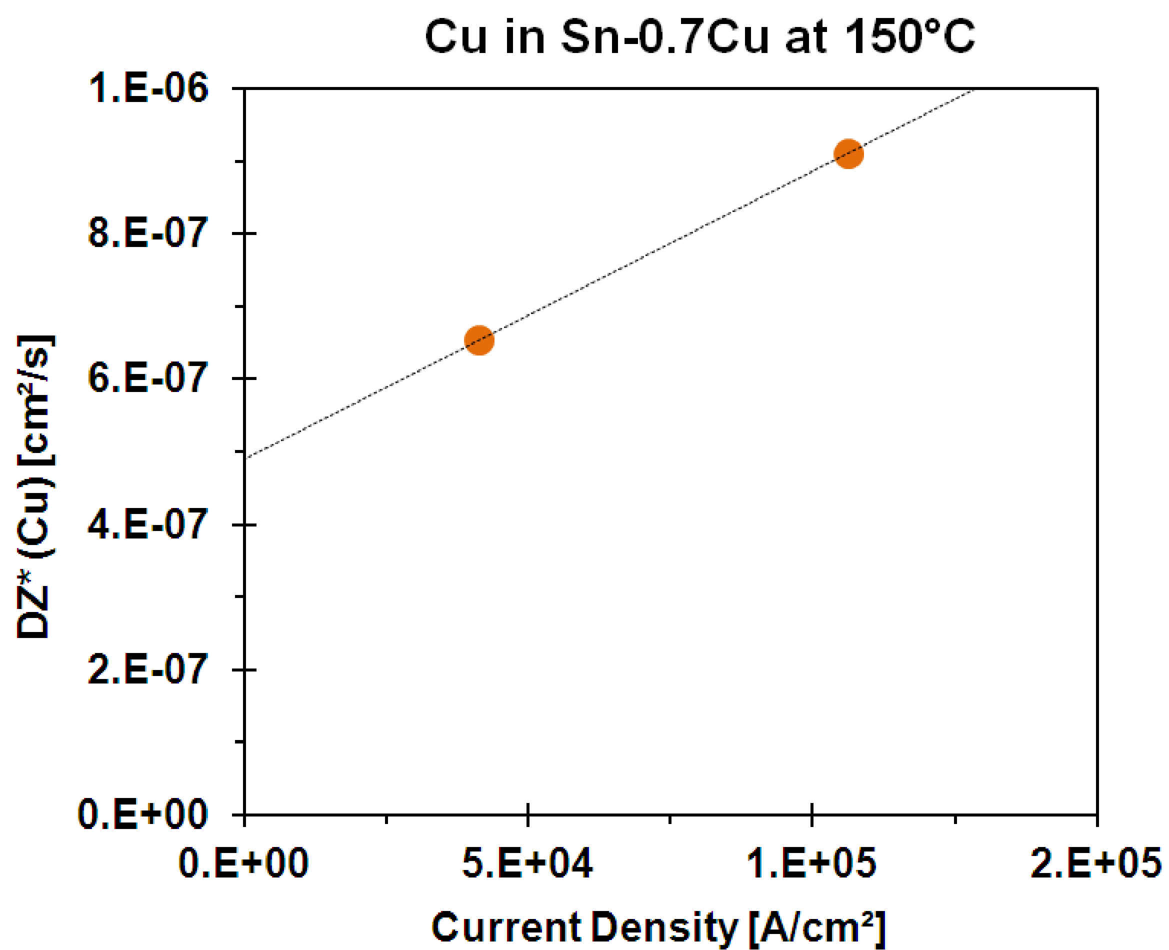

Figure 85. The Measured Product of the Effective Diffusivity and Effective Charge for Copper at 150°C as a Function of Current Density Applied

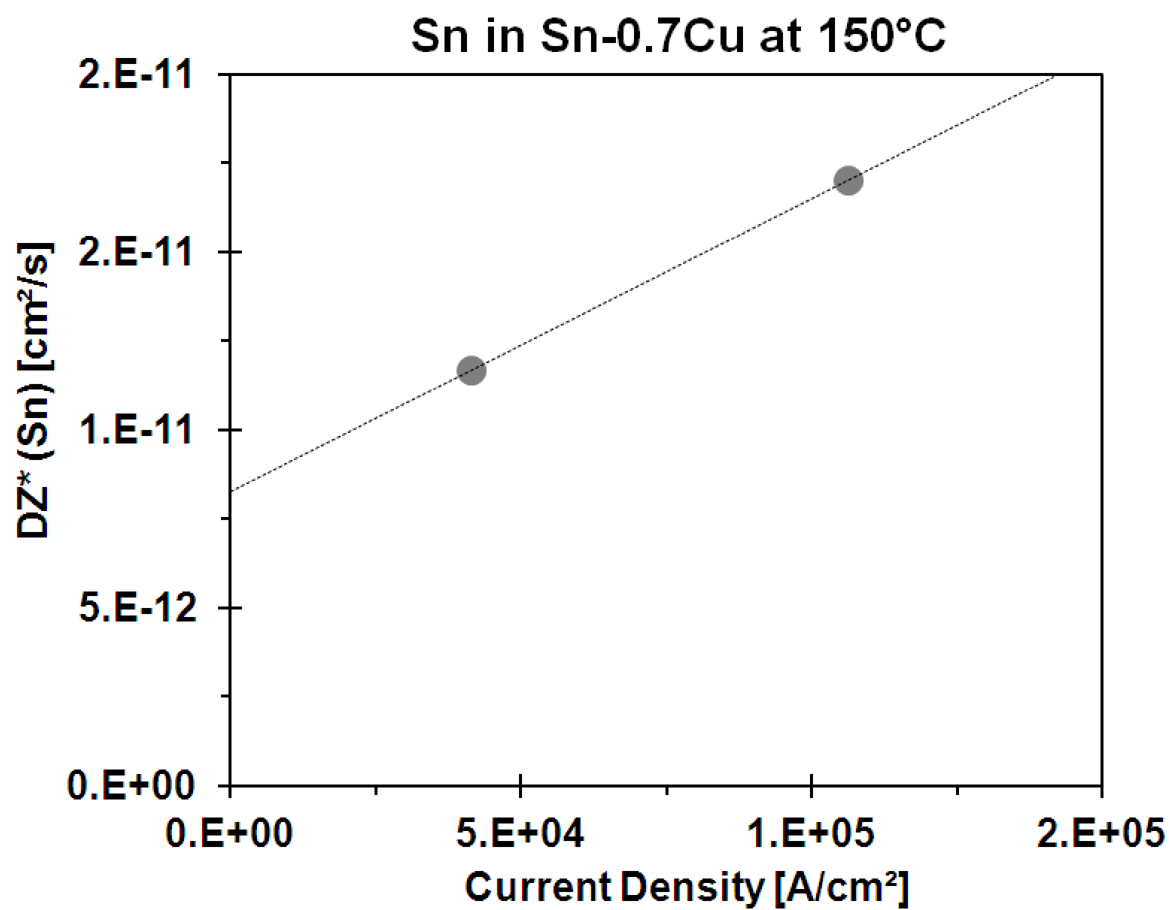

Figure 86. The Measured Product of the Effective Diffusivity and Effective Charge for Tin at 150°C as a Function of Current Density Applied

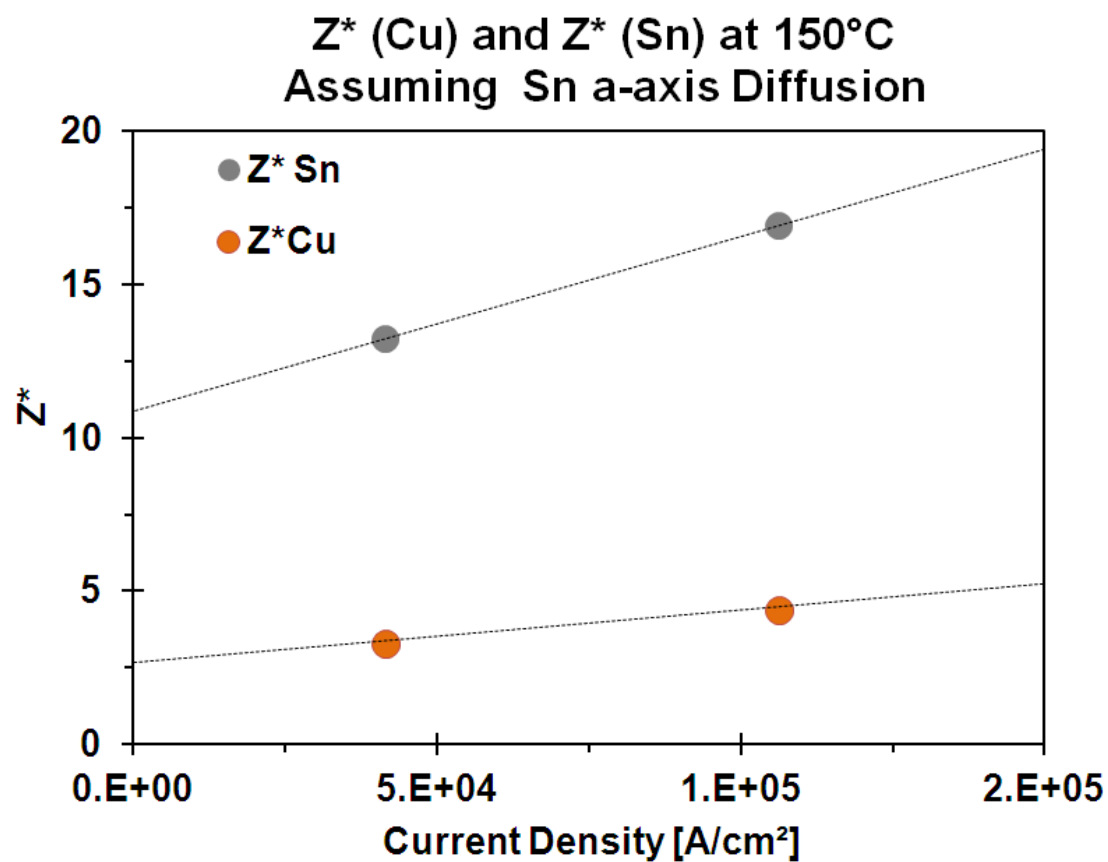

Figure 87. The Inferred Effective Charge of Tin and Copper at 150°C as a Function of Current Density Applied if Diffusion is Predominantly Along the a-axis in Tin, Based on Calculated Values for Diffusivity in Tin Along the a-axis

8.5 SUMMARY

X-ray tomography has been used to quantify microstructural evolution in three surface-encapsulated Sn-0.7Cu solder butt joints on $<250\mu m$ diameter copper wire substrates. The effect of current density and temperature on the dominating failure mode (cathode consumption vs. solder migration) and the apparent $\tilde{D}Z^*$ parameter of copper and tin in the system has been targeted. The intermetallic phase growth as a result of current stressing has been determined to be the most reliable means for quantifying the flux of copper and tin in the system. Based on the measured phase change, quantifications from only the samples tested at 150°C appear reliable. As a result, only the effect of current density on the measured product of effective ion charge and effective diffusivity has been investigated. The failure process at 150°C appears to be neither dominated by solder voiding nor cathode consumption. The $\tilde{D}Z^*$ ratio between tin and copper appears to be a weak function of the current density applied and is nearly constant. The measured ratio from the IMC phase growth indicates that $\tilde{D}Z^*(Cu) \approx 50{,}000 \cdot \tilde{D}Z^*(Sn)$. At about 150°C, $\tilde{D}Z^*(Cu)=6.5E\text{-}7$ cm^2/s while $\tilde{D}Z^*(Sn)=1.2E\text{-}11$ cm^2/s with 4.14E4 A/cm^2 applied current density, and $\tilde{D}Z^*(Cu)=9.1E\text{-}7$ cm^2/s while $\tilde{D}Z^*(Sn)=1.7E\text{-}11$ cm^2/s with 1.06E5 A/cm^2 applied current density. The $\tilde{D}Z^*$ parameter for both tin and copper appears to be a strong function of current density, and is thought to be tied more closely with the effective charge if the diffusion mechanisms for copper and tin through the solder do not change with the applied current density. If this is the case, the effective charge of tin and copper in the system increases with current density applied. If the diffusion mechanism for copper and tin through the tin crystals of the polycrystalline solder is predominantly a-axis, it was determined that $Z^*(Sn) \approx 4 \cdot Z^*(Cu)$. At about 150°C, $Z^*(Cu)=3.3$ while $Z^*(Sn)=13$ with 4.14E4 A/cm^2 applied current density, and $Z^*(Cu)=4.4$ while $Z^*(Sn)=17$ with 1.06E5 A/cm^2 applied current density.

CHAPTER 9

CONCLUSION

For decades, microelectronics manufacturing has been concerned with failures related to electromigration phenomena in conductors experiencing high current densities. The influence of interconnect microstructure on device failures related to electromigration in BGA and flip chip solder interconnects have become of increased interest with increased solder connect densities and the phasing out of lead alloys. Several theoretical and experimental models exist for describing electromigration phenomena in solders. The limitations of techniques using two-dimensional imaging to study electromigration mechanisms are evident in the literature. X-ray computed micro-tomography has proven to be a powerful technique to resolve microstructural phases non-destructively. Recently, x-ray micro-tomography has demonstrated an unrivaled quantification of current stressing induced void growth using both synchrotron and microfocus tube x-rays, but in all cases the study has been limited to the evolution of voids.

This work has demonstrated the capabilities of a custom lab-scale x-ray microtomography tool, and the microstructural measurements which the technique has enabled, specifically with respect to electromigration processes. A design for a custom lab-scale μXCT system to achieve high spatial resolution and sufficient contrast of solder microstructures was developed based on a review of relevant design principles gleaned from the literature. The system design incorporates a dual-target microfocus x-ray source, a lens-coupled CCD-scintillator detector of variable magnification and incorporates a mechanism for simply interchanging the choice of the scintillator material itself. The summation of this custom design is a system with enhanced

versatility through modularity. A custom scan routine, incorporating control over all imaging components, has been written in LabVIEW enabling user-friendly and automated acquisition of the angularly-unique x-ray projections needed for tomographic reconstruction. The computerized aspect of the tomography system, including techniques for projection processing and reconstruction, has been implemented with MATLAB and hinges on cone-beam-weighted filtered-back-projection of the calibrated and filtered radiographs.

A model has been put forth which serves as a powerful means of predicting system performance, specifically in terms of the detected signal rate, as a function of tunable system parameters. The ability to tune such parameters, specifically at the detector, is something which is enabled but the x-ray CT system's open, transparent, modular design. With concern over the detector's energy sensitivity and the polychromatic imaging beam, a detailed and wide-ranging characterization of the system's imaging signal rate under was also performed. These measurements have been compared with expectations from the predictive model which was derived for this very purpose, and have demonstrated satisfactory agreement. As there is a known trade-off between imaging resolution and final detected count rate, whether from the x-ray source or detector conditions, a complete analysis of the tool's spatial resolution as a function of imaging parameters is still needed. The primary motivation for the model's construction, as has been demonstrated in this work, is the much needed capability to optimize the detected x-ray spectrum for maximum attenuation contrast in the imaging of multiphase materials.

In the case of high-energy x-ray imaging, required for solder imaging, the issues associated with 'zinger' noise have been demonstrated. The importance of physical design precaution in the

detector for the reduction of this type of noise has been established and highlighted. One new approach has been put forth for treating 'zinger' noise algorithmically, and has been tested against a known, relatively standard, existing method using simulated x-ray projections on a Shepp-Logan head phantom with artificial noise added to the images. The drawback of this approach, as has been outlined in detail, is that the filtering hinges on at least two distinct projections of each unique sample orientation in which zinger filtering is deemed necessary, which from a practical standpoint, implies a need for two acquisitions for every sample position throughout a tomographic scan. The presently put forth SFA algorithm shows significant benefit to the known method in terms of false positives, false negatives, and true positives in zinger detection. Perhaps most importantly, the newly proposed method offers enhanced performance not only in zinger detection, but also has demonstrated minimized error in the corrected images and the reconstructions there from.

In order to perform material testing under electromigration driving forces with the system, the design of an *in situ* multi-modal sample testing fixture was realized. The design of an electromigration testing fixture for *in situ* μXCT and OM/SEM characterization, specifically for microscale solder interconnects, has been detailed. This utility of the fixture design for accelerated electromigration testing has been demonstrated on the Sn-0.7Cu system. In the preliminary test, the migration of copper, tin species, and the overall solder joint, as well as the formation of copper-tin intermetallic, has been observed and quantified in 3D using lab-scale μXCT. This approach also included imaging parameter selection for enhanced feature contrast through the energy-dependent detection model that was established. The measurements, which

have provided new insight into EM processes in a particular material system, have been enabled by the fixture of custom design.

The effect of current density on the migration of copper and tin in Sn-0.7Cu solder volumes on copper substrates has been investigated in microscale surface-encapsulated solder volumes. The failure process at 150°C appears to be neither dominated by solder voiding nor cathode consumption. The $\tilde{D}Z^*$ ratio between tin and copper appears to be a weak function of the current density applied and is nearly constant. The measured ratio from the IMC phase growth indicates that $\tilde{D}Z^*(Cu) \approx 50{,}000 \cdot \tilde{D}Z^*(Sn)$. At about 150°C, $\tilde{D}Z^*(Cu)$=6.5E-7 cm^2/s while $\tilde{D}Z^*(Sn)$=1.2E-11 cm^2/s with 4.14E4 A/cm^2 applied current density, and $\tilde{D}Z^*(Cu)$=9.1E-7 cm^2/s while $\tilde{D}Z^*(Sn)$=1.7E-11 cm^2/s with 1.06E5 A/cm^2 applied current density. The $\tilde{D}Z^*$ parameter for both tin and copper appears to be a strong function of current density, and is thought to be tied more closely with the effective charge if the diffusion mechanisms for copper and tin through the solder do not change with the applied current density. If this is the case, the effective charge of tin and copper in the system increases with current density applied. If the diffusion mechanism for copper and tin through the tin crystals of the polycrystalline solder is predominantly a-axis, it was determined that $Z^*(Sn) \approx 4 \cdot Z^*(Cu)$. At about 150°C, $Z^*(Cu)$=3.3 while $Z^*(Sn)$=13 with 4.14E4 A/cm^2 applied current density, and $Z^*(Cu)$=4.4 while $Z^*(Sn)$=17 with 1.06E5 A/cm^2 applied current density.

The work here performed was rooted in the need for more accurate and thorough quantification of migrating species in micro-scale lead-free solder joints, and has focused on using 4D microstructural datasets of a resolved second phase acquired with a modular, high-resolution lab-

scale μXCT of a custom construction built for this purpose. The volume evolution data was sought in order to study tin-rich solder migration, metallization consumption, intermetallic formation, and void formation, in a novel way. The volume evolution has enabled estimation of atomic flux under electrically assisted atomic migration, and the technique has provided enhanced understanding of the evolution of solder microstructures in three-dimensions. In particular, the competition between metallization consumption and solder voiding has been quantified for a particular EM inducing environment. In the analysis of the results, a means for extracting the active migratory mechanisms from a rate comparison with known bulk, grain-boundary, dislocation core, and surface diffusion has been suggested. The experimental approach that has been demonstrated is expected to promote the utility of x-ray microtomography characterization and to equip scientists and engineers with a new means for studying material dynamics in microelectronic interconnects.

REFERENCES

(Abtew and Selvaduray, 2000) Abtew, M. and Selvaduray, G. (2000). Lead-free solders in microelectronics. *Materials Science and Engineering: R: Reports*, 27(5):95–141.

(Alam *et al.*, 2006) Alam, M., Wu, B., Chan, Y., and Tu, K. (2006). High electric current density-induced interfacial reactions in micro ball grid array (bga) solder joints. *Acta Materialia*, 54(3):613–621.

(An *et al.*, 2011) An, B., Gu, G., Zhang, W., and Wu, Y. (2011). Shear creep behavior of sn-3ag-0.5cu solder bumps in ball grid array. In *Advanced Packaging Materials (APM), 2011 International Symposium on*, pages 257–261.

(Anas *et al.*, 2011) Anas, E. M. A., Kim, J. G., Lee, S. Y., and Hasan, M. K. (2011). Comparison of ring artifact removal methods using flat panel detector based ct images. *Biomedical engineering online*, 10(1):72.

(Anas *et al.*, 2010) Anas, E. M. A., Lee, S. Y., and Hasan, T. (2010). Removal of ring artifacts in x-ray micro tomography using polyphase decomposition and spline interpolation. In *Electrical and Computer Engineering (ICECE), 2010 International Conference on*, pages 638–641. IEEE.

(APS, 2015) APS (2015). Tomopy, advanced photon source, data exchange.

(Aslund *et al.*, 2010) Aslund, M., Fredenberg, E., Telman, M., and Danielsson, M. (2010). Detectors for the future of x-ray imaging. *Radiation protection dosimetry*, 139(1-3):327–333.

(Basaran *et al.*, 2009) Basaran, C., Li, S., Hopkins, D. C., and Veychard, D. (2009). Electromigration time to failure of snagcuni solder joints. *Journal of Applied Physics*, 106(1):013707.

(Bertheau *et al.*, 2014a) Bertheau, J., Bleuet, P., Hodaj, F., Cloetens, P., Martin, N., Charbonnier, J., and Hotellier, N. (2014a). Reflow processes in micro-bumps studied by synchrotron x-ray projection nanotomography. *Microelectronic Engineering*, 113(0):123–129.

(Bertheau *et al.*, 2014b) Bertheau, J., Hodaj, F., Hotellier, N., and Charbonnier, J. (2014b). Effect of intermetallic compound thickness on shear strength of 25micron diameter cu-pillars. *Intermetallics*, 51(0):37–47.

(Bisogni *et al.*, 2007) Bisogni, M., Del Guerra, A., Lanconelli, N., Lauria, A., Mettivier, G., Montesi, M., Panetta, D., Pani, R., Quattrocchi, M., Randaccio, P., *et al.* (2007). Experimental study of beam hardening artifacts in photon counting breast computed tomography. *Nuclear Instruments and Methods in Physics Research Section A: Accelerators, Spectrometers, Detectors and Associated Equipment*, 581(1):94–98.

(Black, 1969) Black, J. R. (1969). Electromigration failure modes in aluminum metallization for semiconductor devices. *Proceedings of the IEEE*, 57(9):1587–1594.

(Blech and Meieran, 1969) Blech, I. A. and Meieran, E. S. (1969). Electromigration in thin al films. *Journal of Applied Physics*, 40(2):485–491.

(Blech and Tai, 1977) Blech, I. A. and Tai, K. L. (1977). Measurement of stress gradients generated by electromigration. *Applied Physics Letters*, 30(8):387–389.

(Bogno *et al.*, 2013) Bogno, A., Nguyen-Thi, H., Reinhart, G., Billia, B., and Baruchel, J. (2013). Growth and interaction of dendritic equiaxed grains: In situ characterization by synchrotron x-ray radiography. *Acta Materialia*, 61(4):1303–1315.

(Bosiers *et al.*, 2006) Bosiers, J. T., Peters, I. M., Draijer, C., and Theuwissen, A. (2006). Technical challenges and recent progress in ccd imagers. *Nuclear Instruments and Methods in Physics Research Section A: Accelerators, Spectrometers, Detectors and Associated Equipment*, 565(1):148–156.

(Burke, 1986) Burke, E. A. (1986). Energy dependence of proton-induced displacement damage in silicon. *Nuclear Science, IEEE Transactions on*, 33(6):1276–1281.

(Campbell and Huntington, 1969) Campbell, D. R. and Huntington, H. B. (1969). Thermomigration and electromigration in zirconium. *Phys. Rev.*, 179:601–611.

(Chaney and Hendee, 1974) Chaney, E. L. and Hendee, W. R. (1974). Effects of x-ray tube current and voltage on effective focalspot size. *Medical Physics*, 1(3):141–147.

(Chen *et al.*, 2010) Chen, C., Tong, H., and Tu, K. (2010). Electromigration and thermomigration in pb-free flip-chip solder joints. *Annual Review of Materials Research*, 40(1):531–555.

(Chen and Chen, 2001) Chen, C.-m. and Chen, S.-w. (2001). Electromigration effect upon the sn-0.7 wt% cu/ni and sn-3.5 wt ag/ni interfacial reactions. *Journal of Applied Physics*, 90(3):1208–1214.

(Chiu *et al.*, 2006) Chiu, S. H., Shao, T. L., Chen, C., Yao, D. J., and Hsu, C. Y. (2006). Infrared microscopy of hot spots induced by joule heating in flip-chip snag solder joints under accelerated electromigration. *Applied Physics Letters*, 88(2):022110.

(Chiu *et al.*, 2011) Chiu, Y.-T., Liu, C.-H., Lin, K.-L., and Lai, Y.-S. (2011). Supersaturation induced by current stressing. *Scripta Materialia*, 65(7):615–617.
(Datta *et al.*, 2004) Datta, M., Osaka, T., and Schultze, J. W. (2004). *Microelectronic packaging*. CRC press.

(De Man *et al.*, 1998) De Man, B., Nuyts, J., Dupont, P., Marchal, G., and Suetens, P. (1998). Metal streak artifacts in x-ray computed tomography: a simulation study. In *Nuclear Science Symposium, 1998. Conference Record. 1998 IEEE*, volume 3, pages 1860–1865. IEEE.

(De Man *et al.*, 2000) De Man, B., Nuyts, J., Dupont, P., Marchal, G., and Suetens, P. (2000). Reduction of metal streak artifacts in x-ray computed tomography using a transmission maximum a posteriori algorithm. *IEEE transactions on nuclear science*, 47(3):977–981.

(de Paiva *et al.*, 1998) de Paiva, R. F., Lynch, J., Rosenberg, E., and Bisiaux, M. (1998). A beam hardening correction for x-ray microtomography. *Ndt & E International*, 31(1):17–22.

(Deng *et al.*, 2004) Deng, X., Koopman, M., Chawla, N., and Chawla, K. (2004). Young's modulus of (cu, ag)-sn intermetallics measured by nanoindentation. *Materials Science and Engineering: A*, 364(1):240–243.

(Deng *et al.*, 2003) Deng, X., Piotrowski, G., Williams, J., and Chawla, N. (2003). Influence of initial morphology and thickness of cu6sn5 and cu3sn intermetallics on growth and evolution during thermal aging of sn-ag solder/cu joints. *Journal of Electronic Materials*, 32(12):1403–1413.

(Deng *et al.*, 2005) Deng, X., Sidhu, R., Johnson, P., and Chawla, N. (2005). Influence of reflow and thermal aging on the shear strength and fracture behavior of sn-3.5ag solder/cu joints. *Metallurgical and Materials Transactions A*, 36(1):55–64.

(Dierick *et al.*, 2008) Dierick, M., Hoorebeke, L. V., Jacobs, P., Masschaele, B., Vlassenbroeck, J., Cnudde, V., and Witte, Y. D. (2008). The use of 2d pixel detectors in micro- and nano-ct applications. *Nuclear Instruments and Methods in Physics Research Section A: Accelerators, Spectrometers, Detectors and Associated Equipment*, 591(1):255–259. Radiation Imaging Detectors 2007 Proceedings of the 9th International Workshop on Radiation Imaging Detectors.

(Ding, 2007) Ding, M. (2007). Investigation of electromigration reliability of solder joint in flip-chip packages. Copyright - Copyright ProQuest, UMI Dissertations Publishing 2007; Last updated - 2014-01-21.

(Dudek and Chawla, 2008) Dudek, M. and Chawla, N. (2008). Three-dimensional (3d) microstructure visualization of lasn3 intermetallics in a novel sn-rich rare-earth-containing solder. *Materials Characterization*, 59(9):1364–1368.

(Dudek *et al.*, 2010) Dudek, M., Hunter, L., Kranz, S., Williams, J., Lau, S., and Chawla, N. (2010). Three-dimensional (3d) visualization of reflow porosity and modeling of deformation in pb-free solder joints. *Materials Characterization*, 61(4):433–439.

(Feldkamp *et al.*, 1984) Feldkamp, L. A., Davis, L. C., and Kress, J. W. (1984). Practical cone-beam algorithm. *J. Opt. Soc. Am. A*, 1(6):612–619.

(Flynn *et al.*, 1994) Flynn, M. J., Hames, S. M., Reimann, D. A., and Wilderman, S. J. (1994). Microfocus x-ray sources for 3d microtomography. *Nuclear Instruments and Methods in Physics Research Section A: Accelerators, Spectrometers, Detectors and Associated Equipment*, 353(1):312–315.

(Friedli *et al.*, 2013) Friedli, J., Fife, J., Di Napoli, P., and Rappaz, M. (2013). Dendritic growth morphologies in al-zn alloysâ€"part i: X-ray tomographic microscopy. *Metallurgical and Materials Transactions A*, 44(12):5522–5531.

(Gan *et al.*, 2002) Gan, H., Choi, W., Xu, G., and Tu, K. (2002). Electromigration in solder joints and solder lines. *JOM*, 54(6):34–37.

(Gan and Tu, 2002) Gan, H. and Tu, K. (2002). Effect of electromigration on intermetallic compound formation in pb-free solder-cu interfaces. In *Electronic Components and Technology Conference, 2002. Proceedings. 52nd*, pages 1206–1212.

(Garcia *et al.*, 2011) Garcia, L. R., Osório, W. R., and Garcia, A. (2011). The effect of cooling rate on the dendritic spacing and morphology of ag< sub> 3</sub> sn intermetallic particles of a snag solder alloy. *Materials & Design*, 32(5):3008–3012.

(Ghate, 1967) Ghate, P. B. (1967). Some observations on the electromigration in aluminum films. *Applied Physics Letters*, 11(1):14–16.

(Gilleo, 2004) Gilleo, K. (2004). *Area array packaging processes: for BGA, Flip Chip, and CSP*. New York: McGraw-Hill.

(Graafsma and Martin, 2008) Graafsma, H. and Martin, T. (2008). *Advanced Tomographic Methods in Materials Research and Engineering. Detectors for synchrotron tomography. 277–302.* Oxford University Press.

(Hardy *et al.*, 1999) Hardy, T. D., Deen, M., and Murowinski, R. (1999). Effects of radiation damage on scientific charge coupled devices. *Advances in imaging and electron physics*, 106:1–96.

(Hartman and Blair, 1969) Hartman, T. E. and Blair, J. (1969). Electromigration in thin gold films. *Electron Devices, IEEE Transactions on*, 16(4):407–410.

(Herman, 1979) Herman, G. T. (1979). Correction for beam hardening in computed tomography. *Physics in Medicine and Biology*, 24(1):81.

(Ho and Huntington, 1966) Ho, P. and Huntington, H. (1966). Electromigration and void observation in silver. *Journal of Physics and Chemistry of Solids*, 27(8):1319–1329.

(Hobart, 1906) Hobart, J. F. (1906). *Brazing and Soldering...* Derry-Collard Company.
(Hopkinson, 1994) Hopkinson, G. (1994). Radiation effects on solid state imaging devices. *Radiation Physics and Chemistry*, 43(1):79–91.

(Howard and Ross, 1967) Howard, J. K. and Ross, R. F. (1967). Electromigration effects in aluminum film on silicon substrates. *Applied Physics Letters*, 11(3):85–87.

(Hsiao *et al.*, 2008) Hsiao, H.-Y., Liang, S., Ku, M.-F., Chen, C., and Yao, D.-J. (2008). Direct measurement of hot-spot temperature in flip-chip solder joints under current stressing using infrared microscopy. *Journal of applied physics*, 104(3):033708.

(Hsiao *et al.*, 2009) Hsiao, Y., Tseng, H., and Liu, C. (2009). Electromigration-induced failure of ni/cu bilayer bond pads joined with sn (cu) solders. *Journal of electronic materials*, 38(12):2573–2578.

(Hsieh, 1999) Hsieh, J. (1999). Three-dimensional artifact induced by projection weighting and misalignment. *Medical Imaging, IEEE Transactions on*, 18(4):364–368.

(Hu and Huntington, 1985) Hu, C. and Huntington, H. B. (1985). Atom movements of gold in lead-tin solders. *Journal of Applied Physics*, 58(7):2564–2569.

(Hu and Huntington, 1982) Hu, C.-K. and Huntington, H. (1982). Diffusion and electromigration of silver and nickel in lead-tin alloys. *Physical Review B*, 26(6):2782.

(Hu *et al.*, 1983) Hu, C.-K., Huntington, H., and Gruzalski, G. (1983). Atom motions of copper dissolved in lead-tin alloys. *Physical Review B*, 28(2):579.

(Hu *et al.*, 2003) Hu, Y., Lin, Y., Kao, C., and Tu, K. (2003). Electromigration failure in flip chip solder joints due to rapid dissolution of copper. *Journal of materials research*, 18(11):2544–2548.
(Huntington and Grone, 1961) Huntington, H. and Grone, A. (1961). Current-induced marker motion in gold wires. *Journal of Physics and Chemistry of Solids*, 20(1):76–87.

(Huntington and Hu, 1984) Huntington, H. and Hu, C. K. (1984). Atom movement in lead and lead tin solders. In *Materials Science Forum*, volume 1, pages 29–42. Trans Tech Publ.

(Huynh *et al.*, 2001) Huynh, Q. T., Liu, C. Y., Chen, C., and Tu, K. N. (2001). Electromigration in eutectic snpb solder lines. *Journal of Applied Physics*, 89(8):4332–4335.

(Imura *et al.*, 2012) Imura, Y., Yanagida, T., Morii, H., Mimura, H., and Aoki, T. (2012). Reduction of the beam hardening artifacts in the x-ray computer tomography: Energy discrimination with a photon-counting detector. *World Journal of Nuclear Science and Technology*, 2:169.

(Jang *et al.*, 2000) Jang, J. W., Frear, D. R., Lee, T. Y., and Tu, K. N. (2000). Morphology of interfacial reaction between lead-free solders and electroless ni-p under bump metallization. *Journal of Applied Physics*, 88(11):6359–6363.

(Jian and Hongnian, 2006) Jian, F. and Hongnian, L. (2006). Beam-hardening correction method based on original sinogram for x-ct. *Nuclear Instruments and Methods in Physics Research Section A: Accelerators, Spectrometers, Detectors and Associated Equipment*, 556(1):379–385.

(Jiang *et al.*, 2011) Jiang, L., Chawla, N., Pacheco, M., and Noveski, V. (2011). Three-dimensional (3d) microstructural characterization and quantification of reflow porosity in sn-rich alloy/copper joints by x-ray tomography. *Materials Characterization*, 62(10):970–975.

(Kammer and Voorhees, 2006) Kammer, D. and Voorhees, P. (2006). The morphological evolution of dendritic microstructures during coarsening. *Acta materialia*, 54(6):1549–1558.

(Kang and Sarkhel, 1994) Kang, S. and Sarkhel, A. (1994). Lead (pb)-free solders for electronic packaging. *Journal of Electronic Materials*, 23(8):701–707.

(Kariya *et al.*, 2004) Kariya, Y., Hosoi, T., Terashima, S., Tanaka, M., and Otsuka, M. (2004). Effect of silver content on the shear fatigue properties of sn-ag-cu flip-chip interconnects. *Journal of Electronic Materials*, 33(4):321–328.

(Ke *et al.*, 2011) Ke, J., Yang, T., Lai, Y., and Kao, C. (2011). Analysis and experimental verification of the competing degradation mechanisms for solder joints under electron current stressing. *Acta Materialia*, 59(6):2462–2468.

(Kim, 2014) Kim, K. (2014). 3d cone beam ct (cbct) projection backprojection fdk mlem reconstruction - file id 35548.

(Kim *et al.*, 2003) Kim, K., Huh, S., and Suganuma, K. (2003). Effects of intermetallic compounds on properties of sn-ag-cu lead-free soldered joints. *Journal of Alloys and Compounds*, 352(1):226–236.

(Koch *et al.*, 1998) Koch, A., Raven, C., Spanne, P., and Snigirev, A. (1998). X-ray imaging with submicrometer resolution employing transparent luminescent screens. *J. Opt. Soc. Am. A*, 15(7):1940–1951.

(Koo and Jung, 2005) Koo, J.-M. and Jung, S.-B. (2005). Effect of substrate metallization on mechanical properties of sn-3.5ag bga solder joints with multiple reflows. *Microelectronic Engineering*, 82(3):569–574. Proceedings of the ninth european workshop on materials for advanced metallization 2005.

(Krimmel *et al.*, 2005) Krimmel, S., Stephan, J., and Baumann, J. (2005). 3d computed tomography using a microfocus x-ray source: Analysis of artifact formation in the reconstructed images using simulated as well as experimental projection data. *Nuclear Instruments and Methods in Physics Research Section A: Accelerators, Spectrometers, Detectors and Associated Equipment*, 542(1):399–407.

(Krumm *et al.*, 2008) Krumm, M., Kasperl, S., and Franz, M. (2008). Reducing non-linear artifacts of multi-material objects in industrial 3d computed tomography. *Ndt & E International*, 41(4):242–251.

(Kumar *et al.*, 2005) Kumar, A., He, M., and Chen, Z. (2005). Barrier properties of thin au/ni-p under bump metallization for sn-3.5ag solder. *Surface and Coatings Technology*, 198(1):283–286.

(Lara, 2013) Lara, L. (2013). *Effect of Grain Orientation on Electromigration in Sn-0.7 Cu Solder Joints*. PhD thesis, Arizona State University.

(Lee *et al.*, 2001) Lee, T., Tu, K., and Frear, D. (2001). Electromigration of eutectic snpb and snag3.8cu0.7 flip chip solder bumps and under-bump metallization. *Journal of Applied Physics*, 90(9):4502–4508.

(Lewitt and Bates, 1978) Lewitt, R. and Bates, R. (1978). Image-reconstruction from projections. 3. projection completion methods (theory). *Optik*, 50(3):189–204.

(Li *et al.*, 2005) Li, D., Liu, C., and Conway, P. P. (2005). Characteristics of intermetallics and micromechanical properties during thermal ageing of sn-a-cu flip-chip solder interconnects. *Materials Science and Engineering: A*, 391(1):95–103.

(Li *et al.*, 2012) Li, Y., Cai, Y., Pacheco, M., Dias, R. C., and Goyal, D. (2012). Non destructive failure analysis of 3d electronic packages using both electro optical terahertz pulse reflectometry and 3d x-ray computed tomography. In *ISFTA 2012: Conf. Proc. 38th Int. Symp. Test. Failure Anal*, page 95.

(Li *et al.*, 2014) Li, Y., Pacheco, M., Goyal, D., Elmer, J., Barth, H., and Parkinson, D. (2014). High resolution and fast throughput-time x-ray computed tomography for semiconductor packaging applications. In *Electronic Components and Technology Conference (ECTC), 2014 IEEE 64th*, pages 1457–1463.

(Liang *et al.*, 2010) Liang, S., Chen, C., Han, J., Xu, L., Tu, K., and Lai, Y.-S. (2010). Blocking hillock and whisker growth by intermetallic compound formation in sn-0.7 cu flip chip solder joints under electromigration. *Journal of Applied Physics*, 107(9):093715.

(Lin *et al.*, 2006) Lin, D., Srivatsan, T., Wang, G.-X., and Kovacevic, R. (2006). Microstructural development in a rapidly cooled eutectic sn–3.5% ag solder reinforced with copper powder. *Powder technology*, 166(1):38–46.

(Lin *et al.*, 2009a) Lin, H.-J., Lin, J.-S., and Chuang, T.-H. (2009a). Electromigration of sn–3ag–0.5 cu and sn–3ag–0.5 cu–0.5 ce–0.2 zn solder joints with au/ni (p)/cu and ag/cu pads. *Journal of Alloys and Compounds*, 487(1):458–465.

(Lin *et al.*, 2009b) Lin, K., Huang, H., and Chou, C. (2009b). Interfacial reaction between sn1ag0.5cu(co) solder and cu substrate with au/ni surface finish during reflow reaction. *Journal of Alloys and Compounds*, 471(1):291 – 295.

(Lin *et al.*, 2005) Lin, Y., Hu, Y., Tsai, C., Kao, C., and Tu, K. (2005). In situ observation of the void formation-and-propagation mechanism in solder joints under current-stressing. *Acta Materialia*, 53(7):2029–2035.

(Liu *et al.*, 2000) Liu, C., Chen, C., and Tu, K. (2000). Electromigration in sn-pb solder strips as a function of alloy composition. *Journal of Applied Physics*, 88(10):5703–5709.

(Liu *et al.*, 2009) Liu, P., Yao, P., and Liu, J. (2009). Effects of multiple reflows on interfacial reaction and shear strength of snagcu and snpb solder joints with different {PCB} surface finishes. *Journal of Alloys and Compounds*, 470(1):188–194.

(Liu *et al.*, 2008) Liu, Y., Liang, L., Irving, S., and Luk, T. (2008). 3d modeling of electromigration combined with thermal-mechanical effect for ic device and package. *Microelectronics Reliability*, 48(6):811–824. Thermal, Mechanical and Multi-physics Simulation and Experiments in Micro-electronics and Micro-systems (EuroSimE 2007) {IMAPS} Poland 2007.

(Lu *et al.*, 2009) Lu, M., Shih, D.-Y., Goldsmith, C., and Wassick, T. (2009). Comparison of electromigration behaviors of snag and sncu solders. In *Reliability Physics Symposium, 2009 IEEE International*, pages 149–154.

(Lu *et al.*, 2008) Lu, M., Shih, D.-Y., Lauro, P., Goldsmith, C., and Henderson, D. W. (2008). Effect of sn grain orientation on electromigration degradation mechanism in high sn-based pb-free solders. *Applied Physics Letters*, 92(21):211909.

(Ma *et al.*, 2012a) Ma, H., Qu, L., Huang, M., Gu, L., Zhao, N., and Wang, L. (2012a). In-situ study on growth behavior of ag3sn in sn-3.5 ag/cu soldering reaction by synchrotron radiation real-time imaging technology. *Journal of Alloys and Compounds*, 537:286–290.

(Ma *et al.*, 2006) Ma, H., Suhling, J., Lall, P., and Bozack, M. (2006). Reliability of the aging lead free solder joint. In *Electronic Components and Technology Conference, 2006. Proceedings. 56th*, pages 16–pp.

(Ma *et al.*, 2012b) Ma, L., Guo, F., Xu, G., Wang, X., He, H., and Zhao, H. (2012b). Investigation of stress evolution induced by electromigration in sn-ag-cu solder joints based on an x-ray diffraction technique. *Journal of Electronic Materials*, 41(2):425–430.

(Ma *et al.*, 2011) Ma, L., Xu, G., Guo, F., and Wang, X. (2011). Retarding electromigration on the sn-ag-cu solder joints by micro-sized metal-particle reinforcement. In *Electronic Packaging Technology and High Density Packaging (ICEPT-HDP), 2011 12th International Conference on*, pages 1–5.

(Ma *et al.*, 2003) Ma, X., Wang, F., Qian, Y., and Yoshida, F. (2003). Development of cu-sn intermetallic compound at pb-free solder/cu joint interface. *Materials Letters*, 57:3361–3365.

(Maleki *et al.*, 2014) Maleki, M., Cugnoni, J., and Botsis, J. (2014). Isothermal ageing of snagcu solder alloys: Three-dimensional morphometry analysis of microstructural evolution and its effects on mechanical response. *Journal of Electronic Materials*, 43(4):1026–1042.

(Marques *et al.*, 2014) Marques, V., Johnston, C., and Grant, P. (2014). Microstructural evolution at cu/sn-cu/cu and cu/sn-cu/ni-au ball grid array interfaces during thermal ageing. *Journal of Alloys and Compounds*, 613(0):387–394.

(Marshall and Marshall, 2003) Marshall, C. and Marshall, P. (2003). Ccd radiation effects and test issues for satellite designers. *NASA Electronic Parts and Packaging*, page 1053.

(Martin and Koch, 2006) Martin, T. and Koch, A. (2006). Recent developments in x-ray imaging with micrometer spatial resolution. *Journal of Synchrotron Radiation*, 13(2):180–194.

(Masschaele *et al.*, 2007) Masschaele, B., Cnudde, V., Dierick, M., Jacobs, P., Hoorebeke, L. V., and Vlassenbroeck, J. (2007). Ugct: New x-ray radiography and tomography facility. *Nuclear Instruments and Methods in Physics Research Section A: Accelerators, Spectrometers, Detectors and Associated Equipment*, 580(1):266–269. Proceedings of the 10th International Symposium on Radiation Physics {ISRP} 10.

(Mathiesen and Arnberg, 2005) Mathiesen, R. H. and Arnberg, L. (2005). X-ray radiography observations of columnar dendritic growth and constitutional undercooling in an al-30wt%cu alloy. *Acta Materialia*, 53(4):947–956.

(Meng *et al.*, 2009) Meng, F., Zhang, N., and Wang, W. (2009). Virtual experimentation of beam hardening effect in x-ray ct measurement of multiphase flow. *Powder Technology*, 194(1):153–157.

(Meng *et al.*, 2006) Meng, Y., Shaw, C., Liu, X., Lai, C., Tu, S., Altunbas, M., Chen, L., and Wang, T. (2006). Su-ff-i-15: Effects, detection and removal of zingers from scattered x-rays in ccd based cone beam ct. *Medical Physics*, 33(6):2000–2000.

(Menvielle *et al.*, 2005) Menvielle, N., Goussard, Y., Orban, D., and Soulez, G. (2005). Reduction of beam-hardening artifacts in x-ray ct. In *Engineering in Medicine and Biology Society, 2005. IEEE-EMBS 2005. 27th Annual International Conference of the*, pages 1865–1868. IEEE.

(Mertens *et al.*, 2014a) Mertens, J., Williams, J., and Chawla, N. (2014a). Development of a lab-scale, high-resolution, tube-generated x-ray computed-tomography system for three-dimensional (3d) materials characterization. *Materials Characterization*, 92(0):36–48.
(Mertens *et al.*, 2014b) Mertens, J., Williams, J., and Chawla, N. (2014b). A study of pb-rich dendrites in a near-eutectic 63sn-37pb solder microstructure via laboratory-scale micro x-ray computed tomography (microxct). *Journal of Electronic Materials*, pages 1–15.

(Mertens *et al.*, 2014c) Mertens, J. C. E., Williams, J. J., and Chawla, N. (2014c). Note: Design and construction of a multi-scale, high-resolution, tube-generated x-ray computed-tomography system for three-dimensional (3d) imaging. *Review of Scientific Instruments*, 85(1):016103.

(Mizuishi, 1984) Mizuishi, K. (1984). Some aspects of bonding: solder deterioration observed in long-lived semiconductor lasers: Solder migration and whisker growth. *Journal of Applied Physics*, 55(2):289–295.

(Moore *et al.*, 1965) Moore, G. E. *et al.* (1965). Cramming more components onto integrated circuits.

(Mueller, 1998) Mueller, K. (1998). *Fast and accurate three-dimensional reconstruction from cone-beam projection data using algebraic methods*. PhD thesis, The Ohio State University.

(Mueller *et al.*, 1999) Mueller, K., Yagel, R., and Wheller, J. J. (1999). Anti-aliased three-dimensional cone-beam reconstruction of low-contrast objects with algebraic methods. *Medical Imaging, IEEE Transactions on*, 18(6):519–537.

(NIST, 2014) NIST (2014). X-com database. http://physics.nist.gov/PhysRefData/Xcom/html/xcom1-t.html.

(Ogunseitan, 2007) Ogunseitan, O. A. (2007). Public health and environmental benefits of adopting lead-free solders. *JOM*, 59(7):12–17.

(Paciornik and de Pinho Mauricio, 2004) Paciornik, S. and de Pinho Mauricio, M. H. (2004). *ASM Handbook, Digital Imaging*, 9:368.

(Packham, 2010) Packham, D. (2010). Testing and characterisation of scintillator materials for x-ray detection. Master's thesis, University of Surrey, Surrey, UK.

(Padilla *et al.*, 2012) Padilla, E., Jakkali, V., Jiang, L., and Chawla, N. (2012). Quantifying the effect of porosity on the evolution of deformation and damage in sn-based solder joints by x-ray microtomography and microstructure-based finite element modeling. *Acta Materialia*, 60(9):4017–4026.

(Parish, 1990) Parish, M. V. (1990). Development of algorithms for on-focal-plane gamma circumvention and time-delay integration. In *San Dieg-DL Tentative*, pages 120–127. International Society for Optics and Photonics.

(Porter *et al.*, 1991) Porter, D., Easterling, K., and Sherif, M. (1991). *Phase Transformations in Metals and Alloys. 2009*. Boca Raton, FL: CRC Press, 3rd ed. edition.
(Prabhu *et al.*, 2011) Prabhu, K. *et al.* (2011). Reactive wetting, evolution of interfacial and bulk imcs and their effect on mechanical properties of eutectic sn–cu solder alloy. *Advances in colloid and interface science*, 166(1):87–118.

(Qu *et al.*, 2014) Qu, L., Ma, H., Zhao, H., Kunwar, A., and Zhao, N. (2014). In situ study on growth behavior of interfacial bubbles and its effect on interfacial reaction during a soldering process. *Applied Surface Science*, 305(0):133–138.

(Ramanathan *et al.*, 2007) Ramanathan, L. N., Lee, T.-Y., Jang, J.-W., Chae, S.-H., and Ho, P. S. (2007). Current carrying capability of sn0. 7cu solder bumps in flip chip modules for high power applications. In *Electronic Components and Technology Conference, 2007. ECTC'07. Proceedings. 57th*, pages 1456–1461. IEEE.

(Remeysen and Swennen, 2006) Remeysen, K. and Swennen, R. (2006). Beam hardening artifact reduction in microfocus computed tomography for improved quantitative coal characterization. *International journal of coal geology*, 67(1):101–111.

(Ren *et al.*, 2006) Ren, F., Nah, J.-W., Tu, K. N., Xiong, B., Xu, L., and Pang, J. H. L. (2006). Electromigration induced ductile-to-brittle transition in lead-free solder joints. *Applied Physics Letters*, 89(14):141914.

(Rezvani *et al.*, 2007) Rezvani, N., Aruliah, D., Jackson, K., Moseley, D., and Siewerdsen, J. (2007). Oscar: An open-source cone-beam ct reconstruction tool for imaging research. *Medical Physics*, 34(6):2341–2341.

(Rivers, 1998) Rivers, M. (1998). Tutorial introduction to x-ray computed microtomography data processing.

(Rizvia *et al.*, 2006) Rizvia, M., Bailey, C., Chan, Y., and Lu, H. (2006). Comparative wetting behavior of sn-0.7cu and sn-0.7cu-0.3ni solders on cu and ni substrates. In *Electronics Systemintegration Technology Conference, 2006. 1st*, volume 1, pages 145–151.

(Routbort, 1968) Routbort, J. L. (1968). Electromigration in zinc single crystals. *Phys. Rev.*, 176:796–803.

(Sá *et al.*, 2004) Sá, F., Rocha, O. L., Siqueira, C. A., and Garcia, A. (2004). The effect of solidification variables on tertiary dendrite arm spacing in unsteady-state directional solidification of sn–pb and al–cu alloys. *Materials Science and Engineering: A*, 373(1):131–138.

(Sasov *et al.*, 2008) Sasov, A., Liu, X., and Salmon, P. L. (2008). Compensation of mechanical inaccuracies in micro-ct and nano-ct.

(Sasov *et al.*, 2010) Sasov, A., Pauwels, B., Liu, X., and Bruyndonckx, P. (2010). Key components for artifact-free micro-ct and nano-ct instruments. In *SPIE Optical Engineering+ Applications*, pages 78040U–78040U. International Society for Optics and Photonics.

(Sato *et al.*, 2000) Sato, K., Hasegawa, Y., Kondo, K., Miyazaki, K., Matsushita, T., and Amemiya, Y. (2000). Development of a high-resolution x-ray imaging system with a charge-coupled-device detector coupled with crystal x-ray magnifiers. *Review of Scientific Instruments*, 71(12):4449–4456.

(Schena *et al.*, 2005) Schena, G., Favretto, S., Santoro, L., Pasini, A., Bettuzzi, M., Casali, F., and Mancini, L. (2005). Detecting microdiamonds in kimberlite drill-hole cores by computed tomography. *International Journal of Mineral Processing*, 75(3):173–188.

(Schena *et al.*, 2007) Schena, G., Santoro, L., and Favretto, S. (2007). Conceiving a high resolution and fast x-ray ct system for imaging fine multi-phase mineral particles and retrieving mineral liberation spectra. *International Journal of Mineral Processing*, 84(1):327–336. Special Issue To Honor The Late Professor R. Peter King.

(Shao *et al.*, 2004) Shao, T. L., Chen, Y. H., Chiu, S. H., and Chen, C. (2004). Electromigration failure mechanisms for snag3.5 solder bumps on ti-cr/cu and ni(p)/au metallization pads. *Journal of Applied Physics*, 96(8):4518–4524.

(Sidhu and Chawla, 2004) Sidhu, R. and Chawla, N. (2004). Three-dimensional microstructure characterization of ag3sn intermetallics in sn-rich solder by serial sectioning. *Materials Characterization*, 52(3):225–230.

(Sidhu and Chawla, 2006) Sidhu, R. and Chawla, N. (2006). Three-dimensional (3d) visualization and microstructure-based modeling of deformation in a sn-rich solder. *Scripta Materialia*, 54(9):1627–1631.

(Smith *et al.*, 2002) Smith, T. S., Bay, B. K., and Rashid, M. M. (2002). Digital volume correlation including rotational degrees of freedom during minimization. *Experimental Mechanics*, 42(3):272–278.

(Souza *et al.*, 2005) Souza, E. N. d., Cheung, N., and Garcia, A. (2005). The correlation between thermal variables and secondary dendrite arm spacing during solidification of horizontal cylinders of sn–pb alloys. *Journal of alloys and compounds*, 399(1):110–117.

(Sprawls, 2014) Sprawls, P. (2014). The physical princples of medical imaging.

(Stampanoni *et al.*, 2002) Stampanoni, M., Borchert, G., Wyss, P., Abela, R., Patterson, B., Hunt, S., Vermeulen, D., and Rüegsegger, P. (2002). High resolution x-ray detector for synchrotron-based microtomography. *Nuclear Instruments and Methods in Physics Research Section A: Accelerators, Spectrometers, Detectors and Associated Equipment*, 491(1):291–301.

(Stock, 2009) Stock, S. (2009). *Micro Computed Tomography*. CRC Press, Boca Raton, Florida.

(Sun *et al.*, 2006) Sun, P., Andersson, C., Wei, X., Cheng, Z., Shangguan, D., and Liu, J. (2006). High temperature aging study of intermetallic compound formation of sn-3.5ag and sn-4.0ag-0.5cu solders on electroless ni(p) metallization. *Journal of Alloys and Compounds*, 425(1):191–199.

(Sundelin *et al.*, 2006)Sundelin, J. J., Nurmi, S. T., LepistÃƒ, T. K., and Ristolainen, E. O. (2006). Mechanical and microstructural properties of snagcu solder joints. *Materials Science and Engineering: A*, 420(1):55–62.

(Taylor and Lupton, 1986) Taylor, T. and Lupton, L. R. (1986). Resolution, artifacts and the design of computed tomography systems. *Nuclear Instruments and Methods in Physics Research Section A: Accelerators, Spectrometers, Detectors and Associated Equipment*, 242(3):603–609.

(Teramoto *et al.*, 2007) Teramoto, A., Murakoshi, T., Tsuzaka, M., and Fujita, H. (2007). Automated solder inspection technique for bga-mounted substrates by means of oblique computed tomography. *IEEE transactions on electronics packaging manufacturing*, 30(4):285–292.

(Terzi *et al.*, 2010) Terzi, S., Salvo, L., Suery, M., Dahle, A., and Boller, E. (2010). Coarsening mechanisms in a dendritic al–10% cu alloy. *Acta Materialia*, 58(1):20–30.

(Tian *et al.*, 2011) Tian, T., Chen, K., MacDowell, A., Parkinson, D., Lai, Y.-S., and Tu, K. (2011). Quantitative x-ray microtomography study of 3-d void growth induced by electromigration in eutectic snpb flip-chip solder joints. *Scripta Materialia*, 65(7):646–649.

(Tolnai *et al.*, 2012) Tolnai, D., Townsend, P., Requena, G., Salvo, L., Lendvai, J., and Degischer, H. (2012). In situ synchrotron tomographic investigation of the solidification of an almg4. 7si8 alloy. *Acta materialia*, 60(6):2568–2577.

(Tous *et al.*, 2007) Tous, J., Blazek, K., Pena, L., and Sopko, B. (2007). High-resolution x-ray imaging ccd camera based on a thin scintillator screen. *Radiation Measurements*, 42(4):925–928. Proceedings of the 6th European Conference on Luminescent Detectors and Transformers of Ionizing Radiation (LUMDETR 2006).

(Tsuritani *et al.*, 2011) Tsuritani, H., Sayama, T., Okamoto, Y., Takayanagi, T., Uesugi, K., and Mori, T. (2011). Application of synchrotron radiation x-ray microtomography to nondestructive evaluation of thermal fatigue process in flip chip interconnects. *Journal of Electronic Packaging*, 133(2):021007.

(Tsuritani *et al.*, 2007) Tsuritani, H., Sayama, T., Uesugi, K., Takayanagi, T., and Mori, T. (2007). Nondestructive evaluation of thermal phase growth in solder ball microjoints by synchrotron radiation x-ray microtomography. *Journal of Electronic Packaging*, 129(4):434–439.

(Tu, 2011) Tu, K. (2011). Reliability challenges in 3d ic packaging technology. *Microelectronics Reliability*, 51(3):517–523.
(Tu and Zeng, 2001) Tu, K. and Zeng, K. (2001). Tin-lead (snpb) solder reaction in flip chip technology. *Materials Science and Engineering: R: Reports*, 34(1):1–58.

(Tu, 2003) Tu, K. N. (2003). Recent advances on electromigration in very-large-scale-integration of interconnects. *Journal of Applied Physics*, 94(9):5451–5473.

(Uesugi *et al.*, 2011) Uesugi, K., Hoshino, M., and Yagi, N. (2011). Comparison of lens- and fiber-coupled CCD detectors for X-ray computed tomography. *Journal of Synchrotron Radiation*, 18(2):217–223.

(Uhlmann *et al.*, 2008) Uhlmann, N., Salamon, M., Sukowski, F., and Voland, V. (2008). Characterization and comparison of direct and indirect converting x-ray detectors for non-destructive testing (ndt) in low-energy and high-resolution applications. *Nuclear Instruments and Methods in Physics Research Section A: Accelerators, Spectrometers, Detectors and Associated Equipment*, 591(1):46–49. Radiation Imaging Detectors 2007 Proceedings of the 9th International Workshop on Radiation Imaging Detectors.

(Valais *et al.*, 2009) Valais, I., David, S., Michail, C., Nomicos, C., Panayiotakis, G., and Kandarakis, I. (2009). Comparative evaluation of single crystal scintillators under x-ray imaging conditions. *Journal of Instrumentation*, 4(06):P06013.

(Vedula and Munshi, 2008) Vedula, V. and Munshi, P. (2008). An improved algorithm for beam-hardening corrections in experimental x-ray tomography. *NDT & E International*, 41(1):25–31.

(Wang *et al.*, 2011) Wang, M., Williams, J., Jiang, L., De Carlo, F., Jing, T., and Chawla, N. (2011). Dendritic morphology of α-mg in mg-based alloys: three dimensional (3d) experimental characterization by x-ray synchrotron tomography and phase-field simulations. *Scripta Mater*, 65:855–858.

(Wang *et al.*, 2012) Wang, M., Xu, Y., Jing, T., Peng, G., Fu, Y., and Chawla, N. (2012). Growth orientations and morphologies of α-mg dendrites in mg–zn alloys. *Scripta Materialia*, 67(7):629–632.

(Wang *et al.*, 2014) Wang, M., Xu, Y., Zheng, Q., Wu, S., Jing, T., and Chawla, N. (2014). Dendritic growth in mg-based alloys: Phase-field simulations and experimental verification by x-ray synchrotron tomography. *Metallurgical and Materials Transactions A*, 45(5):2562–2574.

(Williams *et al.*, 2010) Williams, J., Flom, Z., Amell, A., Chawla, N., Xiao, X., and De Carlo, F. (2010). Damage evolution in sic particle reinforced al alloy matrix composites by x-ray synchrotron tomography. *Acta Materialia*, 58(18):6194–6205.

(Wood and Nimmo, 1994) Wood, E. and Nimmo, K. (1994). In search of new lead-free electronic solders. *Journal of Electronic Materials*, 23(8):709–713.

(Wu *et al.*, 2004) Wu, A. T., Tu, K. N., Lloyd, J. R., Tamura, N., Valek, B. C., and Kao, C. R. (2004). Electromigration-induced microstructure evolution in tin studied by synchrotron x-ray microdiffraction. *Applied Physics Letters*, 85(13):2490–2492.

(Wu *et al.*, 2012) Wu, S., Hu, Y., Lu, C., Huang, T., Chang, Y., and Liu, C. (2012). Electromigration study on sn (cu) solder/ni (p) joint interfaces. *Journal of electronic materials*, 41(12):3342–3347.

(Xia *et al.*, 2006) Xia, Y., Xie, X., Lu, C., and Chang, J. (2006). Coupling effects at cu(ni)-snagcu-cu(ni) sandwich solder joint during isothermal aging. *Journal of Alloys and Compounds*, 417(1):143–149.

(Xie *et al.*, 2011) Xie, H., Chawla, N., and Shen, Y.-L. (2011). Mechanisms of deformation in high-ductility ce-containing sn–ag–cu solder alloys. *Microelectronics Reliability*, 51(6):1142–1147.

(Xie *et al.*, 2014) Xie, H., Friedman, D., Mirpuri, K., and Chawla, N. (2014). Electromigration damage characterization in sn-3.9ag-0.7cu and sn-3.9ag-0.7cu-0.5ce solder joints by three-dimensional x-ray tomography and scanning electron microscopy. *Journal of Electronic Materials*, 43(1):33–42.

(Xu *et al.*, 2008) Xu, L., Han, J.-K., Liang, J. J., Tu, K., and Lai, Y.-S. (2008). Electromigration induced high fraction of compound formation in snagcu flip chip solder joints with copper column. *Applied Physics Letters*, 92(26):262104–262104–3.

(Xu and Pang, 2006) Xu, L. and Pang, J. (2006). Combined thermal and electromigration exposure effect on snagcu bga solder joint reliability. In *Electronic Components and Technology Conference, 2006. Proceedings. 56th*, pages 6–pp.
(Yamanaka *et al.*, 2010) Yamanaka, K., Ooyoshi, T., and Nejime, T. (2010). Temperature measurement at flip chip solder joint during electromigration test. *Journal of Materials Science: Materials in Electronics*, 21(1):53–57.

(Yang *et al.*, 2008a) Yang, D., Chan, Y., Wu, B., and Pecht, M. (2008a). Electromigration and thermomigration behavior of flip chip solder joints in high current density packages. *Journal of Materials Research*, 23(9):2333–2339.

(Yang *et al.*, 2008b) Yang, D., Chan, Y. C., and Tu, K. N. (2008b). The time-dependent melting failure in flip chip lead-free solder interconnects under current stressing. *Applied Physics Letters*, 93(4):041907–041907.

(Yang *et al.*, 2007) Yang, D., Wu, B. Y., Chan, Y. C., and Tu, K. N. (2007). Microstructural evolution and atomic transport by thermomigration in eutectic tin-lead flip chip solder joints. *Journal of Applied Physics*, 102(4):043502.

(Yazzie *et al.*, 2012a) Yazzie, K., Williams, J., Phillips, N., De Carlo, F., and Chawla, N. (2012a). Multiscale microstructural characterization of sn-rich alloys by three dimensional (3d) x-ray synchrotron tomography and focused ion beam (fib) tomography. *Materials Characterization*, 70:33–41.

(Yazzie *et al.*, 2012b) Yazzie, K., Xie, H., Williams, J., and Chawla, N. (2012b). On the relationship between solder-controlled and intermetallic compound (imc)-controlled fracture in sn-based solder joints. *Scripta Materialia*, 66(8):586–589.

(Yeh *et al.*, 2002) Yeh, E. C. C., Choi, W. J., Tu, K. N., Elenius, P., and Balkan, H. (2002). Current-crowding-induced electromigration failure in flip chip solder joints. *Applied Physics Letters*, 80(4):580–582.

(Yoon and Jung, 2005) Yoon, J.W. and Jung, S.-B. (2005). Interfacial reactions between sn-0.4cu solder and cu substrate with or without enig plating layer during reflow reaction. *Journal of Alloys and Compounds*, 396(1):122–127.

(Zbrzezny *et al.*, 2007) Zbrzezny, A., Snugovsky, P., and Perovic, D. (2007). Impact of board and component metallizations on microstructure and reliability of lead-free solder joints. *Microelectronics Reliability*, 47(12):2205–2214. Electronic system prognostics and health management Thermal, mechanical and multi-physics simulation and experiments in micro-electronics and micro-systems (EuroSimE 2006).

(Zeng *et al.*, 2010) Zeng, G., Xue, S., Zhang, L., Gao, L., Dai, W., and Luo, J. (2010). A review on the interfacial intermetallic compounds between sn-ag-cu based solders and substrates. *Journal of Materials Science: Materials in Electronics*, 21(5):421–440.

(Zhang *et al.*, 2013) Zhang, Z., McGowan, B., Feldmaier, Z., Lloyd, J., McMullen, T., Wilcox, E., and Schultz, S. (2013). Evaluation of constant voltage testing for electromigration study. In *Reliability Physics Symposium (IRPS), 2013 IEEE International*, pages EM–3. IEEE.

(Zhu *et al.*, 2012) Zhu, J., Wang, T., Cao, F., Huang, W., Fu, H., and Chen, Z. (2012). Real time observation of equiaxed growth of sn–pb alloy under an applied direct current by synchrotron microradiography. *Materials Letters*, 89:137–139.